© Copyright 2015

Ivan Li Chuen Yeoh

# Online Self-Calibrating Precision Scanning Fiber Technology with Piezoelectric Self-Sensing

Ivan L. Yeoh

A dissertation

submitted in partial fulfillment of the

requirements for the degree of

Doctor of Philosophy

University of Washington

2015

Reading Committee:

Eric J. Seibel, Chair

Per G. Reinhall

Martin C. Berg

Program Authorized to Offer Degree:

Department of Mechanical Engineering

University of Washington

## Abstract

Online Self-Calibrating Precision Scanning Fiber Technology with Piezoelectric Self-Sensing

Ivan L. Yeoh

Chair of the Supervisory Committee:
Professor Eric J. Seibel
Department of Mechanical Engineering

The scanning fiber technology was invented at the University of Washington more than a decade ago as a novel imaging modality within an extremely compact form factor. Since then, the mechanical design has improved from early 500Hz specimens to recent 11.5kHz prototypes, and systems have been built for pilot studies in minimally invasive surgery and fluorescence imaging with probe diameter as small as 1.1mm. However, the control system (which is crucial for high quality imaging) for these scanning fiber prototypes have not advanced beyond open-loop implementations due to the lack of an appropriate miniature sensor. The absence of closed-loop or adaptive control hinders the performance of scanning fiber systems in practical operating environments.

This dissertation presents three major advancements to the scanning fiber technology. Firstly, this work introduces novel piezoelectric self-sensing methods to the scanning fiber architecture. Not only does piezoelectric self-sensing provide an online miniature sensor, it also functions without any modification to the mechanical structure by using the same piezoelectric elements for both actuation and sensing. A new piezoelectric self-sensing circuit is also described and shown to provide online measurements of scan tip deflection that was hitherto unavailable.

Secondly, this work introduces new electromechanical modeling approaches together with methods for empirical system identification using piezoelectric self-sensing. The nature of piezoelectricity and integration of the new self-sensing circuit mean that the scanning fiber system should be modeled in both the mechanical and electrical domains. This work presents both a physically interpretative and a modal-analysis-driven electromechanical model verified with the actual scanning fiber system. System identification and model reduction techniques are also developed that extract empirical models then used for accurate scan control.

Finally, this dissertation presents the development and verification of two new adaptive control schemes using piezoelectric self-sensing. An adaptive feedforward approach and a run-to-run optimization controller are introduced and experimentally demonstrated to outperform de-facto open-loop control methods even under time-varying mechanical and thermal stress. Together, these contributions enable for the first time self-calibration by the scanning fiber device to maintain high image quality through changing operating conditions, greatly improving the usability and maturity of the scanning fiber technology.

# TABLE OF CONTENTS

# LIST OF FIGURES

# LIST OF TABLES

# ACKNOWLEDGEMENTS

I wish to express my deepest gratitude to Professor Eric Seibel for this opportunity to pursue my dreams and to contribute in an amazing project. I am very grateful to Professor Per Reinhall and Professor Martin Berg for being supportive advisory members. I also thank very much Dr. Brian Schowengerdt, Richard Johnson, Charles Melville, my Human Photonics Laboratory friends and Magic Leap Inc.

# DEDICATION

To my family, my mother, father, sister and aunt.

To the Hope that all things are made beautiful.

# Chapter 1. INTRODUCTION

## 1.1 MOTIVATION

The conventional approach to use a fixed array of millions of electro-optical transducing elements in imaging and display devices hampers further device miniaturization. For imaging, current technologies like Charged-Coupled Device (CCD) and Complementary Metal-Oxide Semiconductor (CMOS) sensors employ large arrays of photo-sensitive cells that convert light into electrical charge. For display, technologies like Liquid-Crystal Display (LCD) and Organic Light-Emitting Diode (OLED) use microscopic arrays of light emitting cells. In both applications, these grids are comprised of tens of millions of electro-optical elements. Besides the intrinsic manufacturing cost and complexity, this electro-optical element array approach trades miniaturization for higher resolution: to acquire high-definition images, a large number (and subsequently a wide area) of imaging cells are needed. The smallest imagers and displays are approaching the size limit at about 3mm-diameter [1].

Device miniaturization is needed to advance endoscopy applications and is highly desirable for new human-computer interfaces. The ability to image inside the human body with endoscopy is indispensible to medical practice and research, but the reach of endoscopic probes into internal organs is limited by the size and rigidity of the endoscope. Conventional Coherent Fiber-optic Bundle (CFB) designs rely on arrays of fiber-optic cables and photo-detectors that cannot achieve both high resolution and Field-of-View (FOV) below about a 3mm-diameter form factor. The rigidity of the thick fiber bundles also poses the problem of safe insertion into sensitive body cavities [1]. In the development of new interface technologies, the miniaturization of displays to the millimeter-scale will open up new classes of ultra-portable projection displays and highly ergonomic wearable displays that have the potential to transform how we interact with information and each other.

## 1.2 SCANNING FIBER TECHNOLOGY: STATE OF THE ART

At the University of Washington, a novel imaging/display solution has been developed where a single optical element – an optical fiber – is spatially scanned by a miniature piezoelectric-tube.

This method enables dramatically compact devices since a single 80-micron diameter fiber that is precisely vibrated replaces the millions of optical transducers in conventional cameras or display panels.

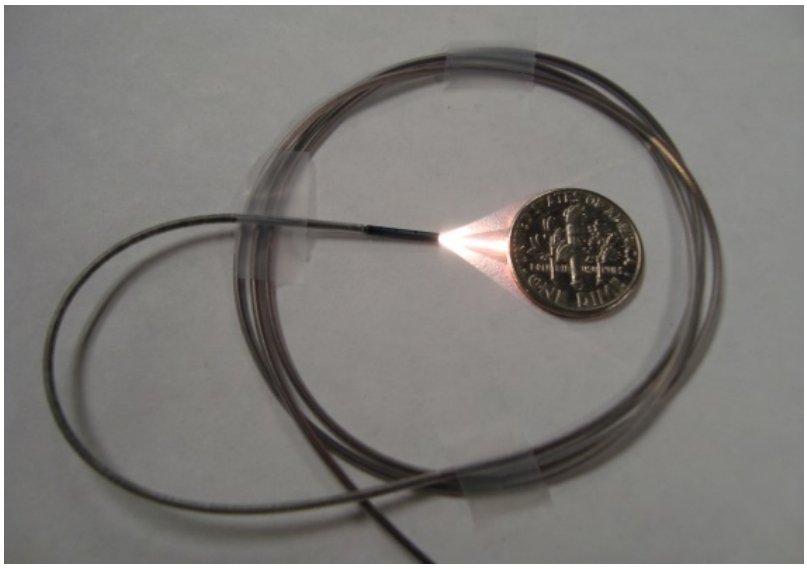

Figure 1.1. 1.2-millimeter diameter flexible Scanning Fiber Endoscope (SFE).

A highly successful application of the scanning fiber technology is in the development of the Scanning Fiber Endoscope (SFE). With the SFE, red-green-blue laser light is steered through the single optical fiber by piezoelectrically exciting the microcantilever close to resonance. Miniature lenses focus the laser light into a small spot on the object or illumination plane (e.g. respiratory track or surgical cavity). This laser spot is rapidly scanned across the field by precise electromechanical actuation while the reflected light is registered to generate images at video rate (30-60fps). The entire scan engine is contained within a 1.2mm-diameter by 9mm-long rigid probe, while the thin electrical wires and optical fibers run through a 2m-long flexible tether. This unprecedented form factor makes possible highly non-invasive medical procedures [2]–[4], small-footprint robotic vision sensors [5], new tools for manufacturing quality control [6], [7] and potentially many more unexplored applications.

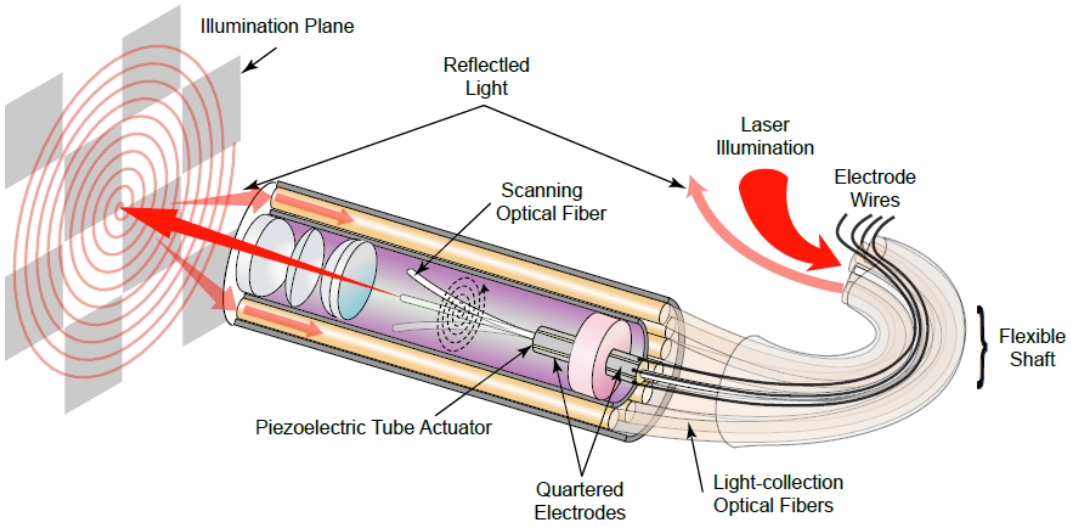


Figure 1.2. The SFE 1.2-millimeter diameter probe houses miniature lenses, a piezoelectric tube and a scanning optical fiber. The 2-meter flexible tether carries the optical fibers and electrode wires.

The state of the art of the SFE is a 1.2-millimeter diameter probe scanned at 11.5kHz, operating in open-loop after an initial optical calibration within a purpose-built chamber. Previous generation SFE designs include the 500Hz scanner studied by Smithwick [8] and the 5kHz design studied by Kundrat [9]. The work in this dissertation was performed on the latest scanner design with a much higher resonant frequency at 11.5kHz. In current Scanning Fiber Endoscope prototypes being used for clinical tests such as published in [10], [11], the latest calibrated open-loop control method presented by Kundrat et al. [9] is the de-facto approach: Prior to use, the endoscope probe is inserted into a calibration chamber where it is coupled to a large external optical position detector that provides measurement of the laser spot position. A trained operator then manually calibrates the device using feedback from the optical position sensor. Finally, the device is uncoupled from the measurement system and used in endoscopic procedures, where operating conditions can be drastically different compared to the calibration chamber.

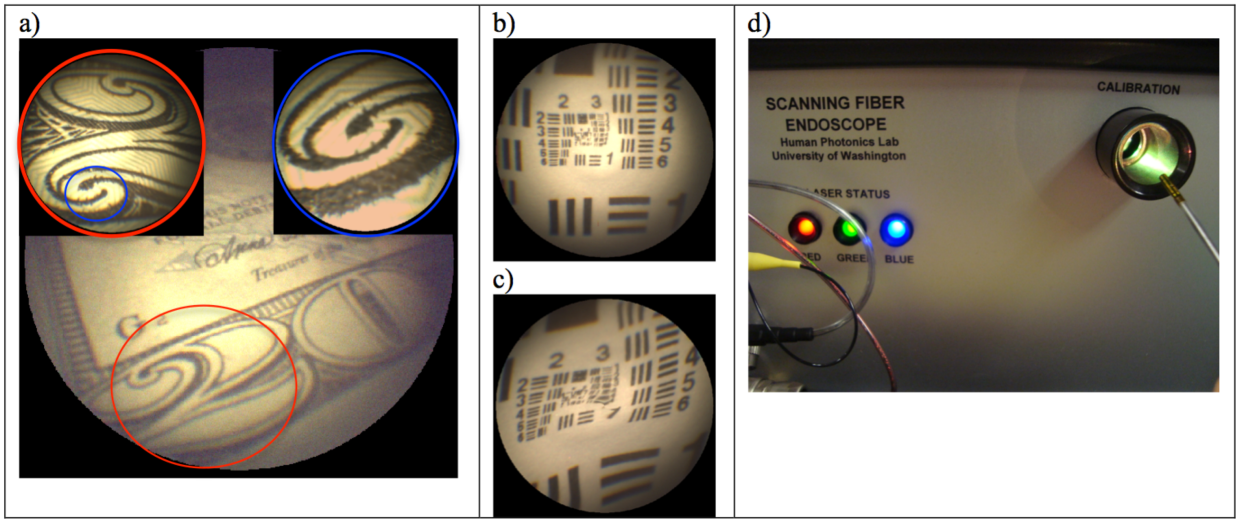


Figure 1.3. a) Images taken with the SFE. By bringing the endoscope closer to the object we get high-resolution zoom-in images. b) Undistorted SFE image. c) Distorted SFE image requiring system recalibration. d) Inserting the probe (upper right) into the calibration chamber for recalibration, a procedure eliminated by this work.

## 1.3 Need for a Better Solution

The use of mechanical scanning shrinks the device dimensions but places stringent requirements for miniature displacement sensors and precise control systems. Because a single element is spatially scanned to (in a sense) simulate an array of optical units, the accuracy and precision with which the optical fiber is positioned over time is crucial for high-quality, distortion-free images. Space is limited within the 1.2mm-diameter probe that houses a 0.8mm-diameter lens assembly, 0.45mm-diameter piezoelectric-tube and other components. The 11.5kHz scan frequency also imposes a high bandwidth requirement on potential sensing modalities. Consequently, until recently no integrated displacement sensor was available to measure the deflections of the optical fiber during operation. As a result, control systems developed for the Scanning Fiber Endoscope have all been open-loop methods which could not adapt to changing operating conditions while in use, e.g. inside a contracting or warming gastrointestinal track during surgery.

A self-calibrating feature must be introduced to the scanning fiber technology to improve its usability and extended-duration applications. Currently, a trained operator must manually and heuristically tune the 20 parameters of the scan input parameters as shown in Figure 1.4, to get an acceptable low-distortion image. This complicated setup precludes plug-and-play usability of the scanning fiber technology. Furthermore, because the manual calibration must be performed while the endoscope probe is coupled within the calibration chamber, the endoscope cannot be recalibrated while it is in use, which is when operating conditions can vary greatly compared to the calibration enclosure. In addition, when the scope probe is sterilized, the elevated clinical sterilization temperature and chemical-material interactions may cause the scanner parameters to drift, necessitating recalibration. Not having to dock the scope probe into a calibration chamber will preserve device sterility, enabling its optimal use in all surgical procedures. Currently, any adjustment to SFE scan operation after sterilization relies on the surgeon holding the scope to a sterile fabric and having an engineer outside the sterile field to observe the captured image and conduct a slow trial and error approach to minimize any obvious image distortions. Finally, self-calibration is a requirement for a scanning fiber display in consumer devices. A display device that needs to be manually recalibrated before every use will not be acceptable for commercialization.

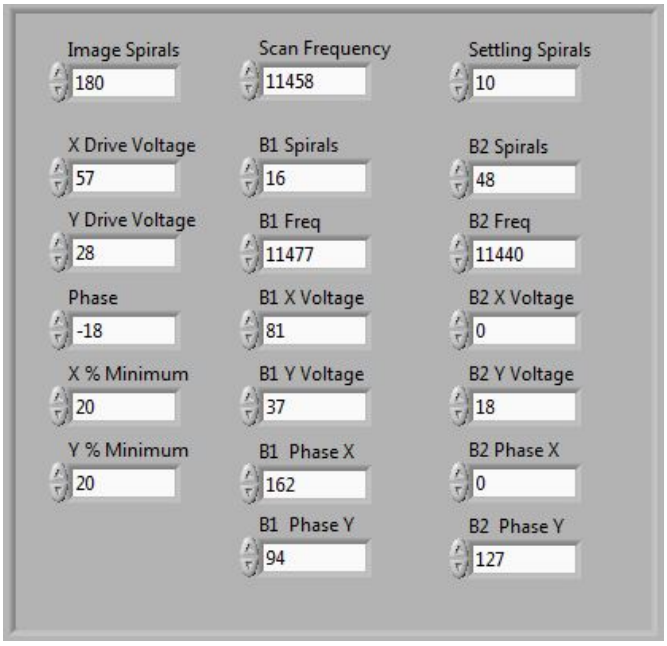


Figure 1.4. Scan input parameters that must be manually selected on current SFE system software.

## 1.4 DISSERTATION ROADMAP

With the goal of advancing the scanning fiber technology to further maturity, three specific aims were set out for this work:

1. Pioneer piezoelectric self-sensing as a miniature sensing modality for the SFE and miniature scanners in general.
2. Develop electromechanical models suitable with piezoelectric self-sensing.
3. Develop an online self-calibrating control scheme.

The chapters of this dissertation are organized as follows:

In Chapter 2, a review of piezoelectricity and sensing will be given before the first method, time-multiplexed piezoelectric self-sensing, is introduced as the initial development towards integrated sensing on the SFE. Time-multiplexed piezoelectric self-sensing will be shown to replace previous optical sensing methods in the de facto calibration algorithm.

In Chapter 3, the second method, simultaneous piezoelectric self-sensing is introduced. The theory behind simultaneous piezoelectric self-sensing will set the foundation for the development of a new piezoelectric self-sensing circuit designed specifically for the scanning fiber device. Implementation details will also be discussed. Simultaneous piezoelectric self-sensing with the SFE is a major contribution of this dissertation and will be the method expanded upon in later sections.

In Chapter 4, electromechanical modeling of the SFE oriented towards scan control will be developed. A review of related and previous work will help frame the unique approach taken in this dissertation on electromechanically modeling the entire system as a circuit-equivalent network. This first modeling approach will be verified with experimental data. A second modeling approach will also be presented that takes inspiration from modal analysis. System identification and model order reduction techniques will be described that enables empirically driven modeling of actual system dynamics.

In Chapter 5, control design for scanning fiber devices is analyzed to inform control system development. Based on the specific operating qualities of the SFE, input shaping methods are presented to achieve better control performance. Appropriate metrics for image quality are discussed and a radial/tangential error convention is defined for quantifying the performance of control methods introduced in later chapters.

In Chapter 6, a new adaptive feedforward controller is presented that incorporates the piezoelectric self-sensing methods developed earlier in this dissertation. The system identification and system inversion algorithms are described. Implementation details, experimental methodology and experimental results demonstrating accurate self-calibration will also be detailed.

In Chapter 7, a novel run-to-run optimization controller is introduced that improves upon the performance of the adaptive feedforward control. A general review of learning-type control is given followed by detailed derivation of the run-to-run optimization method customized for the SFE system. Simulation examples are given to further explore the formulation followed by reports on experimental investigations that demonstrate the improved performance of the optimizing control.

In Chapter 8, further control method explorations in analysis and simulation are discussed. Viability of iterative learning control methods with piezoelectric self-sensing-enabled SFE systems is analyzed and a new complementary observation method is proposed.

Finally, in Chapter 9 the conclusions drawn from this project are discussed with notes directions for future work.

# Chapter 2. TIME-MULTIPLEXED PIEZOELECTRIC SELF-SENSING

To accomplish online recalibration, new displacement measurement modalities must be explored to replace the large optical sensor within the calibration chamber. These measurement modalities must be operational even when the device is in use, so that the scanning fiber system can adapt to changing environmental conditions to maintain high image quality. Alternatives for eliminating image distortion can be distinguished into two general categories: image-based calibration, and miniature sensors.

For an imaging device, image-based calibration, where the captured image is analyzed and used to correct for scan distortion can be employed. Examples have been demonstrated in Atomic Force Microscopy (AFM), where deviation from the intended path is inferred by misaligned points of interest, and used to update the control input [12]. Points of interest in the image are also used to infer the position of the scan to iteratively identify the transfer function dynamics of the system [13]. Image-based calibration have also been used to estimate and compensate for hysteresis effects [14]. Current SFE prototypes can perform image-based calibration as well: By imaging a checkerboard pattern an algorithm detects the corners of the checkerboard and compares the corner positions to an undistorted checkerboard pattern. A warping transform is calculated and its inverse applied to undistort images.

Nonetheless, image-based calibration is not an ideal solution for tackling scan distortion for scanning fiber devices in general. Firstly, image-based calibration typically requires viewing a reference pattern each time a correction is to be performed. The reference pattern – e.g. checkerboard or known molecular structure as in [14], [15] – is required for the algorithm to infer deviations from a perfect scan. This method is not practical for e.g. surgical endoscopy because during operation the reference checkerboard pattern is not viewed. Image based calibration is still not an online correction, though sterility of the probe can be maintained if re-calibration only involves holding the probe to a calibration pattern instead of docking it into a non-sterile calibration chamber. The second drawback of image-based calibration is that it cannot be applied to non-imaging applications of the scanning fiber technology, such as miniature display devices. An ideal solution should be applicable to all scanning fiber devices.

The second approach is to use miniature sensors small enough to fit into the <1.2mm diameter scan probe housing that is also containing a 0.8mm-diameter lens assembly, 0.45mm-diameter piezoelectric-tube and other components. Candidate micro-sensor technologies include electrostatic, capacitive, piezoresistive and piezoelectric elements. Capacitive CMOS sensors have been integrated into microcantilevers [16]. Capacitive sensors have also been used for feedback control of piezoelectric tubes [17], [18] but the bandwidth-limited sensors were external implements and scan frequency was only in the 10's of Hz. Resistive strain-sensing or piezoresistive sensors have also been applied to microcantilevers [19], [20]. Because these sensing methods are separate from the actuation element, additional components must be integrated into the scanning structure, increasing the footprint and complexity of the device, and manufacturing costs.

The fiber scanner already uses piezoelectric elements (a piezoelectric-tube) to actuate the optical fiber. This same piezoelectric-tube may be used as a sensor – with zero modifications to the device. This dissertation was the first work to explore using the piezoelectric-tube already in the scanning fiber system as a miniature sensing modality.

## 2.1 PIEZOELECTRICS

Piezoelectricity is a very useful phenomenon where electrical energy can be converted into mechanical energy and vice versa. Two complementary properties are observed in piezoelectric materials: When a piezoelectric material is mechanically strained, it generates charge due to the *direct piezoelectric effect*. Conversely, when an electric field is applied across a piezoelectric material, it generates strain due to the *converse piezoelectric effect*. The ability to perform mechanical work and sense strain is extremely useful. Electrical energy is ubiquitous and electronics has revolutionized human life. Piezoelectric materials combine all these advantages, so it is no surprise that myriad innovative uses for piezoelectric materials have been and are being discovered. For example, piezoelectric materials are applied in accelerometers and gyroscopes used in navigation systems and automobile safety; structural vibration sensors and active vibration damping (by applying both the direct and converse piezoelectric effect); as magnetic-field-free transformers; as piezoelectric stepper motors and much more. In all these applications, the simplicity of the piezoelectric method is remarkable: by applying an electric

field, the material itself contracts or expands – in contrast to complicated pistons, stator and armature designs for conventional gasoline or electric motors.

The scanning fiber device currently uses the *converse* piezoelectric effect to achieve precise deflection with a simple configuration. This work pursues also recruiting the *direct* piezoelectric effect for integrated sensing.

Piezoelectric materials exhibit directionality in their properties dictated by the orientation of *poling*. Figure 2.1 shows the crystal lattice structure for PZT, a common piezoelectric material. Above the Curie temperature $T_c$, the cubic phase is not polarized as in Figure 2.1a. In order to align the piezoelectric domains, a process called *poling* is performed where a strong electric field is applied across the material above the Curie temperature while it is gradually cooled. Below the Curie temperature, the tetragonal phase has an asymmetrical crystal structure with intrinsic polarization aligned to the poling direction, as shown in Figure 2.1b. Notice that in this structure, the central cation atom (which has a positive charge) is displaced upwards from the center of the crystal lattice. This asymmetry produces a net electric dipole in the crystal lattice. Now, if the crystal structure is strained, the electric dipole will be displaced and an effective electric charge generated. Likewise, if an electric field is applied in the vertical direction, the crystal structure will experience stress and produce strain. Only certain materials with such lattice asymmetry (non-centrosymmetric) can exhibit piezoelectricity. Note that the piezoelectric effect is contingent on the bulk orientation of piezoelectric domains in a polycrystalline piezoelectric material. Similar to magnetic materials, if the dipole directions of the separate crystal grains are randomly organized, the macro-structure will not possess discernible piezoelectric qualities unless poling is applied.

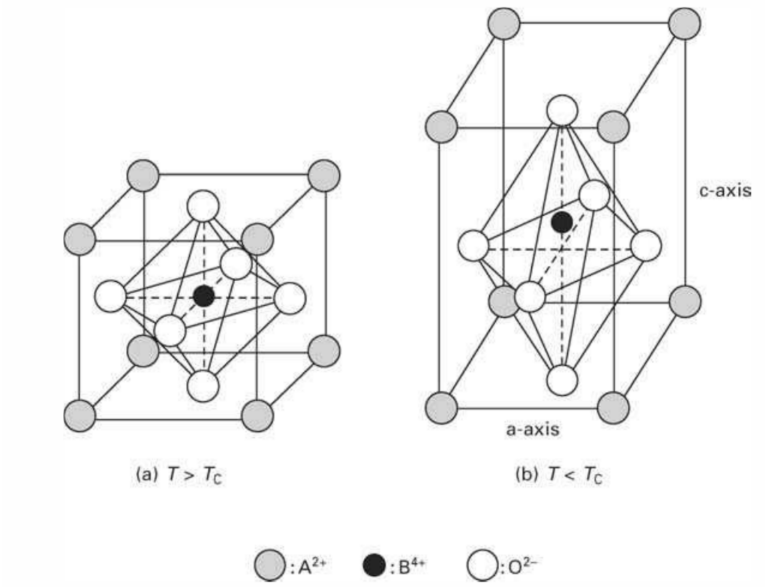


Figure 2.1. Perovskite $ABO_3$ structure of common piezoelectric materials. a) Above the Curie Temperature $T_c$, the cubic state is not polarized. b) Below $T_c$ the tetragonal phase is intrinsically polarized due to off-axis cation B. [21]

The piezoelectric constitutive relations given by the IEEE standard [22] are summarized below.

$$D_i = \varepsilon_{ij}^T E_j + d_{im}^d T_m \tag{2.1}$$

$$S_k = d_{jk}^c E_j + s_{km}^E T_m \tag{2.2}$$

Or equivalently,

$$\begin{bmatrix} \boldsymbol{D} \\ \boldsymbol{S} \end{bmatrix} = \begin{bmatrix} \boldsymbol{\varepsilon}^T & \boldsymbol{d}^d \\ \boldsymbol{d}^c & \boldsymbol{s}^E \end{bmatrix} \begin{bmatrix} \boldsymbol{E} \\ \boldsymbol{T} \end{bmatrix} \tag{2.3}$$

The vector $\boldsymbol{D}$ (3 × 1) is the electric displacement (Coulomb/m$^2$), $\boldsymbol{S}$ (6 × 1) is the strain vector (dimensionless), $\boldsymbol{E}$ (3 × 1) is the electric field (Volt/m) and $\boldsymbol{T}$ (6 × 1) is the stress vector (N/m$^2$). The piezoelectric constants are the $\boldsymbol{\varepsilon}^T$ (3 × 3) dielectric permittivity (Farad/m), the $\boldsymbol{d}^d$ (3 × 6) and $\boldsymbol{d}^c$ (6 × 3) piezoelectric coefficients (Coulomb/N or m/Volt), and the $\boldsymbol{s}^E$ (6 × 6) elastic compliance (m$^2$/N). The piezoelectric coefficient $\boldsymbol{d}^c$ (m/Volt) defines strain per unit electric field at constant stress and $\boldsymbol{d}^d$ (Coulomb/N) defines electric displacement per unit stress at constant electric field. The superscripts *c* and *d* denote the converse and direct piezoelectric effects,

though these coefficients are typically equal. The superscripts *T* and *E* indicate that the quantity is measured at constant stress and constant electric field respectively [23].

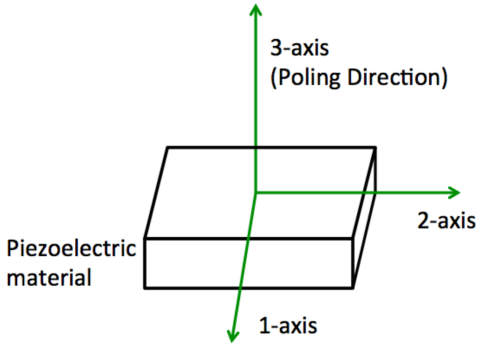


Figure 2.2. Axis convention for piezoelectric element.

The poling direction is usually denoted as the 3-axis while the 1- and 2- axes span the planes orthogonal to the poling direction. Taking into account the symmetry of the tensors, the notation may be reduced to a compressed matrix form by replacing *ij* or *jk* by *m*, where the *ij* or *jk* are valued 1,2,3 and *m* is valued 1,2,3,4,5,6. The convention is summarized in the following table:

Table 2.1. Compressed piezoelectric tensor notation.

| ij or jk | m |
|---|---|
| 11 | 1 |
| 22 | 2 |
| 33 | 3 |
| 23 or 32 | 4 |
| 31 or 13 | 5 |
| 12 or 21 | 6 |

The piezoelectric coefficients $\boldsymbol{d}^d$ can be expressed by:

$$\boldsymbol{d}^d = \begin{bmatrix} 0 & 0 & d_{31} \\ 0 & 0 & d_{32} \\ 0 & 0 & d_{33} \\ 0 & d_{24} & 0 \\ d_{15} & 0 & 0 \\ 0 & 0 & 0 \end{bmatrix} \tag{2.4}$$

$\boldsymbol{d}^c$ is typically the transpose of $\boldsymbol{d}^d$. $d_{31}$, $d_{32}$ and $d_{33}$ relate the normal strain in the 1-, 2- and 3-directions respectively to an electric field along the poling direction, $E_3$. The coefficients $d_{15}$ and $d_{24}$ relate the shear strain in the 1-3 and 2-3 plane to the electric field $E_1$ and $E_2$, respectively. It is not possible to apply or detect shear in the 1-2 plane (orthogonal to poling direction) purely by application or measurement of an electric field within the material [23].

The compliance matrix $\boldsymbol{s}^E$ can be expressed as:

$$\boldsymbol{s}^E = \begin{bmatrix} S_{11} & S_{12} & S_{13} & 0 & 0 & 0 \\ S_{12} & S_{22} & S_{23} & 0 & 0 & 0 \\ S_{13} & S_{23} & S_{33} & 0 & 0 & 0 \\ 0 & 0 & 0 & S_{44} & 0 & 0 \\ 0 & 0 & 0 & 0 & S_{55} & 0 \\ 0 & 0 & 0 & 0 & 0 & S_{66} \end{bmatrix} \tag{2.5}$$

The permittivity matrix $\boldsymbol{\varepsilon}^T$ can be expressed by:

$$\boldsymbol{\varepsilon}^T = \begin{bmatrix} \varepsilon_{11}^T & 0 & 0 \\ 0 & \varepsilon_{22}^T & 0 \\ 0 & 0 & \varepsilon_{33}^T \end{bmatrix} \tag{2.6}$$

The stress vector $\boldsymbol{T}$ is denoted by:

$$\boldsymbol{T} = \begin{bmatrix} T_1 \\ T_2 \\ T_3 \\ T_4 \\ T_5 \\ T_6 \end{bmatrix} = \begin{bmatrix} T_{11} \\ T_{22} \\ T_{33} \\ T_{23} \\ T_{31} \\ T_{12} \end{bmatrix} = \begin{bmatrix} T_{11} \\ T_{22} \\ T_{33} \\ T_{32} \\ T_{13} \\ T_{21} \end{bmatrix} \tag{2.7}$$

Equation 2.1 represents the sensor equation and Equation 2.2 represents the actuator equation [23].

### 2.1.1 *Note on Electric Displacement*

Here the concept of electric displacement is discussed further. According to Encyclopedia Britannica, "electric displacement ... represents that aspect of an electric field associated solely with the presence of separated free electric charges, purposely excluding the contribution of any electric charges bound together in neutral atoms or molecules", "The value of the electric

displacement D may be thought of as equal to the amount of free charge on one plate divided by the area of the plate". The electric displacement for materials is defined as:

$$\boldsymbol{D} = \varepsilon_0 \boldsymbol{E} + \boldsymbol{P} \tag{2.8}$$

$\boldsymbol{D}$ (Coulomb/m$^2$) is the electric displacement field (not to be confused with 'dielectric'), $\boldsymbol{E}$ (Volt/m) is the electric field, $\boldsymbol{P}$ (Coulomb/m$^2$) is the electric polarization, $\varepsilon_0$ (Farad/meter) is the free space permittivity.

$\boldsymbol{P}$, also called polarization density, is the electric dipole moment $\boldsymbol{d}$, per unit volume $\boldsymbol{V}$, in a dielectric:

$$\boldsymbol{P} = \frac{\boldsymbol{d}}{\boldsymbol{V}} \tag{2.9}$$

Assuming a dielectric in its relaxed state has no dipole moment, then for a linear and isotropic dielectric material, the electric polarization $\boldsymbol{P}$ depends linearly and is in the same direction as the applied electric field $\boldsymbol{E}$:

$$\boldsymbol{P} = \varepsilon_0 \chi \boldsymbol{E} \tag{2.10}$$

Where $\chi$ is a material-dependent constant.

Substituting Equation 2.10 into Equation 2.8, we get:

$$\boldsymbol{D} = \varepsilon_0 \boldsymbol{E} + \varepsilon_0 \chi \boldsymbol{E} \tag{2.11}$$

$$\boldsymbol{D} = \varepsilon_0 (1 + \chi) \boldsymbol{E} \tag{2.12}$$

$$\boldsymbol{D} = \varepsilon \boldsymbol{E} \tag{2.13}$$

Where now the material-specific permittivity $\varepsilon$ relates electric field $\boldsymbol{E}$ to the defined quantity electric displacement $\boldsymbol{D}$.

In piezoelectric materials, Equation 2.1 relates electric displacement not only to the applied electric field but also to the material stress.

## 2.2 PIEZOELECTRIC SENSING

Piezoelectric sensing is the application of the direct piezoelectric effect to measure the strain of a piezoelectric element. From Equation 2.1, if the applied electric field is zero i.e. for a sensing element, then the electric displacement $D$ is purely a function of the mechanical stress. The free charge within a piezoelectric sensor is related to the electric displacement by:

$$q = \iint [D_1 \quad D_2 \quad D_3] \begin{bmatrix} dA_1 \\ dA_2 \\ dA_3 \end{bmatrix} \tag{2.14}$$

$dA_1$, $dA_2$ and $dA_3$ are the components of the electrode areas orthogonal to the 1-, 2- and 3- axes respectively. The measured voltage signal $V_c$ is related to the charge by the piezoelectric capacitance $C_p$.

$$V_c = \frac{q}{C_p} \tag{2.15}$$

Thus the measured voltage is related to the piezoelectric strain [23].

Piezoelectric patches as dedicated sensors have been used extensively in the control of microcantilevers [24] and piezoelectric tubes. 12-quadrant piezoelectric tubes have been proposed, where 4 patches are used as integrated sensing elements [25], [26]. The benefit of these methods is that the sensor is closely coupled to the structure. However, because these piezoelectric patches are used only for sensing, less surface area is available for actuation. Also, the sensor and actuators are not collocated.

## 2.3 PIEZOELECTRIC SELF-SENSING

Piezoelectric self-sensing is the dual-use of a piezoelectric element as both an actuator and sensor at the same time. Piezoelectric self-sensing is highly advantageous because it enables collocated control, reduces the complexity of the controlled system, and with proper circuitry enables any piezoelectric actuator to be upgraded into a self-sensing unit. Two methods of piezoelectric self-sensing will be presented in this dissertation: time-multiplexed and simultaneous piezoelectric self-sensing.

*Time-multiplexed piezoelectric self-sensing* is a method where the same piezoelectric element is used for actuation and sensing, but at different times. The piezoelectric patch is switched between the actuation and sensing modes electronically as needed. This method is advantageous in its simplicity, since no additional modifications or additions are needed with the controlled system.

*Simultaneous piezoelectric self-sensing* refers to the use of a piezoelectric element for actuation and sensing at the same time – no switching is needed since actuation and sensing occur concurrently, which is the main advantage of this method. Piezoelectric self-sensing in

literature typically refers to simultaneous self-sensing. This self-sensing method will be expanded upon in Chapter 3, and the bulk of this dissertation concerns using simultaneous piezoelectric self-sensing for SFE self-calibration techniques.

## 2.4 Time-Multiplexed Piezoelectric Self-Sensing for Open Loop Control

Time-multiplexed piezoelectric self-sensing was the first method developed in this work to demonstrate piezoelectric sensing as a miniature sensing modality for the SFE, replacing the optical sensing methods previously used. Time-multiplexed piezoelectric self-sensing is simple to implement and may find application in other piezoelectrically-actuated systems.

This section presents implementation of time-multiplexed piezoelectric self-sensing with the de facto open-loop control previously developed by Kundrat [27], [28] that is used in current state-of-the art SFE prototypes. To understand the context of the problem, the parameters for the open-loop control are first discussed.

### 2.4.1 *Eigendirections*

To achieve whirl-free excitation of the optical fiber, Kundrat introduced the concept of virtual axes, or eigendirections [27], which was based on the concept of two orthogonal linear oscillators [28]. In a separate work, Schitter et al. also consider two orthogonal linear systems to model the dynamics of a piezoelectric tube for scan control purposes [29]. In this section I expand upon Kundrat's eigendirections concept to give a detailed description of the whirling phenomenon as produced by two orthogonal linear systems.

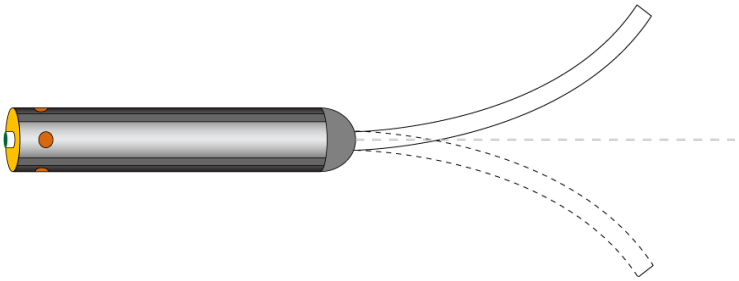

Figure 2.3. Example first mode optical fiber vibration.

In order to achieve high tip displacement and hence high field-of-view, the cantilever is excited at its 1st resonant mode. This mode shape is illustrated in Figure 2.3. Accurate approximation of the 1st mode response is obtained using a linear harmonic oscillator model [28]:

$$\ddot{x} + 2\zeta\omega_0\dot{x} + \omega_0^2 x = \frac{F}{m} \tag{2.16}$$

$x(t)$ is the amplitude, $\zeta$ the effective damping, $\omega_0$ the undamped natural frequency and $m$ the effective mass of the vibration mode respectively, with $F(t)$ as the forcing function. Since this is a 2D scanner, dynamics is modeled as two orthogonal harmonic oscillators:

$$\begin{bmatrix} \ddot{x}_1 + 2\zeta_1\omega_{0,1}\dot{x}_1 + \omega_{0,1}^2 x_1 \\ \ddot{x}_2 + 2\zeta_2\omega_{0,2}\dot{x}_2 + \omega_{0,2}^2 x_2 \end{bmatrix} = \begin{bmatrix} \frac{F_1}{m_1} \\ \frac{F_2}{m_2} \end{bmatrix} \tag{2.17}$$

The subscripts 1 and 2 refer to the Eigendirections 1 and 2 respectively. If the optical fiber is perfectly circular and rotationally symmetric, the parameters in rows 1 and 2 of Equation 2.17 are equal.

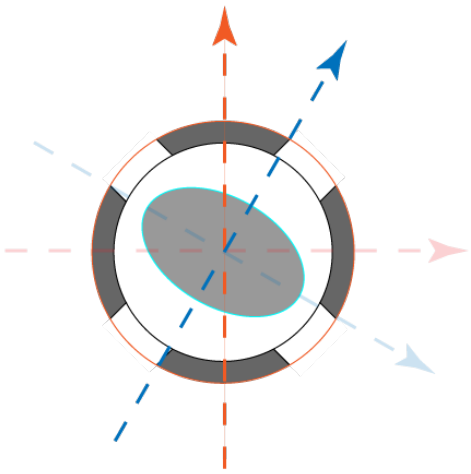

Figure 2.4. The piezoelectric-tube axes (vertical and horizontal axes) do not align with the Eigendirections (rotated axes) due to random fiber ovularity.

Typical manufactured scanners have imperfections and are not rotationally symmetric, exhibiting fiber ovularity as illustrated in Figure 2.4. Thus, the parameters in rows 1 and 2 of Equation 2.17 are not equal. It is crucial to identify the orientations of Eigendirection 1 and 2, with respect to the piezoelectric-tube electrodes: The quartered piezoelectric-tube has its own

two axes corresponding to its electrodes, but these are not aligned with the Eigendirections as depicted in Figure 2.4. The Eigendirections depend on random imperfections or fiber ovularity and vary with each manufactured SFE [27]. Thus, each SFE system has a unique rotation transformation between the piezoelectric-tube axes and the Eigendirections:

$$\begin{bmatrix} F_{1,Eigendirection} \\ F_{2,Eigendirection} \end{bmatrix} = \begin{bmatrix} cos\theta & -sin\theta \\ sin\theta & cos\theta \end{bmatrix} \begin{bmatrix} F_{1,Piezoelectric-tube} \\ F_{2,Piezoelectric-tube} \end{bmatrix} \tag{2.18}$$

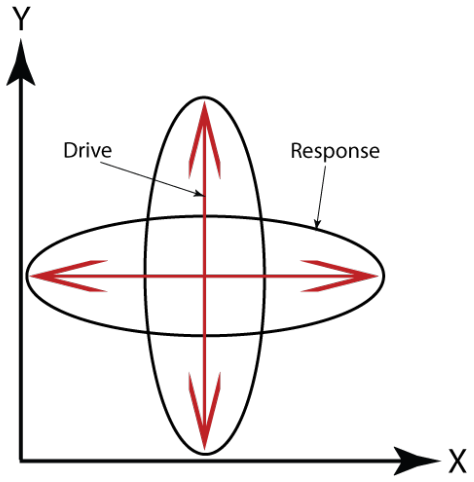


Figure 2.5. Elliptical path response or whirling motion.

If Eigendirections alignment is ignored and a sinusoidal excitation is given $\begin{bmatrix} F_{1,Piezoelectric-tube}(t) \\ F_{2,Piezoelectric-tube}(t) \end{bmatrix} = \begin{bmatrix} \sin(\omega t) \\ 0 \end{bmatrix}$ along one piezoelectric-tube electrode axis, by Equation 2.18 the response of the scanner (on the Eigendirection basis) will be governed by,

$$\begin{bmatrix} \ddot{x}_1 + 2\zeta_1\omega_{0,1}\dot{x}_1 + \omega_{0,1}^2 x_1 \\ \ddot{x}_2 + 2\zeta_2\omega_{0,2}\dot{x}_2 + \omega_{0,2}^2 x_2 \end{bmatrix} = \begin{bmatrix} \frac{cos\theta \sin(\omega t)}{m_1} \\ \frac{sin\theta \sin(\omega t)}{m_2} \end{bmatrix} \tag{2.19}$$

$\omega$ is the excitation frequency and $\theta$ is the angle between the Eigendirection axes and the piezoelectric-tube axes. The resulting motion is,

$$\begin{bmatrix} x_1(t) \\ x_2(t) \end{bmatrix} = \begin{bmatrix} \frac{cos\theta}{m_1\sqrt{\left(2\omega_{0,1}\zeta_1\omega\right)^2 + \left(\omega_{0,1}^2 - \omega^2\right)^2}} \sin\left(\omega t + arctan\left(\frac{2\omega\omega_{0,1}\zeta_1}{\omega_{0,1}^2 - \omega^2}\right)\right) \\ \frac{sin\theta}{m_2\sqrt{\left(2\omega_{0,2}\zeta_2\omega\right)^2 + \left(\omega_{0,2}^2 - \omega^2\right)^2}} \sin\left(\omega t + arctan\left(\frac{2\omega\omega_{0,2}\zeta_2}{\omega_{0,2}^2 - \omega^2}\right)\right) \end{bmatrix} \tag{2.20}$$

Note that since the parameters are not equal, there is a phase difference of $\emptyset = \arctan\left(\frac{2\omega\omega_{0,1}\zeta_1}{\omega_{0,1}^2-\omega^2}\right) - \arctan\left(\frac{2\omega\omega_{0,2}\zeta_2}{\omega_{0,2}^2-\omega^2}\right)$, between the responses along Eigendirection 1 and 2. When $0 < \theta < \frac{\pi}{2}$, this produces to an elliptical path as shown Figure 2.5. This derivation shows that a planar (single-axis) excitation produced unexpected non-planar (ovular) response, or whirling. If the misalignment between drive axes and eigendirections is not taken into account, fiber scan trajectory and consequently image distortion arises.

On the other hand, if we are able to identify the Eigendirection parameter $\theta$, we may derive excitations along each Eigendirection. For example $\begin{bmatrix} F_{1,Piezoelectric-tube}(t) \\ F_{2,Piezoelectric-tube}(t) \end{bmatrix} = \begin{bmatrix} cos\theta \sin(\omega t) \\ -sin\theta \sin(\omega t) \end{bmatrix}$ by Equation 2.18 results in excitation only along Eigendirection 1,

$$\begin{bmatrix} \ddot{x}_1 + 2\zeta_1\omega_{0,1}\dot{x}_1 + \omega_{0,1}^2 x_1 \\ \ddot{x}_2 + 2\zeta_2\omega_{0,2}\dot{x}_2 + \omega_{0,2}^2 x_2 \end{bmatrix} = \begin{bmatrix} \frac{\sin(\omega t)}{m_1} \\ 0 \end{bmatrix} \tag{2.21}$$

Producing the motion,

$$\begin{bmatrix} x_1(t) \\ x_2(t) \end{bmatrix} = \begin{bmatrix} \frac{1}{m_1\sqrt{(2\omega_{0,1}\zeta_1\omega)^2+(\omega_{0,1}^2-\omega^2)^2}} \sin\left(\omega t + arctan\left(\frac{2\omega\omega_{0,1}\zeta_1}{\omega_{0,1}^2-\omega^2}\right)\right) \\ 0 \end{bmatrix} \tag{2.22}$$

Here, planar excitation produced a planar response, as expected.

### 2.4.2 *Extended Mode Shapes*

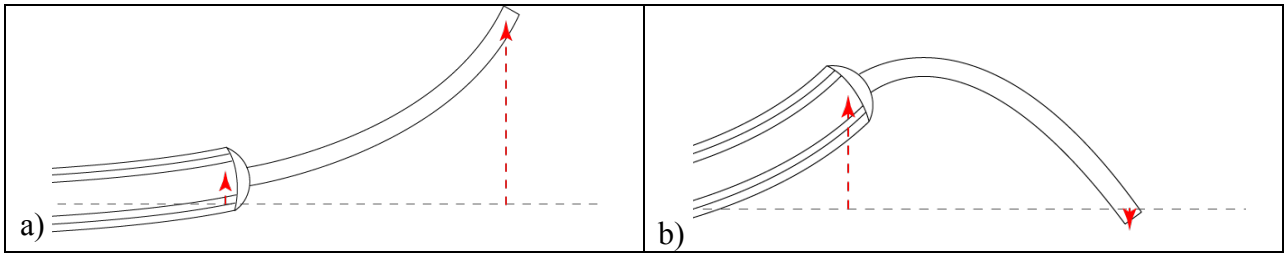


Figure 2.6. a) 1st extended mode shape. b) 2nd extended mode shape. Piezoelectric-tube deflections are considered in these modes.

Previous mechanical analyses of the scanner focused on the optical fiber, which was modeled as a 2D cantilever beam while neglecting the dynamics of the piezoelectric-tube [9]. In this

dissertation, a more complete approach is taken to consider the deformation of the composite piezoelectric-tube and optical-fiber cantilever structure, with the attaching collar as the rigid reference. Examples of the first two extended mode shapes are illustrated in Figure 2.6. The 1st extended mode is the operating mode of the SFE system. As Figure 2.6 shows, the strain of the piezoelectric tube is directly proportional to the deflection of the optical fiber. Hence, by sensing the strain of the piezoelectric-tube the deflection of the optical fiber can be inferred.

Note that the mathematical analyses in Section 2.4.1 are still valid as they were derived for general mode shapes. The extended mode shapes introduced here are necessary to understand the piezoelectric sensing measurements and to give a better representation of the actual scanner deformation. Further development of dynamics modeling based on mode shapes and generalized displacements will be given in a later chapter.

### 2.4.3 *Natural Frequency and Braking Phase*

In the standard open-loop control, the SFE is driven with a ramping sine and a ramping cosine, applied to each Eigendirection: $\begin{bmatrix} F_1(t) \\ F_2(t) \end{bmatrix} = \begin{bmatrix} A_1 t sin(\omega t) \\ A_2 t cos(\omega t) \end{bmatrix}$. $A_1$ and $A_2$ are the excitation amplitudes and the excitation frequency $\omega$ is selected to be $\omega = \frac{\omega_{r,1}+\omega_{r,2}}{2}$. With $\omega_r$ being the resonant frequency of the 1st vibration mode given by,

$$\omega_r = \omega_0\sqrt{1-2\zeta^2} \tag{2.23}$$

$\omega$ is selected such that it is closest to the 1st mode resonant peaks along both Eigendirections in order to generate large scanner deflection and hence high field-of-view. For optimal operation the frequencies $\omega_{r,1}$ and $\omega_{r,2}$ (subscripts 1 and 2 refer to the Eigendirections 1 and 2 respectively) need to be known so that maximum field-of-view is achieved.

After the optical fiber has scanned to its maximum amplitude, it is rapidly brought back to rest during the Braking Phase. Large amplitude square waves (Braking drive) are applied to each Eigendirection to rapidly collapse the scan. The Braking drive needs to be at the 1st damped natural frequency:

$$\omega_d = \omega_0\sqrt{1-\zeta^2} \tag{2.24}$$

The phase must lag the scanner displacement by precisely $\emptyset_{Brake,Rel} = \frac{-\pi}{2}$ rad [1]. To see why, let at a reference time $t = 0$, $x(0) = x_{max} > 0$ and $\dot{x}(t) = 0$. Applying a Braking drive with phase lag $\frac{\pi}{2}$ rad we get,

$$\ddot{x} + 2\zeta\omega_0\dot{x} + \omega_0^2 x = \frac{F_{Brake}(t)}{m} = \begin{cases} \frac{A_{Brake}}{\omega_0^2}, & t = \left[(n-1)T, \frac{nT}{2}\right], \ n = 1,2,3 \ldots \\ \frac{-A_{Brake}}{\omega_0^2}, & t = \left[\frac{nT}{2}, nT\right], \ n = 1,2,3 \ldots \end{cases} \quad (2.25)$$

$T = \frac{2\pi}{\omega_d}$ is the period related to the damped natural frequency. Solving the Initial Value Problem gives,

$$x\left(\frac{nT}{2}\right) = -(e^{\frac{-\pi\zeta}{\sqrt{1-\zeta^2}}})x\left(\frac{(n-1)T}{2}\right) + (1 + e^{\frac{-\pi\zeta}{\sqrt{1-\zeta^2}}})A_{Brake}, \ n = 1,2,3 \ldots \quad (2.26)$$

$$\dot{x}\left(\frac{nT}{2}\right) = 0, \ n = 1,2,3 \ldots \quad (2.27)$$

Note that if $A_{Brake} = \frac{(e^{\frac{-\pi\zeta}{\sqrt{1-\zeta^2}}})x(0)}{1+e^{\frac{-\pi\zeta}{\sqrt{1-\zeta^2}}}}$ then $x\left(\frac{T}{2}\right) = 0$ and $\dot{x}\left(\frac{T}{2}\right) = 0$, i.e. the scanner is brought to rest in $\frac{T}{2}$. In practice this requires application of a very large voltage. Instead, if,

$$A_{Brake} \leq \frac{(e^{\frac{-\pi\zeta}{\sqrt{1-\zeta^2}}})x(\frac{(n-1)T}{2})}{1+e^{\frac{-\pi\zeta}{\sqrt{1-\zeta^2}}}}, \ n = 1,2,3 \ldots \quad (2.28)$$

Then,

$$\left|x\left(\frac{nT}{2}\right)\right| \leq \left|x\left(\frac{(n-1)T}{2}\right)\right|, \ n = 1,2,3 \ldots \quad (2.29)$$

That is, the amplitude of vibration will decrease (more rapidly with larger $A_{Brake}$) until Eq. (15) does not hold. At that point braking must be turned off or the amplitude will start to increase.

Braking must be applied at the precisely $\emptyset_{Brake,Rel} = \frac{-\pi}{2}$ rad or Eq. (12) will not hold. If the Braking phase is incorrect e.g. $\emptyset_{Brake,Rel} = \frac{-3\pi}{2}$, then $\left|x\left(\frac{nT}{2}\right)\right| = \left|(e^{\frac{-\pi\zeta}{\sqrt{1-\zeta^2}}})x(\frac{(n-1)T}{2}) + (1 +\right.$

$e^{\frac{-\pi\zeta}{\sqrt{1-\zeta^2}}})A_{Brake}\Big|$, $n = 1,2,3 \ldots$ that is, the Braking drive can actually increase the amplitude of motion! Note that $\emptyset_{Brake,Rel} = \frac{-\pi}{2}$ is relative to the scanner displacement along an Eigendirection. The scanner response will have an absolute phase $\emptyset_{Motion}$, which depends on the excitation and mechanical properties of the scanner. Thus the absolute Braking phase is $\emptyset_{Brake} = \emptyset_{Brake,Rel} + \emptyset_{Motion}$, which varies between Eigendirections and from system-to-system. Kundrat et al. [28] provide an alternative Braking phase analysis, but for optical position sensor measurements.

In summary, the parameters to be identified to perform the standard open-loop control with the SFE are the eigendirections, the natural frequencies and the braking phases. These parameters were previously identified using an optical position sensor while the SFE probe was within a calibration chamber. In the following sections, time-multiplexed piezoelectric self-sensing will be implemented to identify these parameters for open loop control, leading to integrated sensing and self-contained recalibration.

### 2.4.4 *Experimental Setup*

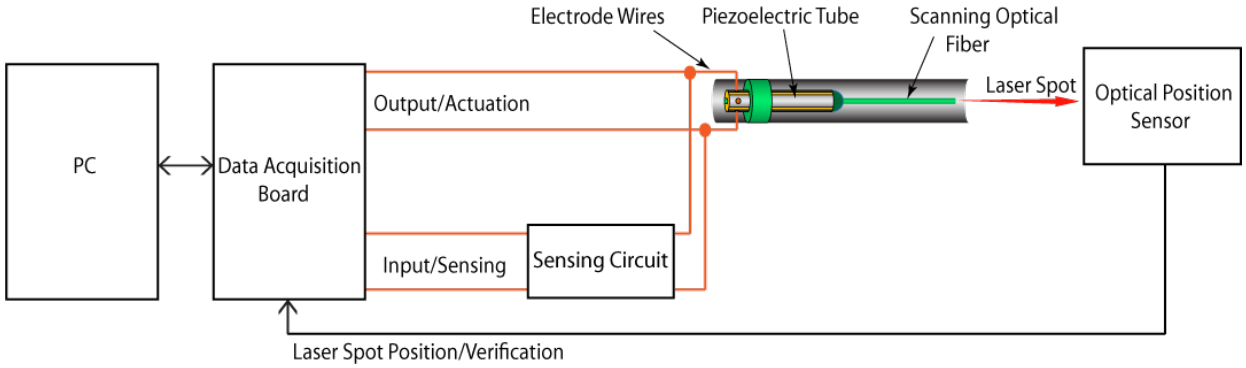


Figure 2.7. Experimental setup of time-multiplexed piezoelectric self-sensing for open-loop control.

Figure 2.7 shows the experimental setup implementing time-multiplexed piezoelectric self-sensing. The SFE scanner was the 11.5kHz prototype [1] which has a 0.45 mm outer diameter

(OD), 4 mm long PZT-5A piezoelectric-tube actuating a 0.080 mm OD and 2.27 mm long length of optical fiber. For higher sensitivity, the signal from the sensing circuit was amplified using an op-amp differential amplifier. A National Instruments PCI-6115 Data Acquisition board operating at 500k samples/s was used to produce the drive signals and to measure the sensor signals. Custom software was written in LabVIEW and operated on a workstation computer. For verification only, a laser diode was coupled to the optical fiber, and an optical position sensor (DL-20, OSI Optoelectronics) was used to measure the position of the scanned laser spot.

The 11.5kHz scanner design has an integrated heater and thermistor within the endoscope probe, which are used to control the temperature of the scan engine. This temperature control is utilized to demonstrate identification of drifting system parameters in later subsections.

### 2.4.5 *Circuit Analysis*

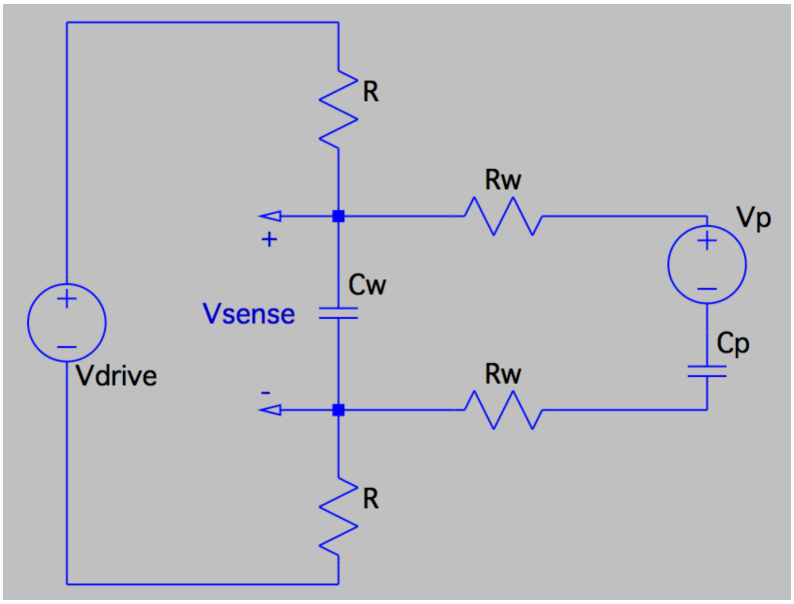


Figure 2.8. Lumped element model of time-multiplexed piezoelectric self-sensing circuit.

The circuit used for piezoelectric sensing is shown in Figure 2.8 with the piezoelectric-tube modeled as a voltage source $V_p(t)$ in series with a capacitor $C_p$. The voltage $V_p(t)$ is the piezoelectrically-generated voltage that is proportional to the strain of the piezoelectric element [30]. When $V_{Drive}(t)$ is active as in Figure 2.8, i.e. when the scanner is being actuated, the sensed voltage $V_{Sense}(t)$ is given in the Laplace domain as:

$$V_{Sense}(s) = \frac{2R_W C_P s+1}{4RR_W C_W C_P s^2+2[R_W C_P+R(C_W+C_P)]s+1} V_{Drive}(s) + \frac{2RC_P s}{4RR_W C_W C_P s^2+2[R_W C_P+R(C_W+C_P)]s+1} V_P(s) \quad (2.30)$$

$R_W$ is the wire resistance, $C_W$ the wire capacitance, $R$ the resistors in Figure 2.8, and $s$ the Laplace variable. Since typically $|V_{Drive}| \gg |V_P|$, in Equation 2.30, $V_{Sense} \cong V_{Drive}$. This means that $V_P$ cannot be directly measured when actuating, as the actuation signal will saturate the electrical channel.

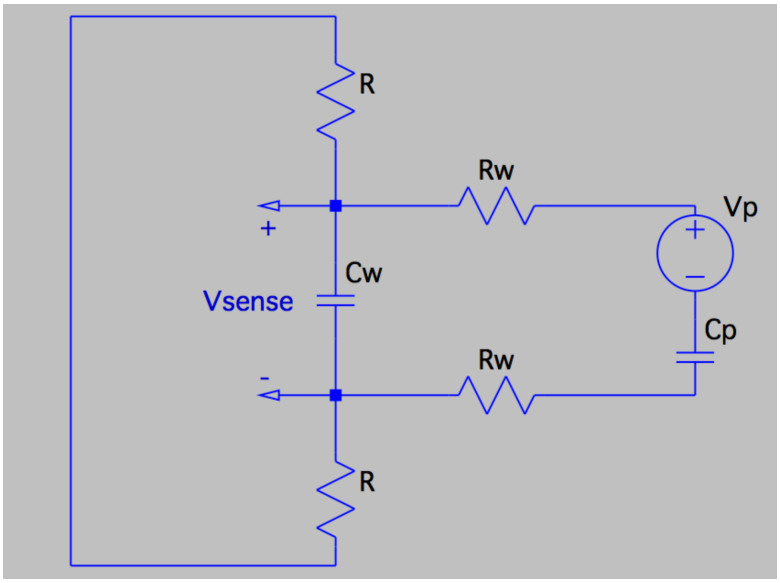


Figure 2.9. Circuit model of time-multiplexed piezoelectric self-sensing circuit when $V_{drive} = 0$.

However, when the drive is not active as in Figure 2.9,

$$V_{Sense}(s) = \frac{2RC_P s}{4RR_W C_W C_P s^2+2[R_W C_P+R(C_W+C_P)]s+1} V_P(s), \qquad V_{Drive}(s) = 0 \qquad (2.31)$$

The piezoelectric-tube strain can be directly measured when not actuating. Note that in Equation 2.31 the piezoelectric signal is band-passed through a filter with poles given by $4RR_W C_W C_P s^2 + 2[R_W C_P + R(C_W + C_P)]s + 1 = 0$ and design variable $R$. The resistors $R$ also determine the voltage drop driving the piezoelectric-tube in Figure 2.8, and the voltage drop measured as $V_{Sense}$ in Figure 2.9.

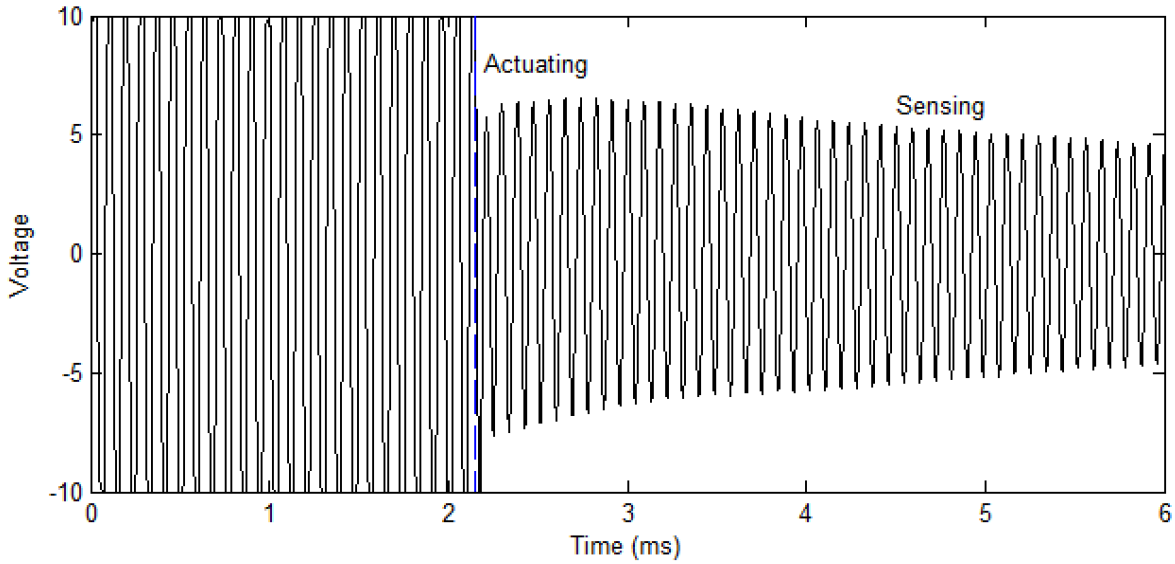


Figure 2.10. Time-multiplexed piezoelectric self-sensing signals, showing the actuating/drive signal and the sensing signal on the same electrical channel at different times.

Figure 2.10 shows the time-multiplexed piezoelectric self-sensing signal in two operating modes. When actuating, as Equation 2.30 predicts, the sensor signal is essentially the drive signal greatly amplified. However, when the drive is turned off the piezoelectric sensor measures the residual oscillations of the scanner, as indicated in Equation 2.31.

Since the SFE scanner is an underdamped resonant system, it will continue to oscillate even after forcing is removed. Hence Equation 2.31 means that a drive signal can be applied to the piezoelectric-tube and then the residual oscillations – which contain information about the system parameters – may be measured via time-multiplexed piezoelectric self-sensing. In the subsequent sections, this approach is developed to identify the optimal open-loop control settings.

### 2.4.6 *Identifying Eigendirections*

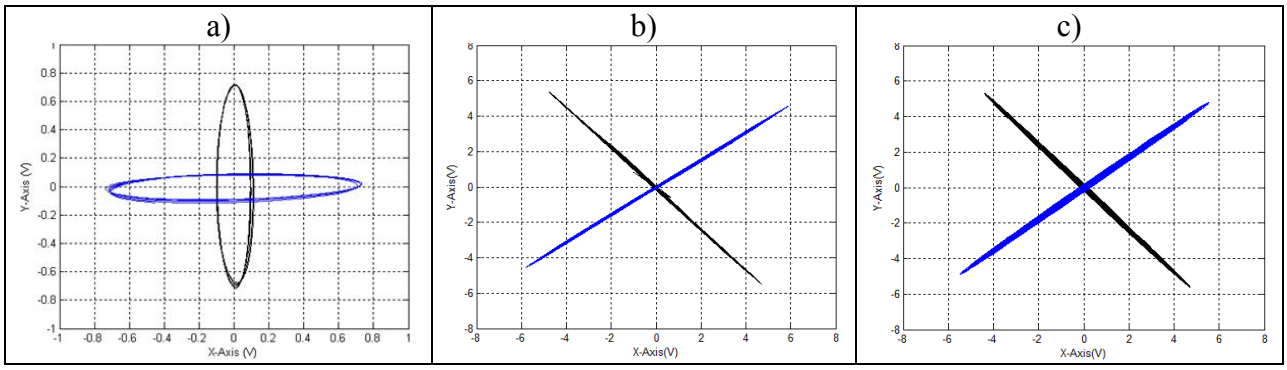


Figure 2.11. a) Whirling motion (low flatness) when $\varphi \neq \theta$. b) Straight-line response (maximal flatness) when $\varphi \cong \theta$, from piezoelectric sensing data. c) Verification of straight-line response, from optical position sensor data.

Kundrat identified the Eigendirections using the optical sensor and a circularity test [9]. In this work I demonstrate identifying the Eigendirections using time-multiplexed piezoelectric self-sensing and a flattening criterion.

By applying electrical drive signals to the piezoelectric-tube the force acting on the cantilevered fiber scanner can be controlled. To identify the Eigendirections, the following diagnostic signal is applied,

$$\begin{bmatrix} F_{1,Piezoelectric-tube}(t) \\ F_{2,Piezoelectric-tube}(t) \end{bmatrix} = \begin{bmatrix} cos\alpha \sin(\omega_{nom} t) \\ -sin\alpha \sin(\omega_{nom} t) \end{bmatrix} \tag{2.32}$$

With $\omega_{nom}$ a nominal guess of the resonant frequency and $\alpha$ as a 'test angle' that is swept from 0 to $\pi$ rad. From Equation 2.18, when $\alpha = \theta$ (the Eigendirection angle), a line-response as in Equation 2.22. When forcing is turned off, Equation 2.22 at $t = T_{final}$ gives the initial conditions for the free decay. The free oscillations calculate to:

$$\begin{bmatrix} x_{1,decay}(t) \\ x_{2,decay}(t) \end{bmatrix} = \begin{bmatrix} A_1 e^{-\zeta_1 \omega_{0,1} t} \sin(\omega_{d,1} t + \varphi_1) \\ 0 \end{bmatrix} \tag{2.33}$$

Where the amplitude $A_1$ and phase $\varphi_1$ depend on the initial conditions. Equation 2.33 describes a one-dimensional signal. For line geometry the flattening criterion:

$$f = \frac{a-b}{a} \tag{2.34}$$

where $a$ is the semi-major axis length and $b$ is the semi-minor axis length, will be maximum valued at 1. By sweeping $\alpha$ from 0 to $\pi$ rad, maximum flatness is achieved when $\alpha \cong \theta$, hence the Eigendirection parameter $\theta$ can be identified.

Figure 2.11b shows the result of this identification procedure. When $\alpha \cong \theta$ maximal flatness is achieved. The optical position sensor data in Figure 2.11c also verifies that whirling was eliminated when driving along the correctly identified Eigendirections.

### 2.4.7 *Identifying Natural Frequencies*

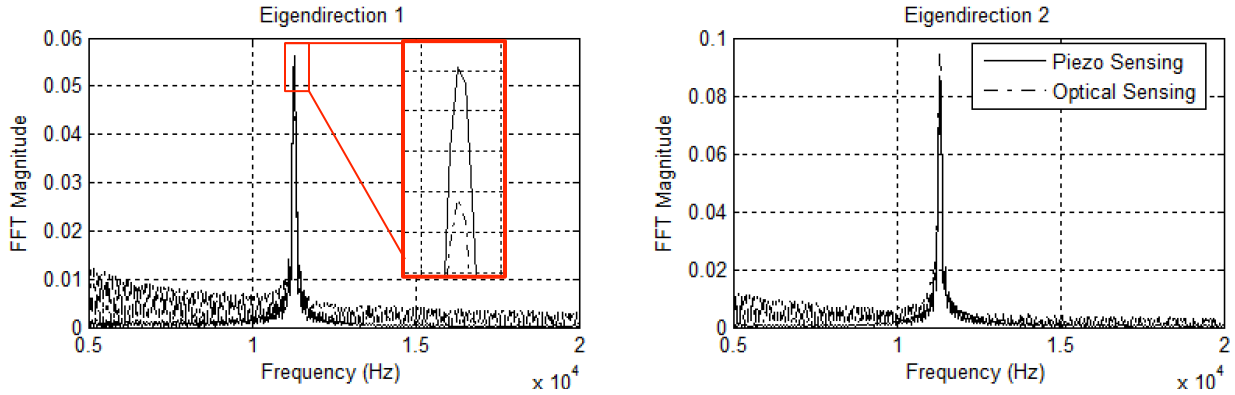


Figure 2.12. Identifying 1st damped natural frequency from the prominent peak in the FFT magnitude spectrum.

In previous works, the natural frequencies were identified by measuring the time between successive zero-crossings with the optical position detector [9], [28]. Here I present identifying the natural frequencies from the Discrete Fourier spectrum of the time-multiplexed sensing signal.

Comparing Equation 2.23 and 2.24, when effective damping $\zeta$ is small $\omega_r \cong \omega_d$. For the SFE system $\omega_d$ may be accurately measured and $\omega_r$ approximated as discussed. $\omega_d$ is needed for precise braking along each Eigendirection. Since $\omega_r$ is different along each eigendirection, the drive frequency is typically slightly off-resonance between the two Eigendirections, meaning an accurate value of $\omega_r$ is not as crucial.

Once the Eigendirections are identified, the diagnostic signal $\begin{bmatrix} F_{1,Piezoelectric-tube}(t) \\ F_{2,Piezoelectric-tube}(t) \end{bmatrix} = \begin{bmatrix} cos\theta \sin(\omega_{nom} t) \\ -sin\theta \sin(\omega_{nom} t) \end{bmatrix}$ is applied and then forcing is turned off. This produces free oscillations along Eigendirection 1 as described in Equation 2.33. The Fourier transform of $x_{1,decay}(t)$ is:

$$X_{1,decay}(\omega) = \frac{B_1\omega_{d,1} + C_1(\zeta_1\omega_{0,1} + j\omega)}{\omega_{d,1}^2 + (\zeta_1\omega_{0,1} + j\omega)^2} \tag{2.35}$$

$j$ is the imaginary unit, $\omega$ the frequency variable of the Fourier transform and $B_1$ and $C_1$ are coefficients that depend on the initial conditions before free decay. The magnitude plot of Equation 2.35 will have a peak at $\omega = \omega_{d,1}$. From the measured samples of $x_{1,decay}(t)$, the discrete Fast Fourier Transform (FFT) is computed and $\omega_{d,1}$ is identified from the peak in the FFT magnitude plot. This process is repeated for Eigendirection 2. Figure 2.12 shows FFT magnitude plots of data taken with piezoelectric sensing. Very prominent peaks allow us to identify $\omega_d$ accurately. Also in Figure 2.12, data from the optical position sensor verifies the identified natural frequencies.

### 2.4.8 *Identifying Braking Phases*

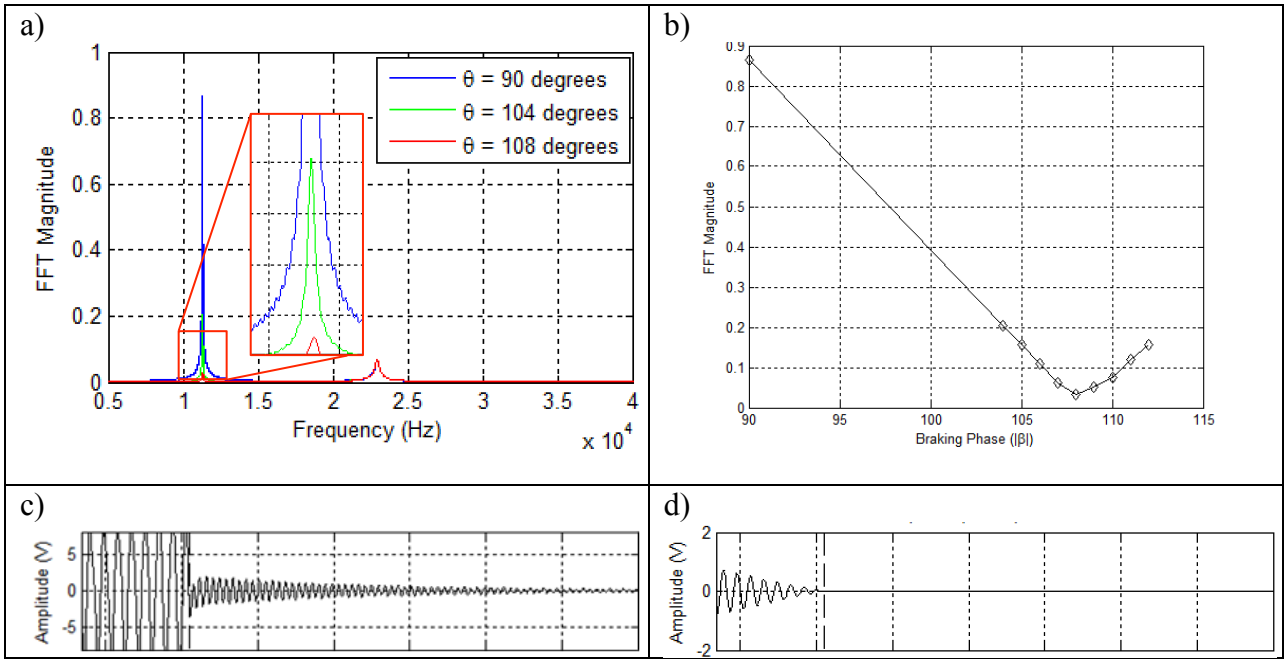

Figure 2.13. a) FFT magnitude peak height changes with different Braking phases. b) Optimum Braking phase identified from minimum FFT magnitude peak height. c) Time-multiplexed sensing signal after Braking. d) Optical position sensor signal after Braking, showing that the scanner is brought rapidly to rest.

Kundrat proposed identifying the Braking phase indirectly using displacement, natural frequency and velocity estimates of the linear model [28]. In this work I propose identifying the Braking phase directly with the Discrete Fourier transform of the piezoelectric self-sensing signal and empirical optimization.

Braking must be applied at a precise phase $\emptyset_{Brake}$ to bring the scanner as close to rest as possible. The exact value of $\emptyset_{Brake}$ is determined empirically by sweeping a 'test' phase $\beta$ between $\frac{-\pi}{4}$ and $\frac{-3\pi}{4}$ rad. The displacement and velocity of the scanner will be minimum when $\beta \cong \emptyset_{Brake}$.

Typically the SFE is operated in the 1st extended mode as illustrated in Figure 2.6a. Due to discontinuous forcing, the 2nd and higher extended modes will inadvertently be slightly excited. From Figure 2.6b we predict that the 2nd extended mode incorporates large relative deformations of the piezoelectric-tube compared to the 1st extended mode. As such, it is difficult to separate the amplitudes of the 1st and 2nd extended modes just by observing the piezoelectric-tube displacement (using time-multiplexed piezoelectric self-sensing), when the amplitude of the 1st mode is small. To precisely identify $\emptyset_{Brake}$ small residual vibrations of the 1st extended mode need to be quantified.

To separate the amplitudes of the 1st and 2nd extended modes, this work applies frequency analysis. The damped natural frequency of the 2nd extended mode is much higher than that of the 1st extended mode, thus each mode will have distinct peaks in the frequency spectrum. From Equation 2.35, for free decay on Eigendirection 1, the height of the FFT magnitude peak at $\omega = \omega_{d,1}$, $|X_{1,decay}(\omega_{d,1})|$ is proportional to $\sqrt{(B_1\omega_{d,1} + C_1\zeta_1\omega_{0,1})^2 + (C_1\omega_{d,1})^2}$ where $B_1$ and $C_1$ are directly proportional the initial displacement, $x_i$ and the initial velocity, $v_i$ at the onset of free decay:

$$B_1 = \frac{v_i + \zeta_1\omega_{0,1}x_i}{\omega_{d,1}} \tag{2.36}$$

$$C_1 = x_i \tag{2.37}$$

This shows that $|X_{1,decay}(\omega_{d,1})|$ is proportional to the initial displacement and velocity of the 1st extended mode on Eigendirection 1, providing a means of measuring how much 'at rest' the 1st extended mode is.

The following procedure identifies the Braking phases: On Eigendirection 1, scan the SFE with the nominal ramping sinusoid then apply Braking. During Braking, use a 'test' phase $\beta$ that is swept between $\frac{-\pi}{4}$ and $\frac{-3\pi}{4}$ rad for different trials. This constitutes the diagnostic signal. After Braking in each trial, measure $|X_{1,decay}(\omega_{d,1})|$. The minimum $|X_{1,decay}(\omega_{d,1})|$ will indicate $\beta \cong \emptyset_{Brake,1}$. Repeat on Eigendirection 2 to identify $\emptyset_{Brake,2}$

Figure 2.13a shows the FFT magnitude plot for different identification trials. Note that the height of the first peak changes for different Braking phases as predicted by Equations 2.35-2.37 Figure 2.13b shows that the optimal Braking phase is identified by tracking the height of the spectrum peak for different $\beta$ and finding the minimum point. Figure 2.13c shows the piezoelectric sensing signal after optimal Braking. Time-multiplexed piezoelectric self-sensing tracks the position of the piezoelectric-tube. Since Braking was effective, lower frequency oscillations of the 1st extended mode are absent but higher frequency residual vibration of the 2nd extended mode is detected. Figure 2.13d shows the optical position sensor data, which tracks the position of the optical fiber tip. As expected, since the 1st extended mode is practically at rest, the deflections of the optical fiber tip are negligible.

### 2.4.9 *Parameter Tracking*

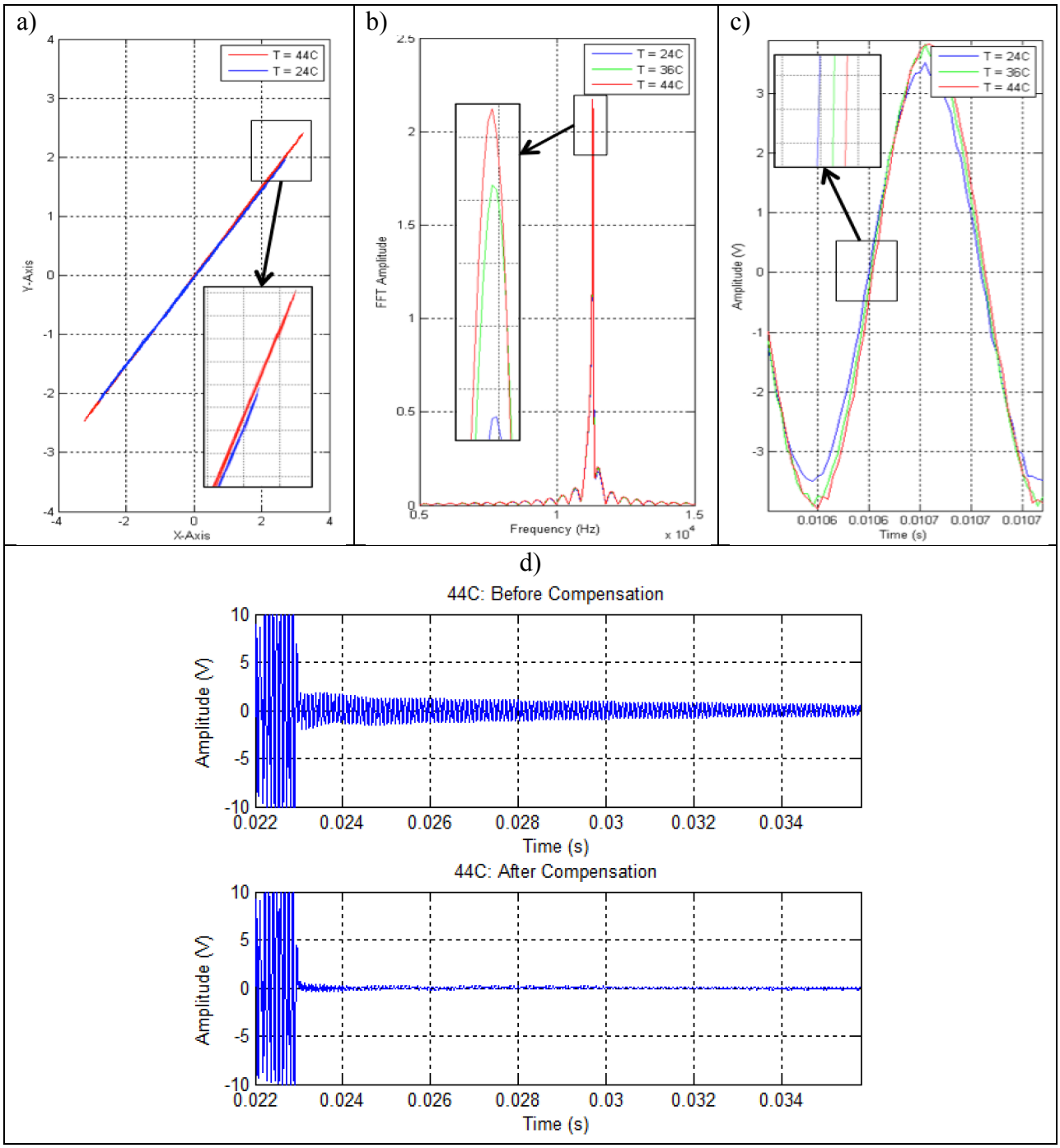


Figure 2.14. Time-multiplexed self-sensing data over changing operating temperature (T) from 24°C to 44°C: a) Tracking Eigendirections. b) Tracking first natural frequency. c) Tracking phase. d) Time-multiplexed self-sensing signals indicate that scan control and Braking is much more effective after recalibrating for temperature changes (heating from 24°C to 44°C).

Now that the pertinent parameters of the system can be identified via time-multiplexed piezoelectric self-sensing, it follows that these parameters can be tracked over changing operating conditions. The Eigendirections and 1st extended mode damped natural frequencies of an SFE scanner drift very little over time. To identify new values for these parameters, the system will periodically repeat procedures described in Sections 2.4.6 and 2.4.7. In addition, the algorithm initializes with good guesses of the new parameter values since parameter drifts are continuous processes, thus reducing the number of identification iterations necessary. Each identification iteration takes less than 50 milliseconds (at most 25k data samples needed at 500k samples/s) and will not be noticeable or disruptive to the endoscope operator.

The SFE is more sensitive to Braking phase inaccuracies. To identify new Braking phases the procedures described in Section 2.4.8 may be repeated, or alternatively the amount of change in the time-signal phase $\emptyset_{Motion}$ can be used. Since $\emptyset_{Brake} = \frac{-\pi}{2} + \emptyset_{Motion}$ the change in $\emptyset_{Motion}$ is equal to the change in $\emptyset_{Brake}$. The Braking phase can be rapidly updated with this approach.

Experimental results demonstrate the efficacy of the piezoelectric sensing method to track the system parameters over changing operating temperature. Figure 2.14a shows the Eigendirections identified at two very different temperatures revealing a 1.1° clockwise rotation at 44°C relative to 24°C. Figure 2.14b shows the tracked damped natural frequency peaks at different temperatures indicating a slight decreasing trend. Figure 2.14c shows the time signal, with observed phase drift as temperature increases. Figure 2.14d shows the scanner displacement profile at 44°C before and after recalibration with the piezoelectric sensing approach. Before recalibration, the scanner is still vigorously vibrating when the next image cycle begins, leading to distorted pictures as in Figure 1.3c. After recalibration, scan control and Braking is much more effective and the scanner is brought to rest before the next image cycle, producing clear distortionless images as in Figure 1.3b. All the designed identification procedures have quantifiable measures to optimize: maximize flatness to find the Eigendirections, locate spectrum peak (maximum value) to identify damped natural frequencies, and minimize spectrum height to find Braking phases. Thus, the system can be computer-automated to repeat these identification steps periodically to recalibrate itself without human assistance. Since the piezoelectric sensor is

inside the tiny endoscope probe, this is a fully self-contained process that maintains high image quality, making the endoscope operation simple and employable in lengthy medical procedures.

## 2.5 SUMMARY

This chapter began with a review of methods to maintain high image quality with the scanning fiber technology. Miniature sensing is the ideal approach but before this work no appropriate sensing modality was developed. Piezoelectricity was then reviewed and the concepts of piezoelectric sensing and self-sensing were presented as a new integrated sensing approach for the scanning fiber technology. The first technology developed in this work, time-multiplexed piezoelectric self-sensing was detailed in this chapter. Time-multiplexed piezoelectric self-sensing was developed to identify all the open-loop control parameters previously obtained with optical sensing within a calibration chamber. Thus, integrated sensing is shown for the first time to eliminate the need for an external sensor, advancing the applicability of the scanning fiber device.

# Chapter 3. SIMULTANEOUS PIEZOELECTRIC SELF-SENSING

While time-multiplexed piezoelectric self-sensing requires electronically switching the piezoelectric element between actuation and sensing modes another method, *simultaneous piezoelectric self-sensing*, does not require switching between modes. The same piezoelectric element can actuate and sense at the same time.

Simultaneous sensing and actuation is a powerful tool, with the uninterrupted signals enabling different adaptive control methods for the scanning fiber technology. The remainder of this work will focus on simultaneous piezoelectric self-sensing. In literature, 'piezoelectric self-sensing' typically refers to simultaneous self-sensing.

## 3.1 SIMULTANEOUS SELF-SENSING FORMULATION

Simultaneous piezoelectric self-sensing operates on the basic principle of isolating the sensor signal from the actuation signal, where both signals are simultaneously active on the same electrical channel. There are a number of closely related approaches to piezoelectric self-sensing. A pioneering work by Dosch, Inman and Garcia [30] derived widely-used piezoelectric models for strain and stress self-sensing. In this formulation, for strain sensing the piezoelectric constitutive equations may be rearranged to:

$$E_3 = \frac{D_3}{\varepsilon^S} - \frac{e_{13}S_1}{\varepsilon^S} \tag{3.1}$$

$E$ is the electric field along the poling direction 3, $D$ the electric displacement along 3, $S$ the strain along 1, $e$ a piezoelectric constant and $\varepsilon^S$ the material permittivity. Multiplying by an equivalent thickness $t$ we get an expression for the voltage $v$ across the piezoelectric element:

$$v = E_3 t = \frac{D_3 t}{\varepsilon^S} - \frac{e_{13}S_1 t}{\varepsilon^S} \tag{3.2}$$

The voltage across the piezoelectric element can be interpreted as being the combined contribution of free charge displacement (common in regular capacitive materials) and piezoelectric strain polarization (unique to piezoelectric materials), defined below:

$\frac{q_f}{A} = D$, free charge per area on the piezoelectric element

$\frac{q_p}{A} = eS$, piezoelectric polarization charge per area due to strain

As defined, $q_p$ is distinct from $q_f$ though the modeled circuit elements are in series. By defining a piezoelectric capacitance measured at constant strain:

$$C_p^S = \frac{\varepsilon^S A}{t} \tag{3.3}$$

The equation for voltage across a piezoelectric element simplifies to:

$$v = \frac{q_f}{C_p^S} - \frac{q_p}{C_p^S} \tag{3.4}$$

$q_p$ is the charge proportional to strain. Since $v = q/C$, an equivalent circuit with the piezoelectric material is shown below, where $v_p$ is proportional to strain and $v$ is the voltage across the piezoelectric element:

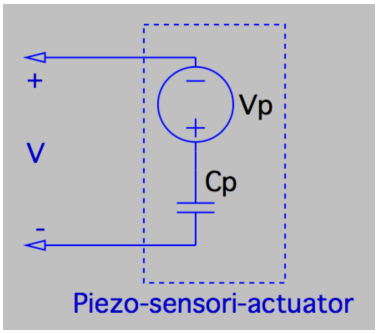


Figure 3.1. Standard model for piezoelectric element.

A similar model for stress sensing was also proposed by Dosch et al. where the stress-sensing model was derived from the following instead of Equation 3.1:

$$E_3 = \frac{D_3}{\varepsilon^T} - \frac{e_{13} T_1}{\varepsilon^T} \tag{3.5}$$

The final equations for piezoelectric voltage in both sensing models are identical except for the definition of the piezoelectric capacitance.

$$v = \frac{q_f}{C_p^S} - \frac{q_p}{C_p^S}, \text{ strain sensing.}$$

$$v = \frac{q_f}{C_p^T} - \frac{q_p}{C_p^T}, \text{ stress sensing.}$$

For strain sensing, $C_p^S$ is defined as the piezoelectric capacitance measured at constant strain while for stress sensing, $C_p^T$ is defined as the piezoelectric capacitance measured at constant strain.

## 3.2 Sensor and Actuator Relationships

To apply the piezoelectric self-sensing formulations to a specific controlled structure, the sensor and actuator equations must be specified. The sensor relationship defines the how the self-sensing signal is related to the structural deformations. The actuator relationship defines how the applied voltage affects the structural deformation.

The sensor equation is found by determining from the structure geometry, how deformations of the structure affect the piezoelectric patch stress or strain, which are directly sensed. For instance in Dosch et al. the structure was a simple cantilever with a piezoelectric patch on one side. The sensing relationship was derived where the stress in the piezoelectric patch was inversely related to the curvature of the cantilever [30].

Similarly, the actuator equation is found by identifying from the structure geometry, how the stress and strain of the piezoelectric patch applies forces or moments to the overall structure. The forces or moments on the overall structure are then related to the actuation voltage by the piezoelectric constitutive equations e.g. Equation 2.1 and 2.2, which tie the stress or strain to the electric displacements. For example in the case of a simple cantilever beam with a piezoelectric patch on one side, strain in the piezoelectric patch will introduce a distributed moment on the overall structure across the length of the piezoelectric patch [30].

In all previous work with the SFE, only an actuator equation was derived, since piezoelectric sensing was not yet introduced. For the optical fiber with base-excitation models used by Smithwick [8] and Kundrat [9], the dynamics of the piezoelectric tube are not considered, thus the simple assumption that applied voltage is proportional to lateral base-displacement was used, based on analytical work on piezoelectric tubes with quartered electrodes [31], [32]. The applied voltage was assumed to elicit a piezoelectric-tube deflection, which was then taken as the base excitation of the optical fiber cantilever.

This work considers the dynamics of the piezoelectric-tube together with the dynamics of the optical fiber. As such, of interest is not just the static deflection but also the dynamic response of the electromechanical system. Analytical solutions can be derived from the constitutive equations and tube geometry [33]–[35]. More controls-holistic approaches have been

demonstrated, where the transfer function from input to response is experimentally determined via system identification [18], [36], [37].

Hagood and Anderson et al. derive the self-sensing formulation similar to Dosch et al. but in a more general manner [38], [39]. The piezoelectric constitutive equations are used, with the strain-displacement and electric field-potential relationships defined in terms of generalized coordinates with structural and potential mode shapes governed by the system boundary conditions. These relationships are then substituted into Hamilton's equation to derive the governing equations for the dynamical system. Hagood and Anderson et al. arrive at he following actuator equation:

$$M\ddot{r} + Kr - \theta v = B_f f \tag{3.6}$$

- and sensor equation:

$$\theta^T r + C_p v = B_q q \tag{3.7}$$

$M$ and $K$ are mass and stiffness matrices, $C_p$ and $\theta$ are capacitance and coupling matrices, $v$ the electrode voltage, $f$ the applied force, $q$ the electrode charge, and $r$ the generalized coordinates tied to the displacement mode shapes.

This work takes inspiration from Equations 3.6 and 3.7, where the dynamics of the entire structure with the self-sensing actuator and sensor relationships are concisely described in modal or generalized displacement dynamics and an output equation. In later sections I develop system identification techniques to empirically derive relationships similar to Equations 3.6 and 3.7 that are then used to model and control the scanning system.

## 3.3 Self-Sensing Circuit Review

Simultaneous piezoelectric self-sensing is generally implemented using bridge circuits. To isolate the direct-piezoelectric effect voltage $v_p$, Dosch et al. proposed strain and strain-rate sensing circuits, shown in Figure 3.2 and Figure 3.3 respectively. In these configurations, the sensor reading is the differential voltage $v_{sensor} = v_1 - v_2$. In each of these circuits, there exist two similar branches, one with the piezoelectric actuator, and a balance branch with balancing components to subtract out the voltage accumulated across the internal piezoelectric capacitance.

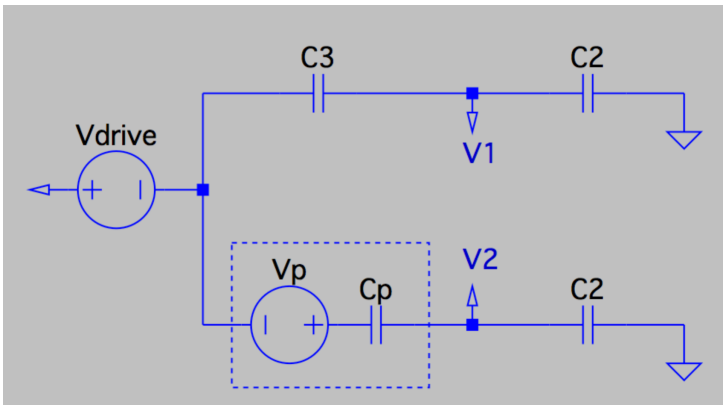


Figure 3.2. Dosch et al. strain sensing circuit.

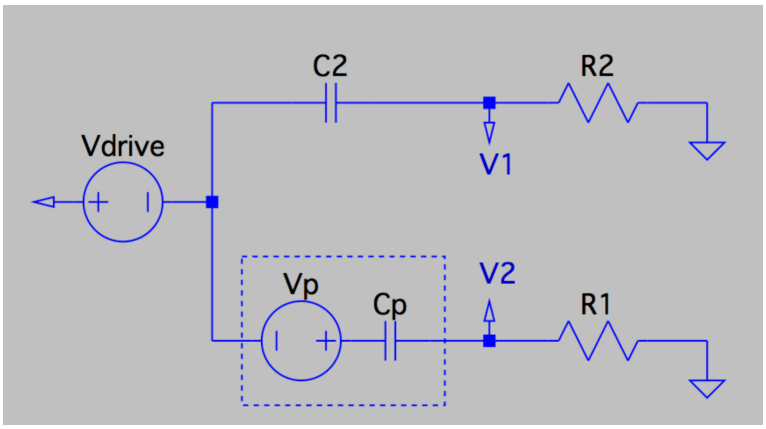


Figure 3.3. Dosch et al. strain-rate sensing circuit.

Kuiper et al. implemented a self-sensing design very similar to Dosch et al. in Figure 3.2, but formulated the sensing equation slightly differently by starting with constitutive equations directly cast in the displacement and force variables [40]. Hagood et al. [38] also derive circuits almost identical to Dosch et al. for strain and strain rate sensing, though Hagood et al. arrived at the design from a different formulation based on the sensor Equation 3.7. Jones et al. [41] follow a simplified derivation from the piezoelectric constitutive equations and propose a capacitive Wheatstone bridge identical to the strain sensing architecture in Figure 3.2.

Miyahara et al. [42] also formulate the self-sensing problem slightly differently, where deflections of a microcantilever are directly related to the piezoelectric charge displacement or current. This current is assumed to be shunted by a capacitance related to the cantilevered microstructure structure. A balance branch is constructed to cancel out the effect of the shunt capacitance, resulting in a circuit topology very similar to Dosch et al [30].

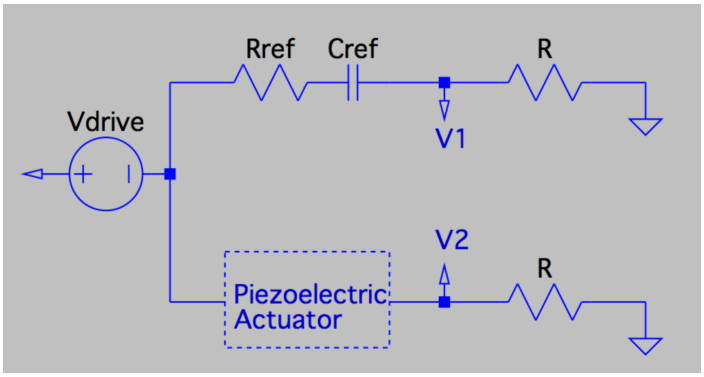


Figure 3.4. Miyahara et al. deflection sensing circuit.

Non-bridge circuit self-sensing methods are also available, that estimate the accumulated charge on the piezoelectric element by measuring the current through the actuator [43], [44]. This method is similar to Miyahara et al. [42] but without a complementary branch to subtract out shunt or parasitic capacitance effects. In [38] a neural network is used to learn the relationship between sensing voltage and the low-frequency displacements, because the charge-displacement assumptions were affected dielectric leakage.

## 3.4 Hysteresis in Piezoactuators

Piezoelectric materials exhibit hysteresis between the voltage input and displacement response. The degree of hysteresis behavior is dependent on the type of piezoelectric material and the manufacturing process [21]. A wide range of methods has been proposed to model and predict the hysteretic behavior of piezoelectric materials. These include empirical models [45], polynomial models [46], neural networks [47], [48], and phenomenological operators [44], [49], [50]. Phenomenological models particularly the Maxwell Slip [44], [51] and the Preisach model [52], [53] are widely used because their general accuracy and of numerical tractability [49]. Both the Maxwell Slip and the Preisach model approximate hysteretic behavior through the summation of a large number of elementary nonlinear units. In the case of the Maxwell Slip, the units are elasto-slide [51] or zener-capacitor [44] elements; in the Preisach model the units are relay-switch ‘hysterions’.

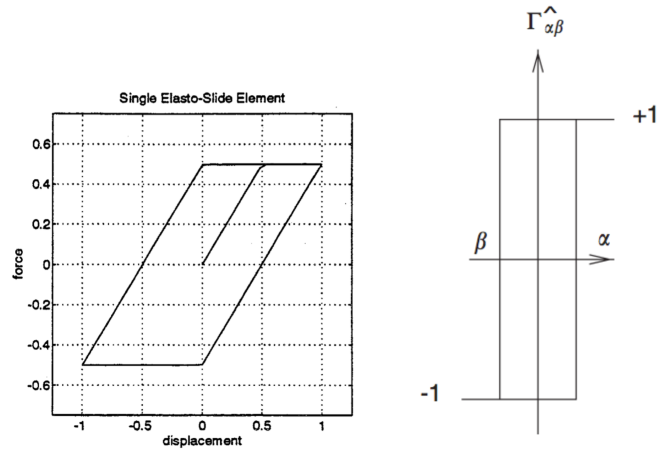


Figure 3.5. a) Response profile of Maxwell Slip elementary unit. b) Response profile of Preisach model elementary unit.

Both of these elementary units have similar response profiles and are aggregated to give a macro-scale hysteretic response. In the Preisach model, the response is given by the integral or numerical summation:

$$x(t) = \iint \mu(\alpha, \beta)\gamma_{\alpha\beta}[u(t)]d\alpha d\beta \tag{3.8}$$

$\gamma_{\alpha\beta}[u(t)]$ is the unit hysterion, $\mu(\alpha, \beta)$ is the weight for the particular hysterion at a given $\alpha, \beta$, and the integral is computed over the entire $\alpha, \beta$ space.

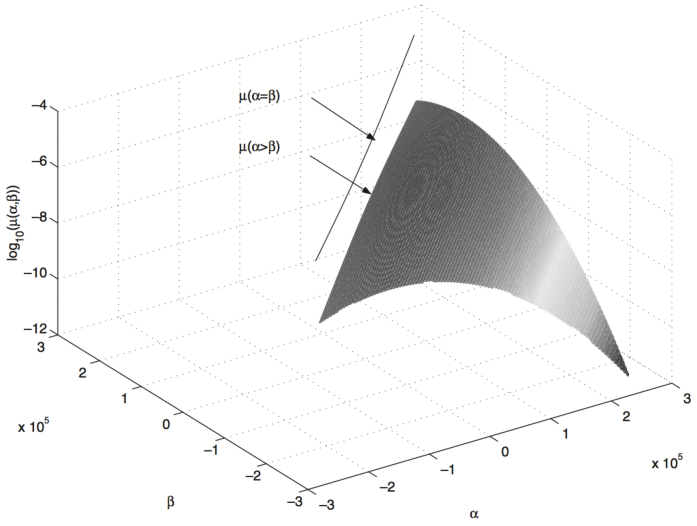


Figure 3.6. Example $\mu(\alpha, \beta)$ weighting function over the $\alpha, \beta$ space [52].

Approaches to obviate the reduction in precision caused by hysteresis include: hysteretic model inversion, feedback methods, charge drives and capacitor insertion. Hysteretic model inversion involves identifying the parameters of a model e.g. Preisach, and then inverting the model to find an input the compensated for the nonlinearity. Numerically tractable models like Maxwell Slip and Preisach are favored but precision and memory or computation load remain tradeoffs [46]. High-gain feedback can be used to regulate-out the effect of hysteresis in conjunction with other control methods [54] but should be carefully designed to avoid instability due to hysteresis-induced phase errors [53].

Driving a piezoactuator with applied charge instead of voltage has been shown to dramatically reduce hysteresis between input and displacement. According to Newcomb and Flynn, to a first approximation, the piezoelectric constitutive Equation 2.1 for electric displacement can be recast as:

$$\boldsymbol{D} = \varepsilon \boldsymbol{E} = \varepsilon_0 \boldsymbol{E} + \boldsymbol{P} = \varepsilon_0 \boldsymbol{E} + \chi(t)\boldsymbol{E} \tag{3.9}$$

$\chi(t)$ is the material susceptibility which is not a constant, giving rise to the nonlinear relationship between polarization $\boldsymbol{P}$ and electric field $\boldsymbol{E}$. Since in practice $\chi \gg \varepsilon_0$ we have the relationship:

$$\Delta \boldsymbol{D} \approx \Delta \boldsymbol{P} \tag{3.10}$$

The change in polarization $\boldsymbol{P}$ is directly related to piezoelectric material strain, while the change in electric displacement $\boldsymbol{D}$ is directly related to charge accumulation [55]. Thus by imposing a charge, a displacement results with little hysteresis between these variables, making the relationship between the input and output significantly more linear [55], [56]. However, the electronic design of charge drives are more complicated and suffer from stability and bandwidth issues though various improved circuit designs have been proposed [37], [57], [58]. A simpler electrical modification is the capacitor insertion method, where a large capacitor is inserted in series with the piezoelectric actuator to regulate the charge accumulation. The drawback of capacitor insertion is the significant loss of actuation power due to voltage drop across the series capacitance [56].

In this work, the approximation is made that any hysteresis in the system manifests as a phase and amplitude adjustment to a sinusoidal response. As previously discussed, a direct modeling of hysteresis adds significant numerical complexity to the model. Moderate adjustments of general models e.g. in phase and amplitude will be more applicable to a controls-

oriented system description. Another important reason that the phase-amplitude adjustment approximation suffices is the single-frequency actuation used in the SFE. This narrow-band operation is unique in the SFE and should be taken into consideration when designing its control system. A previous work on feedback and feedforward control using optical detectors also accounts for hysteresis with a time delay [59]. The degree of hysteresis is also material and structure dependent. In the 11.5kHz SFE considered in this work, hysteresis of the piezoelectric tube was minimal such that the phase-amplitude adjustment approximation works well. Finally, it has been demonstrated that a single-frequency excitation though a piezoactuator exhibiting hysteresis results in harmonics of the excitation frequency in the displacement response [49]. Noting that in the SFE scan engine, the piezoelectric tube displacement is the input to the overall cantilevered structure operated at resonance, this high quality-factor resonance will greatly attenuate the response of the system to the hysteresis-generated harmonics [59].

## 3.5 New Self-Sensing Circuit

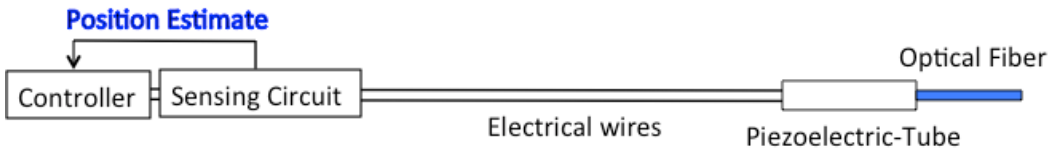


Figure 3.7. Low-footprint self-sensing is implemented with a sensing circuit at the proximal end of the device.

In this work, the structure to be controlled for 2-dimensional vibration is the SFE scan engine comprised of a piezoelectric-tube and a cantilevered optical fiber. In order to maintain the slender 1-mm size of the endoscope, a low-footprint self-sensing approach was implemented as in Figure 3.7: the *sensor* is the piezoelectric tube at the distal end within the scan engine, with a *sensing circuit* located at the proximal end. This self-sensing circuit taps into the base of the 2-m long electrical wires to give measurements of the bending-displacement of the piezoelectric tube, the methods of which will be described in this section.

This work presents a new piezoelectric self-sensing circuit tailored to the SFE application. The SFE scan engine uses a piezoelectric tube common to other piezoactuation applications, but

the SFE has a unique electrical configuration: With the scan engine attached at the distal end of a 2-m long tether, only the + and − signals of the drive voltage are wired to each piezoelectric-tube axis, without any physical grounding. This precludes direct use of the grounded-load or unipolar design of most piezoelectric self-sensing circuits in literature e.g. [30], [38], [40], [60]. The 2-m long tether also introduces distributed wire resistance and capacitance that must be taken into account for accurate remote self-sensing.

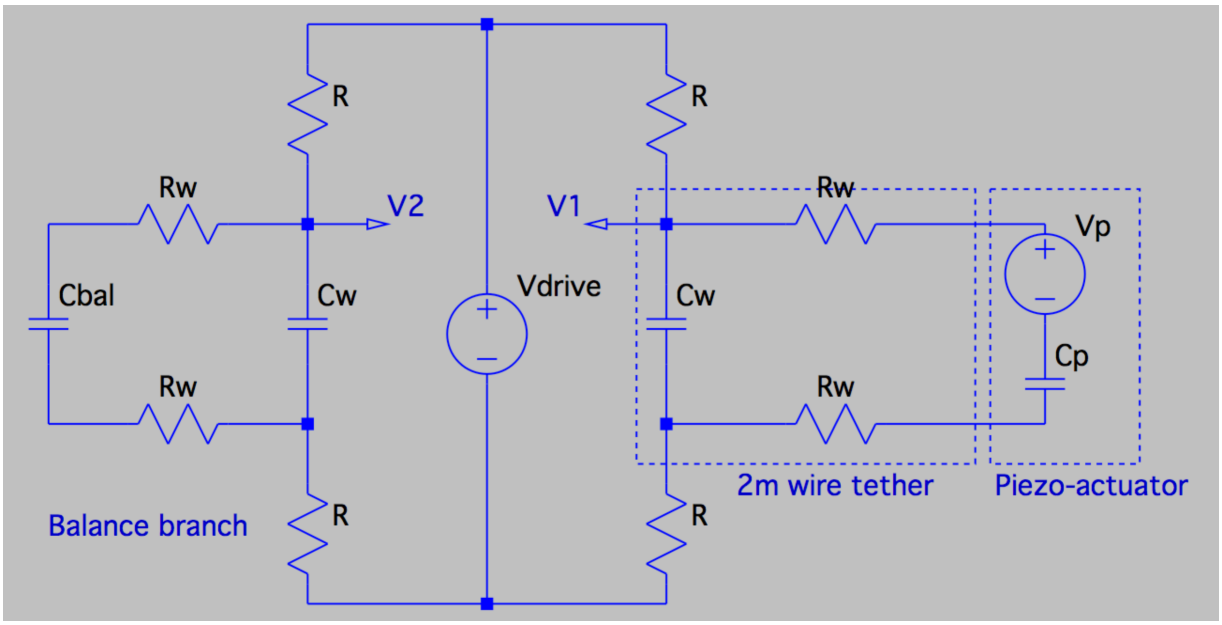


Figure 3.8. New bipolar piezoelectric self-sensing circuit design for the scan engine.

Figure 3.8 shows our piezoelectric self-sensing circuit design. One of the unique features of this circuit is that it is bipolar (that is, the drive voltages for the piezoelectric-tube load are always differential across each pair of the quadrant-electrodes. The core of the piezoelectric-tube is hollow and metallized, serving as a virtual ground). This is in contrast to most piezoelectric circuits in literature [40], [44], [60], [61] with unipolar circuits, where one side of the piezoelectric load is at or referenced to the ground potential. Another specialization of our self-sensing circuit is that the reference/balance branch is not purely capacitive e.g. $C_{bal}$, but also balances the wire and electrical port impedances with $R_w$ and $C_w$.

The piezoelectric tube is modeled following the self-sensing formulation previously discussed with a capacitance $C_p$ in series with an internal voltage source $V_p$ where $V_p$ is proportional to the normal strain [30], [38]. The piezoelectric-tube is highly stiff and bends

incrementally while exciting the optical fiber to large resonant deflection. Thus, only the piezoelectric material strain along the length of the tube (1-axis) is considered; strains in the other two normal directions are considered negligible. The self-sensing circuit then isolates $V_p$ to give a measure proportional to the small bending-displacement of the piezoelectric tube.

A general derivation of the relationship between $V_p$ and the strain of the piezoelectric material is given in this section.

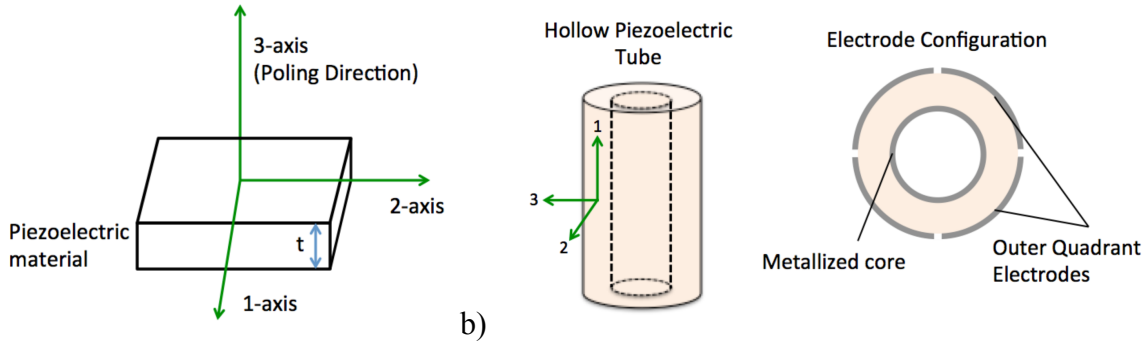


Figure 3.9. a) Axes convention for a piezoelectric material with respect to poling direction. b) Electrode configuration on the piezoelectric tube within the SFE.

Figure 3.9 shows the axes convention for a piezoelectric material poled in the 3-direction. The electric field in the 3-direction $E_3$, is related to the electric displacement in the 3-direction $D_3$, and the strain in the 1-direction $S_1$ as in Equation 3.1. In the section Simultaneous Self-Sensing Formulation, Equation 3.4 was derived where $q_p$ is the charge proportional to strain. Since $v = q/C$, Equation 3.4 is further simplified to,

$$v = \frac{q_f}{C_p^S} - V_p \tag{3.11}$$

An equivalent circuit with the piezoelectric material is shown in Figure 3.1. $v$ is the voltage across the piezoelectric element. From Equation 3.2 and Equation 3.11, we find that $V_p$ is proportional to the normal strain of the piezoelectric material along the 1-direction,

$$V_p = \frac{e_{13}\, S_1 t}{\varepsilon^S} \tag{3.12}$$

The preceding discussion has established that the internal piezoelectric voltage $V_p$ is proportional to the piezoelectric strain. Next, the relationship between that piezoelectric strain and piezoelectric tube bending is derived following Chen [31].

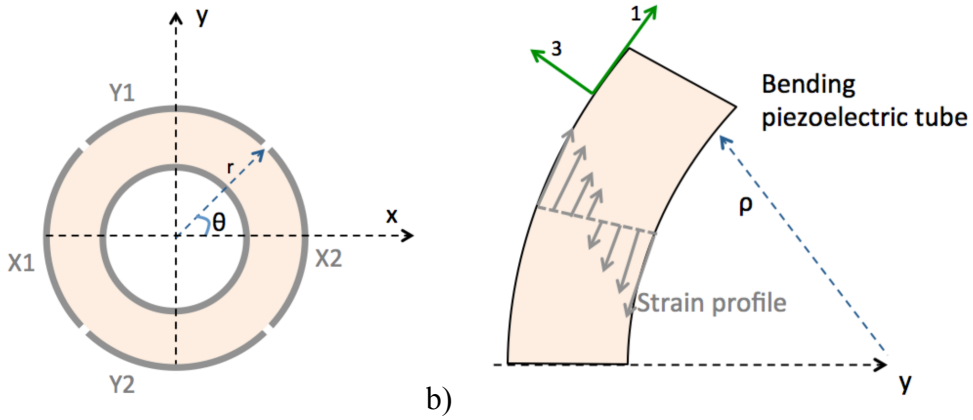


Figure 3.10. a) Electrode configuration with respect to the bending axes. b) The piezoelectric tube bending along the y-axis direction, with radius of curvature ρ.

Figure 3.10 shows the electrode configuration and bending along the defined y-axis, with bending radius of curvature ρ. The strain $S_1$ is proportional to the bending radius:

$$S_1 = -\frac{y}{\rho} \tag{3.13}$$

Building on Equation 3.12 and Figure 3.10, the total piezoelectric voltage generated by the bending of the cylindrical piezoelectric tube will be the integral around the circumference of the Figure 3.10a. Examining the geometry will help simplify the integral: Since bending is along the y-axis only, the x-axis electrodes X1 and X2 straddle the neutral axis and their strain integral will cancel out to zero. The strain along Y2 will be the negative mirror of the strain along Y1. This, we can find the total piezoelectric voltage by integrating the strain only on one quadrant, from $\theta = \frac{\pi}{4}$ to $\theta = \frac{\pi}{2}$ and multiplying by 4. Using a shell approximation, we integrate along a shell of radius r,

$$V_{p,total} = 4\int_{\frac{\pi}{4}}^{\frac{\pi}{2}} -\frac{y}{\rho} d\theta$$

$$V_{p,total} = -\frac{4}{\rho}\int_{\frac{\pi}{4}}^{\frac{\pi}{2}} r sin\theta d\theta = -\frac{2\sqrt{2}r}{\rho} \tag{3.14}$$

Equation 3.14 shows that the piezoelectric voltage is inversely proportional to the radius of curvature of the bending piezoelectric tube. That is, if the piezoelectric tube is not bent (radius of

curvature is infinite), the piezoelectric voltage is zero. As the piezoelectric tube bending increases, the piezoelectric voltage increases.

The bending of the piezoelectric tube is assumed to be separable to two bending moments about the y- and the x- axes, producing piezoelectric voltages along the Y and X electrodes respectively. This approximation is valid for small bending displacements, which is the case for the SFE scanner geometry: For the SFE piezoelectric tube of length about 2mm, diameter 0.45mm and wall thickness 0.15mm, a high voltage of 100V generated across the electrodes Y1-Y2 corresponds to an very small deflection of less than 0.4 microns [1,25]. Expanding on the small bending approximation, the bending of the piezoelectric tube is related to the transverse defection of the piezoelectric tube:

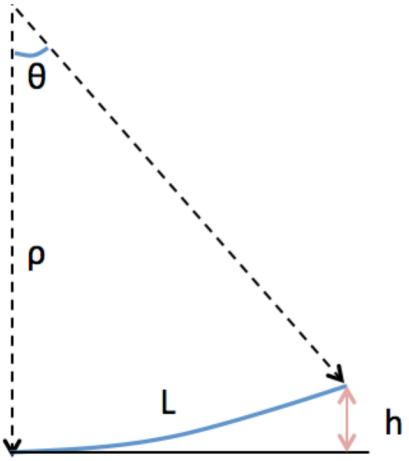


Figure 3.11. Tip deflection as related to bending radius for small bending approximation.

From Figure 3.11, the deflection $h$ of a piezoelectric tube of length $L$ and bending radius $\rho$ is given by,

$$h = \rho(1 - cos\theta) = p\left(1 - \cos\left(\frac{L}{\rho}\right)\right) \tag{3.15}$$

Taking the first order Taylor expansion of $\cos\left(\frac{L}{\rho}\right) \approx 1 - \frac{1}{2}\frac{L^2}{\rho^2} + \cdots$, we get:

$$h \approx \frac{1}{2}\frac{L^2}{\rho} \tag{3.16}$$

Combining Equation 3.14 and Equation 3.16, it is shown that by the small bending approximation, the piezoelectric voltage $V_{p,total}$, is proportional to the transverse deflection of the piezoelectric tube $h$:

$$V_{p,total} = -\frac{4\sqrt{2}r}{L^2}h \tag{3.17}$$

$r$ the radius, and $L$ the length of the piezoelectric tube, are constants. More detailed treatment of piezoelectric tube bending can be found in e.g. [34], [35].

The preceding discussion has related the *internal* piezoelectric voltage $V_p$ to the bending of the piezoelectric tube. However from Figure 3.1, the voltage $V_p$ is not directly measureable because the voltage across the piezoelectric-material electrodes is $v$. Next, this work will show how the new piezoelectric self-sensing circuit isolates $V_p$ as the measured output of the circuit $V_{meas}$, to finally establish this new method of self-sensing the bending of the SFE piezoelectric tube.

The input voltage is $V_{drive}$, which excites the scanner to resonate in a controlled trajectory. $R_w$ and $C_w$ on the left of Figure 3.8 model the resistance and capacitance of the 2-m wire-tether of the endoscope. These elements and the piezoelectric capacitance $C_p$ are mirrored on the left branch of Figure 3.8. The measurement output of the self-sensing circuit is given by:

$$V_{meas}(t) = V_1(t) - V_2(t) \tag{3.18}$$

In Laplace-domain circuit analysis,

$$V_1(t) - V_2(t) =$$
$$\frac{1}{2}\left[\frac{\frac{1}{sC_w}||\left(\frac{1}{sC_p}+2R_w\right)}{2R+\frac{1}{sC_w}||\left(\frac{1}{sC_p}+2R_w\right)}V_{drive}(s) - \frac{\frac{1}{sC_w}||\left(\frac{1}{sC_{bal}}+2R_w\right)}{2R+\frac{1}{sC_w}||\left(\frac{1}{sC_{bal}}+2R_w\right)}V_{drive}(s) + \frac{\frac{1}{sC_w}||2R}{\frac{1}{sC_p}+2R_w+\frac{1}{sC_w}||2R}V_p(s)\right] \tag{3.19}$$

If $C_{bal} = C_p$ i.e. the reference capacitance exactly matches the equivalent piezoelectric capacitance, then the first two terms in Equation 3.19 cancel out, and we get a strain-measurement sensor signal from the self-sensing circuit:

$$V_{meas}(t) = \frac{1}{2}\left[\frac{\frac{1}{sC_w}||2R}{\frac{1}{sC_p}+2R_w+\frac{1}{sC_w}||2R}V_p(s)\right] \tag{3.20}$$

Where $||$ is the parallel element operator, $a||b = \frac{a\cdot b}{a+b}$. This measurement of $V_p$ has previously been shown to be proportional to the small bending displacements of the piezoelectric tube.

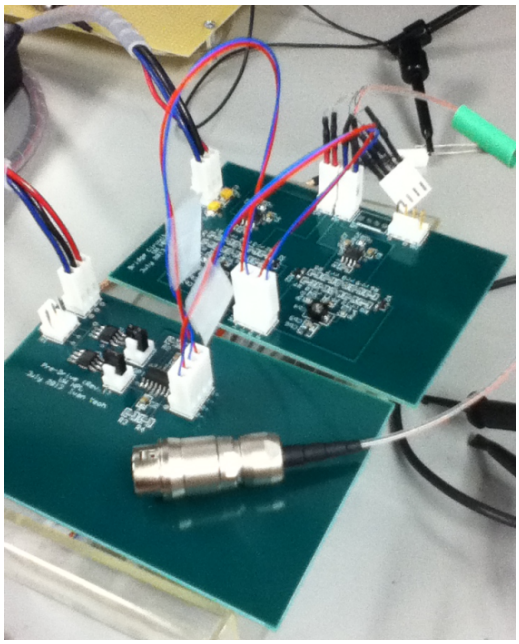

Figure 3.12. New simultaneous piezoelectric self-sensing printed circuit boards.

Figure 3.12 shows the new simultaneous piezoelectric self-sensing circuit together with a custom drive circuit implemented on printed circuit boards. The layout, design and assembly were fully self-developed. Design and part details are included in the Appendix section.

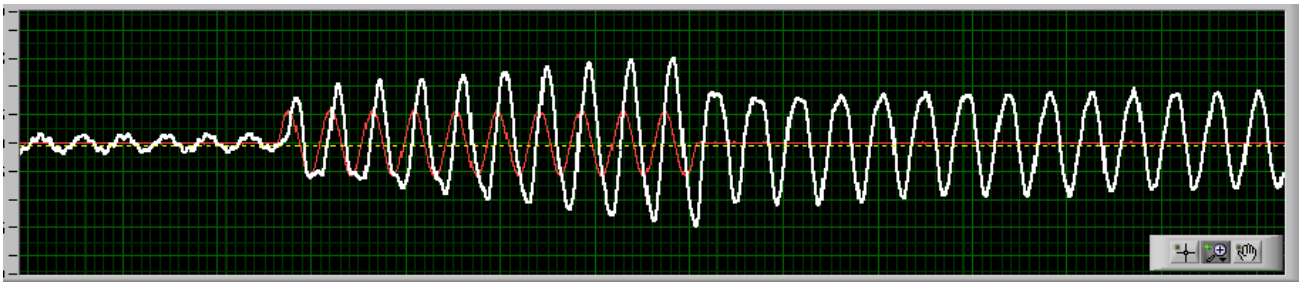

Figure 3.13. Simultaneous piezoelectric self-sensing signals. Red – actuation signal. White – sensing signal.

Figure 3.13 shows the simultaneous piezoelectric self-sensing signals as captured by custom LabVIEW driver software. The actuation signal is in Red, the sensor signal in White. Notice that in comparison to Figure 2.10, the drive signal contribution to the sensor output is mostly cancelled out and the growing oscillations of the piezoelectric tube can be observed even as actuation is applied. Figure 3.13 demonstrates simultaneous piezoelectric self-sensing operation.

In practice piezoelectric self-sensing circuits are difficult to sufficiently balance [38], [39], [61] leading to a measurement signal that is an unknown weighted sum of the drive and sensing signals. This signal contamination degrades sensing and can cause closed loop systems incorporating piezoelectric self-sensing to go unstable if unaccounted for. In this work, the assumption that the bridge circuit is perfectly balanced is not taken. New methods developed in this dissertation are robust enough to account for $C_{bal} \neq C_p$ as described in later sections.

## 3.6 SUMMARY

This chapter presented simultaneous piezoelectric self-sensing, which enables actuating and sensing with the same piezoactuator and at the same time. The formulation and typical circuit topologies for simultaneous piezoelectric self-sensing were reviewed before a novel piezoelectric self-sensing circuit was introduced in this dissertation. The electrical dynamics of this self-sensing circuit was analyzed and the design implemented in custom printed circuit boards. This new self-sensing architecture is the basis for later electromechanical modeling and adaptive control techniques developed in this dissertation.

# Chapter 4. ELECTROMECHANICAL MODELING OF THE SCANNING FIBER TECHNOLOGY

With the development of time-multiplexed and simultaneous piezoelectric self-sensing, the first specific aim to pioneer piezoelectric self-sensing as a miniature sensing modality for the SFE and miniature scanners has been accomplished. The next aim is to develop electromechanical models suitable with piezoelectric self-sensing. This will enable correct use of the sensing signals toward introducing precision self-calibrating algorithms for the scanning fiber technology.

## 4.1 Previous Work in Modeling the Scanning Fiber System

Initial investigations by Smithwick et al. approached the modeling of the SFE by considering the optical fiber alone, as cylindrical cantilevered beam with nonlinear dynamics. The piezoelectric tube was assumed to be massive and stiff enough as to not be affected by the fiber motion [62]. As such, the cantilever beam only models the optical fiber, with the piezoelectric tube deflection providing the base excitation. Smithwick's motivation was for a dynamic model that is simple yet able to explain all the dynamical phenomena relevant to the scanning fiber operation. In particular, the dynamic model was to be able to explain all types of motion-related (discounting optical and other phenomena) scan distortions expressed by the scanning fiber device. Primary distortions reported by Smithwick et al. include the following.

Amplitude jump phenomena – when scanning at a constant frequency and input amplitude, small disturbances can cause the optical fiber displacement response to change dramatically [8], [62]. This is related to the bending over of the frequency response of nonlinear systems, which results in a 'jump' between two stable regions as illustrated below. While the jump phenomena is predicted by the nonlinear dynamics considered by Smithwick, the experimental data did not exhibit a strong bending over in the frequency response [8], [62].

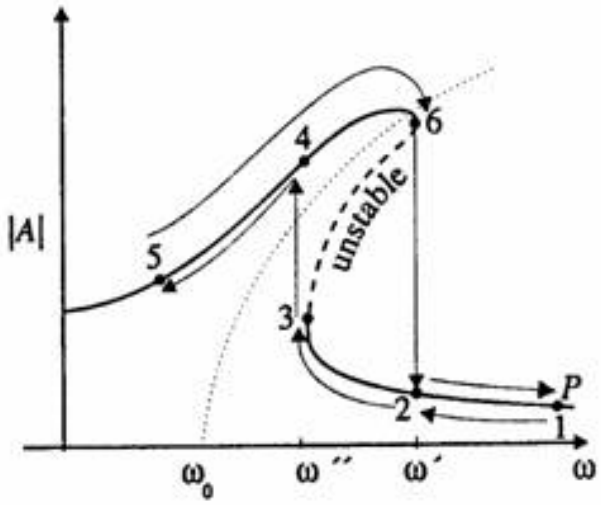


Figure 4.1. Amplitude jump phenomenon. Nonlinear dynamical systems may exhibit nonsymmetrical frequency responses with multiple stable and unstable curves close to the resonance frequency.

Whirling – When excitation at the resonant frequency was input to only one electrode axis, the displacement response for a perfect and linear system should only be along that axis. However, Smithwick measured response along the both orthogonal axes, producing an elliptical fiber-tip path in a phenomenon called whirling. This whirling was associated with out-of-plane instabilities in nonlinear cantilever systems [8].

Ovular scan – When the inputs to each of the two electrode axes are equal amplitude sine and cosine signals respectively, the expected response is a circular scan. However it was observed that ovular scans result. Smithwick et al. attributed this phenomenon to linear fiber asymmetry effects [8].

Morphing circles – With inputs to each of the two electrode axes as triangle modulated sine and cosine signals respectively, the expected response is a set of growing and shrinking concentric circles. However, in experiments the resulting scans started out ovular then morphed in orientation and aspect ratio over the modulation periods [8].

To account for these image distortion causing phenomena, Smithwick et al. derived a set of coupled Duffing's equations that included aerodynamic damping starting from the nonlinear integro-differential equations derived by Pai and Nayfeh [63] which expanded on the work of Haight and King [64], and Crespo da Silva and Glynn [65], [66]. Here the main findings of these

references are reviewed: Haight and King investigated the vibrations of slender rods with nearly equal principal moments of inertia of the uniform cross-section, with excitation always in only one direction of a principal axis of inertia [64]. Haight and King found that in addition to the in-plane instability associated with the jump phenomenon, instability with respect to out-of-plane perturbations is also present for some sets of input amplitude and frequencies. This out-of-plane instability is reported to result in elliptically shaped harmonic solutions. The position of the instability region changes with natural frequency ratio of the principal axes as shown in Figure 4.2, and its extent is also reduced or eliminated by higher system damping [64].

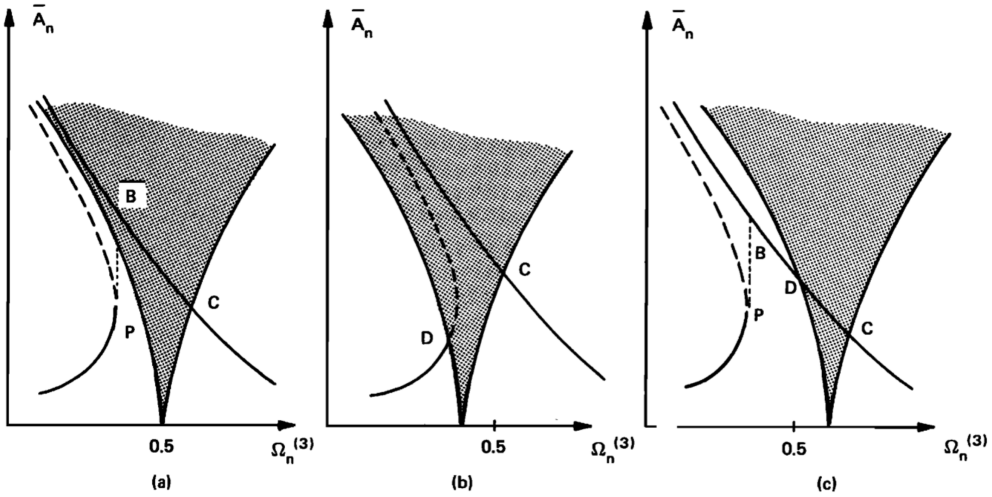


Figure 4.2. Regions of out-of-plane instability (grey area) for three different rods (circular cross-section, circular with parallel flats and driven parallel to flats, circular with parallel flats and driven perpendicular to flats) examined by Haight and King [64].

Pai and Nayfeh performed a quantitative analysis of the out-of-plane instability for laterally excited cantilever beams. They found that the instability region is influenced by principal axis stiffness ratios, forcing frequency, system damping and mode number [63]. Pai and Nayfeh also found that the out-of-plane motions could manifest as steady whirling, unsteady whirling or even chaotic traces as depicted in Figure 4.3.

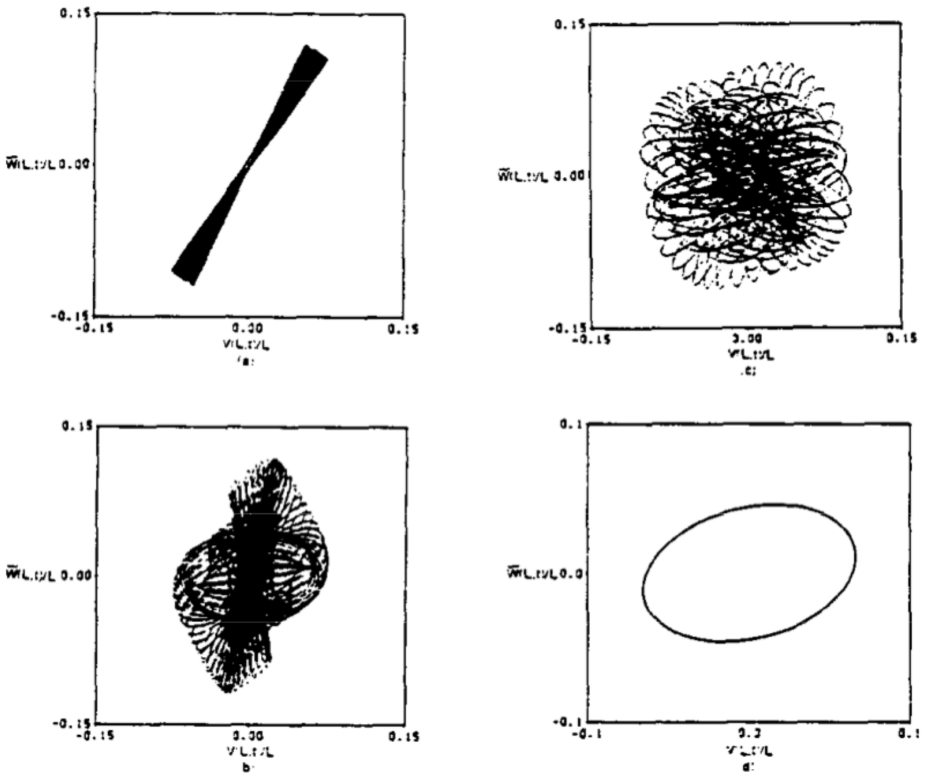

Figure 4.3. Various tip motion traces when out-of-plane instability occurs according to Pai and Nayfeh [63].

The coupled Duffing's equations that included aerodynamic damping used for analysis by Smithwick et al. was,

$$\ddot{p} + \bar{\varepsilon} b \dot{p} + \bar{\varepsilon}\bar{\alpha}|\dot{p}|\dot{p} + p = -\bar{\varepsilon} p(p^2 + q^2) - \varepsilon_2 p(\dot{p}^2 + \dot{q}^2) + \bar{\varepsilon}\bar{C}v_z \tag{4.1}$$

$$\ddot{q} + \bar{\varepsilon} b \dot{q} + \bar{\varepsilon}\bar{\alpha}|\dot{q}|\dot{q} + \omega_y^2 q = -\bar{\varepsilon} q(p^2 + q^2) - \varepsilon_2 q(\dot{p}^2 + \dot{q}^2) + \bar{\varepsilon}\bar{C}v_y \tag{4.2}$$

$p$ and $q$ are the mode displacements along the cantilever-transverse z and y axes respectively, $\bar{C}v_z$ and $\bar{C}v_y$ the excitation along the z and y axes respectively, $b$ and $\bar{\alpha}$ the damping parameters, $\bar{\varepsilon}$ and $\varepsilon_2$ the condensed nonlinearity coefficients [8], [67].

Equations 4.1 and 4.2 are detailed nonlinear models used by Smithwick in analyzing the theoretical response of a coupled Duffing's dynamical system. Importantly, the above equations were then decoupled and simplified for nonlinear control design [59], [68] into,

$$\ddot{p} + b_z \dot{p} + \omega_z^2 p = -\varepsilon_z p^3 + C_z v_z \tag{4.3}$$

$$\ddot{q} + b_y \dot{q} + \omega_y^2 q = -\varepsilon_y q^3 + C_y v_y \tag{4.4}$$

These equations were further simplified to the linear form for feedback control design [8], [68] to,

$$\ddot{p} + b_z\dot{p} + \omega_z^2 p = C_z v_z \tag{4.5}$$

$$\ddot{q} + b_y\dot{q} + \omega_y^2 q = C_y v_y \tag{4.6}$$

In summary, Smithwick began with coupled nonlinear Duffings equations to gain understanding of the optical fiber deflection response to voltage inputs at the piezoelectric-tube electrodes. Beyond quantitative analysis, the dynamic equations were simplified into uncoupled weakly nonlinear or linear systems as in Equations 4.3-4.6 for control system design. Thus, Equations 4.3-4.6 move towards the approach taken later by Kundrat in linear modeling of the optical fiber with virtual axes excitation to decouple the system response, which are discussed next.

In a subsequent investigation, Kundrat accounted for the apparent coupled nonlinear response by introducing virtual axes excitation, arriving at two closely linear orthogonal systems. Kundrat found that the piezoelectric-tube electrode axes are not aligned with the principal axes or Eigendirections of the cantilever beam [9]. The piezoelectric-tube has four quadrant electrodes, each electrode pair representing one axis of forcing. In previous analyses, Smithwick implicitly assumed that the principal axes of the cantilever beam model and the electrode actuation axes were aligned. Kundrat introduced the concept of driving along the Virtual Axes (VA) which are a set of rotated axes addressed by a linear combination of the piezoelectric-tube axes [27],

$$\widehat{\boldsymbol{VE1}} = [\cos(\theta_1)\,\hat{\boldsymbol{x}}_1 + \sin(\theta_1)\,\hat{\boldsymbol{x}}_2] \tag{4.7}$$

$$\widehat{\boldsymbol{VE2}} = [\cos(\theta_2)\,\hat{\boldsymbol{x}}_1 + \sin(\theta_2)\,\hat{\boldsymbol{x}}_2] \tag{4.8}$$

$\hat{\boldsymbol{x}}_1$ and $\hat{\boldsymbol{x}}_2$ are the electrode input axes vectors, $\theta_1$ and $\theta_2$ are the Eigendirection angles, $\widehat{\boldsymbol{VE1}}$ and $\widehat{\boldsymbol{VE2}}$ are the virtual axes vectors.

In Kundrat's investigation, a 30-node finite-element numerical model for the optical fiber was constructed based on nonlinear cantilever beam theory, and also using the equations derived by Pai and Nayfeh as the starting point [9]. Numerical integration was performed using the Nonlinear Newark's Method. This numerical model was used for investigating the effects of different strategies of braking, fiber asymmetry and large displacement dynamics.

From experimental results, Kundrat et al. showed that with proper alignment of forcing with the Eigendirections, the nonlinear distortion effects such as out-of-plane instability and bending-over of the frequency response in jump phenomena was eliminated.

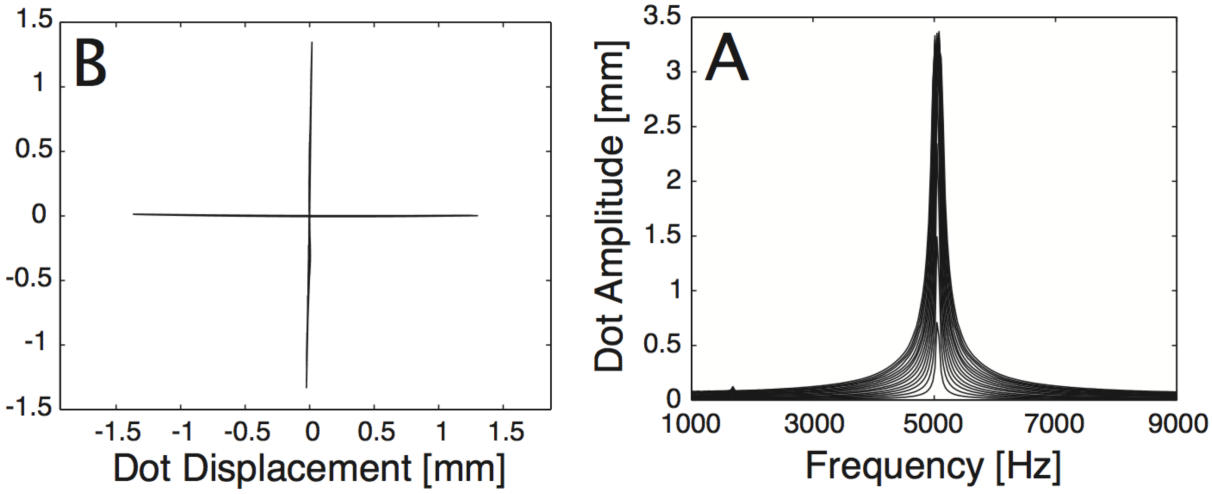


Figure 4.4. Elimination of axes-coupling and linearity of frequency response demonstrated by Kundrat et al. [9], [27].

In summary, by properly realigning the actuation axes, Kundrat was able to model the dynamics of the optical fiber with two orthogonal linear systems. Figure 4.4 from Kundrat's work shows the decoupled response of the two orthogonal axes, and the remarkable linearity of the system's frequency response [9], [27].

## 4.2 New Electromechanical Modeling Approach

This work expands upon the investigations of Smithwick and Kundrat but takes a substantially different approach to modeling the dynamics of the scanning fiber system. Firstly, not only the optical fiber but also the piezoelectric tube is considered as the dynamical structure. Previously, the dynamics of the piezoelectric-tube were ignored and the piezoelectric-tube was assumed to give a certain base-excitation to the optical fiber. Secondly, not only the mechanical domain will be included into the model, but also the electrical domain dynamics. This means that the vibrational structure and the sensing circuit will be considered to give a full description of the simultaneous piezoelectric self-sensing system. Thirdly, a more data-driven and controls-

oriented approach will be taken for system modeling. Instead of deriving the system dynamics from first principles, general model formats will be adapted to the scanning fiber response via system identification and modal analysis techniques. These strategies will result in effective models for adaptive control that is applicable to different devices that vary in parameters under manufacturing uncertainty.

Two distinct but related modeling methods are developed in this dissertation. The first is a *complete circuit equivalent* of the electromechanical system, including the scan engine and the simultaneous self-sensing circuit. This complete model is used to analyze the simultaneous piezoelectric self-sensing approach and the integrated system dynamics in general. The second modeling method is an *empirical modal analysis* based on the results of the electromechanical circuit equivalent. The pertinent mode dynamics of the system are extracted and the reduced-order model produced is highly compatible with the adaptive control techniques developed in later sections.

## 4.3 Circuit Equivalent Electromechanical Model

The first electromechanical model introduced is a circuit equivalent that models the scan engine in the mechanical domain and the new self-sensing circuit in the electrical domain. These domains are combined in a full circuit analogue. By modeling the entire piezoelectric self-sensing circuit, imbalances in the bridge topology are taken into account.

### 4.3.1 *Model Derivation*

This work considers that the mechanical scan engine – including the piezoelectric-tube and the optical fiber – is separable into two linear orthogonal dynamical systems. This assumption build upon the investigation of Kundrat [9], [28] and is an approach used in related work on piezoelectric-tube control [29]. Kundrat et al. have shown that within the range of operation of up to 30V actuation, the scanner's fiber deflection responds linearly and is decomposable into 2 orthogonal Eigendirections. The feedforward control design of Kundrat at al. in [27] and the baseline closed-loop control model of Smithwick et al. in [59], [69] for SFE scan tracking was based on a simple harmonic oscillator or mass-spring-damper form for the system dynamics:

$$\ddot{x} + 2\zeta\omega_n\dot{x} + \omega_n^2 x = F \tag{4.9}$$

Furthermore from performed experiments, the transfer function from input-to-fiber deflection along each Eigendirection has two distinct resonant modes at around 11.5kHz and 22.5kHz, as shown in Figure 4.5. The simple form of the system transfer function makes it easy to fit a lumped-mass model to the data. Since the frequency of excitation of the structure is narrow-band at the 1st resonance (to excite the fiber to resonance), the system is also less sensitive to modeling errors at frequencies far from 11.5kHz.

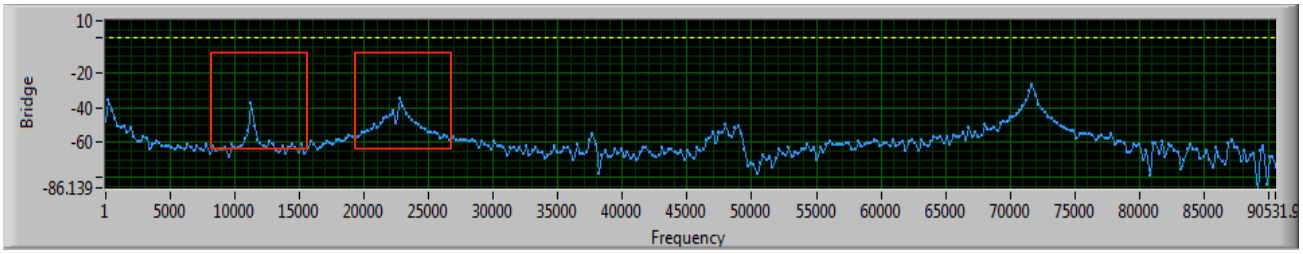


Figure 4.5. Experimental input-to-piezo deflection amplitude (y-axis) versus frequency excitation (x-axis), with the first two resonant modes clearly identifiable.

Given the availability of the newly developed piezoelectric miniature sensor, a data-driven or empirical modeling philosophy is taken by selecting the most general model form that sufficiently explains the experimental transfer function. Figure 4.6 shows the lumped-mass model of the mechanical scanner along one Eigendirection. Following the Kundrat et al. approach of using Virtual Axes to excite along the scanner Eigendirections, this work expands the model to two linear double mass-spring-dampers by mechanically lumping the optical fiber and piezoelectric tube with the mounting collar as the rigid reference.

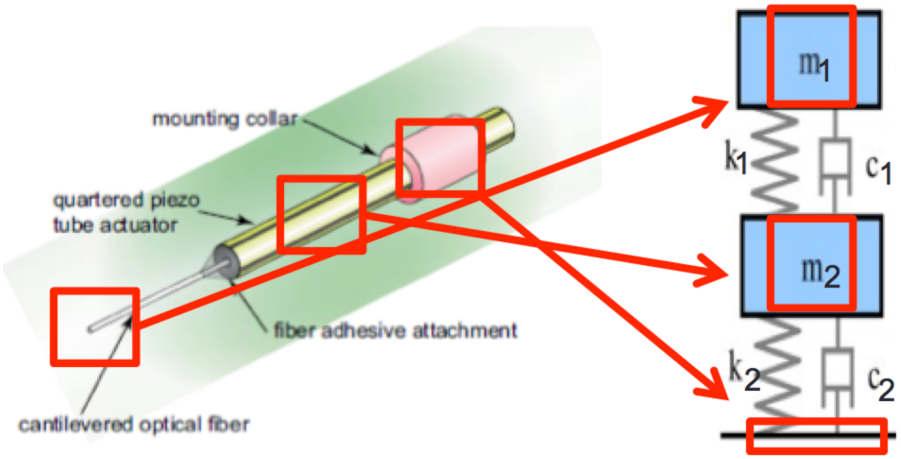


Figure 4.6. Lumped model of the mechanical scanner.

To unify the mechanical model with the self-sensing circuit model, the mechanical elements are converted into their circuit equivalents. Velocity is analogous with voltage and force analogous with current. The electrical resistor is analogous to the mechanical damper, with governing equations,

$$V = Ri \quad \leftrightarrow \quad v = \frac{1}{c} f \tag{4.10}$$

With voltage $V$, resistance $R$, current $i$ and velocity $v$, damping $c$, force $f$.

The electrical inductor is analogous to the mechanical spring, with governing equations,

$$V = L\frac{di}{dt} \quad \leftrightarrow \quad x = \frac{1}{k} f; v = \frac{1}{k}\frac{df}{dt} \tag{4.11}$$

With voltage $V$, inductance $L$, current $i$ and velocity $v$, stiffness $k$, force $f$.

The electrical capacitor is analogous to the mechanical mass, with governing equations,

$$i = C\frac{dV}{dt} \quad \leftrightarrow \quad f = m\frac{dv}{dt} \tag{4.12}$$

With current $i$, capacitance $C$, voltage $V$ and force $f$, mass $m$, velocity $v$.

The circuit equivalent model will have portions in the mechanical and electrical domains. The piezoelectric-tube acts as a transducer between these two domains. To develop a transducer model for the piezoelectric element, we begin with the familiar form introduced by Dosch et al. shown in Figure 4.7, where $v_p = K_p x$ is the piezoelectric voltage proportional to the

piezoelectric displacement $x$. The piezoelectric element here transforms between current-voltage and force-velocity.

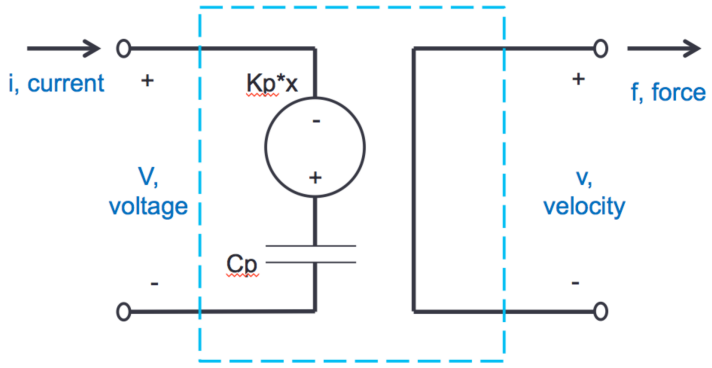


Figure 4.7. Internal voltage source model of piezoelectric transducer.

In order for the model to be consistent with the electrical-mechanical analogies, it is transformed by converting the piezoelectric voltage source to a current source via Norton's equivalence [70]. The voltage drop contributions of $V_p$ can be subsumed into an equivalent charge across $C_p$ provided by an internal current source, as shown in Figure 4.8.

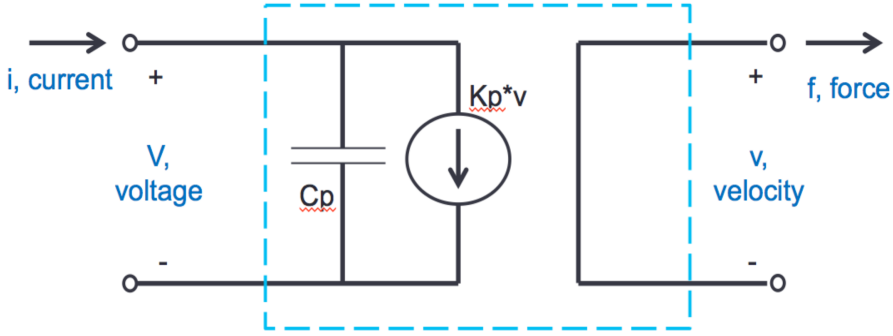


Figure 4.8. Internal charge source model of piezoelectric transducer.

Energy/power conservation should also be applied to the transducer block, providing an additional constraint equation,

$$Power\ in = Power\ out + Rate\ of\ energy\ storage$$

$$Vi = vf + V\frac{dq}{dt} \tag{4.13}$$

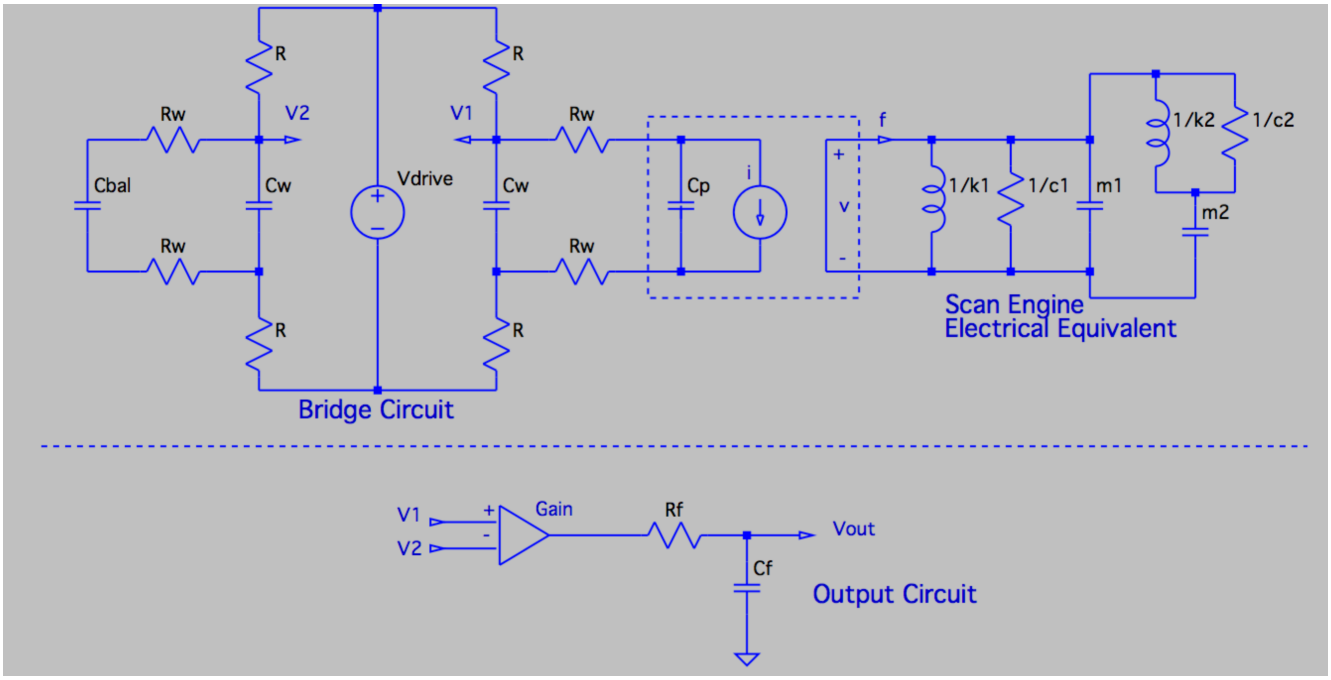


Figure 4.9. Full electro-mechanical model of the scanner.

Combining the mechanical and electrical subsystems using the circuit element produces the full electro-mechanical circuit equivalent model of the scanner as shown in Figure 4.9 for one active Eigendirection. The full circuit model also includes the gain of the differential amplifier and it general low-pass filtering characteristic in the output circuit subsystem.

This linear model can be cast into state space form as:

$$\dot{x} = Ax + Bu$$
$$y = Cx$$

$$A = \begin{bmatrix} -\frac{\frac{1}{R}+\frac{1}{R_w}}{2C_{w1}} & \frac{1}{2C_pR_w} & 0 & 0 & 0 & 0 & 0 & 0 & 0 \\ \frac{1}{2C_{w1}R_w} & \frac{-1}{2C_pR_w} & 0 & 0 & -\frac{k_p}{m_1} & 0 & 0 & 0 & 0 \\ 0 & 0 & 0 & 0 & \frac{k_1}{m_1} & 0 & 0 & 0 & 0 \\ 0 & 0 & 0 & 0 & \frac{k_2}{m_1} & -\frac{k_2}{m_2} & 0 & 0 & 0 \\ 0 & \frac{k_p}{C_p} & -1 & -1 & -\frac{c_1+c_2}{m_1} & \frac{c_2}{m_2} & 0 & 0 & 0 \\ 0 & 0 & 0 & 1 & \frac{c_2}{m_1} & -\frac{c_2}{m_2} & 0 & 0 & 0 \\ 0 & 0 & 0 & 0 & 0 & 0 & -\frac{\frac{1}{R}+\frac{1}{R_w}}{2C_{w2}} & \frac{1}{2C_bR_w} & 0 \\ 0 & 0 & 0 & 0 & 0 & 0 & \frac{1}{2C_{w2}R_w} & \frac{-1}{2C_bR_w} & 0 \\ gain\frac{1+off_1}{2R_fC_{w1}} & 0 & 0 & 0 & 0 & 0 & gain\frac{1+off_2}{2R_fC_{w2}} & 0 & -\frac{1}{R_fC_f} \end{bmatrix} \quad B = \begin{bmatrix} \frac{1}{R} \\ 0 \\ 0 \\ 0 \\ 0 \\ 0 \\ \frac{1}{R} \\ 0 \\ 0 \end{bmatrix}$$

$$C = \begin{bmatrix} 0 & 0 & 0 & 0 & 0 & 0 & 0 & 0 & \frac{1}{C_f} \end{bmatrix} \tag{4.14}$$

The input $u(t)$ represents the drive voltage, the output $y(t)$ the self-sensing voltage, and the 8 states $x = [Q_{w1} \quad Q_{w2} \quad Q_p \quad Q_b \quad i_1 \quad i_2 \quad Q_1 \quad Q_2 \quad Q_f]$ correspond to the charge on $C_{w1}$ and $C_{w1}$, charge on piezoelectric capacitance $C_p$ and balance capacitance $C_b$, analogous force through $k_1$ and $k_2$, analogous charge across $m_1$ and $m_2$, and charge across filtering capacitor $C_f$ respectively.

The full circuit modeling approach taken in this dissertation supplements the simultaneous piezoelectric self-sensing implementation by accounting for bridge circuit imbalance. As previously described, piezoelectric self-sensing circuits are difficult to sufficiently balance [38], [39], [61] leading to degradation of the sensing signal. Since $C_{bal}$ and $C_p$ are both included as elements in the circuit equivalent model, the case where $C_{bal} \neq C_p$ is a trivial scenario that can be simulated by the model.

### 4.3.2 *Model Verification*

To verify the presented electro-mechanical model, the model parameters were fit to experimental self-sensing data using grey-box identification and Matlab nonlinear optimization functions. The identified model is then used to predict the output and states of the electromechanical system given an input. The experimentally measured piezoelectric self-sensing output versus the electromechanical model prediction are compared:

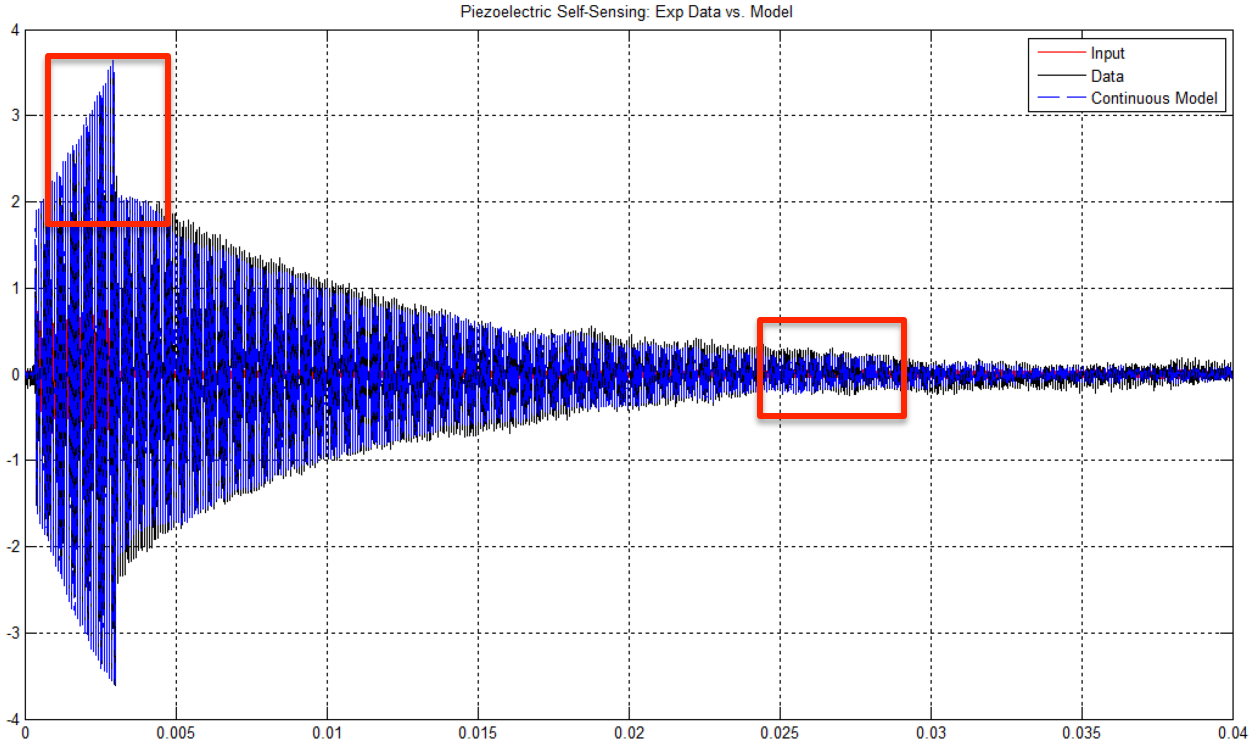


Figure 4.10. Comparison between experimental data and the electromechanical model prediction.

Zooming into the boxed sections:

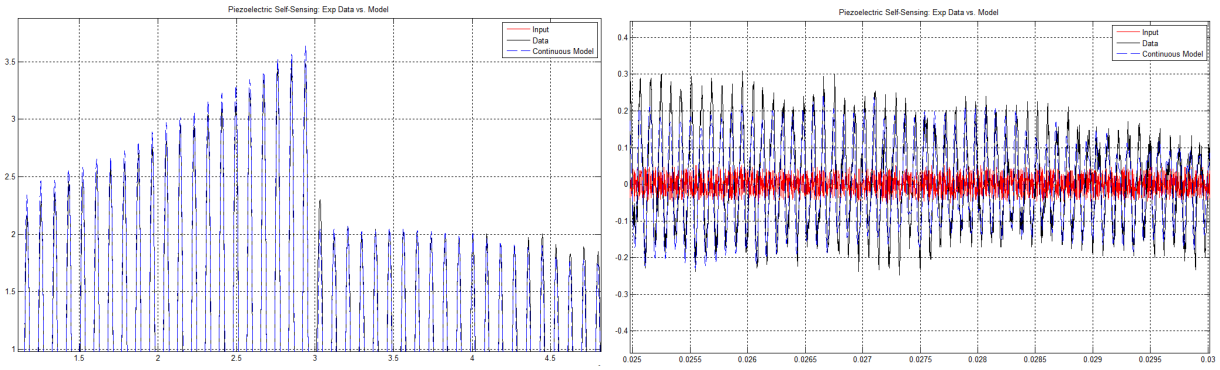


Figure 4.11. Comparison between experimental data and the electromechanical model prediction – zoom in.

Results show that there is a good match between the experimental data and the identified model, even in the presence of substantial output sensor noise. Importantly, the model is able to capture the effects of bridge circuit imbalance, which results in the ‘finning’ shape to the output signals when actuation is active. The controller to be designed must be robust to bridge circuit imbalance and thus a model that predicts the ‘finning’ effect will greatly inform later controller design.

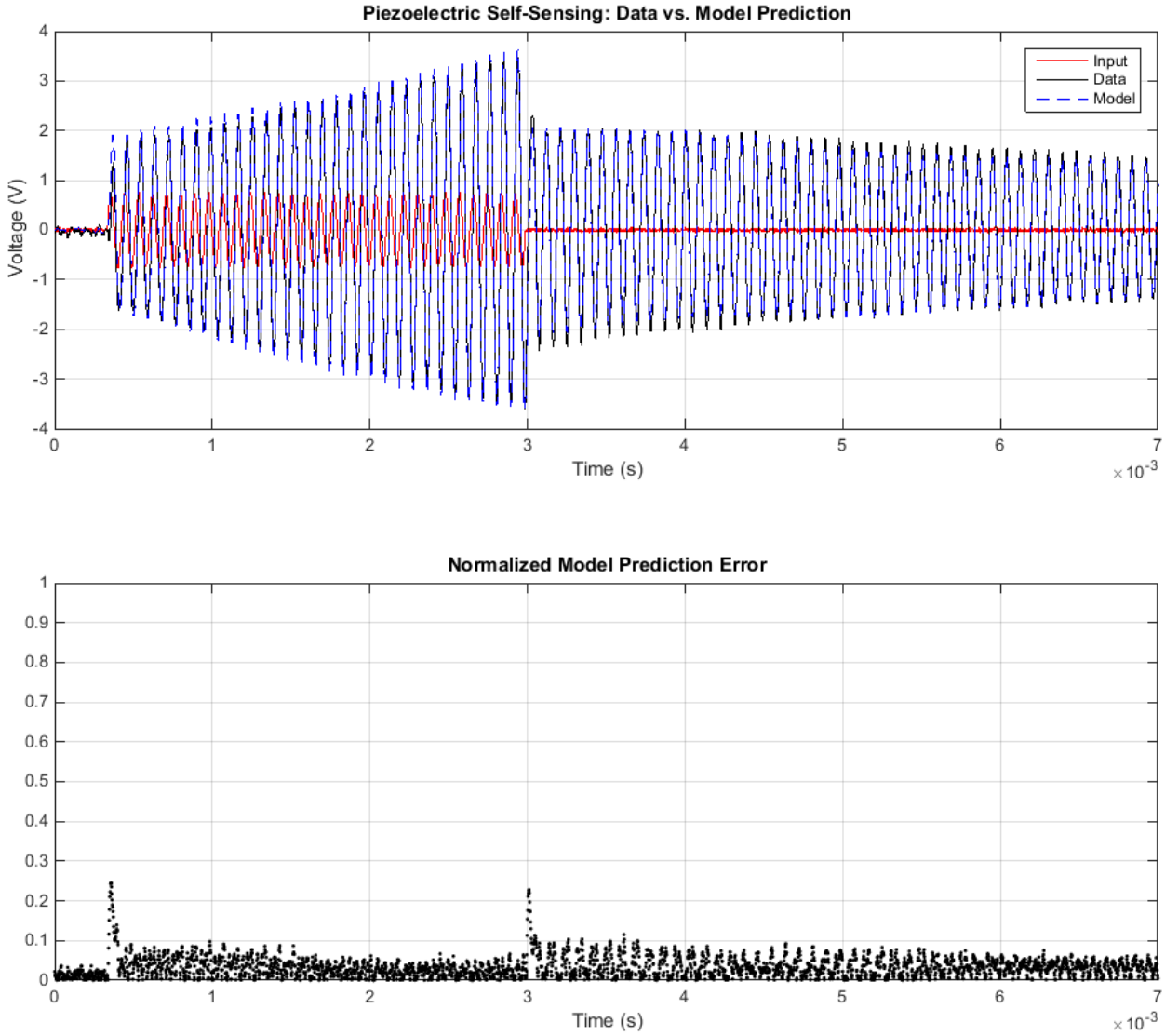


Figure 4.12. a) Time- profile comparison between experimental data and model prediction. b) Plot of normalized error between experimental data and model prediction.

Further, Figure 4.12b plots the normalized (with respect to maximum amplitude) error between the experimental data and the model prediction; the maximum prediction error was 24.6%, and the mean prediction error was 2.2% of the maximum signal amplitude. This experimental data shows that the expanded model - which includes the capacitive bridge circuit - is able to predict the effects of the circuit imbalance that manifests as feed-though when the actuation signal is active ($t<0.03s$) as in Figure 4.12a. Self-sensing is made robust to variations in reference

capacitor values because the capacitor values are included in the system identification parameters.

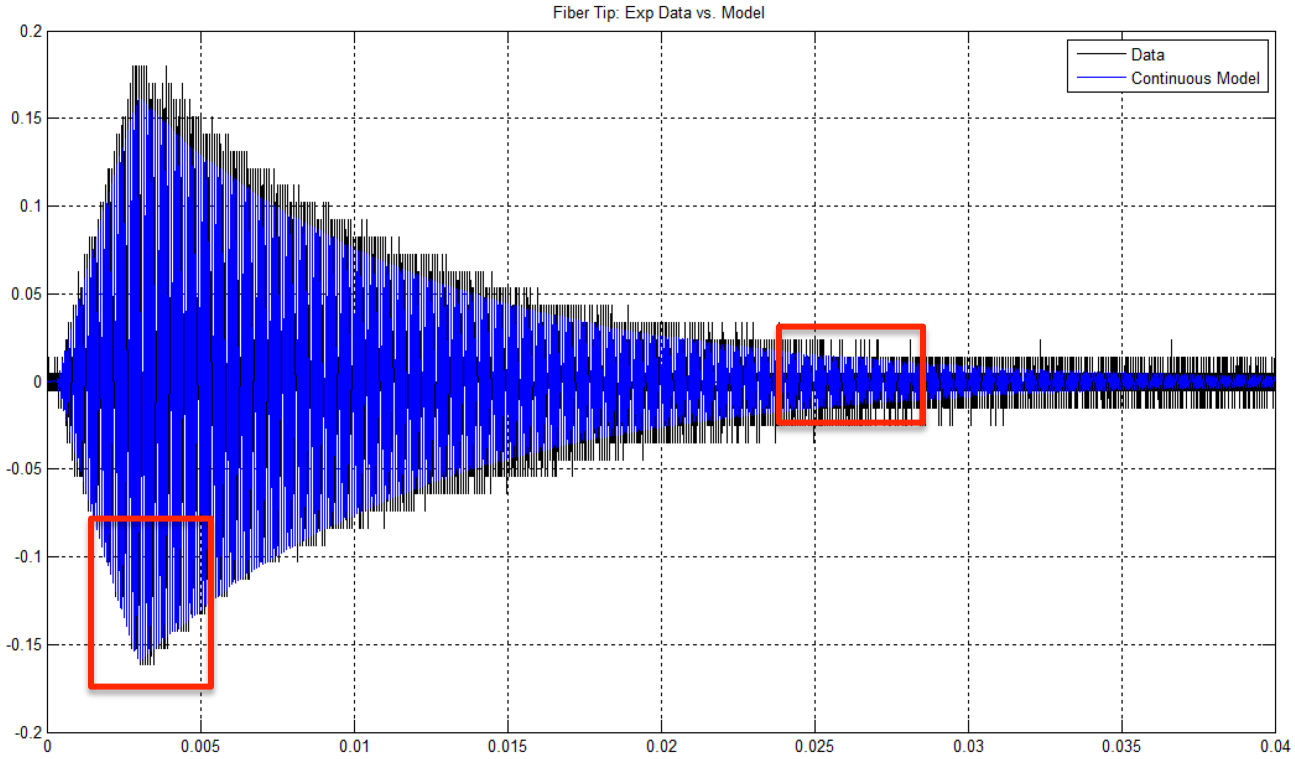


Figure 4.13. Comparison between laser spot position data and the electromechanical model prediction.

Zooming into the selected portions:

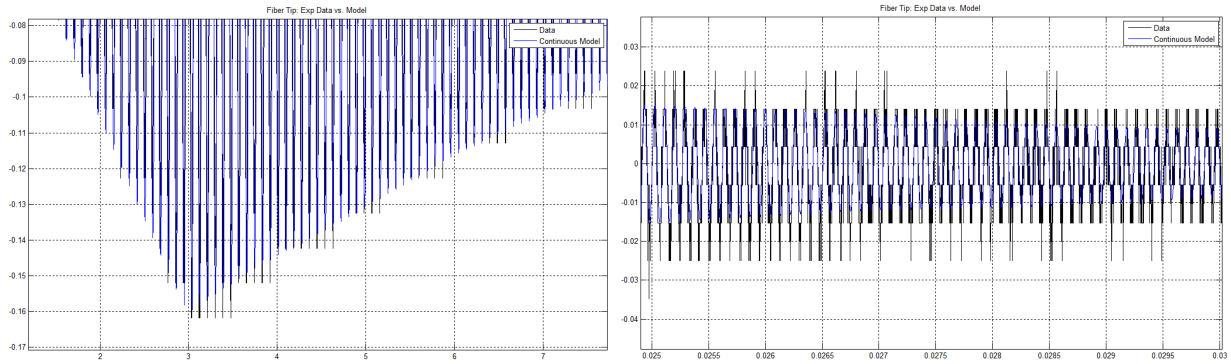


Figure 4.14. Comparison between laser spot position data and the electromechanical model prediction – zoom-in.

Simultaneous piezoelectric self-sensing enables measurement of the strain of the piezoelectric tube, but the control target is optical fiber tip deflection. The latter output is not

directly measureable using piezoelectric self-sensing, but it is implicit as a mechanical displacement state within the full electromechanical model. In the model, the expected displacement of the optical fiber tip may be simulated. To verify that this internal state is able to predict the optical fiber displacement, the optical fiber displacement ground-truth is recorded using an optical position sensor. Comparison between the model prediction and the optical position sensor data is shown in Figure 4.14, showing that the electromechanical model can accurately model the dynamics of the piezoelectric tube and the optical fiber state as well.

### 4.3.3 *Piezoelectric-Tube Cross-Coupling*

The concepts of Virtual Axes excitation and Eigendirection response as introduced by Kundrat are important to simplify the electromechanical modeling of this work. The circuit equivalent model depicted in Figure 4.9 is a flattened model with the mechanical equivalent sub-circuit representing one Eigendirection. Excitation and analysis of the orthogonal eigendirections are made possible with Virtual Axes or combinatorial excitation [27]: There are two identical simultaneous piezoelectric self-sensing circuits, one for each electrical axis of the piezoelectric tube. The response between each self-sensing circuit channel and each Eigendirection is experimentally identified and used for Virtual Axes excitation.

In practice, depending on manufacture quality, a piezoelectric-tube will have some degree of capacitive non-symmetry. For any electrode quadrant, since differential voltages give the drive signal, one of the adjacent electrodes will be at +V while the other at –V potential. If the capacitive coupling of one electrode between its two adjacent electrodes is exactly equal, the coupling contributions of the adjacent electrodes will cancel out. If however the capacitive coupling of one electrode between its two adjacent electrodes is uneven, the coupling contributions of the adjacent electrodes will not cancel out. A small signal coupling will result between the two electrical axes of the piezoelectric tube. Kuiper et al. used manually tuned auxiliary capacitors to cancel out the effects of capacitive cross coupling [40].

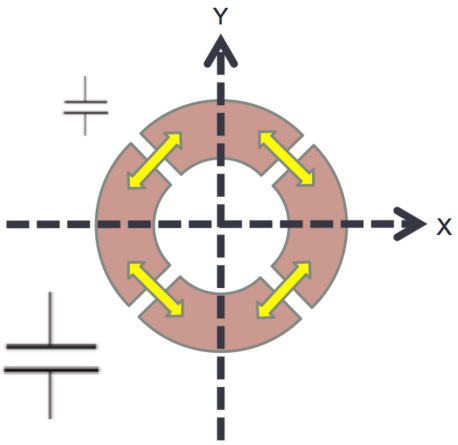


Figure 4.15. The case where capacitive coupling between electrode quadrants is not uniform leads to capacitive cross-coupling between electrical axes of the piezoelectric-tube.

This coupling is typically very small and does not affect the actuation dynamics. When identifying the circuit equivalent model, the capacitive cross coupling will be assimilated into the perceived bridge imbalance and not affect the estimated resonant dynamics of the mechanical structure.

However, capacitive coupling influences simultaneous piezoelectric self-sensing because the small measurement signal is amplified up to 500x by differential amplifiers. Any weak coupling signal from the other electrical axis will show up in the measurement.

To illustrate the effect of capacitive coupling on the simultaneous piezoelectric self-sensing signals, Figure 4.16 shows experimental data where only one electrode axis is actuated (Red) with a burst sinusoidal excitation at the mechanical resonance followed by a long rest period, and the sensing signal on the other electrode axis is recorded (Blue). The predicted mechanical response is a whirling deflection of the scanner starting at rest and then decaying when actuation is turned off. The predicted electrical signal at the orthogonal electrode axis is a sensing signal starting at zero that grows with the whirling response of the scanner and also decays when actuation is turned off.

Figure 4.16 and Figure 4.17 show the drive signal of Channel 2 (Red) and the sensing signal of Channel 1 (Blue). It is expected that the sensing signal (Blue) would start from rest, and not have any discontinuities, since it is a pure sensing signal (actuation only given on the other electrode axis). However, because there is capacitive coupling between the electrical channels,

the sensing signal on Channel 1 (Blue) is confounded – the signal does not start from rest and exhibits a discontinuity when the voltage on the orthogonal axis is turned off.

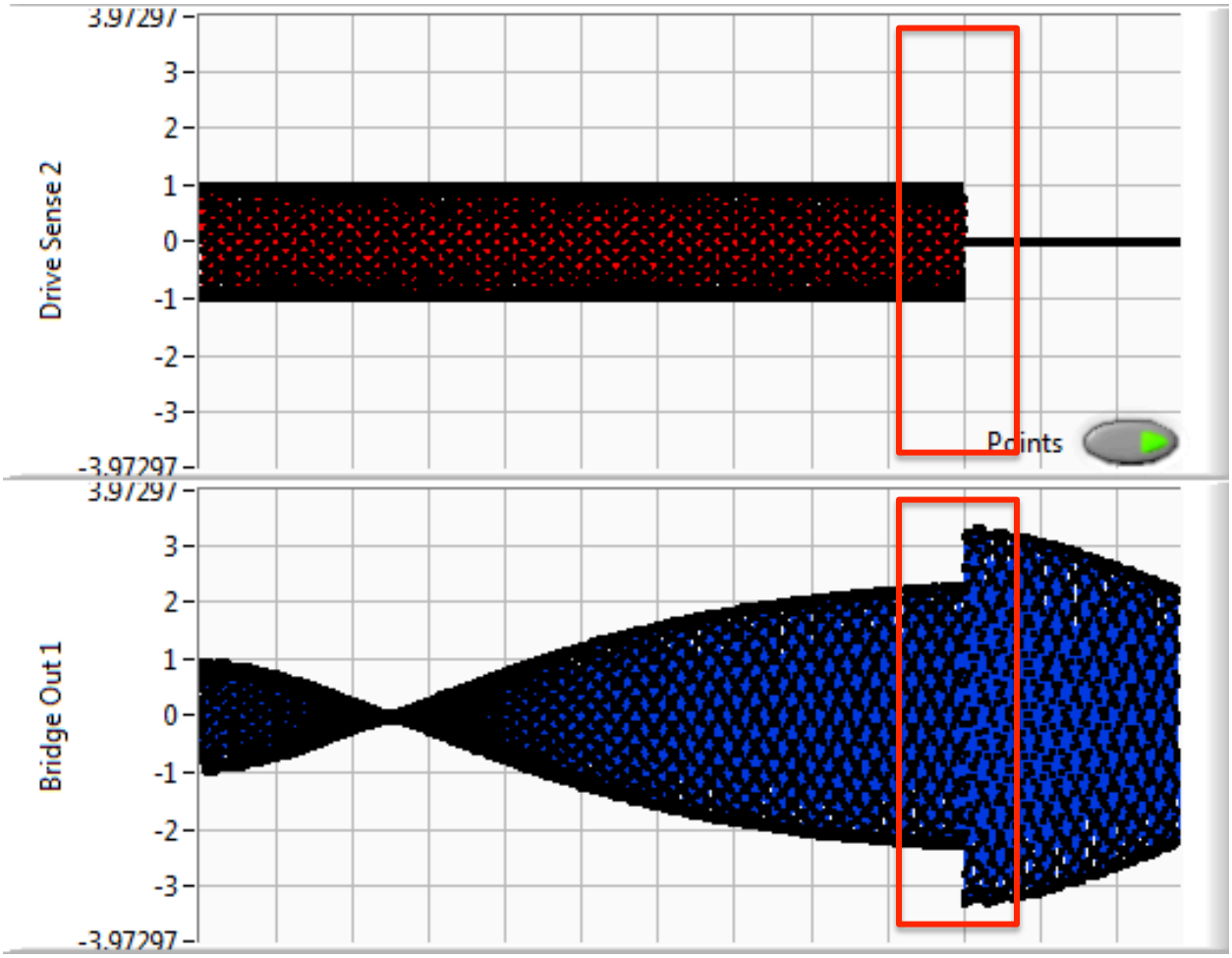


Figure 4.16. Actuating on one electrode axis and sensing on the other. The coupling of the electrical signal from Channel 2 (Red) to Channel 1 (Blue) is evident in the sensing signal (Blue) that is not expected of whirling response starting from rest.

Zooming into the selected portions,

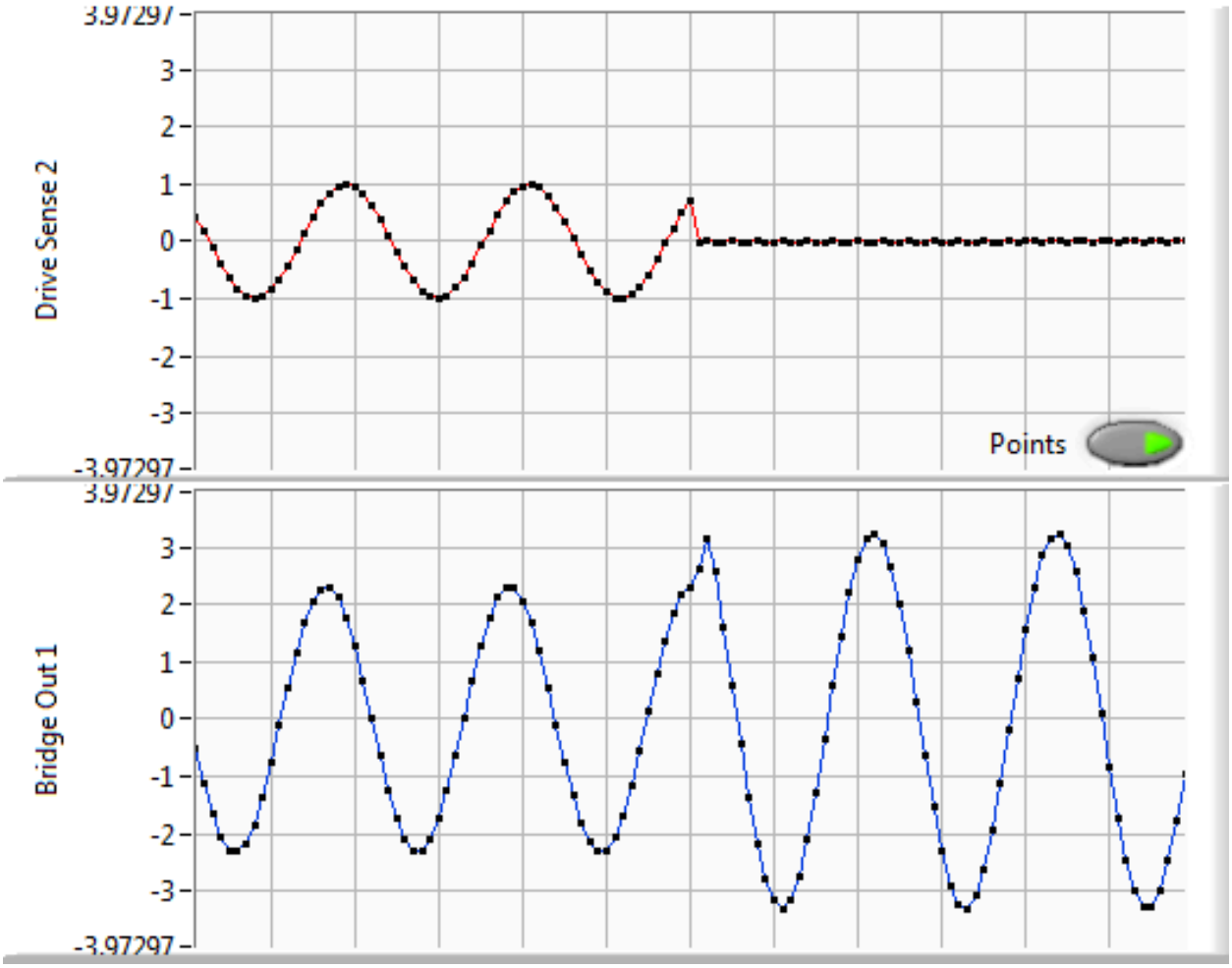


Figure 4.17. Actuating on one electrode axis and sensing on the other. Zoom-in showing coupling from Channel 2 (Red) to Channel 1 (Blue) producing discontinuities in the sensing signal (Blue).

This work proposes a simple solution to capacitive cross coupling of the piezoelectric tube, by identifying the coupling between the electrode axes and then subtracting out the coupling contributions: At different frequencies off resonance, give an excitation on Channel 1 only, and measure the response on Channel 2. A system without capacitive coupling will not register a signal on Channel 2, but typical systems will record a coupling signal. Fit the coupling signal to a simple transfer function with no complex poles:

$$G_{coupling}(s) = \frac{s+a}{s+b} \tag{4.15}$$

Where $a$ and $b$ are the fitted parameters. This simple transfer function will not affect identification of the mechanical scanner dynamics because it cannot represent the underdamped oscillations of the scan engine. Finally, use $G_{coupling}$ to remove contribution of the coupling signal into the simultaneous piezoelectric self-sensing signal.

Figure 4.18 and Figure 4.19 show the result of this compensation algorithm. The same experiment is repeated with an excitation given only in Channel 2 (Red) and the sensing signal measured in Channel 1 (Blue). Now, as expected the sensing signal (Blue) starts from rest and traces the growing and then decaying oscillations of the mechanical structure, since it is a pure sensing signal (actuation only given on the other electrode axis). Because capacitive coupling between the electrical channels has been removed, the signal now starts from rest does not exhibit a discontinuity when the voltage on the orthogonal axis is turned off.

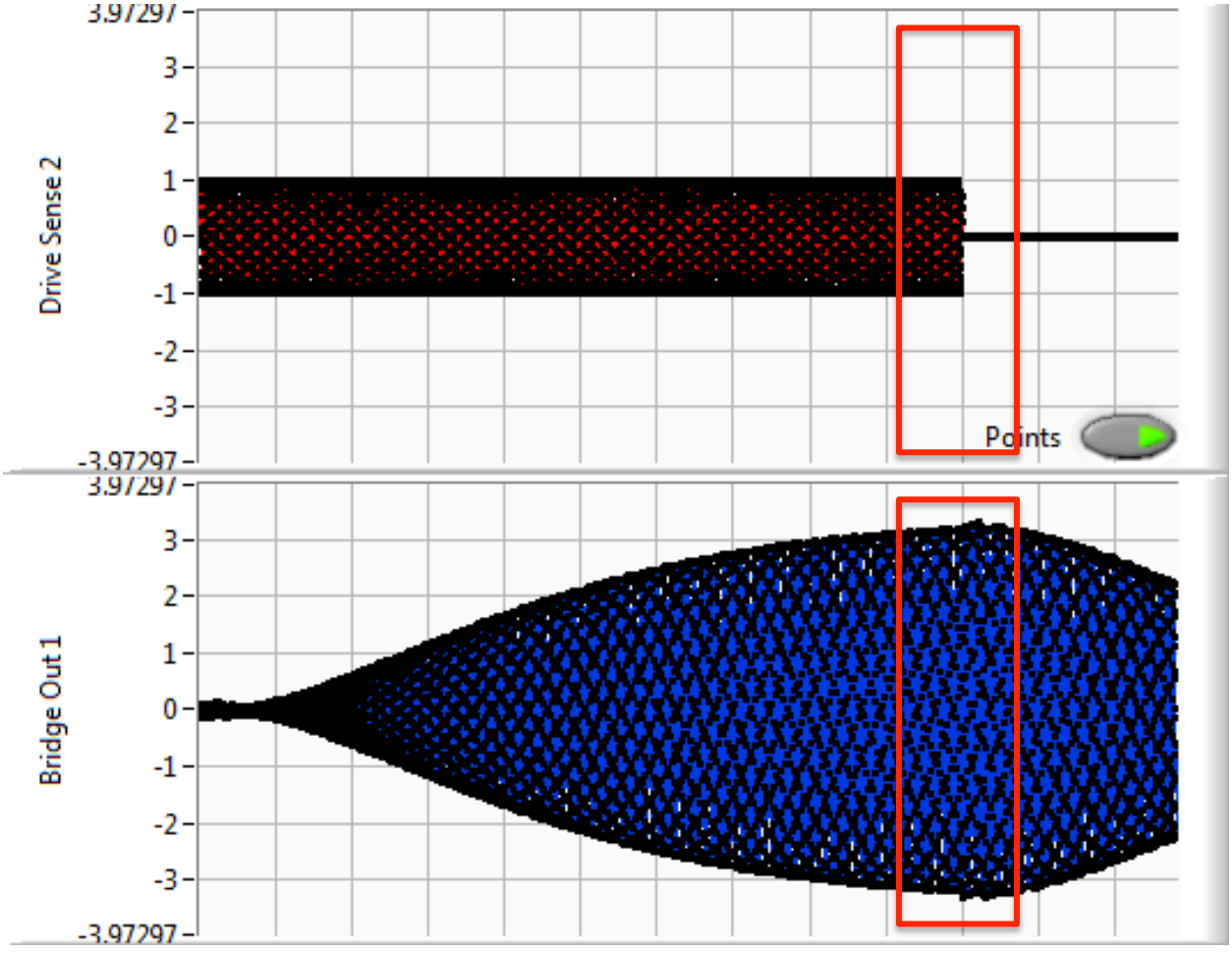

Figure 4.18. Actuating on one electrode axis and sensing on the other. The coupling of the electrical signal from Channel 2 (Red) to Channel 1 (Blue) is removed and the sensing channel (Blue) traces the growing and decaying oscillations of the mechanical scanner without signal degradation.

Zooming into the selected regions,

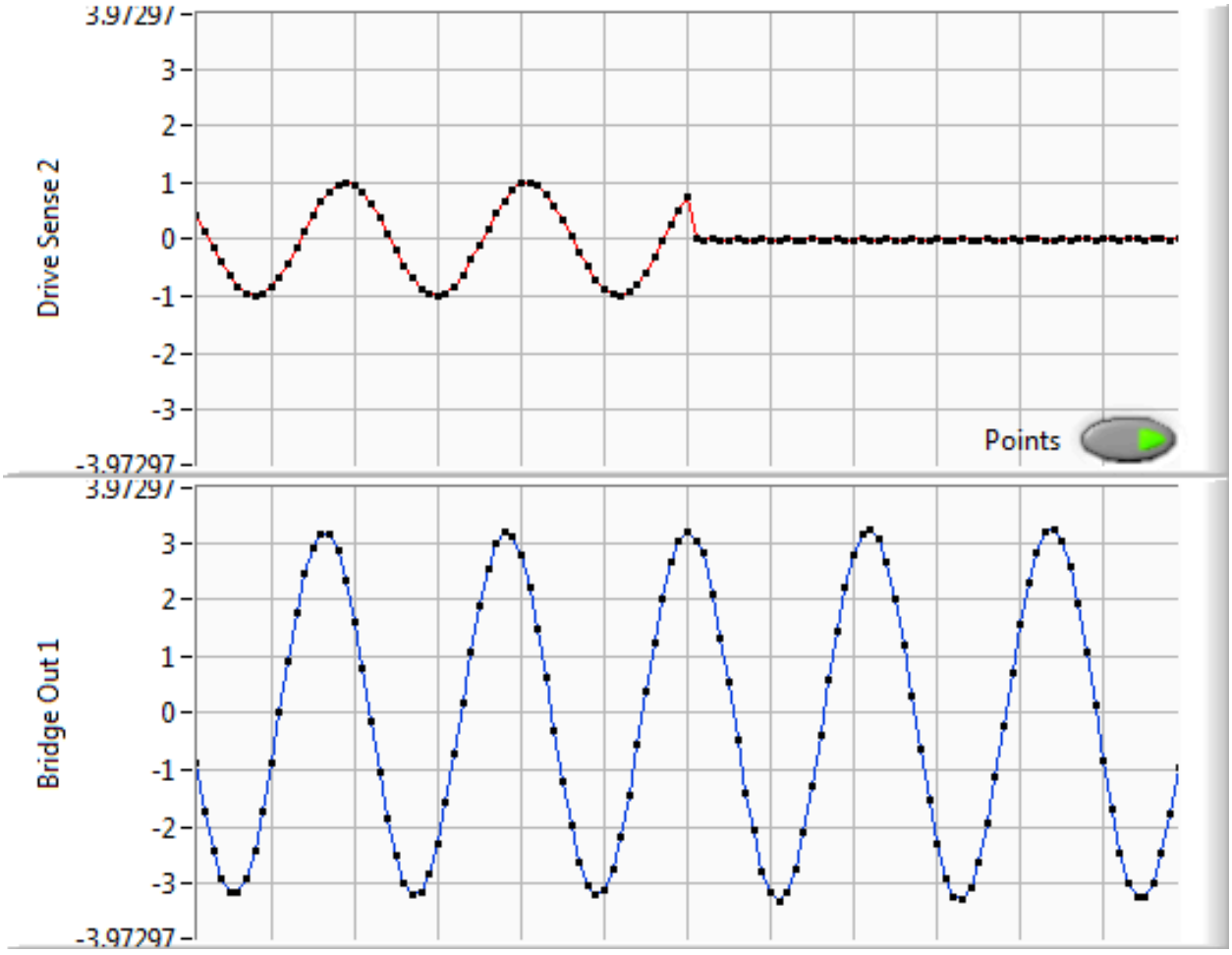


Figure 4.19. Actuating on one electrode axis and sensing on the other. Zoom-in showing non-coupling between Channel 2 (Red) and Channel 1 (Blue) with the sensing signal (Blue) completely continuous even when the voltage on the other channel is abruptly removed.

### 4.3.4 *Asymmetric Channel Gains*

A second practical implementation note concerns the unequal gain between voltage and actuation force of the two electrode axes. According to the theory of principal axes and Virtual Axes excitation [9], the two Eigendirections should be orthogonal to each other. In practice, the Eigendirection angles are not exactly $\frac{\pi}{2}$ offset, leading to signals that are not precisely orthogonalized. This non-orthogonality is an artifact of the asymmetric channel gains, and may be compensated for to fully orthogonalize the electrical channels. Asymmetric channel gains can be caused by e.g. differences in the driving electronics or the efficiency of the piezoelectric-tube along different axes.

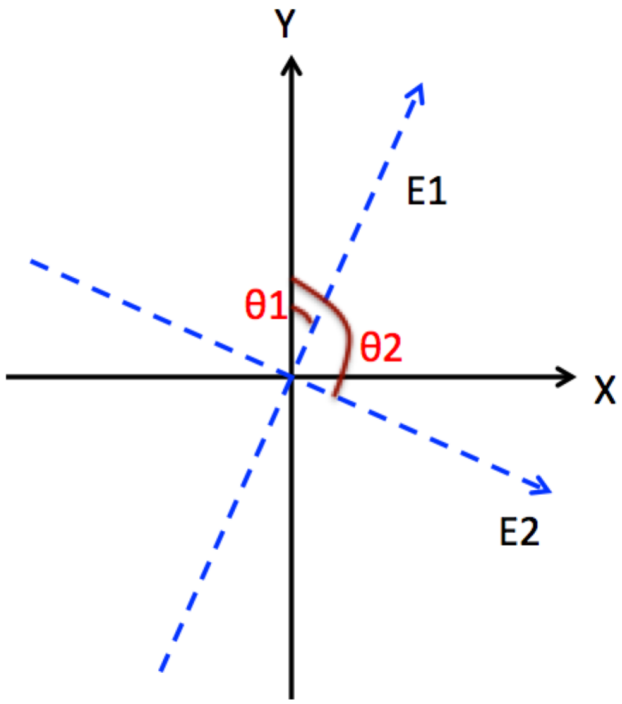


Figure 4.20. Diagram showing the relative orientation of the electrode axes X and Y with the Eigendirections 1 and 2.

In a perfect system where the two Eigendirection angles $\theta_1$ and $\theta_2$ are orthogonal, the two electrode axes $X$ and $Y$ have orthogonal contributions from the Eigendirections or Virtual Axes vectors $VE_1$ and $VE_2$:

$$X = [\sin(\theta_1)\, VE_1 + \sin(\theta_2)\, VE_2] \tag{4.16}$$

$$Y = [\cos(\theta_1)\, VE_1 + \cos(\theta_2)\, VE_2] \tag{4.17}$$

$X$ and $Y$ are the x- and y- electrode axis *voltages* respectively, and $VE_1$ and $VE_2$ are the virtual excitations at the respective virtual axes angles, which are translated to actual drive voltages according to the above relationships.

An asymmetric gain can be modeled as an additional multiplier $k$ to one of the electrode channels,

$$kX = [\sin(\theta_1)\, VE_1 + \sin(\theta_2)\, VE_2] \tag{4.18}$$

$$Y = [\cos(\theta_1)\, VE_1 + \cos(\theta_2)\, VE_2] \tag{4.19}$$

The experimentally identified eigendirections are typically calculated by taking the ratios of the electrode actuation voltages needed to achieve response only along that eigendirection:

$$\tan(\widetilde{\theta_1}) = \frac{X_1}{Y_1} \tag{4.20}$$

$$\tan(\widetilde{\theta_2}) = \frac{X_2}{Y_2} \tag{4.21}$$

$\widetilde{\theta_1}$ and $\widetilde{\theta_2}$ are only estimates of the true Eigendirection angles and typically $\widetilde{\theta_2} \neq \widetilde{\theta_1} + \frac{\pi}{2}$.

However, what is *actually* happening is that the actuation $X$ was modified by the coefficient $k$ and the true Eigendirection angles were excited:

$$\tan(\theta_1) = \frac{kX_1}{Y_1} \tag{4.22}$$

$$\tan(\theta_2) = \frac{kX_2}{Y_2} \tag{4.23}$$

Given initial non-orthogonal estimates $\widetilde{\theta_1}$and $\widetilde{\theta_2}$ we may identify $\theta_1$ and $\theta_2$ by imposing the constraint that $\theta_2 = \theta_1 + \frac{\pi}{2}$. Comparing Equations 4.20-4.23, the following relationships are derived:

$$k\tan(\widetilde{\theta_1}) = \tan(\theta_1) \tag{4.24}$$

$$k\tan(\widetilde{\theta_2}) = \tan\left(\theta_1 + \frac{\pi}{2}\right) \tag{4.25}$$

The only unknowns in Equations 4.24 and 4.25 are $k$ and $\theta_1$. By solving these equations simultaneously the values of $k$, $\theta_1$ and $\theta_2$ are identified.

## 4.4 EMPIRICAL MODAL REPRESENTATION

The circuit-equivalent electromechanical model has been very useful in understanding the scan engine system that has been extended with the new simultaneous piezoelectric self-sensing circuit, and improved the techniques of self-sensing measurements. However in this work, the circuit-equivalent electromechanical model was not directly used for control system design. In this section a second but related modeling approach is presented that is oriented towards empirical modal analysis of the system dynamics, which is then used for adaptive control of real devices. Modal modeling and concepts of experimental modal analysis will be relied upon in later sections on system identification and control.

### 4.4.1 *Modal Analysis*

Representing the system dynamics in terms of mode shapes and generalized displacements is an alternative to the element-lumping approach performed in the Circuit Equivalent Electromechanical Model section. Reconsider the piezoelectric-tube and optical fiber cantilever structure: Instead of lumping the structure into two point masses, two other modeling approaches could be taken.

The first alternative approach is to analytically calculate the dynamic response based on continuum mechanics. The Euler-Bernoulli dynamics beam equation,

$$\rho A \frac{\partial^2 v}{\partial t^2} + \frac{\partial^2}{\partial x^2}\left(EI \frac{\partial^2 v}{\partial t^2}\right) = 0 \tag{4.26}$$

where $\rho A$ is the mass-per-unit length, $E$ the elastic modulus, $I$ the area moment of inertia, $v$ the transverse displacement, $x$ the distance along the cantilever, and $t$ time; was used by Smithwick et al .for analysis of the fiber optic cantilever. Since the piezoelectric-tube portion of the scanner was not considered, Smithwick et al. took EI to be a constant along the length of the cantilever [8], [62]. The solution of the Euler-Bernoulli equations gives an infinite number of natural frequencies,

$$\omega_n = \frac{c_q(\beta_n l)^2}{l^2}, \quad c_q = \sqrt{\frac{EI}{\rho A}}, \quad cosh\beta_n l cos\beta_n l = -1, \quad n = 1,2,3 \ldots \tag{4.27}$$

and corresponding mode shapes of the optical fiber cantilever given by,

$$\phi_n(x) = c\cos(\beta_n x) + d\sin(\beta_n x) + e\cosh(\beta_n x) + f\sinh(\beta_n x) \tag{4.28}$$

where $c, d, e, f$ depend on the boundary conditions. These linear mode shapes were then used as the assumed mode shapes for Smithwick et al.'s reduction of Pai and Nayfeh's partial integro-differential equations into ordinary differential equations via Galerkin's method [8], [62].

The second alternative approach is to discretize the mechanical structure (e.g. using finite element methods) and then perform numerical analysis of its dynamics. Kundrat performed a finite-differencing method based on the following governing equations of a nonlinear cantilever beam:

$$\rho A\ddot{u} + c_x\dot{u} + EI_x u'''' = -EI_x[u'(u'u'' + v'v'')']' \tag{4.29}$$

$$\rho A\ddot{v} + c_y\dot{v} + EI_y v'''' = -EI_y[v'(u'u'' + v'v'')']' \tag{4.30}$$

where '$\dot{u}$' represent temporal derivatives, '$u'$' represent spatial derivatives, $u$ and $v$ are the two orthogonal transverse displacements along the cantilever. Finite differencing put the above governing equations into the following form,

$$M\ddot{u} + C\dot{u} + Ku = -f(u, u, t) \tag{4.31}$$

where $M$ is the mass matrix, $C$ the damping matrix, $K$ the stiffness matrix, $u$ the displacement vector and $f$ a nonlinear function [71]. The linear form of the above equation was also considered,

$$M\ddot{u} + C\dot{u} + Ku = F \tag{4.32}$$

where $F$ is the forcing function. To form the damping matrix $C$, Kundrat used a simplified Raleigh damping model, where the damping matrix is proportional to the stiffness matrix, $C = \gamma K$ [71]. Where $M$ is positive definite and $K$ is positive semi-definite, the solution can be described in terms of the natural frequencies $\omega_n$ and mode shapes $\phi_n$ found by solving the eigenvalue problem:

$$[-\omega_n^2 M + j\omega_n C + K]\phi_n = 0, \;\; n = 1,2,3 \ldots \tag{4.33}$$

The detailed solution can be found in e.g. [72], [73]. Further, if $C$ is proportional to $K$ (i.e. Raleigh damping, which is a subset of the modal damping model) [72] then the matrices $M, C, K$ can all be diagonalized by the mode shape matrix $\phi$ (which is identical to the mode shape matrix in the undamped case) [72], [73],

$$\phi^T[M\ddot{u} + C\dot{u} + Ku]\phi = \phi^T[F]\phi \tag{4.34}$$

This will transform Equation 4.32 into:

$$\tilde{M}\ddot{p} + \tilde{C}\dot{p} + \tilde{K}p = \tilde{F} \tag{4.35}$$

$$\phi^T M\phi = \tilde{M} = \begin{bmatrix} \ddots & & \\ & m_n & \\ & & \ddots \end{bmatrix},\ \phi^T C\phi = \tilde{C} = \begin{bmatrix} \ddots & & \\ & c_n & \\ & & \ddots \end{bmatrix},\ \phi^T K\phi = \tilde{K} = \begin{bmatrix} \ddots & & \\ & k_n & \\ & & \ddots \end{bmatrix} \tag{4.36}$$

Since $\tilde{M}, \tilde{C}, \tilde{K}$ are diagonal, this results in $n$-uncoupled differential equations describing the displacement $p_n$ of the $n$-vibration modes. The transformed forcing input $\tilde{F}$ is the equivalent contribution of the forcing input $F$ to each orthogonal vibration mode.

The modal damping assumption leads to mode shapes where every point along the structure moves in tandem and crosses the zero-axis at the same time [72], [73]. Figure 2.6 shows the first two modes that we expect of the piezoelectric-tube and fiber-optic structure. Smithwick et al. or Kundrat et al. did not consider these extended modes because the piezoelectric tube was assumed to be rigid. As verification of the above expected mode shapes, Figure 4.21 shows the result of Finite Element Analysis (FEA) using the Abaqus software. The FEA model was of the piezoelectric-tube and fiber-optic scanner, including the epoxy material at the joints, with the dimensions and material properties of the FEA model matched to the actual scanners. Figure 4.21 shows the top-view (looking opposite from the optical fiber tip) of the first and second mode of the structures. As expected, the 1st mode (at 10.8kHz) has the piezoelectric-tube bending (very slightly) in tandem with the optical fiber, in the same direction. The 2nd mode (at 24.6kHz) has the piezoelectric tube bending in the opposite direction to the optical fiber. (Note that the electromechanical model in Section 4.3 leads to the general viscous damping assumption, where the points along the mode shape can have phase lead/lags with respect to each other [73]).

Equations 4.35 and 4.36 also closely follow Equations 3.6 and 3.7 derived by Hagood and Anderson for simultaneous piezoelectric self-sensing of cantilevered structures [38] repeated here,

$$M\ddot{r} + Kr - \theta v = B_f f$$

$$\theta^T r + C_p v = B_q q$$

The actuator Equation 3.6 can be interpreted as the input voltage $v$ exciting the controllable mode displacements $r$ through the coupling matrix $\theta$ that is dictated by the geometry of the

piezoelectric patches. The idea of *Empirical Modal Representation* is to arrive at similar modal descriptions of the self-sensing system dynamics using empirical or system identification methods.

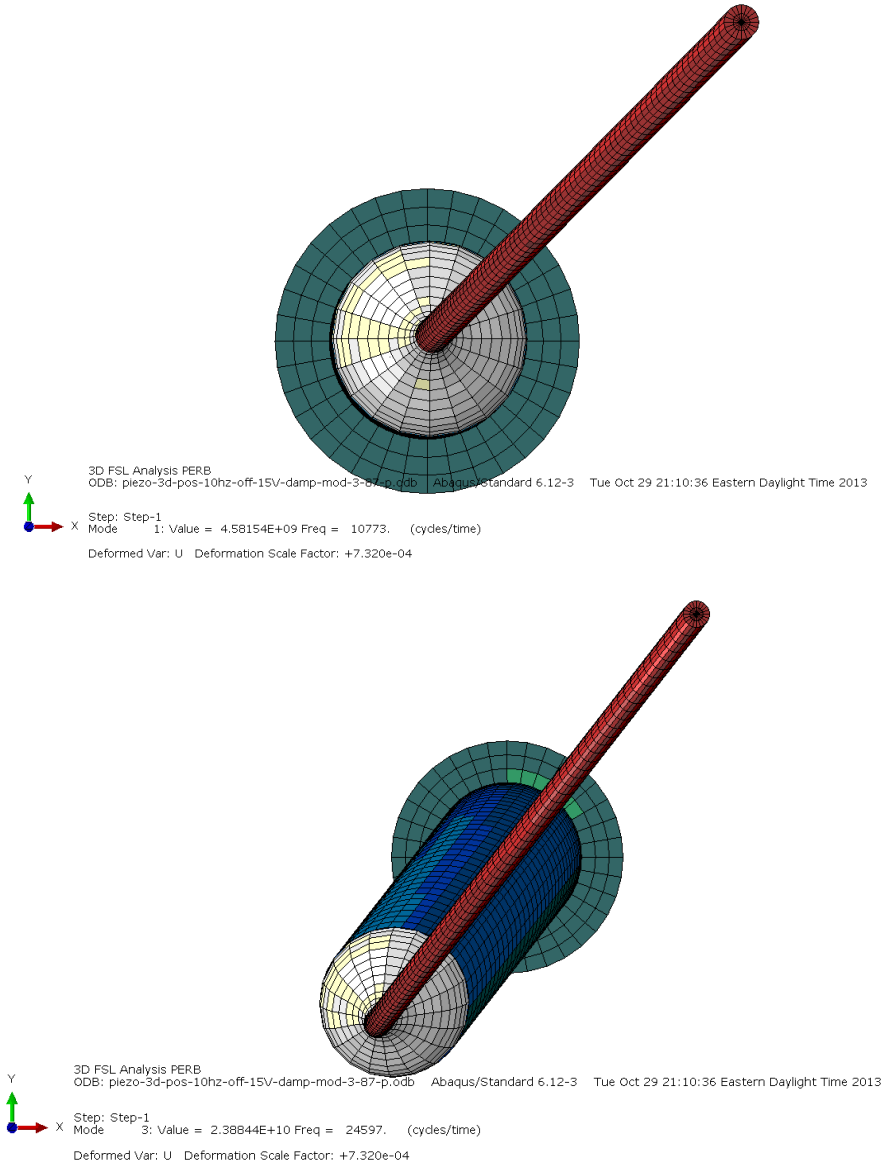


Figure 4.21. a) First mode of the scanner via FEA. b) Second mode of the scanner via FEA.

This work builds upon the concept of mode shapes and the orthogonality of the normal modes. (Note that orthogonality of modes can be violated if a system is 'open', i.e. connected to other systems or if its edges dissipate energy into its supports [73]. This work assumes that the system is closed.)

A few important results follow from knowing the mode shapes and assuming their orthogonal dynamics. Firstly, since the piezoelectric-tube and the fiber-optic move in tandem, by sensing the displacement of the piezoelectric-tube the position and phase of the fiber-optic tip can be inferred. The optical fiber tip displacements are important since in imaging and display applications the laser beam emanates from the fiber tip. Secondly, methods in experimental modal analysis may be applied where the transfer function from excitation to response at different structural points are used to identify the parameters of the uncoupled differential equations in Equations 4.35 and 4.36. The use of system identification to accurately determine the dynamics of the different vibration modes that are then controlled motivates the *Empirical Modal Representation* modeling approach.

### 4.4.2 *System Identification*

System identification is the determination of model parameter values from experimental data. System identification is important to properly apply mathematical models to real systems because nominal model values cannot accurately match the variations in actual systems. Variations in systems can occur from device-to-device, or even over time. System identification requires empirical input-output data for the system under testing. As such, sensing modalities (which were developed in previous chapters concerning piezoelectric self-sensing) are a prerequisite for applying system identification.

A number of approaches to system identification are discussed here. If the structure of the model is known, grey-box identification methods can be applied to find the values of the unknown parameters. Grey box identification was applied to the Circuit Equivalent Electromechanical Model, using Matlab-based numerical optimization to minimize the prediction error. The identified models closely predicted the system outputs when compared to experimental data as presented in the Model Verification section. The drawback of grey-box identification using numerical prediction-error minimization was the computing time required (2-3 minutes).

An alternative method using the ARMAX model for the input-output data assumes a general format for the system transfer function,

$$A(q)y(t) = B(q)u(t) + C(q)e(t) \tag{4.37}$$

where $q$ is the forward-time-shift operator, $y(t)$ the output signal, $u(t)$ the input signal, $e(t)$ random noise, $A, B, C$ represent operators on the respective signals. To compute the ARMAX parameter estimates, the Prediction Error Method (PEM) is used. The prediction error $\epsilon$ is the difference between the measured and expected output:

$$\epsilon(t,\theta) = y(t) - \hat{y}(t,\theta) = y(t) - f_{t|t-1}(\theta) \tag{4.38}$$

where $\theta$ is some parameter vector, $\hat{y}(t,\theta)$ the predicted output at $t$, and $f_{t|t-1}(\theta)$ a function that predicts the output based on past information and the model parameters. Typically, numerical optimization is performed to find the best parameter estimate $\hat{\theta}$ that minimizes a loss function based on the prediction error $\epsilon$:

$$\hat{\theta} = \min_{\theta} J(\epsilon(\theta)) \tag{4.39}$$

where the loss function can be e.g. $J(\epsilon) = \epsilon^2$ [74]. The ARMAX model accounts for correlated noise but its solution is typically not analytical. Another method to account for the case where noise $e(t)$ is correlated with past data is to use the Instrumental Variables Method (IVM). Here, an instrument $Z(t)$ can be any vector that is uncorrelated to the noise but correlated with the past data:

$$E\{Z(t)^* e(t)\} = 0, \;\; E\{Z(t)^* \varphi(t)\} \; has \; full \; rank$$

where $\varphi(t)$ is the regressor vector containing past data (assuming nonzero system delay), and $Z^*$ represents the conjugate transpose of $Z$. The parameter estimate using IVM can be found analytically via:

$$\hat{\theta} = \left(\frac{1}{N}\sum_{t=1}^{N} Z(t)^* \, \varphi(t)\right)^{-1} \left(\frac{1}{N}\sum_{t=1}^{N} Z(t)^* \, y(t)\right) \tag{4.40}$$

The simpler ARX model has the general form:

$$A(q)y(t) = B(q)u(t) + e(t) \tag{4.41}$$

where $e(t)$ is assumed to be independent and identically distributed. This model is the simplest to fit to experimental data, but if the output noise is sufficiently correlated with past data the parameter estimate using the ARX model can be significantly biased.

In this work, a High-Order Batch Least Squares (HOBLS) with a modified ARX format is developed for use with the Empirical Modal Representation model. With this approach, the aims of matching the data and interpreting the identified model are handled separately. To accurately match the experimental input-output data, first a high order simple ARX model (30-50) is assumed and Batch Least Squares applied on the data. To match the model order in the Circuit Equivalent Model, we may wish to set $n = 9$ for the regression model. However, in practice the disturbance $e(t)$ is typically not Gaussian white, leading to poor data-fitting [74]. Equation 4.41 is expanded to handle colored noise by introducing a general noise filter $\frac{1}{D(q)}$ and rearranging back into ARX format:

$$A(q)y(t) = B(q)u(t) + \frac{1}{D(q)}e(t) \tag{4.42}$$

$$[A(q)D(q)]y(t) = [B(q)D(q)]u(t) + e(t) \tag{4.43}$$

$$\tilde{A}(q)y(t) = \tilde{B}(q)u(t) + e(t) \tag{4.44}$$

Now Equation 4.44 is in the general ARX form with independent identically distributed disturbance, but the order of $\tilde{A}, \tilde{B}$ has increased. Bringing the formulation back into the ARX form is beneficial as it allows use of very efficient and analytic Least Squares solving methods such as Batch Least Squares.

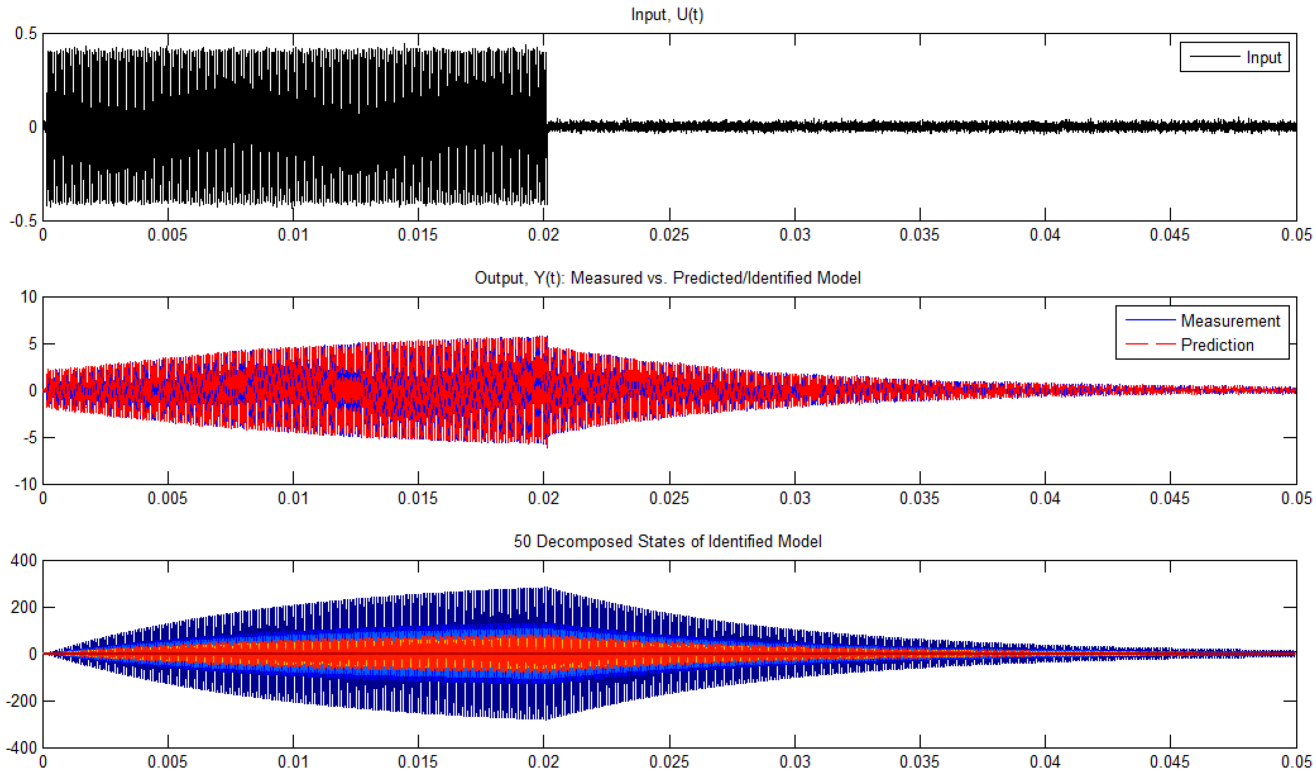


Figure 4.22. a) Top: Input data. b) Middle: Measured output data vs. predicted output of the identified high-order model. c) Bottom: The 50 simulated states of the high-order identified model. Note that the state trajectories all look similar.

Figure 4.22 shows the result of the HOBLS identification with a model order of 50. Despite the presence of correlated noise, the identification process converges to an accurate model describing the input-output relationship. Figure 4.22a shows the input and output used for system identification and also the simulated trajectories of the identified system model, is similar to where we excite the system at the 1$^{st}$ mode resonance then turn off the actuation. The mechanical scanner responds to the resonant excitation with ramping-amplitude oscillations, which then take time to decay. By matching a model to this data, both the 'finning' effect due to bridge circuit imbalance, and the mechanical properties of the resonant scanner are captured mathematically.

### 4.4.3 *Model Order Reduction*

After obtaining a model with excellent match to the experimental data, useful features need to be extracted from the sprawling model through model order reduction. HOBLS identification gives us coefficients of the numerator $\tilde{B}(q)$ and denominator $\tilde{A}(q)$ of the modeled transfer function [75]. If we put this transfer function into the canonical state space form, all the 50 states are coupled and it is not clear how we can reduce the system model, as shown in Figure 4.22c.

This work proposed use of the modal canonical state-space realization to decouple the states of the dynamical model. After transforming to the modal canonical realization, the $A$ matrix of this state space form will consist of block diagonal entries, with each block corresponding to an eigenvalue $\lambda$ or conjugate eigenvalue pair $\sigma \pm i\omega$, e.g.

$$A = \begin{bmatrix} \sigma_1 & \omega_1 & 0 & 0 \\ -\omega_1 & \sigma_1 & 0 & 0 \\ 0 & 0 & \lambda_2 & \cdots \\ 0 & 0 & \vdots & \ddots \end{bmatrix} \tag{4.45}$$

These eigenvalues can be interpreted to correspond to the natural frequencies and mode shapes of a mechanical system as previously formulated in Equations 4.35 and 4.36. Furthermore, in this canonical realization, the states are interpreted to correspond to the generalized displacements and are now similar to the format of Hagood and Anderson in Equations 3.6 and 3.7.

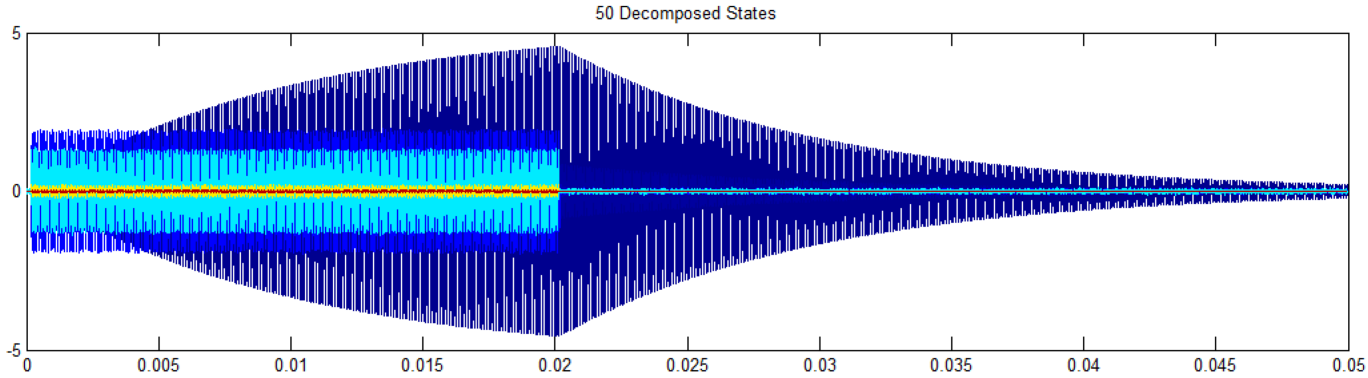


Figure 4.23. Transformed identified model states.

Figure 4.23 shows the result of transforming the HOBLS model into a modal canonical realization. Following the interpretation of the states as the generalized displacements of the respective system mode shapes, it is found that only two states (the darkest blue traces in Figure 4.23) undergo sustained underdamped oscillations when the system is excited at the 1$^{st}$ mode

resonance. All the other state trajectories do not exhibit sustained oscillation as would be expected for un-excited system modes.

Inspection of the eigenvalues of the block-diagonal entry of the A-matrix corresponding to the sustained-oscillation pair of states, it is found from the eigenvalues that the equivalent natural frequency is 13.322kHz. The nominal 1$^{st}$ mode natural frequency for the actual mechanical scanner was 13.3kHz. The equivalent natural frequencies of the eigenvalues of other block-diagonal A-matrix entries are much further distanced, the closest being at 22.671kHz, which is close the nominal 2$^{nd}$ mode natural frequency of the mechanical scanner at 22.520kHz. The above matching natural frequency estimates demonstrate that actual system information can be extracted from the high-order model.

Model order reduction will be further developed in Chapter 6 on Adaptive FeedForward Control to isolate the mode dynamics of the scan engine for adaptive control applications.

## 4.5 SUMMARY

This chapter began with a review of the modeling efforts and approaches previously taken with the scanning fiber technology. The key differences taken by this work in modeling the system are that the piezoelectric-tube dynamics are now considered, the electrical domain is included for full electro-mechanical modeling, and that data-driven or empirical approaches are favored for control-oriented modeling. Two electromechanical modeling techniques are presented in this dissertation: a circuit equivalent model and an empirical modal representation approach. The circuit equivalent model afforded new insights into the interaction of the system with simultaneous piezoelectric self-sensing. The empirical modal representation delivers a concise description of the relevant mode dynamics, which will be used in later section on the control of the resonant scanning system.

# Chapter 5. ONLINE CONTROL DESIGN FOR THE SCANNING FIBER TECHNOLOGY

The goal of this dissertation is to develop the scanning fiber technology into an online self-calibrating device. The term *online* is defined as *while the device is in use*, and *self-calibrating* is defined as *no user interaction required for maintaining high image fidelity*. Taken together, the desired control scheme should enable the system to adjust to changing operating conditions while maintaining scan accuracy in a process that is invisible to the user.

## 5.1 Previous Control Design with the Scanning Fiber System

In this section, the three control designs proposed by previous works the Scanning Fiber Endoscope are reviewed. All control designs proposed before required use of an eternal optical position sensor and thus could not recalibrate while the device is in use.

### 5.1.1 *Error Space Controller*

Figure 5.1 shows the block diagram of the error space controller proposed by Smithwick et al. [69]. This control method used feedback linearization to linearize the system dynamics to the form:

$$\ddot{p} + b_z\dot{p} + \omega_z^2 p = C_z v_z \tag{5.1}$$

$$\ddot{q} + b_y\dot{q} + \omega_y^2 q = C_y v_y \tag{5.2}$$

$p$ and $q$ are the mode displacements along the cantilever-transverse z and y axes respectively, $\mathrm{C_z}v_z$ and $\mathrm{C_y}v_y$ the excitation along the z and y axes respectively, $b_z$ and $b_y$ the damping parameters, $\omega_z$ and $\omega_y$ the natural frequencies of the mode under consideration.

Linear control theory is applied to derive the error space controller. The controller itself can be generally described as having a feedforward block, a state-feedback block for stabilization and an observer block for state estimation.

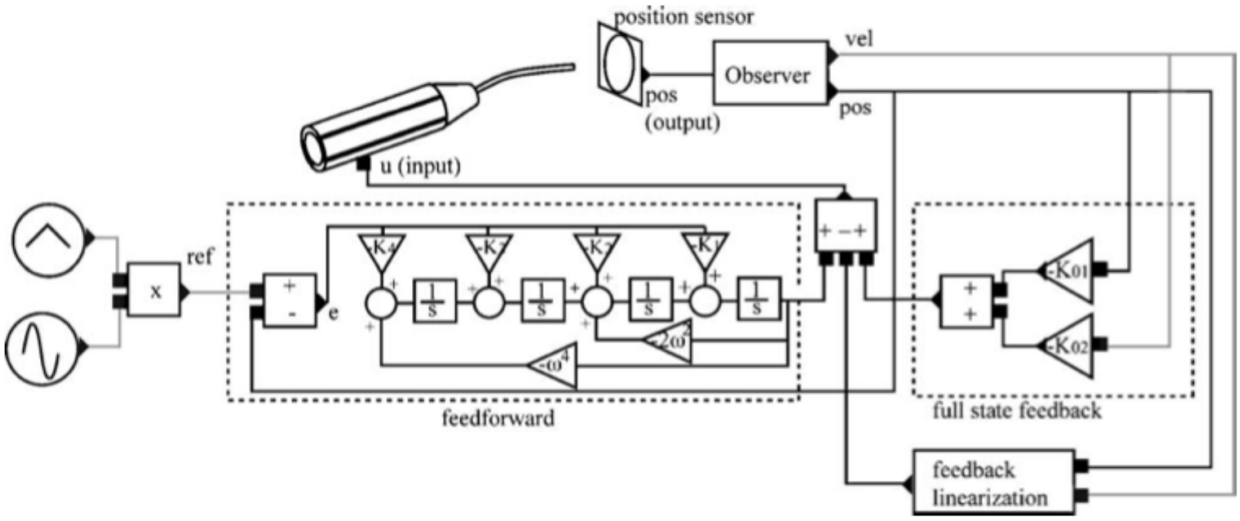


Figure 5.1. Error Space Controller diagram [69].

The general form of the reference signal must be pre-defined and used to derive the controller. The selected reference signal was a triangle-modulated sinewave defined as:

$$r(t) = \begin{cases} tsin(\omega t) & ,if\ 0 \le t \le \frac{T}{2} \\ (T-t)\sin(\omega t) & ,if\ \frac{T}{2} \le t \le T \end{cases} \tag{5.3}$$

In the Laplace domain, the above equation has the least common denominator corresponding to the differential equation $r^{iv} + 2\omega^2\ddot{r} + \omega^4 r = 0$; The reference signal must satisfy this relationship. For the linear system in state space form:

$$\dot{\bar{x}} = \bar{F}\bar{x} + \bar{G}u \tag{5.4}$$

$$z = \bar{H}\bar{x} \tag{5.5}$$

$$\bar{x} = \begin{bmatrix} x \\ \dot{x} \end{bmatrix} \quad u = F_x \quad \bar{F} = \begin{bmatrix} 0 & 1 \\ -\omega^2 & -b \end{bmatrix} \quad \bar{G} = \begin{bmatrix} 0 \\ C \end{bmatrix} \quad \bar{H} = [1 \quad 0] \tag{5.6}$$

The error was defined as,

$$e = z - r \tag{5.7}$$

Defining the error-space state as,

$$\xi = \bar{x}^{iv} + 2\omega^2\ddot{\bar{x}} + \omega^4\bar{x} \tag{5.8}$$

And the error-space control input as,

$$\mu = \bar{u}^{iv} + 2\omega^2\ddot{\bar{u}} + \omega^4\bar{u} \tag{5.9}$$

Substituting into the state-space equations, the overall system described in error-space becomes:

$$\dot{\zeta} = A\zeta + B\mu \tag{5.10}$$

$$\zeta = [e \quad \dot{e} \quad \ddot{e} \quad \dddot{e} \quad \xi^T]^T \quad A = \begin{bmatrix} 0 & 1 & 0 & 0 & \bar{0} \\ 0 & 0 & 1 & 0 & \bar{0} \\ 0 & 0 & 0 & 1 & \bar{0} \\ -\omega^4 & 0 & -2\omega^2 & 0 & H \\ \bar{0} & \bar{0} & \bar{0} & \bar{0} & F \end{bmatrix} \quad B = \begin{bmatrix} 0 \\ 0 \\ 0 \\ 0 \\ G \end{bmatrix} \tag{5.11}$$

Smithwick et al. then define a state-feedback type control law of the form:

$$\mu = -[K_4 \quad K_3 \quad K_2 \quad K_1 \quad \bar{K}_0] \ [e \quad \dot{e} \quad \ddot{e} \quad \dddot{e} \quad \xi^T]^T \tag{5.12}$$

The gains were found using LQR, which guarantees regulation of the error to zero in an ideal noiseless system.

For the full state feedback in Equation 5.12, the velocity of the fiber tip was estimated by taking a filtered derivative of the optically measured fiber tip position. It was found that position measurement filtering was needed to stabilize the system [69]. In the implementation of the error space controller, feedback linearization was omitted because it was found to be ineffective due to actuator delays [69]. As such, a fully linear controller was applied to the presumed non-linear system with good tracking results [69].

To populate the model parameter values, a sample-by-sample identification of the system frequency response was constructed experimentally. First the scanner was excited along only one (piezoelectric-tube) axis at a constant amplitude and frequency and the steady-state response was recorded. The excitation frequency was then swept over a range of frequencies of interest. From the stored data, the amplitude and phase of the response is calculated at each frequency to construct a frequency response plot similar to Figure 5.2. Next, the experimental frequency response data points are graphed together with the analytical frequency response predicted by the nonlinear dynamical model. The parameters of the nonlinear model are manually adjusted until there is a good visual fit between the experimental data and the analytical model [62].

With a 1V, 1Hz triangle-modulated 500Hz sinusoid reference, the error space controller achieved good tracking with reported 1-3% tracking error [69]. The error space controller required use of an optical position sensor for real-time feedback.

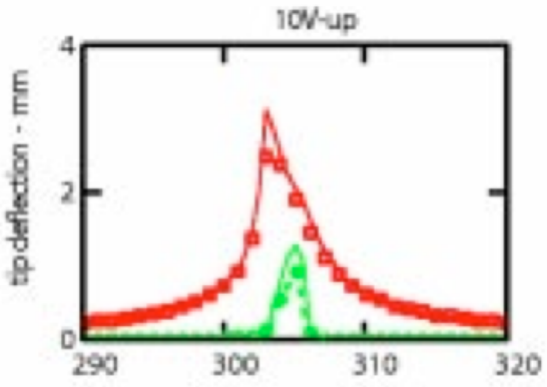


Figure 5.2. Sample-by-sample frequency response experimental identification and manual data fitting used for error space controller model [8].

### 5.1.2 *Hybrid Nonlinear Adaptive Controller*

The error space controller previously described required real-time feedback. The sensor used was an optical sensor much larger than the Fiber Scanner and a beam splitter was used to redirect a portion of the scanned laser. As such, the overall optical system was much larger and not applicable as a miniature endoscope or display.

To maintain the miniature profile of the Fiber Scanner, Smithwick et. al. introduced another control strategy called the hybrid nonlinear adaptive controller [58]. This was a *two-stage* control methodology that also uses feedback linearization to simplify the system dynamics to the linear models used for the error space controller in Equations 5.1 and 5.2. In addition, the controller took into account the actuator delay by forward-shifting the control signal, which was made possible by its feedforward architecture. Furthermore, no real-time feedback was used. During the identification stage, batch processing was performed on the optical position data. No sensor was used During the subsequent open-loop operational stage.

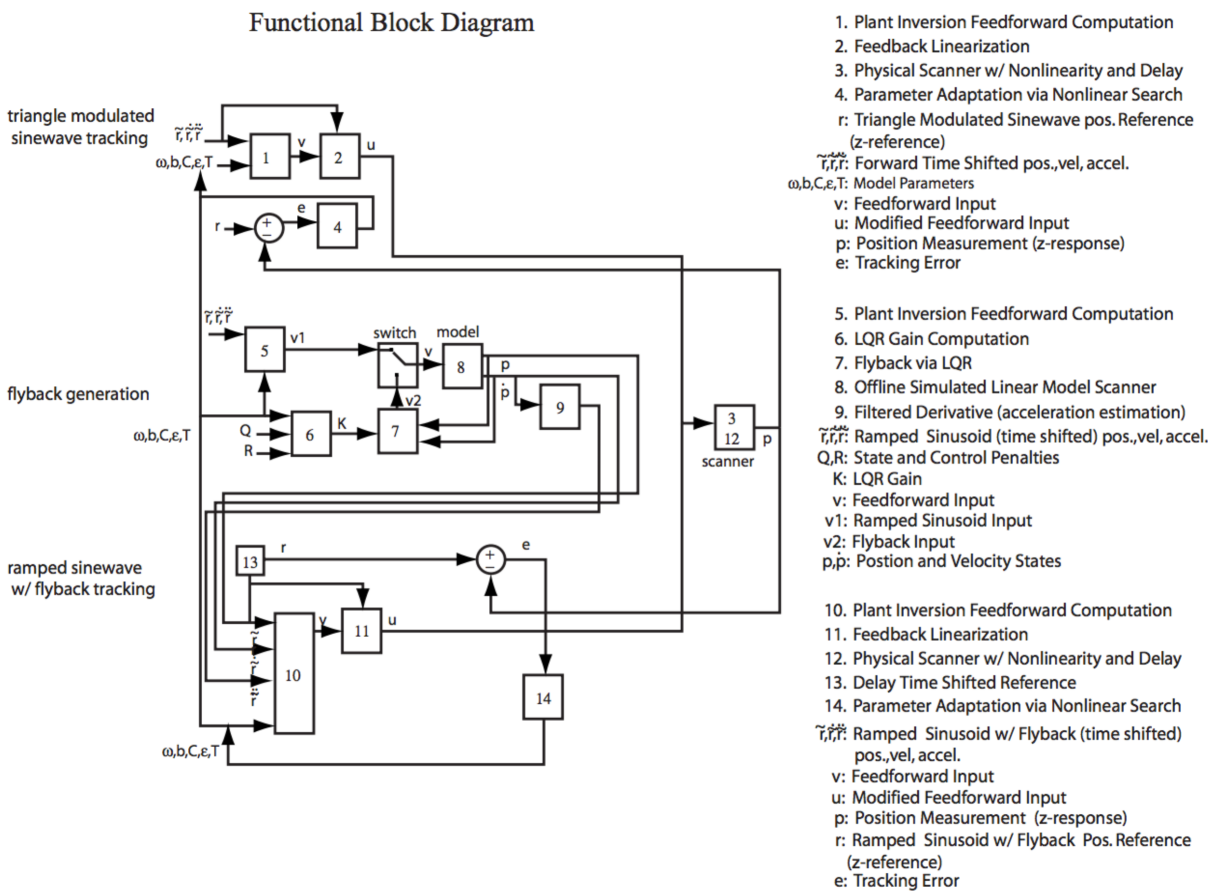


Figure 5.3. Functional block diagram of the hybrid controller [59].

Figure 5.3 shows the functional block diagram for the two-stage control strategy. In the first stage, the SFE was coupled to an optical position detector for dynamics identification and trajectory calculation. The first control stage has 3 sub-stages. Initially, the system is made to track a triangle-modulated sinusoid with initial guesses for the parameters in the nonlinear model being used for feedback linearization and feedforward via linearized plant-inversion. The unknown actuator delays are also included in the guessed parameters. These parameters are then iteratively refined with each batch of position sensor data using nonlinear least-squares [59]. Once the parameter estimates reached a certain tolerance level, the next sub-stage, flyback generation, is executed. Instead of a triangle-modulated sinusoid, the desired trajectory is changed to a ramping sinusoid followed by a rapid regulation to zero. The rapid regulation is called the flyback, and this trajectory is optimally calculated using saturated LQR (simulation using the identified model parameters) to keep the control inputs within actuation reach. The

rapid regulation is designed to achieve high frame-rates. In the last sub-stage, the iterative parameter identification is repeated but now for the modified flyback trajectory. The final estimated parameter values are then used for the second stage control [59].

The second control stage was an open-loop control. The Fiber Scanner was decoupled from the external optical sensor, returning it to a miniature form factor whence it is used as an endoscope. During this second-stage operation, the stored parameters identified during the first stage are used to generate the control signal. Thus, in this stage the controller is no longer adaptive. Overall, good tracking was achieved for the trajectory with flyback with reported maximum error of about 4%. In the implementation of the hybrid controller, it was reported that the nonlinear search to identify the model parameters took a total of about 8 minutes [59].

### 5.1.3 *Open Loop Control with Identified Braking Parameters*

Kundrat et al. proposed another open-loop-with-initial-identification control scheme based on a different set of assumptions about the system dynamics. With the introduction of Virtual Axes excitation the system could be excited along its actual Eigendirections, leading to linear motion along two orthogonal axes. Hence, Kundrat et. al. worked on the assumption of uncoupled linear systems along each eigendirection [9],

$$\ddot{x} + 2\zeta\omega_n\dot{x} + \omega_n^2 x = F \tag{5.13}$$

$x$ is the mode displacement, $\zeta$ the damping factor, $\omega_n$ the natural frequency and $F$ the forcing input. Furthermore, a very specific scan trajectory and input signal was used for the Scanning Fiber imaging system. Figure 5.4 shows the scan trajectory, which has three distinct stages. During the Imaging stage, the scan is assumed to trace growing spirals. Next in the Braking stage, the scan trajectory is brought rapidly to rest. Finally in the Settling stage, any residual vibration is allowed to decay, so that the next imaging stage starts with the same initial conditions. Image capture is only performed during the Imaging stage.

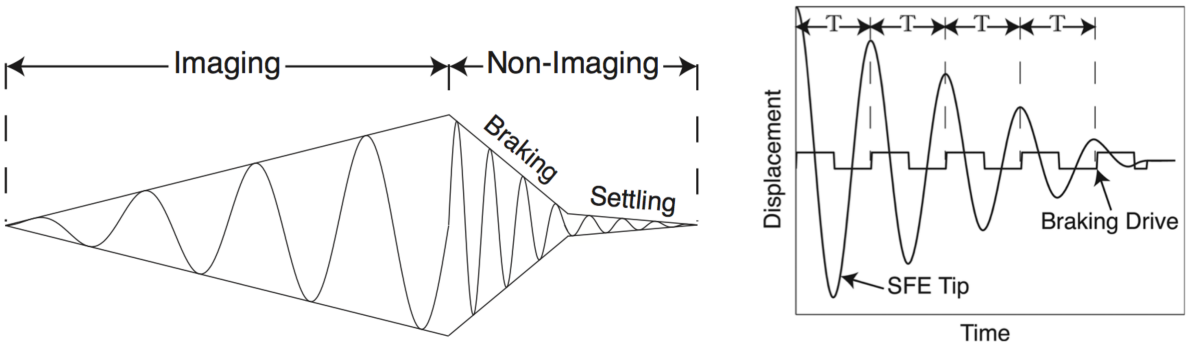


Figure 5.4. a) Left: Scan profile of the Scanning Fiber Endoscope. b) Right: Braking control to bring the scanner to rest [9], [28].

The control signals during the Imaging stage are a set of ramping sine and cosine waveforms. During the Braking stage, the control signal is a square wave to emulate bang-bang control. There is no control signal during the Settling stage. Because of the very formatted nature of the input signal and assumed trajectory, the only parameters to be identified are the parameters that will give effective Braking. If Braking is done efficiently, the Fiber Scanner could be brought very rapidly to rest, resulting in higher frame rates. As such, the Braking parameters are the damped natural frequency and the braking phase along each Eigendirection. These parameters are identified during calibration, where the Fiber Scanner is coupled to an external optical position sensor. After the Braking parameters are identified, the Fiber Scanner is decoupled from the optical sensor and put to use in an open-loop configuration. If Braking parameters can be precisely identified to achieve rapid reduction of fiber motion, up to a 99.8% reduction in vibration amplitude after 5 cycles of Braking could be achieved [9], [28].

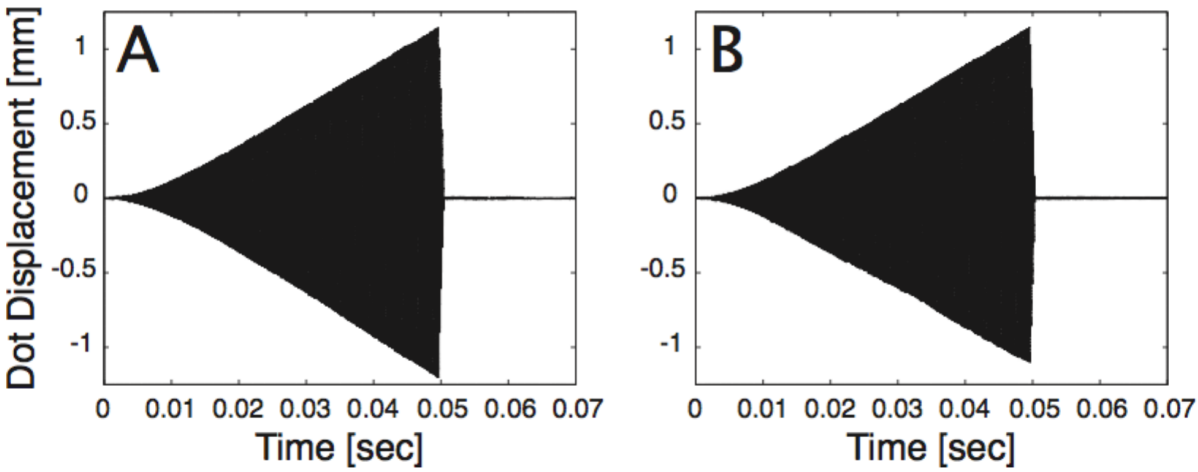


Figure 5.5. The fiber tip trajectory over the course of the standard open-loop control. Deflections increase from rest in a ramping spiral, which is rapidly collapsed by Braking [9], [28].

The actual trajectory of the fiber during the Imaging stage was assumed to be a perfect ramped spiral. In practice, the scan trajectory does not trace out uniformly expanding spirals hence image distortion is still present after the application of this controller. A parallel effort that is integrated into current SFE prototypes is the image remapping procedure. The above open loop controller gets the scan trajectory close to the reference. The remaining image distortion is calibrated out using actual time-position measurements of the laser spot that are stored in a lookup table.

### 5.1.4 *Scanning Fiber Technology Control State-of-the-Art*

None of the previously described controller can recalibrate the device outside of the calibration chamber due to reliance on the optical position sensor. The de facto controller in all SFE prototypes use the pre-calibrated open-loop strategy described previously by Kundrat et al: Prior to use, the device is coupled to a large external optical position detector that provides measurement of the laser spot position. A trained operator using feedback from the optical position sensor then manually calibrates the device. Finally, the device is uncoupled from the measurement system and used in endoscopic procedures, where operating conditions can be drastically different compared to the calibration chamber.

This work has introduced a powerful new miniature sensing modality, simultaneous piezoelectric self-sensing, that allows measurement of scan engine deflections at any time without need for coupling to a calibration chamber. Next, adaptive control algorithms are developed to enable online self-calibration of the scanning fiber device to maintain high image quality.

## 5.2 Analysis of System Characteristics

Control system design should also be informed by the specific operating characteristics of the system to be controlled. The scanning fiber technology operates in unique patterns and is applied to specific fields that afford more innovation in controller architecture. Instead of pursuing a perfect tracking adaptive controller, certain constraints on the control system may be relaxed by analyzing the requirements of imaging and display products.

*Periodic Operation/Trajectory*

For both imaging and projection display applications, the trajectory of the Fiber Scanner is periodic because images are generated frame-by-frame. For consistent image quality, the trajectory at each period should be the same. (Non-periodic trajectories of the image cursor are imaginable but are not useful in the current context). The periodic nature of the trajectories opens up the possibility of applying periodic/iterative control methods to the problem [76], [77].

*Image Capture*

In single-image capture applications, for example in photography, the requirement for accurate tracking by the optical fiber is only active over relatively brief intervals. Before and after the image-capture sequence, the system is free to track any trajectory or perform other operations. Here, we can make use of the non-imaging time to perform accurate system identification, particularly if the trajectory to be tracked during imaging is not persistently exciting enough to closely identify the system parameters [74], [75], for example using probing signals.

*Video Capture/Display*

The concept of probing signals is still applicable in video capture. Video streams are typically not composed of a sequence of completely rendered, equally-temporally-spaced image frames. Instead, in most video cameras, a high degree of compression is applied to the images as they are streamed. The compression method usually only encapsulates information about which portions of an image has changed from the previous frames [78]. Thus, it is possible that frame-rate can be dropped periodically as required by an adaptive control algorithm to perform system probing while masking the dropped frame in the video compression algorithm.

*Wearable Displays*

Wearable displays, particularly eye-projection modalities, present an attractive area for deployment and growth of the fiber scan technology. Again, the concept of probing signals can be applied for more accurate/efficient system identification if the human physiology is considered. Wearable displays are unique in that typically only a single user will be viewing the projected images, as opposed to the shared perception of TV or computer screens. As such, if the display system is able to detect when the user is not looking, the free time can be used for system probing/self-calibration. The most obvious time when a user does not perceive the projected image is during eye blinking, which lasts between 100-400 milliseconds [79] and occurs about 1-5 times per 10s (varying sources) [79]–[81]. For a 60 frame-per-second (fps) display, one frame will take only 16.67 milliseconds. Hence, up to 6-120 frames are available to perform system probing every 10 seconds. Another eye activity during which visual information is not processed is saccading. Saccades are rapid eye movements between points of interest. During the eye movement which lasts between 20-100 milliseconds and occurs about once a second [82], a person does not visually perceive [83]. This provides 1-10 additional free frames during which to perform control optimization.

Table 5.2. Duration and frequency of eye actions during which visual stimulus is not processed, with corresponding free frames afforded in a 60fps system.

| | Duration (ms) | Frequency (per 10s) | Free frames (per 10s) |
|---|---|---|---|
| Eye Blink | 100-400 | ~1-5 | 6-120 |
| Saccade | 20-100 | ~10 | 12-60 |

*Slowly Varying System Parameters*

The system of interest is comprised of the electrical circuitry and the mechanical scanner. The parameters of the electrical circuit are assumed to be almost constant. Dramatic aging/temperature change or catastrophic events like short-circuiting can change the parameters of the electrical components are not considered. The mechanical scanner is the most sensitive part of the system. Kundrat reported that the epoxy used to assemble the system changes hardness with temperature and this is assumed to be the main cause of performance drift [9]. A temperature change of 7 degrees was shown to degrade system performance (efficacy of Braking) by 1.77% [9]. From first-hand experience with the SFE, once the system was manually calibrated, the image quality remains stable for many hours, and often much longer than that. As such, it is appropriate to assume that the parameters of the system to be controller vary slowly. Moving to mass-consumer applications like pocket projectors or wearable displays, the operating temperature of the an engine may change more rapidly. However, with proper thermal insulation, the system will not experience rapid parameter changes.

In summary, the periodic operation of the scanning fiber technology makes possible application of periodic or learning control theory. The periodic operation is also amenable to probing signals for periodic system identification. Applications in imaging and display afford much idle time in comparison to other controls applications, making periodic and probing control strategies attractive to pursue. The slowly-varying system also relaxes requirement for real-time feedback control, but the need for adaptation is present because temperature drifts will occur over the operation of the scanning fiber device.

## 5.3 Narrow Band Actuation and Input Shaping

Another important characteristic of the scanning fiber technology is that excitation is very narrow-band. This is because only one vibration mode of the scanner is excited at resonance to produce large deflections directly related to field-of-view. The narrow-band nature of the input signals can be advantageous in a number of ways. For mitigating hysteresis in the piezoelectric actuator, a narrow-band input approximation justifies approximating the hysteresis as a constant phase delay or as a simple low-pass filter. The phase distortions from any unmodeled off-resonance dynamics can also be collapsed into a single low-pass approximation, since the phase

contribution of all these elements are sampled at only one point on the frequency spectrum with single-frequency operation i.e. the phase contribution of a complex set of unmodeled dynamics can be approximated by a simple filter at the narrow frequency band of interest. Given that only the 1st mode is excited for high-FOV imaging, there are other vibration modes that should not be inadvertently excited. If these modes are modeled, the resulting trajectory distortion may be determined and compensated for. For unmodeled modes, this disturbance is not well defined. Meckl made the case that simply filtering the control input to avoid exciting at unmodeled frequencies is not a good approach because it will distort the final trajectory and lengthen the duration of actuation [84]. Simply truncating the filtered control signal will also lead to distorted trajectories. Instead, Meckl proposed that the reference input be shaped such that it has minimal energy at unwanted frequency bands [84].

This work proposes an input-shaping technique to avoid excited unwanted structural modes by analyzing and selecting envelopes based on the spectral energy density. The requirement for the scan trajectory is that is fills the view area, so that imaging or projection pixels are close to uniform. There is some freedom of choice in the actual scan trajectory. Since the carrier frequency of the trajectory must be close to the mechanical resonance, much of the input shaping is related to designing an envelope for the periodic trajectory. Figure 5.6 shows the frequency power spectrum for the control inputs corresponding to different trajectory envelopes. The red vertical line indicates the resonant frequency of the 2nd mode, which should not be excited. Note that most of the energy of the different control signals is concentrated around the 1st mode resonance, as expected.

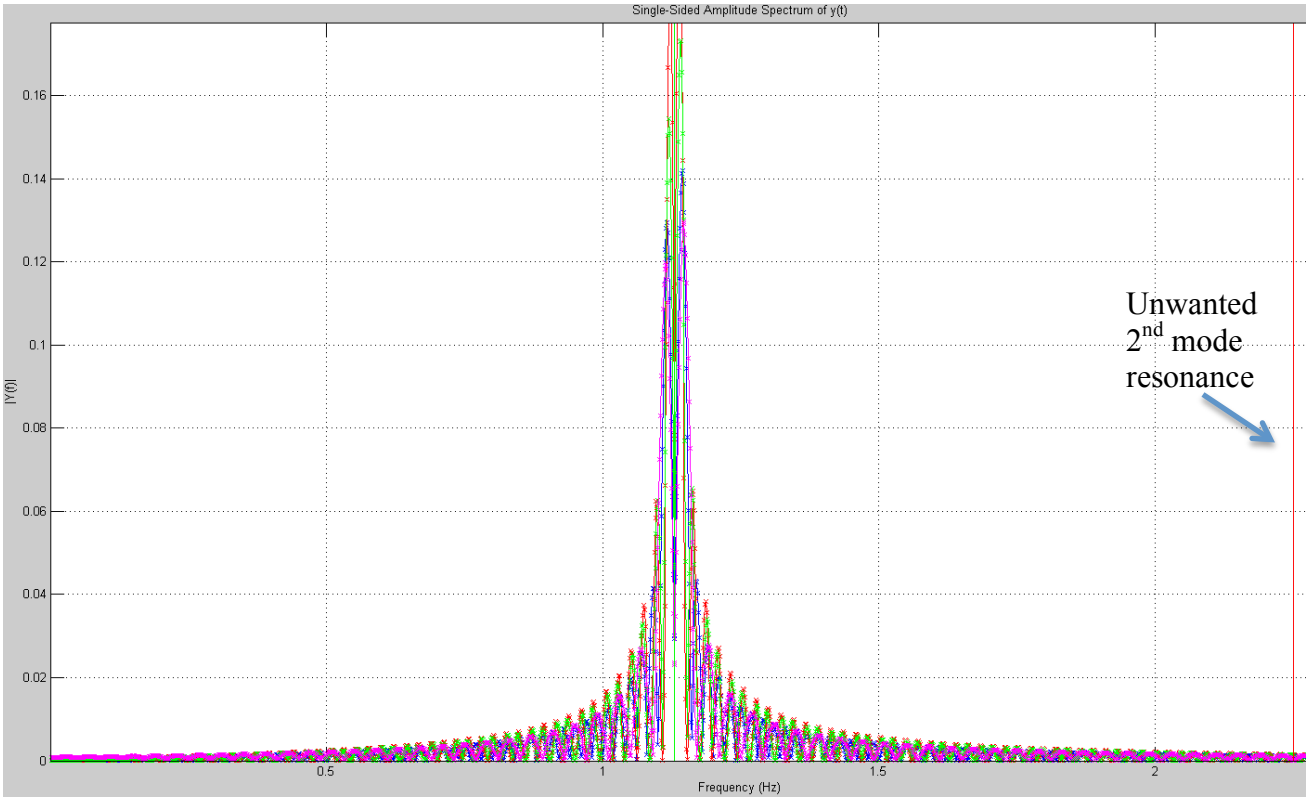


Figure 5.6. The frequency power spectrum of different control inputs corresponding to different desired trajectories.

Zooming into the region close to the undesired 2nd mode resonance in Figure 5.7, note that there are varying amounts of power close to 22.520kHz (2nd mode resonance peak). From this plot, it is predicted that the sine-tooth trajectory will produce the least excitation in the undesired 2nd mode.

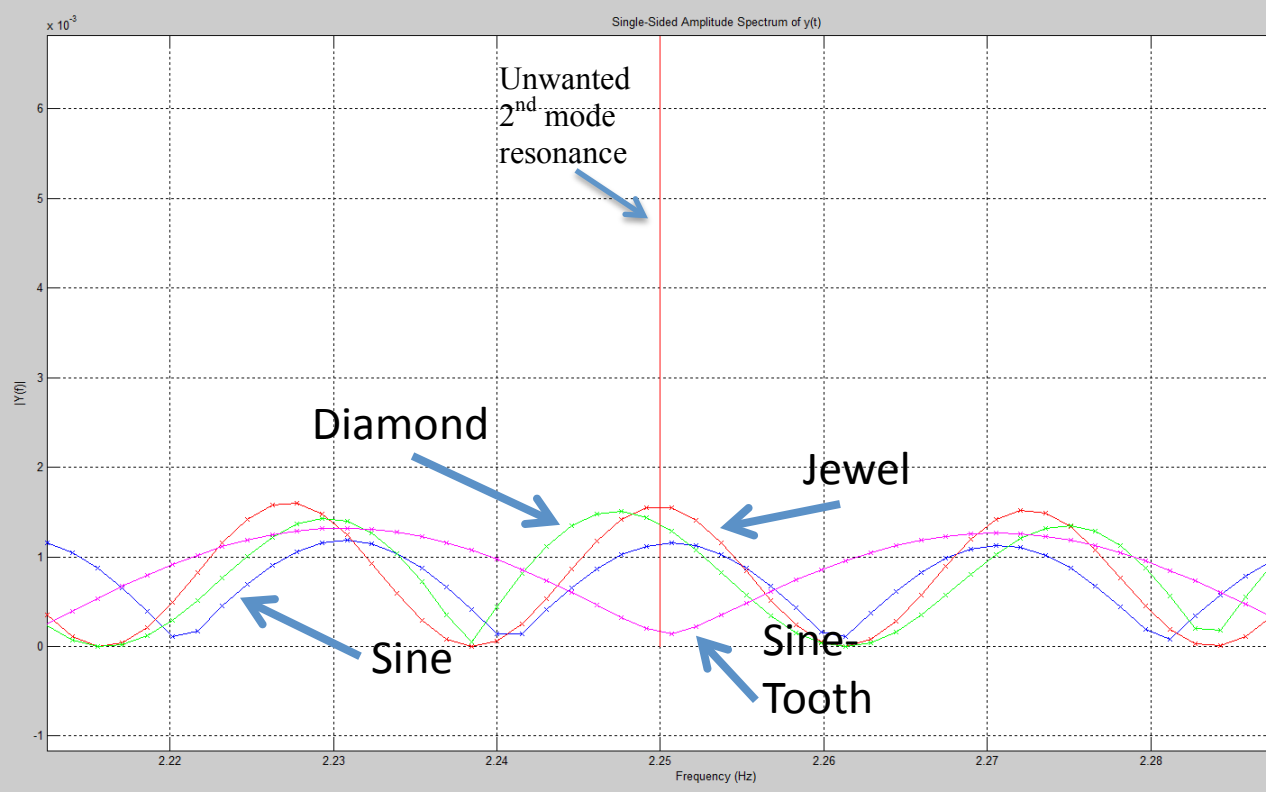


Figure 5.7. Zoom in close to the unwanted 2nd mode resonance frequency.

Figure 5.8 shows the Sine, Jewel, Sine-Tooth and Diamond Envelopes under consideration. (Figure 5.8 shows the experimentally achieved tracking of these custom trajectories using the Adaptive Feedforward Control approach introduced in the next chapter.)

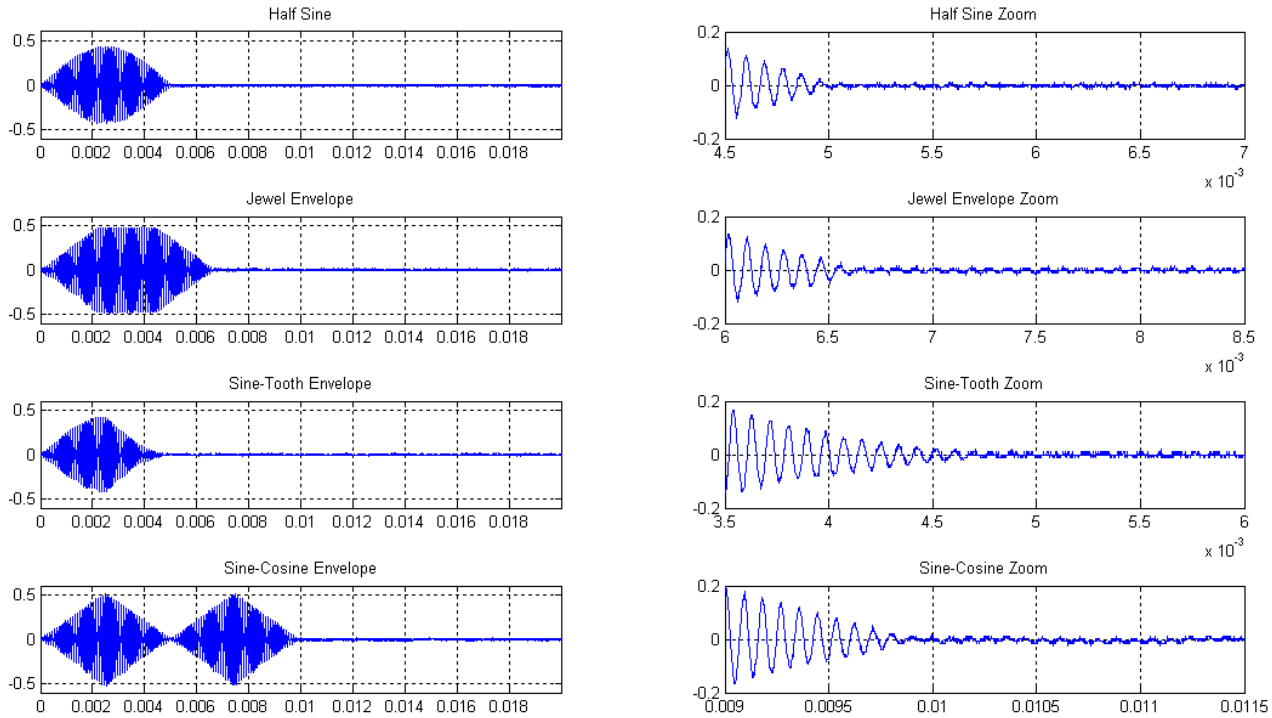


Figure 5.8. Sine, Jewel, Sine-Tooth and Diamond Enveloped scan trajectories experimentally recorded.

From experimental data, the above prediction that Sine-Tooth excitation pattern will excite the 2nd mode minimally is proven. Figure 5.9 shows the residual vibrations of the scanner using the Diamond trajectory. High amplitude vibrations at about 22.5kHz are observed, even though the excitation was at 11.3kHz, indicating that the 2nd mode was inadvertently excited.

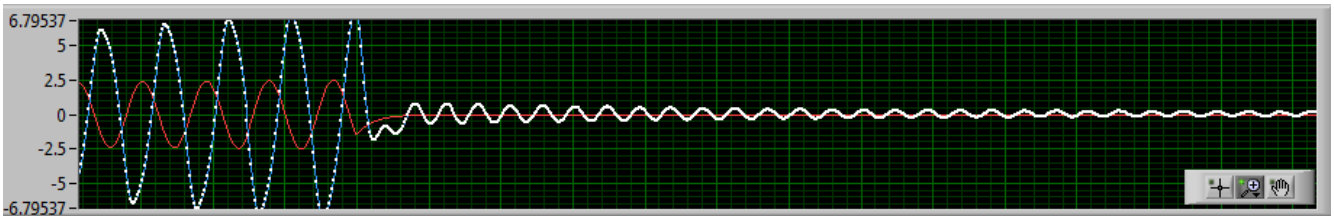


Figure 5.9. Residual vibration at the higher 2nd mode frequency is evident when using the Diamond trajectory. Red – Actuation signal, White – Simultaneous piezoelectric self-sensing signal.

Figure 5.10 shows the residual vibrations when the Sine-Tooth trajectory, which was predicted to excite the 2nd mode the least was used. Here the high-frequency residual vibration observed previously has been mostly eliminated. These compared trajectories were of the same maximum scan amplitude.

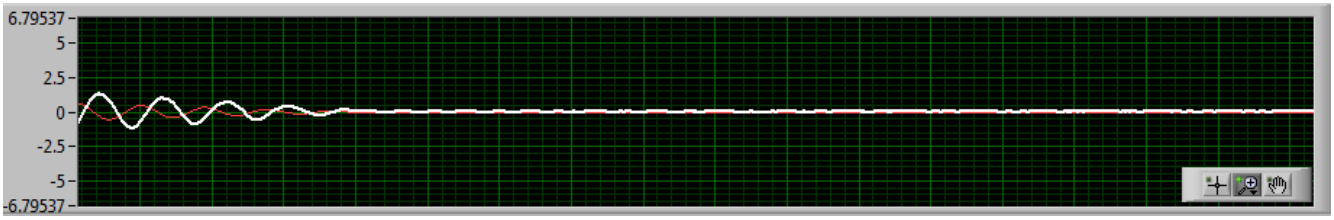


Figure 5.10. Residual vibration at the higher 2nd mode frequency is almost absent when using the Sine-Tooth trajectory. Red – Actuation signal, White – Simultaneous piezoelectric self-sensing signal.

## 5.4 TESTING

Since the Scanning Fiber Technology is primarily applied to imaging/display, the verification of the performance of a Scanning Fiber system should take into account the quality of images that are produced.

### 5.4.1 *Image Quality Assessment*

The assessment of image quality is an ongoing and active field of research. This is within the context of the myriad ways in which digital images are captured, processed and presented, leading to many different forms of degradation of image quality that can be difficult to compare and quantify [85]. For example, broadcast television images are subject to random pixel noise that produces artefacts as in Figure 5.11a, while JPEG compressed images exhibit a blocky texture as in Figure 5.11b.

Figure 5.11. a) Random pixel noise image. b) JPEG compression artefact image [85].

A simple method to quantify image fidelity is to treat images as vectors of pixel values:

$$\boldsymbol{x} = \{x_i | i = 1,2,3 \dots N\} \tag{5.14}$$

Then, the Mean Square Error (MSE) is used as a distance measure between a reference image $\boldsymbol{r}$ and a produced image $\boldsymbol{x}$:

$$MSE = \frac{1}{N} ||\boldsymbol{x} - \boldsymbol{r}||_2^2 \tag{5.15}$$

However, the MSE does not take into account the Human Visual System (HVS). For example, an image that is slightly zoomed-in will have large MSE because the pixels are all shifted, but is much more acceptable to a human observer than an image that has speckle noise but with lower MSE [85].

Because these images are ultimately consumed by humans, the field of modern image quality assessment is concerned with the *perceived* quality of images, regardless of the type of degradation or distortion in the images. Human perception and the Human Visual System (HVS) physiology is taken into account either directly or indirectly for various measures of image quality. These metrics can be separated into Subjective and Objective Image Quality Measures.

In subjective image quality measures, a group of people visually assesses images and scores them, to produce a Mean Opinion Score (MOS). This is considered to be the most reliable way to assess image quality, but is time consuming and not practical for automated applications.

Objective image quality measures aim to produce algorithms that quantify the *perceived* quality of an image. These algorithms do not require human input, but model or approximate

they way humans would experience an image. This approach is far more involved than taking the Euclidean distance of two image vectors. For example, many modern algorithms process the image based on models of neural processes within the HVS, and others apply machine learning to further emulate human perception [85].

Objective image quality measures can be categorized into Full Reference (FR), No Reference (NR) or Reduced Reference (RR) approaches. FR measures compare the fidelity of a reproduced image to the original image, which is completely available to the algorithm. NR measures score the quality of a reproduced image based on intrinsic qualities, independent of the original image. RR measures fall somewhere in between the two extremes, where the image assessment algorithm has some information about the original image, for example image features or geometry [85].

FR measures are the most widely researched, and many algorithms have been proposed: Daly Model, Lubin Model, Teo-Heeger Model, Watson's Wavelet Model, Spatial Domain Structural Similarity, Complex Wavelet Domain Structural Similarity Index, Visual Information Fidelity Measure and more [85].

While it is good to review the current state of image-quality assessment, the holistic, human-perception-based approach of such image-quality measures is not the best way to test and verify the scanning fiber technology. The aforementioned image-quality measures are largely focused on image degradation caused by processing, such as video compression, or transmission of data through lossy channels. This dissertation develops the Scanning Fiber Technology at the device level and at this lower-level, the aim is to 'put pixels at the correct spot'. Artefacts caused by image compression or digital transmissions are higher-level phenomena that the underlying scanning fiber device should be agnostic towards.

### 5.4.2 *Information Display Measurement Standards*

Understanding the device-level performance quantification, display device measurement standards are reviewed to find useful performance measures. The Society for Information Display (SID) and the Video Electronics Standards Association (VESA) have jointly produced the Information Display Measurements Standard (IDMS). The IDMS lays out in detail

measurements standards for all pertinent aspects of image displays including color-, spatial-, uniformity-, viewing-angle, physical- aspects and many more [86]. These measurement standards are adopted by industry (producers of TVs, projectors etc.) to compare and advertise their products. (Note that the IDMS specifies the measurement methods, but does not prescribe acceptable value ranges, which are the discretion of other parties.)

Device properties such as color fidelity and viewing angle are not directly related to the scanning control of the Fiber Scanner, and will not be reviewed in detail. However, measurements for linearity, waviness and large-area distortions are relevant for quantifying distortions of the Scanning Fiber devices. The detailed procedures for these tests can be found in [86].

The linearity test in the IDMS aims to quantify non-uniform density of pixels in a display device. In this test, uniformly pixel-distanced lines are projected by the display. If the display were completely linear, all the lines will be equally spaced. Deviations from the average spacing for pixels along the horizontal and vertical axes are used as a measure of display linearity, as shown in Figure 5.12.

The waviness test characterizes distortions typical in scanned projectors such as Cathode Ray Tubes (CRT)s where straight lines become bent. The Scanning Fiber Technology produces similar distortion features. In the waviness test, lines along the top, center and bottom of the display are projected. A linear fit is then performed on these lines, and the waviness measure is the peak-to-peak (PTP) deviation of the measured coordinates from the corresponding points along the fitted lines as shown in Figure 5.13.

Finally, the large-area distortion test characterizes common trapezium, rotation, orthogonal and pincushion distortions exhibited by displays such as CRTs. The procedure is similar to the waviness test, where horizontal and vertical lines are projected along sides and center of the display. Then, linear and polynomial fits are performed on the projected lines. The parameters of these fitted lines are used as a measure of the large-area distortion, as shown in Figure 5.14.

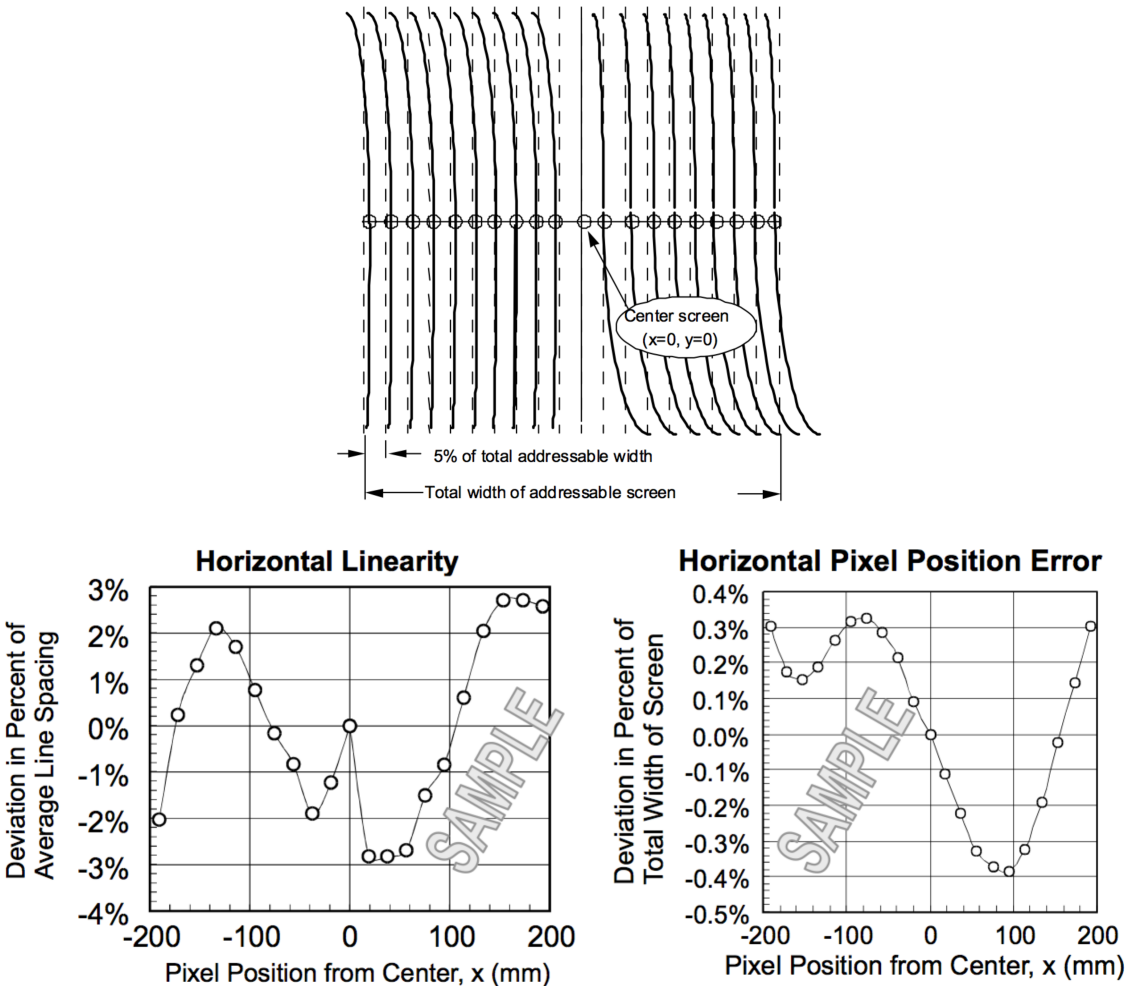


Figure 5.12. The linearity test [86].

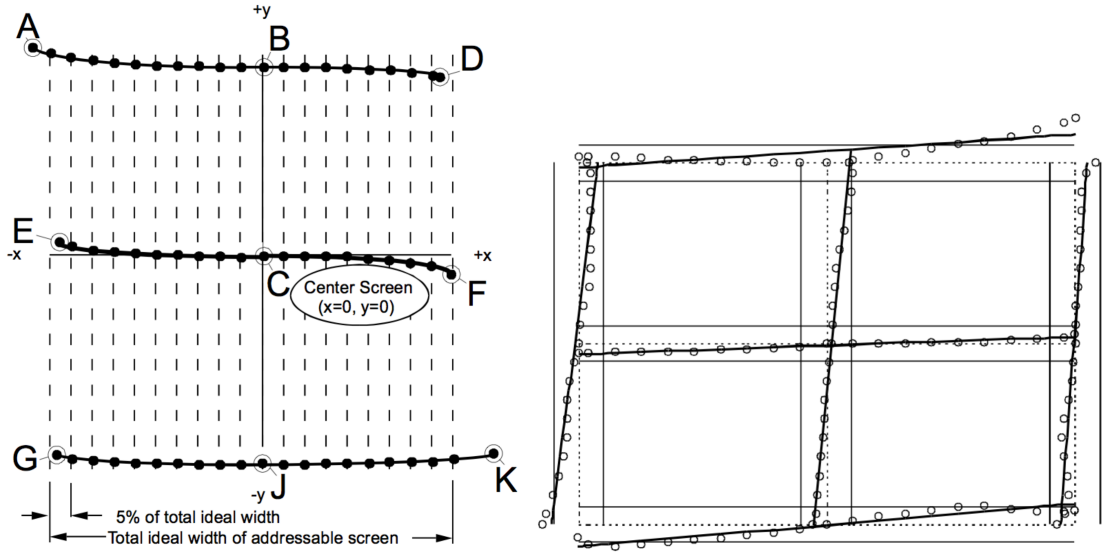

Figure 5.13. The waviness test. Pixel positions are fitted to a straight line and deviations are quantified [86].

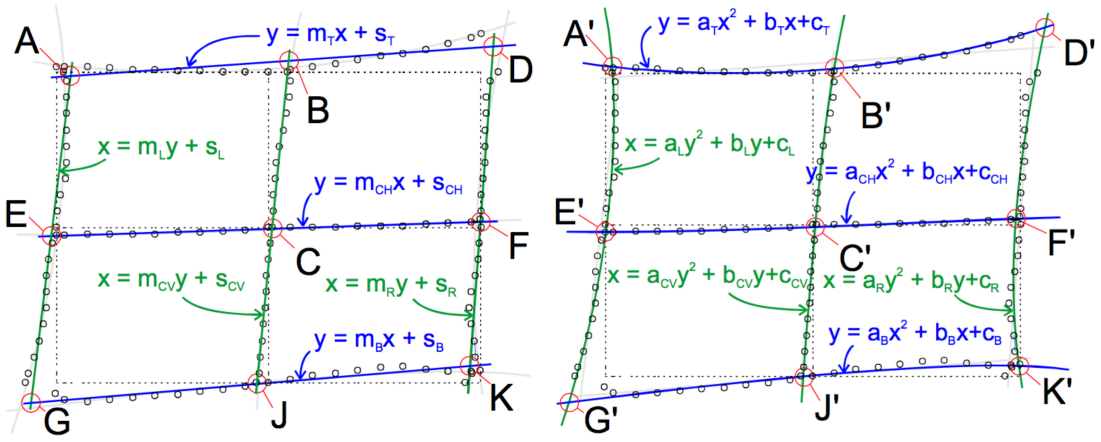


Figure 5.14. Large-area distortion test quantifying skewing, rotation and pin-cushioning [86].

### 5.4.3 *Suitable Testing Method*

The method by which to test, verify and present the performance of the Scanning Fiber Technology in this work will be based on the idea of 'putting pixels at the right locations', which is the device-level purpose of the scanning fiber technology. Within this paradigm the linearity, waviness and large-area distortion measures of the IDMS are relevant, but not ideal for a number of reasons. Firstly, the scanning fiber will mainly operate in spiral scan patterns, which is a novel scanning profile. Though the IDMS considers scanning display architectures like the CRT or flying laser spot devices, the scan method is assumed to be raster, thus the tests discussed are really tailored to rectangular scan areas and profiles. Secondly, the IDMS tests are macroscopic tests, i.e. not every pixel is queried. Instead, linearity only along the horizontal and vertical axes, overall skewing of a quadrant and etc. are quantified. A more detailed test method is needed, where the correct positioning of every pixel is accounted for

In this work, a radial-tangential or radial-phase error metric introduced by Smithwick et al. [59], [69] is employed to quantify the performance of scan controllers. The simple experimental setup is shown in Figure 5.15. The scanning fiber will be operated to scan a laser spot onto an

optical position sensor. Using an optical position sensor, location of the laser spot can be tracked at sampling rates of 20MHz and above.

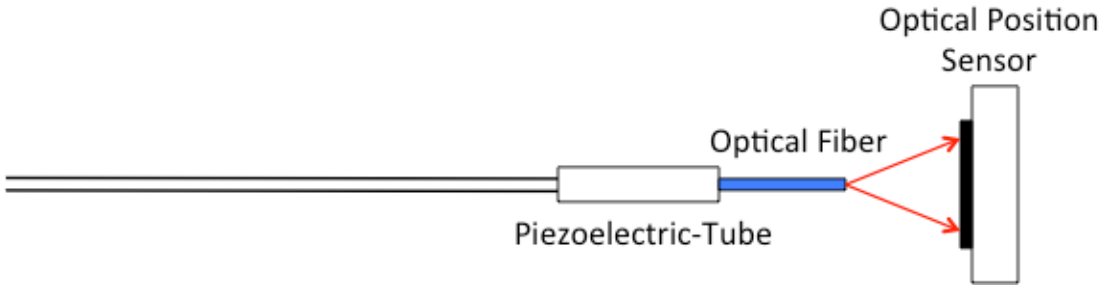


Figure 5.15. Scanning Fiber performance test setup.

Assuming that the desired locations for the image pixels are as shown in Figure 5.16a, the optical position sensor is used to measure the achieved location of each sample location. Figure 5.16b shows an example of a desired location O versus the achieved position X of a given pixel.

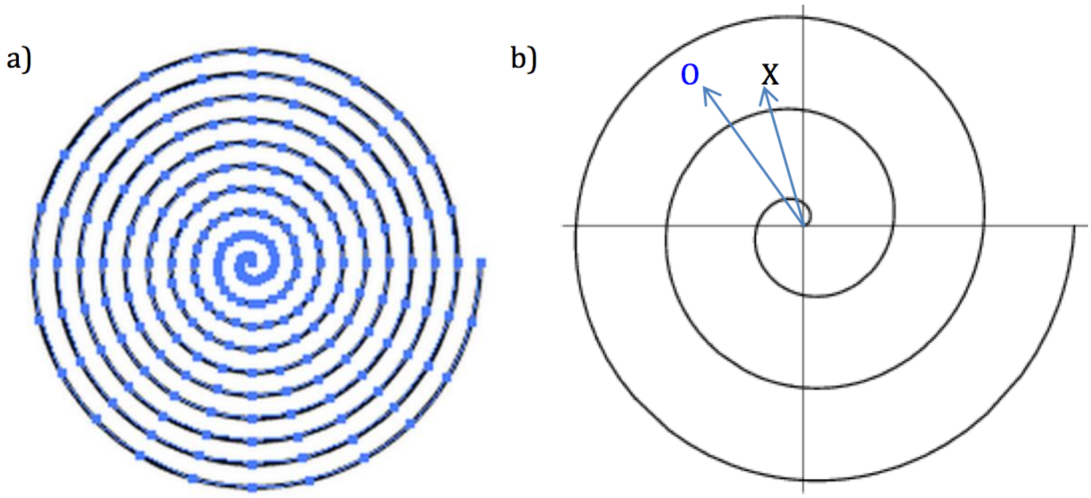


Figure 5.16. a) Example of desired pixel locations on a spiral. b) Example of the error between a desired location O and an achieved location X for a given pixel.

Using polar coordinates to describe the desired and the achieved positions for a given pixel,

$$\boldsymbol{x}_{pixel} = a\hat{\boldsymbol{r}} + b\widehat{\boldsymbol{\theta}} \tag{5.16}$$

Where $\hat{\boldsymbol{r}}$ and $\widehat{\boldsymbol{\theta}}$ are the radial and angular directions respectively, then we can quantify the radial and phase error of each pixel respectively as:

$$\Delta_{radial} = a_{achieved} - a_{desired} \tag{5.17}$$

$$\Delta_{phase} = b_{achieved} - b_{desired} \tag{5.18}$$

There are many benefits to using the radial/phase error convention. Firstly, the radial and angular directions are orthogonal, thus the measure is not redundant. Secondly, based on the image size and pixel size, we may calculate in units of pixel error. In addition, the radial/phase error measure is very intuitive: the result can be interpreted as "pixel 'x' is radially extended by ½ pixels and clockwise rotated by 1°." Finally, the performance errors for each two-dimensional pixel can be presented compactly in two linear plots for radial and tangential error respectively. In comparison, just a visual assessment of the achieved scan image will not give much of a quantitative gauge of the imaging performance.

## 5.5 SUMMARY

This chapter began with a review of previous control design efforts for the scanning fiber technology and found that in the absence of a miniature displacement sensor, all controllers so far have operated in open loop after an initial calibration with a calibration chamber. The operating characteristics of the scanning fiber device were then scrutinized, revealing that the periodic operation, idle time and slowly varying system afford unique control design opportunities. Finally, proper quantification of the scanning fiber device performance was investigated in the context of imaging or display devices, and a radial-tangential error metric was proposed.

# Chapter 6. ADAPTIVE FEEDFORWARD CONTROL

The contribution of this dissertation in introducing simultaneous piezoelectric self-sensing and electromechanical modeling methods for the scanning fiber technology has set the stage for developing online calibration methods for the scanning fiber device. This chapter presents an adaptive feedforward algorithm based on signal-probing system identification and exact inversion of isolated system dynamics.

## 6.1 SYSTEM PROBING IDENTIFICATION

An adaptive controller must be able to respond to changes in its operating environment; in this proposed algorithm adaptation is achieved via periodic system probing. Drifts in the operating condition, for example during surgery within biological environments, will cause the parameters of the scan engine to deviate from its initial state. As such, an adaptive controller must be able to accurately detect the system drift and compensate its control effort to maintain scan-tracking performance. The adaptive controller presented in this chapter performs system re-identification by exciting the scan engine with a special sinusoidal probing signal at the system resonance. This probing signal causes the 1st structural mode – which is the mode of interest – to be excited with strong residual vibrations containing information about the 1st mode dynamics. The excitation and response signal are recorded and analyzed via High Order Batch Least Squares (HOBLS). Then, Model Order Reduction is performed on the identified transfer function to extract only the 1st mode dynamics. These steps of the system probing identification are detailed below.

To speed up computation and allow for rapid system identification and re-calibration, this dissertation develops a Batch Least Squares method for finding the best-fit parameter values. This new BLS approach can be implemented recursively [74], [75] and is more efficient than structured or state-space model-based methods. In the 9-state model in Circuit Equivalent Electromechanical Model - if the circuit component values are precisely measureable, there still remains 7 model unknowns, $C_p$, $m_1$, $c_1$, $k_1$, $m_2$, $c_2$, $k_2$. Given a set of experimental data, a constrained optimization for example using Matlab's idgrey() function can solve for the best-fit parameter values, but the computation takes up to 3-minutes.

Batch Least Squares (BLS) identifies a transfer function from input-output data. Experimental data used for system identification is digitally sampled, meaning that the signals are in discrete time space. We discretize the system model and reformulate it in transfer function form. Because this is a model of measurement of a dynamical system a measurement noise term $e(t)$ is added to the equation:

$$(1 + a_1 q^{-1} + \cdots a_n q^{-n}) y(t) = (b_0 + b_1 q^{-1} + \cdots b_m q^{-m}) u(t) + e(t)$$

$$A(q)y(t) = B(q)u(t) + e(t) \tag{6.1}$$

$q$ the forward time-shift operator [74], [75], $u(t)$ and $y(t)$ the input and output respectively, $e(t)$ Gaussian white noise. Solving for $y(t)$ and rearranging, the general form results as,

$$y(t) = [y(t-1) \ldots y(t-n)\, u(t) \ldots u(t-m)] \begin{bmatrix} -a_1 \\ \vdots \\ -a_n \\ b_0 \\ \vdots \\ b_m \end{bmatrix} + e(t)$$

$$= \Phi_t^T \theta^0 + e(t) \tag{6.2}$$

Solving for the best-fit parameters $\hat{\theta}$ using batch least squares gives [74], [75],

$$\hat{\theta} = (\Phi^T \Phi)^{-1} \Phi^T Y \tag{6.3}$$

Where $Y$ and $\Phi$ are the output and regressor vectors respectively, over the measurement duration.

BLS is expanded to a High-Order Batch Least Square (BLS with a higher order transfer function) to better handle measurement noise [74]. To match the model order in Circuit Equivalent Electromechanical Model a 9$^{th}$ order regression model would be required. However, in practice the disturbance $e(t)$ is typically not Gaussian white, leading to poor data-fitting [74]. Equation 6.1 is expanded to handle colored noise by introducing a general noise filter $\frac{1}{D(q)}$ and rearranging back into Auto-Regressive with Exogenous Input (ARX) format,

$$A(q)y(t) = B(q)u(t) + \frac{1}{D(q)} e(t)$$

$$[A(q)D(q)]y(t) = [B(q)D(q)]u(t) + e(t)$$

$$\tilde{A}(q)y(t) = \tilde{B}(q)u(t) + e(t) \tag{6.4}$$

$\tilde{A}(q)$ may be set to a high (e.g. 50 versus the minimum order 4 for a double mass-spring-damper system) order to give very good data fit.

Finally, the high-order transfer function is separated into independent subsystems and the dynamics of interest is extracted. Since we are implementing an adaptive feedforward control for 1st mode resonant vibration, we are primarily interested in the transfer function from input to 1st mode excitation amplitude. In other words, we wish to determine the relationship between the input and the generalized displacement of the 1st vibration mode. We may extract the 1st mode dynamics by first converting the identified transfer function $y(t) = \frac{\tilde{B}(q)}{\tilde{A}(q)}u(t)$ into a modal state-space form,

$$\dot{x} = Ax + Bu$$

$$y = Cx$$

Here the $A$ matrix of the modal state-space form will consist of block diagonal entries $a_{i,jk}$, with each block $a_i$ corresponding to an eigenvalue or conjugate eigenvalue pair, e.g. $\sigma_1 \pm \omega_1$,

$$A = \begin{bmatrix} \sigma_1 & \omega_1 & 0 & 0 & 0 & \cdots \\ -\omega_1 & \sigma_1 & 0 & 0 & 0 & \cdots \\ 0 & 0 & \sigma_2 & \omega_2 & 0 & \cdots \\ 0 & 0 & -\omega_2 & \sigma_2 & 0 & \cdots \\ 0 & 0 & 0 & 0 & \lambda_3 & \cdots \\ \vdots & \vdots & \vdots & \vdots & \vdots & \ddots \end{bmatrix} = \begin{bmatrix} a_{1,11} & a_{1,12} & 0 & 0 & 0 & \cdots \\ a_{1,21} & a_{1,22} & 0 & 0 & 0 & \cdots \\ 0 & 0 & a_{2,11} & a_{2,12} & 0 & \cdots \\ 0 & 0 & a_{2,12} & a_{2,22} & 0 & \cdots \\ 0 & 0 & 0 & 0 & a_3 & \cdots \\ \vdots & \vdots & \vdots & \vdots & \vdots & \ddots \end{bmatrix} \quad (6.5)$$

The $B$ and $C$ coefficients corresponding to the block diagonals are,

$$B = \begin{bmatrix} b_{1,11} & b_{1,12} & b_{1,13} & b_{1,14} & b_{1,15} & \cdots \\ b_{1,21} & b_{1,22} & b_{1,23} & b_{1,24} & b_{1,25} & \cdots \\ b_{2,11} & b_{2,12} & b_{2,13} & b_{2,14} & b_{2,15} & \cdots \\ b_{2,21} & b_{2,22} & b_{2,23} & b_{2,24} & b_{2,25} & \cdots \\ b_{3,11} & b_{3,12} & b_{3,13} & b_{3,14} & b_{3,15} & \cdots \\ \vdots & \vdots & \vdots & \vdots & \vdots & \ddots \end{bmatrix}$$

$$C = \begin{bmatrix} c_{1,1} & c_{1,2} & c_{2,1} & c_{2,2} & c_3 & \cdots \end{bmatrix} \quad (6.6)$$

The block-diagonal form of the transformed state space model decouples the interaction of the model states into separable sub-systems. The independent resonant dynamics of the different modes of the vibrational system is extracted using the coefficients $a_i$, $b_i$, and $c_i$. The mode resonant frequency corresponding to this sub-system is given by $\omega_i$.

$$\dot{x}_i = a_i x_i + b_i u$$

$$y_i = c_i x_i \quad (6.7)$$

The 1st mode resonant dynamics are identified along each Eigendirection. The system identification method presented here is performed sequentially along each Eigendirection of the scanner. A sinusoid-burst excitation at the nominal 1st mode frequency:

$$u(t) = \begin{cases} \sin(\omega_0 t), & t_0 < t < t_1 \\ 0, & Otherwise \end{cases} \tag{6.8}$$

The above probing signal input to the system to excite the 1st mode resonance, while piezoelectric self-sensing signal is recorded.

As a demonstration, Figure 6.1a shows the piezoelectric self-sensing measurement signal with sinusoidal input active from 0s to 0.02s. Data was captured from 0.01s until 0.03s, showing the 1st mode decaying vibrations after 0.02s. Figure 6.1a shows a close match between the sensor data trace (black) and the 1st mode response prediction (blue). Using the method previously described, the 1st mode dynamics was accurately isolated and model-predicted from the input.

In Figure 6.1b, the predicted response was then subtracted from the measurement signal, resulting in a residue signal with no resonant or underdamped response. The residue signal is largely due to feedthrough of the drive input caused by capacitive bridge circuit imbalance. The presented data-driven system identification method is able to isolate and tolerate considerable sensing circuit imbalance, while still extracting the modal parameters. In the following sections, the extracted model is applied to accurately control the optical fiber tip trajectory.

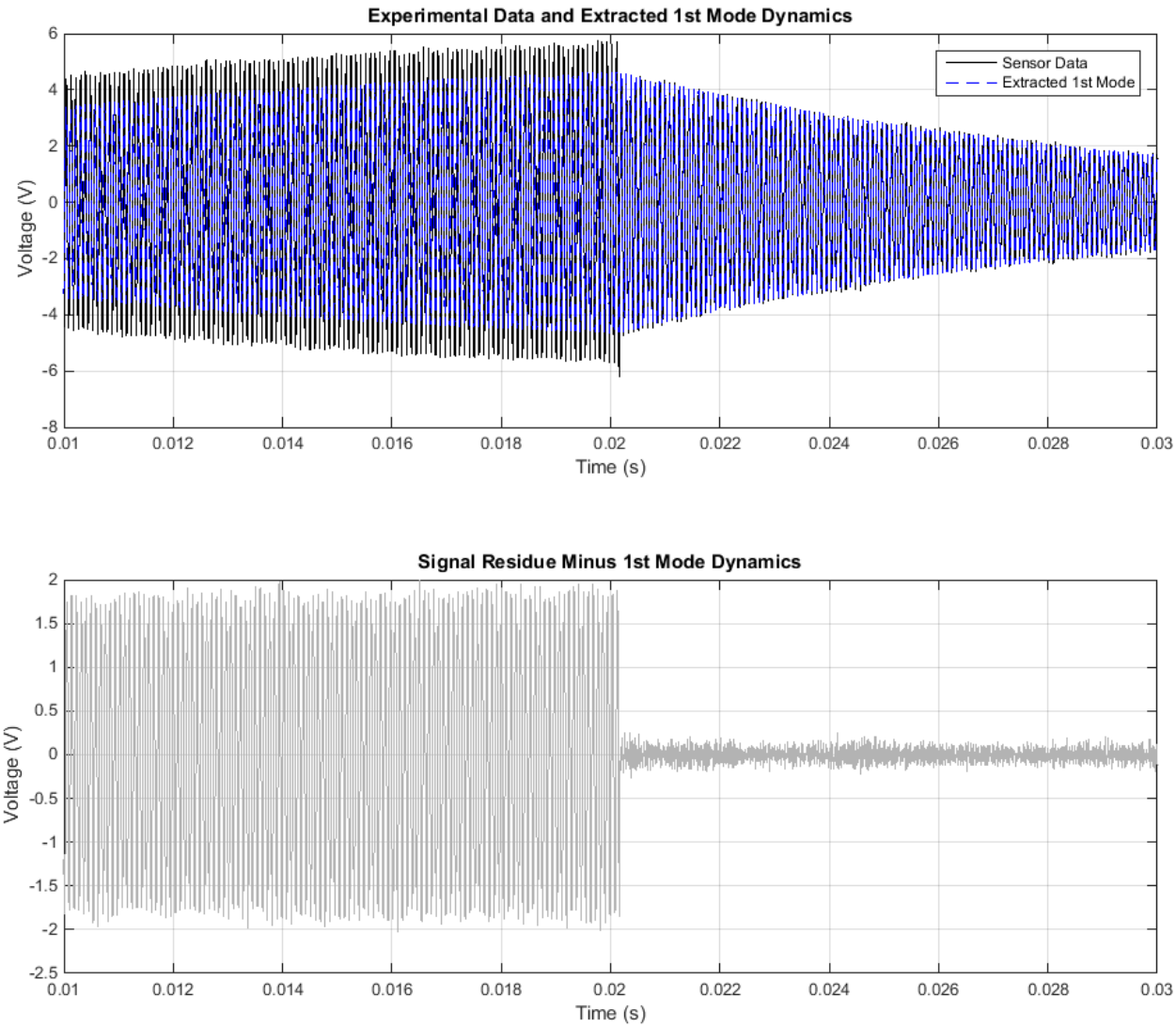


Figure 6.1. a) 1st mode dynamics identified and extracted from piezoelectric self-sensing signal. b) Measurement minus 1st mode residue. The remaining signal is largely input feedthrough due to capacitive bridge imbalance.

## 6.2 System Inversion

The adaptive controller introduced in this work updates it control effort by inverting the identified system dynamics. Exact inversion is performed on the reduced-order model to give the control input needed to achieve an arbitrary, sufficiently smooth trajectory. The sub-system models extracted into the form of Equation 6.7 may be exactly inverted to calculate the control

inputs needed to achieve specific scan trajectories. For instance with the SFE the 1st resonant mode of the scanning cantilever is to be controller to achieve high optical fiber deflection. The dynamics of the 1st resonant mode is extracted from the block diagonal subsystem with $\omega_i$ closest to the expected 1st mode resonance.

The input-to-1st mode dynamics isolated from the system identification steps can be described as a 2nd order system:

$$\dot{x}_d = a_1 x_d + b_1 u_{ff}$$
$$y_d = c_1 x_d \tag{6.9}$$

$y_d$ is the desired output trajectory and $x_d$ is the state trajectory vector associated with that output. $u_{ff}$ is the required feed-forward input to achieve the desired trajectory. $a_1$, $b_1$ and $c_1$ are the model coefficients identified for the 1st mode dynamics.

Given an arbitrary but sufficiently smooth (continuous 2nd derivative) desired trajectory $y_d$, the required input $u_{ff}$ to achieve $y_d$ can be calculated as [87],

$$u_{ff} = \frac{1}{c_1 a_1^{r-1} b_1}\left[\frac{d^r}{dt^r} y_d - c_1 a_1^r x\right] \tag{6.10}$$

$r$ the relative degree of the system, given by $r = \#poles - \#zeros$.

In Equation 6.10, the state trajectory $x$ is the only unknown. Equation 6.10 may be substituted into the dynamics Equation 6.9 to generate the $x$-trajectory that is then back-substituted into Equation 6.10 to find the feedforward input. For more efficient computation, a reduced-order inverse can also be used [88].

Next, some considerations on system inversion are discussed, particularly non-minimum phase systems and numerical accuracy. The transfer function given by the model-reduction of the canonical state space realization introduced in Model Order Reduction guarantees a minimum phase equation. Nonetheless, exact inversion is applicable to non-minimum phase systems as well. Exact inversion of periodic trajectories of linear non-minimum phase systems is possible by first separating the stable and unstable internal dynamics of the inverse system, then solving for the control input in two separate steps: solve the stable subsystem forward in time, solve the unstable subsystem backward in time, then recombine to get the solution [87]. Exact inversion of non-minimum phase systems can also be performed directly in the frequency domain [87], [89].

Inversion of nonlinear non-minimum phase systems can be done iteratively and is presented in e.g. [90].

The 1st mode isolated dynamics is of the harmonic oscillator of the form similar to Kundrat [9],

$$\ddot{y} + 2\zeta\omega_n\dot{y} + \omega_n^2 x = u \tag{6.11}$$

The input-output transfer function will be,

$$\frac{Y(s)}{U(s)} = \frac{1}{s^2+as+b} \tag{6.12}$$

Given a desired trajectory $Y_d(s)$, the control input $U_{ff}(s)$ via exact inversion is simply a linear combination of the desired trajectory and its derivatives:

$$U_{ff}(s) = s^2 Y_d(s) + asY_d(s) + bY_d(s) \tag{6.13}$$

If the desired trajectory is discontinuous or has dramatic change in its derivatives e.g. envelopes with sharp turning points, the numerically calculated control input $U_{ff}$ will not be accurate. Because the system is operated close to its resonance point, thus the denominator in Equation 6.12 is close to 0. Small inaccuracies in the derivatives of $Y_d$ used to calculate $U_{ff}$ will be greatly amplified by the numerically unstable transfer function. Figure 6.2 shows that the simulated trajectory (green) does not match the desired trajectory (blue) using exact inversion of the desired trajectory if the trajectory is at the resonance of the system dynamics.

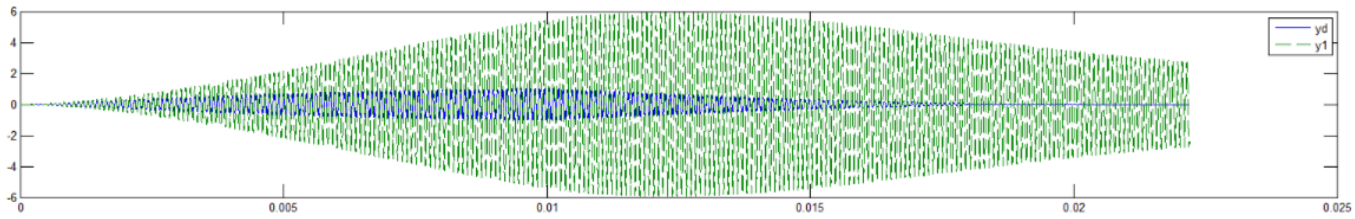


Figure 6.2. Numerical error in calculating the exact inverse leads to large tracking error.

This numerical issue can be mitigated by decreasing the time-step (increasing the samples/time) of the exact inverse calculation. By increasing the number of samples 10-50x, the numerical error is reduced to arbitrarily low levels, as shown in Figure 6.3.

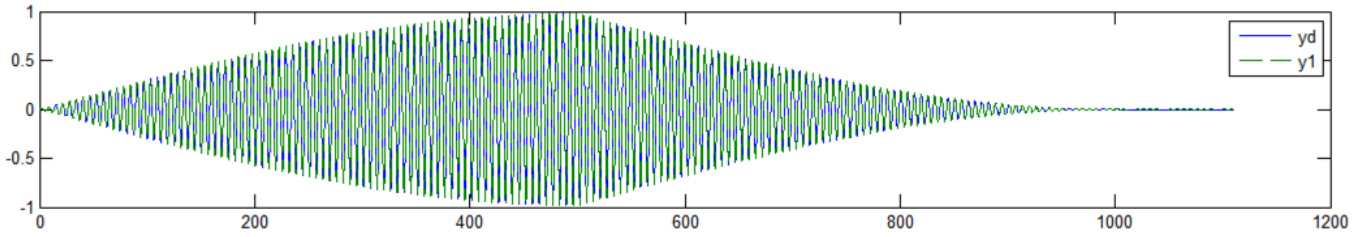


Figure 6.3. Numerical error eliminated by over-sampling in calculation.

Note that for a given desired periodic trajectory, the calculation of the control input will not be made more computationally expensive by increasing the sample points as described above. The numerical work-around is only for finding the derivatives of $Y_d$, which are then down-sampled to the original system time-step. These derivatives are stored, and as system identification updates the model parameters, new control inputs $U_{ff}$ can be generated by simply taking linear combinations of the stored derivatives as described in Equation 6.13.

## 6.3 Experiment Methodology

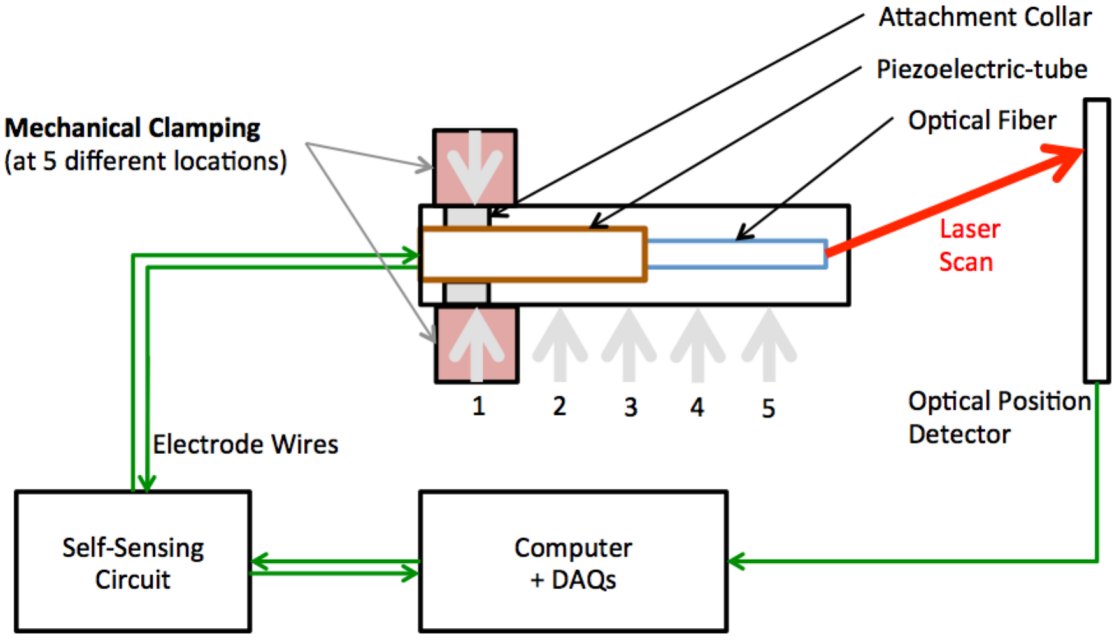


Figure 6.4. Adaptive control for varying mechanical stress experimental setup.

To quantify the performance of the introduced adaptive controller, an 11.5kHz SFE prototype was put under changing mechanical stress. The performance of the new adaptive controller was compared to the standard open-loop control method [28] (which does not update its control input after calibrating for the initial operating condition). To quantify trajectory tracking/image error, the radial-phase error convention is used, as described in Suitable Testing Method.

Figure 6.4 shows the experimental setup. A PZT-5A piezoelectric-tube of 0.45-mm outer diameter, 4-mm length, and a cantilevered optical fiber of 0.08-mm outer diameter and 2.27mm length constitute the SFE scan engine, with 1st mode resonant frequency at about 11.5kHz. A National Instruments PCI-6115 Data Acquisition (DAQ) card operating at 500k samples/s was used to produce the control drive and to measure the self-sensing signals. For verification purposes, a 520-nm laser diode (Thorlabs) was coupled to the optical fiber, and an optical position sensor (DL-20, OSI Optoelectronics) was used to measure the scanned laser spot trajectory.

For comparison with previous open-loop control methods, the desired trajectory $r_1(t)$ was chosen to be 180 imaging spirals of uniformly ramping amplitude, followed by a non-imaging collapsing time. Each spiral is constituted by a sine and a cosine of frequency 11.315kHz, one on each Eigendirection,

$$r_1(t) = A_0 t sin(\omega_0 t),\ 0 \le t < 180T_0 \tag{6.14}$$

To capture images, a 2D scan is spanned by actuation in both Eigendirection 1, $r_1(t)$ and Eigendirection 2, $r_2(t)$. The trajectory $r_2(t)$ is exactly the same as $r_1(t)$ except that $\cos(\omega_0 t)$ replaces the sinusoid. $T_0$ is the period corresponding to $\omega_0$ and $A_0$ scales the maximum scan amplitude.

The experiment is designed to investigate the scan accuracy between the de facto open loop control versus the proposed adaptive feedforward method under changing mechanical stress. The procedure is as follows:

Unclamped: Initially the scan probe was rested in a V-groove to simulate the starting operative state of the scanner, docked within the calibration chamber. The open loop control is initialized in this unclamped state. The performance of the open loop control versus the proposed adaptive controller is quantified.

Clamped: Next, the scanner was mechanically clamped sequentially at five different positions as in Figure 6.4, to simulate the scanner being removed from the calibration chamber and inserted into e.g. the gastro-intestinal or respiratory tracts for medical use, where changing mechanical stresses will be applied to the scan probe. During operation, the open loop method cannot re-calibrate, but the adaptive controller utilizing piezoelectric self-sensing is able to update its control inputs. The scan accuracies obtained with the baseline open loop and the new adaptive controller are recorded for the five different clamping configurations.

## 6.4 Results and Interpretation

The scan accuracies of the open loop versus the presented adaptive feedforward control are compared in the unclamped state and then in different clamped configurations to demonstrate the advantage and robustness of the adaptive controller under changing operating conditions.

Unclamped

An endoscope probe was initially in a resting/mechanically-unstressed condition representative of the calibration chamber. The open loop controller was initialized in this unclamped state. Figure 6.5a shows the 20 scan parameters that need to be manually configured for the open loop protocol. Figure 6.5b shows the laser scan result of a correctly calibrated open loop control. The straight bright line indicates that braking is correct along the first eigendirection. The small bright spot shows that braking is correct along the second eigendirection and the fiber is brought rapidly to rest before the next scan cycle. (Note that in practice the laser is turned off during braking and settling such the bright line and spot is not normally visible). The open loop control is not reinitialized in later parts of the experiment because in practice, recalibration can only be done within the calibration chamber.

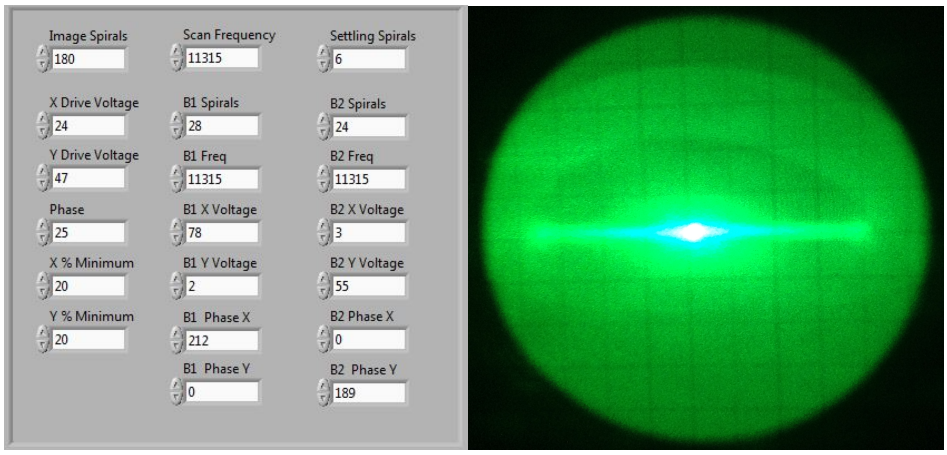


Figure 6.5. a) 20 scan parameters manually configured for the de facto open-loop control. b) Result of correctly calibrated open loop control, showing straight braking lines and settling point.

Using a Position Sensitive Detector (PSD), the scanned laser spot positions were recorded and compared with the desired trajectory to measure scan accuracy. This measurement is repeated three times in the unclamped case. Figure 6.6a and Figure 6.6b show 2-D plots of the achieved scan trajectory with the open-loop and the adaptive feed-forward controllers. Qualitatively the adaptive feed-forward tracks the spiral scan more accurately. Figure 6.6c and Figure 6.6d show quantitatively the squared error in the normalized-radial and phase/tangential components. There is clearly a reduction in the overall error using the adaptive feed-forward method, in the unclamped state.

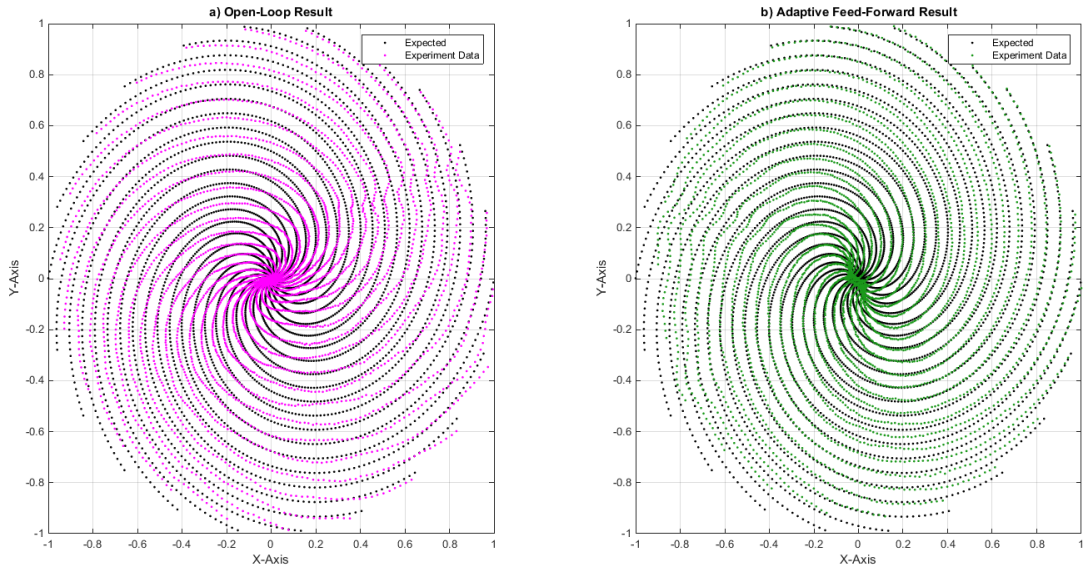

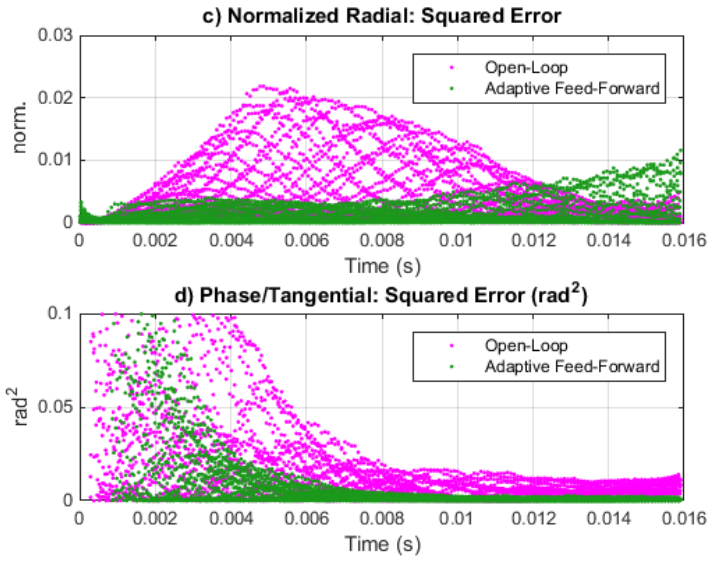


Figure 6.6. Unclamped: a) 2-D scan result with open-loop control. b) 2-D scan result with adaptive feed-forward control. c) Normalized squared radial error compared between open-loop and adaptive feed-forward result. d) Phase/tangential squared error compared between open-loop and adaptive feed-forward result.

Clamped

Next, the scan probe was clamped in 5 different configurations to introduce varying mechanical stress. This procedure replicates the operating conditions during surgery or manipulation of the ultrathin and flexible SFE within small ducts where tissue contact is unavoidable. Figure 6.7a and Figure 6.7b show 2-D plots of the achieved scan trajectory with the open-loop and the adaptive feed-forward controllers respectively. Qualitatively the adaptive feed-forward tracks the spiral scan much more accurately. Figure 6.7c and Figure 6.7d show quantitatively the squared error in the normalized-radial and phase/tangential components. In the clamped state, the adaptive feed-forward clearly outperforms the open-loop because the new adaptive controller is able to update its control input in response to changing operating conditions to maintain high image quality.

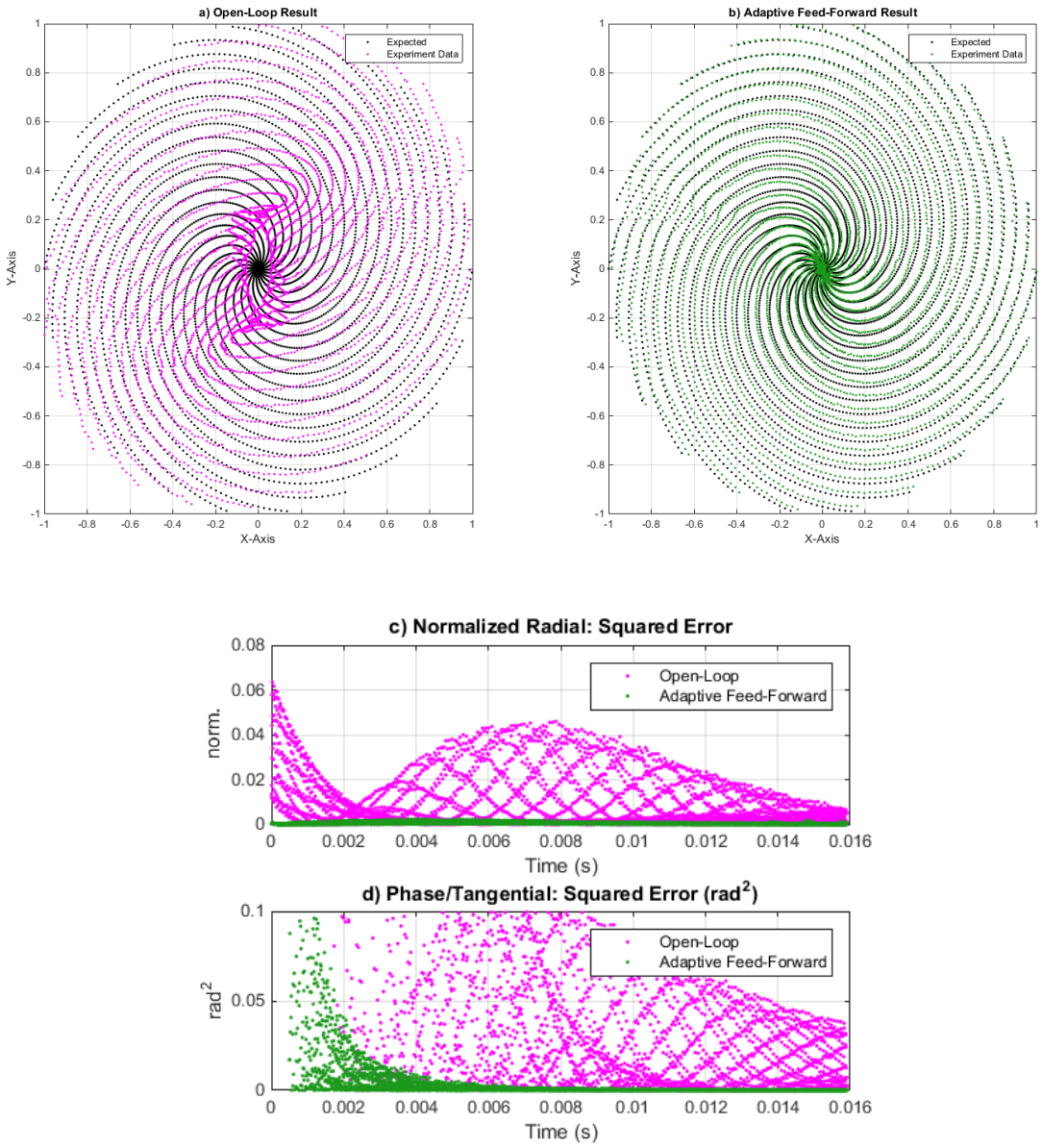


Figure 6.7. Clamped: a) 2-D scan result with open-loop control. b) 2-D scan result with adaptive feed-forward control. c) Normalized squared radial error compared between open-loop and adaptive feed-forward result. d) Phase/tangential squared error compared between open-loop and adaptive feed-forward result.

Figure 6.8 graphs the radial and tangential mean squared error (MSE) for the unclamped and then the clamped configurations. In the Unclamped configurations, the open-loop and adaptive feed-forward scan accuracies are steady over three trials, with the new adaptive feed-forward method achieving higher accuracy. In the five Clamped configurations, the error for the open-

loop controller shoots up by a factor of 2-3 because it is unable to adjust to the changing mechanical stress. On the other hand, the adaptive controller maintains a much lower level of scan error over the five different clamping conditions. The standard deviation in the radial MSE is 0.027 for the open-loop case, while the standard deviation in the radial MSE is 0.008 for the adaptive feed-forward controller.

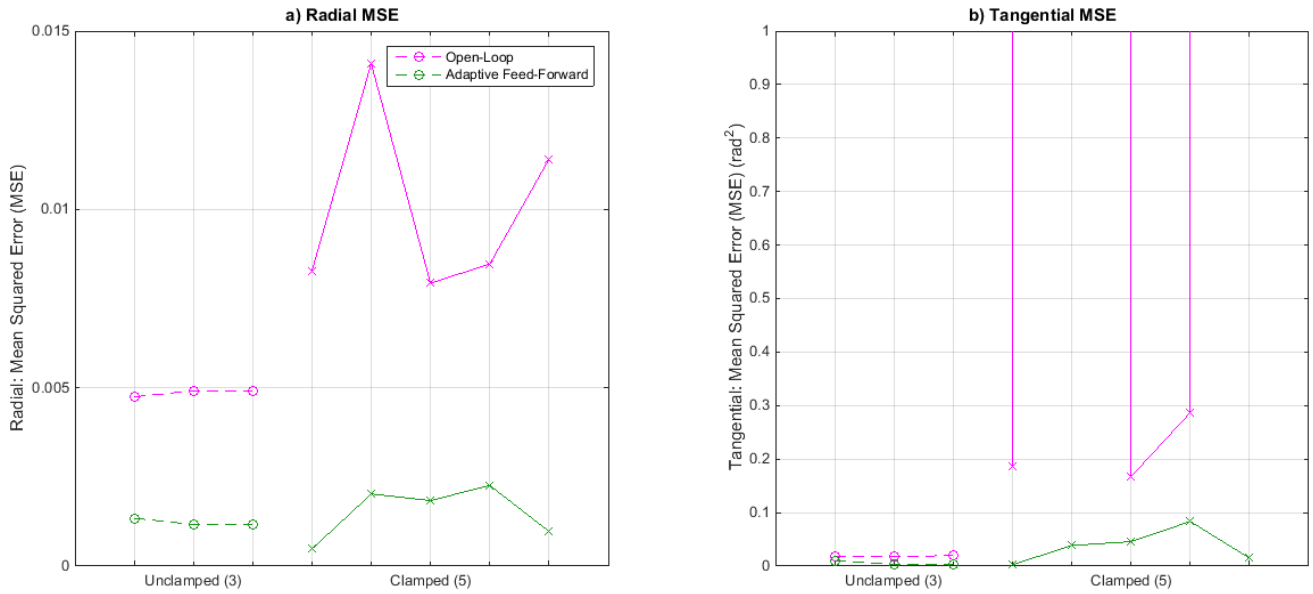


Figure 6.8. Radial and Phase/Tangential Mean Squared Error (MSE) over 3 unclamped tests and 5 clamped tests, achieved by open-loop versus adaptive feedforward method.

Image Quality

To visually compare the image quality produced by the open loop and the new adaptive controller, during each scanned video frame laser light was modulated through the optical fiber to project target images as in Figure 6.9a. The projected images were then captured using a hand-held camera. Figure 6.9b shows the Unclamped initial image quality of the de facto open-loop controller. Even with manual tuning of the scan parameters, image distortions are still present. Figure 6.9c shows the open-loop image quality after Clamping at position 1. Under various mechanical stresses, the response of the scanner can change dramatically, leading to severe image distortions.

Figure 6.9d shows the Unclamped initial image quality of the new adaptive feed-forward controller. Image quality is improved over the open-loop method. Figure 6.9e shows the image

quality after Clamping at Position 1. Even in the extreme case of hard mechanical clamping at the base of the piezoelectric actuator (e.g. Position 1 - Figure 6.4), the image quality is largely maintained and far better than the open-loop result, because the adaptive controller can auto-calibrate to the new stress conditions.

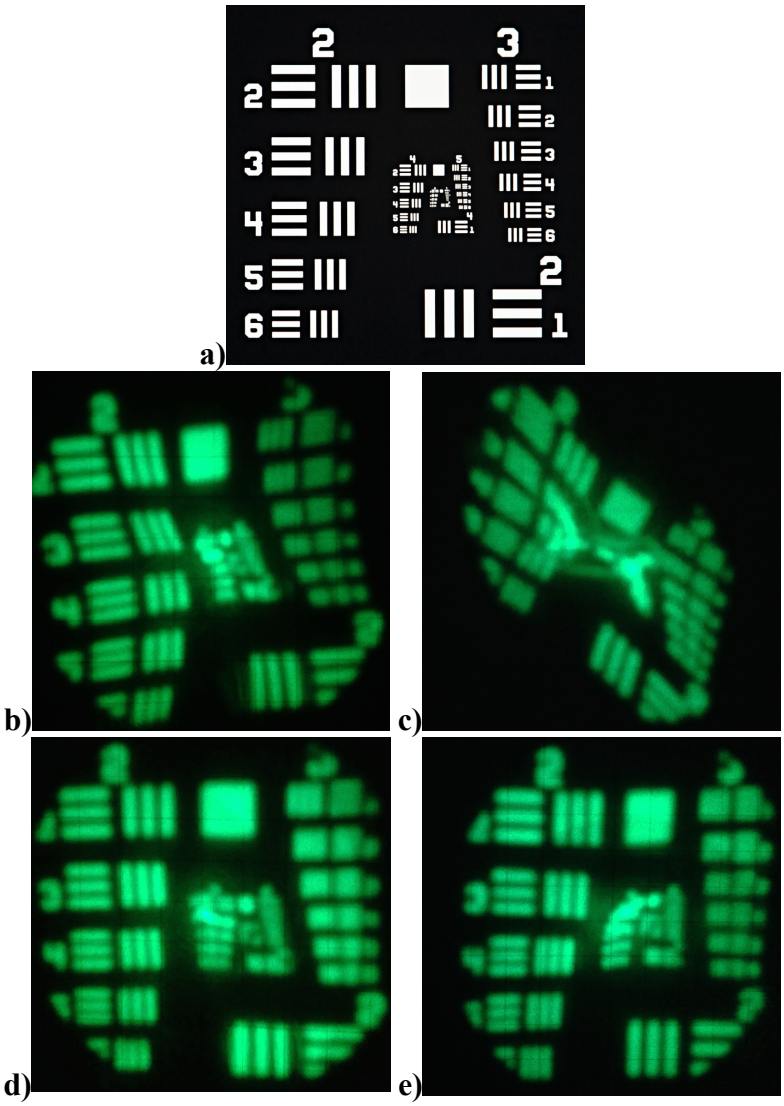


Figure 6.9. a) Target image to be laser-projected. b) Open-loop scan Unclamped. c) Open-loop scan after Clamped. d) Adaptive feed-forward scan Unclamped. e) Adaptive feed-forward scan after Clamped.

## 6.5 DISCUSSION

The above experimental results demonstrate for the first time a closed loop adaptive controller utilizing the integrated piezoelectric tube as an online miniature sensor. All previously demonstrated controllers required an external optical sensor for pre-calibration, then operated in open loop [27], [28], [59]. The open loop controller in [27], [28] was used as the baseline method in the experiments for this article. A closed loop controller should be able to compensate for the changing stresses while maneuvering the endoscope e.g. taking a biopsy within the respiratory or digestive tract while maintaining image quality with the correct scan trajectory. From Figure 6.9, the different stresses clearly alter the open and closed loop responses but the closed loop controller always preserves higher scan accuracy. Figure 6.8 quantitatively shows that the controller consistently maintains a lower scan error by compared to the open loop approach in both the unclamped and especially the mechanically clamped case.

For each 180 imaging spirals, the manually tuned open-loop control required 58 cycles of non-imaging braking and settling time, resulting in a frame rate of 45.45Hz. The adaptive feedforward controller was set up to track a scan trajectory of 180 imaging spirals and 36 non-imaging contracting spirals, resulting in a frame rate of 50Hz. Thus, the adaptive feedforward controller enabled slightly higher frame rates in addition to maintaining high image quality with varying mechanical disturbance. Higher frame rates during endoscopic surveillance can allow the endoscope to move more rapidly during diagnostic inspections, such as flexible cystoscopy [3].

Compared to the uncontrolled case, scan trajectory error has been significantly reduced using the adaptive controller. Scan accuracy may be further improved by implementing model/control-point optimization methods that are developed in the next Chapter. Also, the system identification method thus proposed requires a 40-ms burst sinusoidal excitation as the probing signal. Imaging is interrupted during system probing, though the 40-ms blanking may not be noticeable at the 15Hz imaging frame rates that are acceptable in many endoscopic applications. During long endoscopic procedures, the recalibration may be user initiated to minimize the risk of the interruption to high frame rate imaging In the next chapter, a further method of online system optimization is introduced to remove this calibration probing or blanking interval.

In a non-adaptive or open-loop system, certain disturbances can cause the output to be grossly in error. In Figure 6.8, we find that the Clamped Positions 2 and 5 result in extremely high scan error compared to other Clamped positions, meaning that in this particular stress configuration, the scan engine dynamics is significantly distorted. The widely varying open-loop performance versus the steady adaptive controller result highlights the advance of this work's adaptive feed-forward controller in maintaining scan accuracy without manual intervention, accomplishing a stable, self-calibrating imaging system.

Two final comments on the image quality of current SFE prototypes: i) In SFE prototypes 'pixel distortion remapping' is performed where the trajectory distortion is recorded by the optical detector within the calibration chamber, and used to pre-warp the SFE images. This is an additional open loop image-correction that was not performed in this investigation, since this work is focused on the actual trajectory accuracy. ii) Mechanical disturbances during maneuvering, biopsy or even surgery within the ducts of soft tissue organs in the body are not expected to perturb the SFE as significantly as physically clamping the fiber scanner. Thus, the mechanical clamping experiments in this investigation represent worst-case mechanical perturbations.

## 6.6 SUMMARY

This chapter presented a new adaptive control algorithm for the scanning fiber technology. The adaptive controller uses a signal-probing system identification to periodically identify a new dynamical model of the device, which may be undergoing changing operating conditions. The identified model is reduced and only the 1$^{st}$ mode dynamics are retained. This reduced-order model is then inverted via exact inversion to calculate a new control input needed to maintain the desired scan trajectory. Experiments were conducted to compare this new adaptive controller to the standard open loop control used in all current SFE prototypes. Mechanical stress on the scan probe was varied and the scan accuracy of the open loop versus the adaptive controller was analyzed, showing adaptation to changing environments and consistently higher scan accuracy with the proposed adaptive control method.

# Chapter 7. RUN-TO-RUN OPTIMIZATION CONTROL

This work has demonstrated for the first time with the scanning fiber technology, use of the same miniature piezoelectric-tube for both actuation and also collocated sensing [91], which has enabled exploration and implementation of new online and adaptive control strategies. Use of the piezoelectric tube (previously functioning only as an actuator) as also a sensor is made possible by the new simultaneous piezoelectric self-sensing circuit. This simple electronics-retrofitting process means that no bulk is added to the Scanning Fiber Endoscope probe, maintaining its slim form factor while providing measurements of the optical fiber deflection during use with changing operating conditions. In the previous chapter, a new adaptive feedforward controller, using the piezoelectric self-sensing measurements was shown to maintain 2-3 times better scan accuracy compared to the de facto open-loop method in experiments simulating changing in-use structural stress.

In the most recently developed controller, a 40-millisecond system identification procedure (during which the sensing signal is processed) is automatically performed whenever the system should update its control signal. That system identification repeatedly modifies the dynamics model of the scanner, which is used to calculate an exact-feedforward input to achieve a given desired trajectory. With that innovation, the Scanning Fiber Endoscope is now able to auto-calibrate to maintain high image quality while in use.

Nonetheless, there are a number of limitations with the previously introduced adaptive feedforward controller that this chapter will improve upon by presenting a novel run-to-run optimization controller. i) Firstly, each time the controller updates, a 40-millisecond interval results during which no images are channeled. Though for infrequent updates this brief blanking may be unnoticed, the interval could be reduced or eliminated. ii) Secondly, each update of the control point is an independent calculation: the controller re-identifies the system dynamics de novo. No error information from the performance of previous control signals is used to refine or inform the subsequent updates. iii) Lastly and relatedly, there is no feedback loop designed to converge the system to zero tracking error. As mentioned above, since each system identification instance is independent, there is a certain level of stochastic error at each update, which could be regulated by a learning controller.

As a follow up development, this chapter will introduce and demonstrate a run-to-run controller formulated on a feedforward with exact model-inversion framework that can progressively optimize to the best-achievable tracking trajectory.

## 7.1 Run-to-Run Control

This section will review run-to-run control and establish why run-to-run control is suitable with the scanning fiber technology. Design of a control system for the Scanning Fiber Endoscope should be informed by the specific qualities of its operation. i) Foremost, the reference trajectory is periodic and constant frame-to-frame. Ideally the optical fiber should start from rest, spiral outwards then inwards to scan a circular image field, returning to its initial resting state. This trajectory and timing should be exactly repeated for each image frame for consistent undistorted images. ii) Secondly, exogenous disturbances to the system are on a much slower timescale than the periodic trajectory. At video rates, the period of each trajectory is on the order of tens of milliseconds (e.g. 16ms). Temperature and structural stress changes during operation are typically on the order of seconds. Thus, the system disturbance is slower than the operating timescale by 50x or more.

These properties make learning-type control methods suitable for our problem. The three main classes of learning controllers are briefly summarized. Repetitive Control is applied to track periodic references or to reject periodic exogenous disturbances [77]. Repetitive control is a continuous-operation controller, where a time-delay block within the controller acts as the internal model capable of generating arbitrary periodic signals.

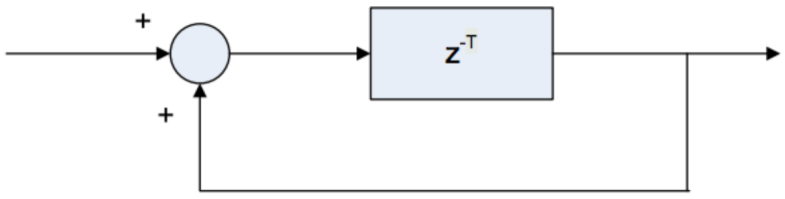


Figure 7.1. A time-delay block within the repetitive controller generates the internal model for arbitrary periodic signals.

Repetitive control is designed to handle periodic references and disturbances similar to the control types described later, but it requires continuous measurement, does not allow batch data processing and is typically formulated in the frequency domain [77]. These restrictions make repetitive control not the most suited for our periodic trajectory-tracking application compared to other learning-type controllers.

Iterative Learning Control is another class of controllers designed to track periodic trajectories. With iterative learning control, the problem is formulated in explicit periods $k = 1,2,3$ ... with fixed duration $T$. The control input at each iteration period is modified by the tracking error achieved in the previous iteration [77],

$$u(t,k) = u(t,k-1) + Ke(t,k-1) \tag{7.1}$$

$u(t,k)$ is the control input profile over $t$ for iteration $k$, $e(t,k-1)$ the error profile over $t$ for iteration $k-1$, and $K$ is the learning gain. Notice that: i) The control input at $t$ is informed by an error measure at exactly $t$ (instead of $t - \Delta t$) of the previous run. ii) Measurement of the error over the entire period $t \in [0,T]$ is required. The former observation explains why iterative learning control can outperform feedback controllers with inherent error-to-input delay if the disturbance is periodic or slowly changing. The latter observation means that iterative learning control can only be applied where continuous measurement or estimation of the tracking error is available.

With the scanning fiber endoscope, recent introduction of piezoelectric self-sensing allows for continuous observation of scan deflection. However, the quality of the measurement signal is dependent on accurate tuning or balancing of the sensing circuit, which can be difficult to achieve [38], [61]. In Adaptive FeedForward Control, this work tackled circuit bridge imbalance by modeling the imperfection. In this chapter, this dissertation will explore another control strategy (run-to-run) that relaxes the requirement for continuous measurements while still regulating the error over iterations.

Run-to-run control is a learning control class that can utilize sparse or non-continuous sampling of the plant output or states, to iteratively improve upon the control input. Generally, a linear (in parameters) regression model is used to describe the plant [77], [92], [93]:

$$z(k) = Av(k) + b(k) + \varepsilon \tag{7.2}$$

$z(k) \in \mathbb{R}^m$ is a vector of system measurements, either direct (e.g. sparse output measurements during a run) or indirect (e.g. output-measurement-derived quality metrics). $v(k) \in \mathbb{R}^n$ is a vector of input parameters. The control input $u(t)$ is typically a time-profile signal, but it is finitely parameterized by $v(k)$ e.g. a switching signal is defined by a set of amplitudes and transition times. $A \in \mathbb{R}^{mxn}$ is a matrix relating the input parameters to the output metrics, $b(k) \in \mathbb{R}^m$ a vector describing disturbances or drifts to the system that the input should compensate for run-to-run. $\varepsilon \in \mathbb{R}^m$ denotes the random within-run disturbances that run-to-run control typically cannot reject.

The most basic run-to-run controllers attempt to estimate $b(k)$ to give the input that will achieve the desired output profile $z^*(k)$. The Exponentially Weighted Moving Average (EWMA) filter method iteratively estimates:

$$b(k) = \lambda[z(k-1) - Av(k-1)] + (1-\lambda)b(k-1) \tag{7.3}$$

To calculate the control parameters (and consequently the control input) for each iteration:

$$v(k) = A^{-1}[z^*(k) - b(k)] \tag{7.4}$$

An improvement to EWMA relaxes the assumption that matrix $A$ is fixed, and uses adaptive control methods to iteratively estimate both $A(k)$ and $b(k)$ [92]:

$$K(k) = P(k-1)\varphi(k)[\lambda + \varphi^T(k)P(k-1)\varphi(k)]^{-1} \tag{7.5}$$

$$P(k) = \frac{[I - K(k)\varphi^T(k)]P(k-1)}{\lambda} \tag{7.6}$$

$$\theta(k) = \theta(k-1) + K(k)[z(k) - \varphi^T(k)\theta(k-1)] \tag{7.7}$$

$\theta(k) = [A(k) \quad b(k)]^T$ is the vector of the current estimate of $A(k)$ and $b(k)$. $\varphi(k) = [v(k) \quad 1]^T$ is the current regressor vector such that $z(k) = \varphi^T(k)\theta(k)$.

Another approach to run-to-run control is to treat the periodic tracking problem as an iterative optimization procedure, termed run-to-run optimization in this paper. In essence, each period or run represents an empirical integration of the system equations that can produce measurements of e.g. the state paths, terminal cost and objective function. At the conclusion of each run, the control effort can be updated using these measurements and by applying techniques from numerical optimization with the goal of converging to the optimal cost value.

Run-to-run optimization as defined above is a broad category that can be further classified based on how the optimization updates are implemented [94]. Model-explicit optimization uses a model of the system dynamics to compute the local gradient based on current measurements [94], [95]. In [96], a nominal model of a chemical process was used together with continuous measurements to approximate the gradient and direction of improvement to optimize production. Model-explicit optimization has a number of drawbacks including requirement for reasonably accurate model and high computational cost in calculating optimal policy [94].

In contrast, model-implicit optimization schemes do not rely on model-based gradients to compute the next-iteration control inputs. In general, the input is parameterized by a lower dimension vector $\pi$, such that the control input is a function of time and the parameterization values $\pi$: $u(\pi, t)$. A simple model-implicit approach, termed evolutionary optimization [94], [97] sequentially perturbs $\pi$ while registering the change in a performance index denoted here as $J$, in order to empirically determine the local gradient and hence the direction of improvement.

Further, if we parameterize or define measures $I$ of the system response, such that the output is a function of time and the parameterization values $I$: $y(I, t)$, then the cost function or performance index of the system is also a function of this parameterization: $J(I)$. The problem statement is then:

$$\min_{\pi}\{J(I)\}$$

$$such\ that: y(I,t) = \mathcal{H}\{u(\pi,t)\} \tag{7.8}$$

$u(\pi, t)$ and $y(I, t)$ may also need to satisfy various constraints, and $\mathcal{H}\{\}$ encapsulates the plant dynamics. $(\pi^*, I^*)$ represents the optimal point. Thus, there is a mapping $\mathcal{M}$ between the input parameters $\pi$ and output parameters $I$:

$$I = \mathcal{M}(\pi) \tag{7.9}$$

In [94], [95] it is suggested that the parameterization $I$ be chosen as measurement-constructs related to the necessary conditions for optimality. In [97] $I$ is chosen as parameters with target values that are necessary for optimality; e.g. $I$ as the terminal values for output levels, which are constrained to be 0 at $t_{final}$ for an optimal solution. In addition, the mapping $\mathcal{M}$ was linearized about the operating point, and a feedback-iterative update law was proposed:

$$\pi(k) = \pi(k-1) + G[I(k-1) - I^*] \tag{7.10}$$

At each run $k = 1,2,3 \ldots$ the input parameterization is updated by the measurement-derived metrics $I$ of the previous run. In [97], [98] a run-to-run algorithm of the form in Equation 7.10 was used to optimize insulin dosages for diabetic patients.

There are a number of limitations with the run-to-run optimization implementations previously reported, but inspired by these investigations this work will formulate a run-to-run optimization method more applicable to the Scanning Fiber control. The drawbacks of the model-explicit run-to-run optimization [96] include need for continuous measurement and intensive computation. The optimality-condition parameterization approach in [95], [95], [97] is instructive, but many assumptions and simplifications e.g. regulating only the terminal constraints or assuming nearly linear mapping $\mathcal{M}$, are required for practical implementation. Furthermore, most of the theory was developed for chemical or biological process control, where the dynamics of the system are slower and the control inputs are usually parameterized by arcs and transition times [97]. In the present application, we are dealing with a resonant mechanical system at the micro- to millisecond timescales, and we wish to track or scan arbitrary trajectories. In the next section, this dissertation will present a new run-to-run optimization control tailored for periodic feedforward systems using exact inversion.

## 7.2 Run-to-Run Optimization within Exact Inverse Framework

This section will detail a novel formulation of run-to-run control within the context of exact inversion, and prove the convexity of the formulation to guarantee convergence to a global performance optimum. Run-to-run optimization implementations usually need to be tailored to the specific application; this work presents a run-to-run optimization formulation designed for the Scanning Fiber Endoscope that should be applicable to many similar mechanical scan-tracking problems.

As typified in [92], [93], [96], [98], practical implementations of run-to-run optimization are usually modified or tuned (e.g. model simplification, selection or interpretation of output parameters, and heuristics for nominal solutions) to specific applications – in these examples anticoagulant dosing, polysilicon etching, thermal processing and insulin dosing respectively. This is in contrast to feedback or PID controllers that are more readily applied to a broad range

of problems. One explanation is that because run-to-run optimization operates on a reduced set of parameters, much freedom is available to the control system designer to specify the input parameterization $\pi$ and the sparse output measures $I$.

### 7.2.1 *Problem Formulation*

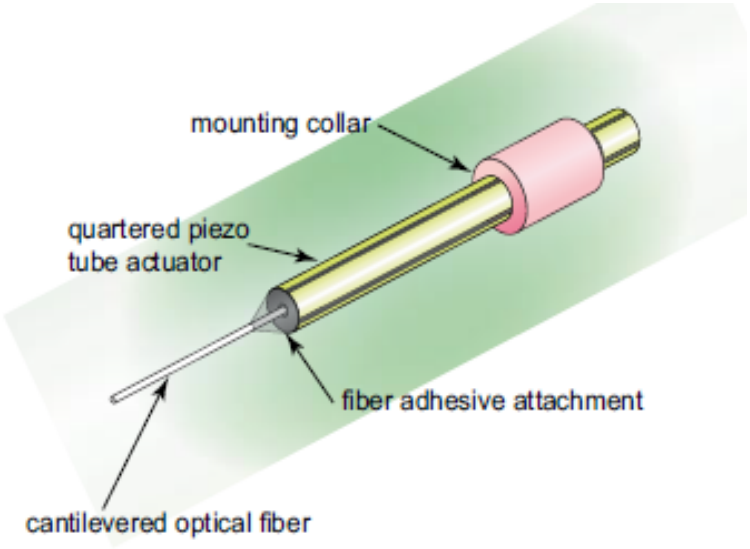


Figure 7.2. The SFE scan engine consisting of a piezoelectric-tube and a cantilevered optical fiber [1].

The electromechanical system to be controlled is the Scanning Fiber Endoscope scan engine. Specifically, the goal is to precisely control the trajectory of the optical fiber tip over time, such that the laser beam emanating from the fiber tip is accurately steered to capture images at video rates (30-60fps). The transverse deflections of the piezoelectric-tube plus optical fiber structure span a 2-dimensional space. In [27], the 2-dimensional scans were shown to be decomposable into two closely-linear, orthogonal axes or vibration systems called the Eigendirections. In Adaptive FeedForward Control this work presented a piezoelectric self-sensing method where the mode dynamics of the structure along each eigendirection could be identified.

To achieve large structural deflection (and hence field-of-view), the scan engine is actuated close to its 1st mode resonant frequency, and the damping of the structure is minimized (high Q). Given such operating conditions, the contributions of the higher-order modes may be discounted.

Then, from the system identification methods demonstrated in Adaptive FeedForward Control, we are able to empirically isolate a transfer function for the 1st mode dynamics:

$$Y(s) = G(s)U(s) \tag{7.11}$$

Given a periodic desired trajectory $y_d(t)$ or $Y_d(s)$, exact inversion was used in Adaptive FeedForward Control, to achieve tracking with mean error of 1-2% of maximum amplitude. With exact inversion, the control input is directly calculated using the identified system transfer function:

$$U_{ff}(s) = G^{-1}(s)Y_d(s) \tag{7.12}$$

In the previous adaptive feedforward controller developed, at each controller update the system transfer function $G(s)$ was re-identified and the exact inverse input $u_{ff}(t)$ re-calculated. The newer contribution of this chapter is a run-to-run optimization method that will instead iteratively refine $G(s)$ and $u_{ff}(t)$ to converge to improved tracking accuracy.

### 7.2.2 *Controller Derivation*

Trajectory error – modeling error relationship

Since the measureable variable is the directly related system output or the achieved trajectory, we begin by tying the trajectory error to the modeling error, which is important when applying system inversion.

Let the true system be defined as:

$$G_0(s): U(s) \rightarrow Y(s)$$

$$Y(s) = G_0(s)U(s) \tag{7.13}$$

$U(s)$ the input, $Y(s)$ the output, and $G_0(s)$ true plant.

Consider the most general desired output trajectory $y(t) = \delta(t)$ (a desired trajectory may be discretely approximated by a pulse train or a sequence of varying-amplitude impulses). The feedforward input corresponding to the unit impulse is:

$$G_0(s): u_{ff0}(t) \rightarrow \delta(t)$$

$$G_0(s): U_{ff0}(s) \rightarrow 1$$
$$1 = G_0(s)U_{ff0}(s)$$
$$U_{ff0}(s) = G_0^{-1}(s) \tag{7.14}$$

$u_{ff0}(t)$ the feedforward input.

Introduce a modeling error when calculating exact inverse input:

$$U_{ffe}(s) = G_0^{-1}(s) + \Delta G(s) \tag{7.15}$$

$\Delta G(s)$ the error in modeling the system inverse, $U_{ffe}(s)$ the error-contaminated feedforward input.

The achieved trajectory $y_e(t)$ using the error-contaminated control input:

$$G_0(s): U_{ffe}(s) \rightarrow Y_e(s)$$
$$\begin{aligned} Y_e(s) &= [G_0^{-1}(s) + \Delta G(s)]G_0(s) \\ &= 1 + \Delta G(s)G_0(s) \\ &\equiv 1 + G_e(s) \\ y_e(t) &= \mathcal{L}^{-1}\{1 + G_e(s)\} \\ &= \delta(t) + g_e(t) \end{aligned} \tag{7.16}$$

The trajectory error is $g_e(t)$, defined as $G_e(s) \equiv G_0(s)\Delta G(s)$, i.e. the response of the true system to a 'spurious input' $\Delta G(s)$ due to modeling error.

Interpreting system energy

Next, this work proposes a unique parameterization of the system output by estimating the total system mechanical energy. This sparse mapping is then applied for run-to-run optimization and is shown to produce a convex cost surface.

Interpret the plant as a system of particles with total energy given by the sum of potential and kinetic energies. Given some state-space realization describing the trajectory:

$$y(t) = Ce^{At}\boldsymbol{x}(0) + \int_0^t Ce^{A(t-\tau)}Bu(\tau)d\tau + Du(t) \tag{7.17}$$

Where the states $\boldsymbol{x}(t)$ represent the displacement and velocities of the particles. Consider $t \geq 0^+$ where $u_{ffe}(t) = 0$ [see Note 1],

Output:

$$y_e(t) = g_e(t) = Ce^{At}\boldsymbol{x}(0^+) \tag{7.18}$$

Displacements vector:

$$\boldsymbol{d}(t) = C_d e^{At}\boldsymbol{x}(0^+) \tag{7.19}$$

Velocities vector:

$$\boldsymbol{v}(t) = \dot{\boldsymbol{d}}(t) = C_d A e^{At}\boldsymbol{x}(0^+) \equiv C_v e^{At}\boldsymbol{x}(0^+) \tag{7.20}$$

Energy:

$$E_e(t) = K[e^{At}\boldsymbol{x}(0^+)].^2 + M[e^{At}\boldsymbol{x}(0^+)].^2 \tag{7.21}$$

$K$, $M$ are some constants related to the stiffness and mass vectors, $[\ldots].^2$ represents element-wise squaring.

Note 1:

For systems with no zeros, from Equation 7.15, errors in estimating the pole positions gives $\Delta G(s) = \mathrm{P}(s)$, a polynomial in $s$, resulting in $u_{ffe}(t) = 0 \mid t \geq 0^+$. This is the case considered further.

For more general systems consider that with stable inversion $u_{ffe}(t) \to 0, t \to \infty$ or $u_{ffe}(t) \cong 0 \mid t \geq t_f$, then the approximation that the input is zero can be used after $t \geq t_f$.

Note that this analysis only considers amplitude- and time-bounded *periodic* desired trajectories and stable plants such that $|y(t)| \leq M;\ y(t) = 0|\ t > t_{bound};\ y(t) = y\big(t + T_{period}\big), T_{period} > t_{bound};\ u_{ffe}(t) \to 0 | t \to t_{bound}$.

Modeling error – residual energy relationship produces convex problem

With the residual energy measure given by Equation 7.21, we now tie that error measure to the modeling error and show that the residual-energy versus model-error problem is convex.

Define a measure of modeling error with the integral:

$$\int_{-\infty}^{\infty} |G_e(f)|^2 df \tag{7.22}$$

We can relate modeling error to time-domain response using Parseval's theorem:

$$\int_{-\infty}^{\infty} |G_e(f)|^2 df = \int_{-\infty}^{\infty} |g_e(t)|^2 dt \cong \int_{0^+}^{\infty} g_e(t)^2 dt \tag{7.23}$$

$g_e(t)$ is real-valued and is the causal response to $u_{ffe}(t)$ [Note 1].

From Equation 7.20,

$$\int_{0^+}^{\infty} g_e(t)^2 dt = \int_{0^+}^{\infty} [C e^{At} \boldsymbol{x}(0^+)]^2 dt \tag{7.24}$$

Notice that in Equation 7.21, energy $E_e(t)$ is a convex function of $\boldsymbol{x}(0^+)$, optimal point at 0. ($e^{At}$ non-varying for a given $G_0(s).$) In Equation 7.24, modeling error is also a convex function of $\boldsymbol{x}(0^+)$, optimal point also at 0. Thus, if we solve for optimality using Equation 7.21, we will also find the *optimal point* for Equation 7.24.

In addition, Equation 7.21 is a convex function of $\boldsymbol{x}(0^+)$ at any time $t_S \geq 0^+$,

$$E_e(t_S) = K[e^{At_S} \boldsymbol{x}(0^+)].^2 + M[e^{At_S} \boldsymbol{x}(0^+)].^2 \tag{7.25}$$

Thus optimizing using a single sample of $\boldsymbol{x}(0^+)$ (per period of repeating trajectory) is sufficient to find the optimal input.

Defining suitable parameter space

Though Equation 7.24 and 7.25 are convex in $\boldsymbol{x}(0^+)$, we do not directly adjust the state $\boldsymbol{x}(0^+)$. Instead, we adjust the estimated system model $\Delta G(s)$ via a parameterization. This parameterization must be chosen such that convexity or quasi-convexity is preserved.

As an example, consider the case where $G_0^{-1}(s)$ is a polynomial in $s$. Then the model error $\Delta G(s) = a_0 + a_1 s + a_2 s^2 + ..$ is also a polynomial in $s$ parameterized by its coefficients.

Now,

$$U_{ffe}(s) = G_0^{-1}(s) + a_0 + a_1 s + a_2 s^2 + ..$$

$$u_{ffe}(t) = \mathcal{L}^{-1}\{G_0^{-1}(s)\} + a_0 \delta(t) + a_1 \dot{\delta}(t) + a_2 \ddot{\delta}(t) + .. \tag{7.26}$$

Solving for $\boldsymbol{x}(0^+)$,

$$\boldsymbol{x}(0^+) = Ce^{At}\boldsymbol{x}(0) + \int_0^{0^+} Ce^{A(t-\tau)}Bu_{ffe}(\tau)d\tau$$

$$= Ce^{At}\boldsymbol{x}(0) + \int_0^{0^+} Ce^{A(t-\tau)}B[\mathcal{L}^{-1}\{G_0^{-1}(s)\} + a_0\delta(\tau) + a_1\dot{\delta}(\tau) + a_2\ddot{\delta}(\tau)+..]d\tau$$

$$=Ce^{At}\boldsymbol{x}(0) + \int_0^{0^+} Ce^{A(t-\tau)}B[\mathcal{L}^{-1}\{G_0^{-1}(s)\}]d\tau + a_0\int_0^{0^+} Ce^{A(t-\tau)}B[\delta(\tau)]d\tau +$$

$$a_1\int_0^{0^+} Ce^{A(t-\tau)}B[\dot{\delta}(\tau)]d\tau + a_2\int_0^{0^+} Ce^{A(t-\tau)}B[\ddot{\delta}(\tau)]d\tau +.. \quad (7.27)$$

Equation 7.27 shows that $\boldsymbol{x}(0^+)$ is affine in the coefficients $a_0, a_1, a_2, ...$ Hence by composition principles, Equation 7.21, 7.24 and 7.25 are also convex in the coefficients $a_0, a_1, a_2, ...$

### 7.2.3 *Simulation Example*

In this section the proposed run-to-run optimization controller is simulated on a simple numerical example to illustrate the algorithm and controller performance.

Given a system representing a mass-spring-damper (or identified mode dynamics) of the form:

$$\dot{\boldsymbol{x}} = \begin{bmatrix} 0 & 1 \\ -2.25 & -0.03 \end{bmatrix}\begin{bmatrix} x \\ \dot{x} \end{bmatrix} + \begin{bmatrix} 0 \\ 0.1 \end{bmatrix}u$$

$$y = [1 \quad 0]\boldsymbol{x} \quad (7.28)$$

Figure 7.3a shows the desired amplitude- and time-bounded trajectory (black trace) where $y_d(t \geq 200) = 0$. Using the exact inverse method described in [87], the feedforward input is calculated. The Equation 7.28 system response is simulated for exact inversion without (blue trace) and with (red trace) modeling error $\Delta G$. Without modeling error, the achieved response matches the desired trajectory. With modeling error, the system response deviates from desired and there are residual oscillations after $t \geq 200$.

The system in Equation 7.28 represents a common case where displacement measurements (continuous or infrequent) of a mechanical system are available as the output. For such a system, the energy definition is straightforward e.g.:

$$E(t) = \boldsymbol{K}\boldsymbol{x}(t).^2 + \boldsymbol{M}\boldsymbol{x}(t).^2$$

$$E(t) = [2.25 \quad 0]\begin{bmatrix} x(t) \\ \dot{x}(t) \end{bmatrix}.^2 + [0 \quad 1]\begin{bmatrix} x(t) \\ \dot{x}(t) \end{bmatrix}.^2 \tag{7.29}$$

The constant vectors $\boldsymbol{K}$ and $\boldsymbol{M}$ represent the nominal stiffness and mass of the particle system in Equation 7.28. Figure 7.3b plots the defined energy measure $E(t)$ of the system over time for cases without (blue trace) and with (red trace) modeling error. The black vertical line delineates when the input $u(t)$ and desired trajectory $y_d(t)$ is 0 for $t \geq (t_f = 200)$. Without modeling error, the energy measure is 0 after $t \geq 200$ as expected, but with modeling error, the energy measure is nonzero for $t \geq 200$ but decays to 0 since the system is stable and dissipative.

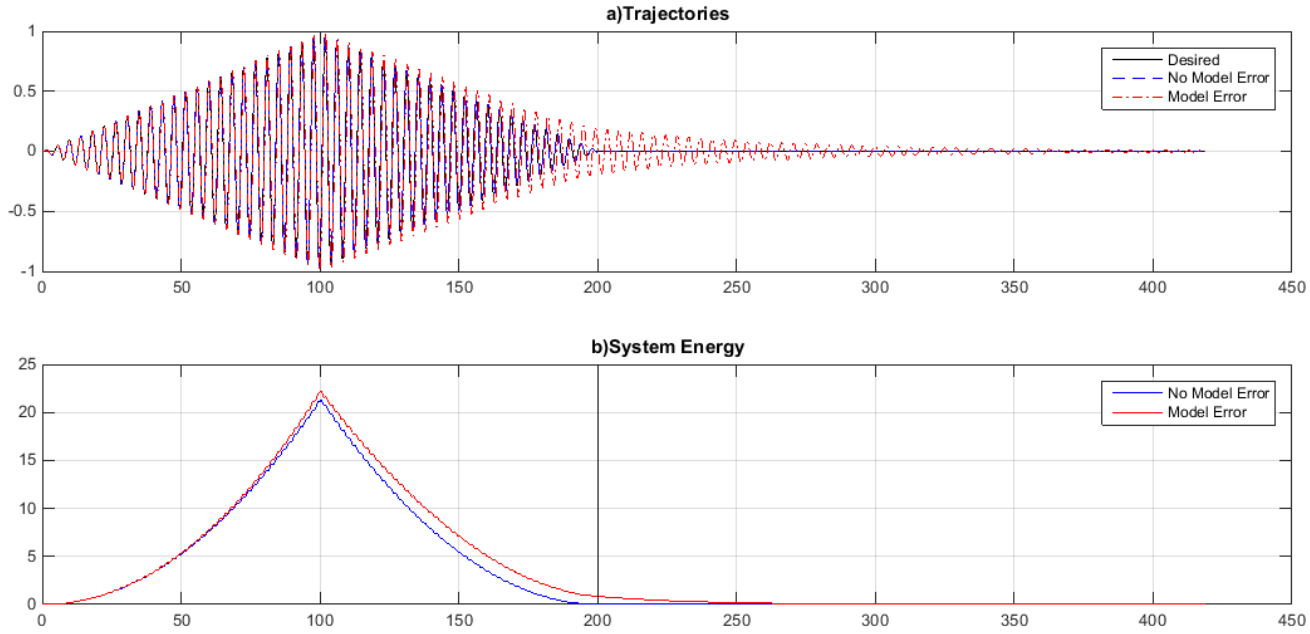


Figure 7.3. a) Desired and achieved trajectories for cases without and with modeling error. b) Energy measure over time for cases without and with modeling error.

The transfer function of the system in Equation 24 can be cast into the general form:

$$G(s) = \frac{1}{s^2 + as + b} \tag{7.30}$$

As discussed with Equation 7.27, we take $a$ and $b$ to be the parameterization for the input $u_{ff}(t)$ and predict the energy measure to be convex over this space. Figure 7.4 plots the energy measure $E(t)$ with a single sample at time $t = 200$ for different values of error in the model parameters $\Delta a$ and $\Delta b$. Figure 7.4 demonstrates that the energy surface is indeed convex with no local minima at e.g. large $\Delta a$ but negative $\Delta b$, and that the optimum point is at 0 modeling error

$\Delta a = \Delta b = 0$. This single-sample measurement convexity in Figure 7.4 means that by measuring the system just once per run we will be able to quantify the optimality of the current model and identify a global performance optimum.

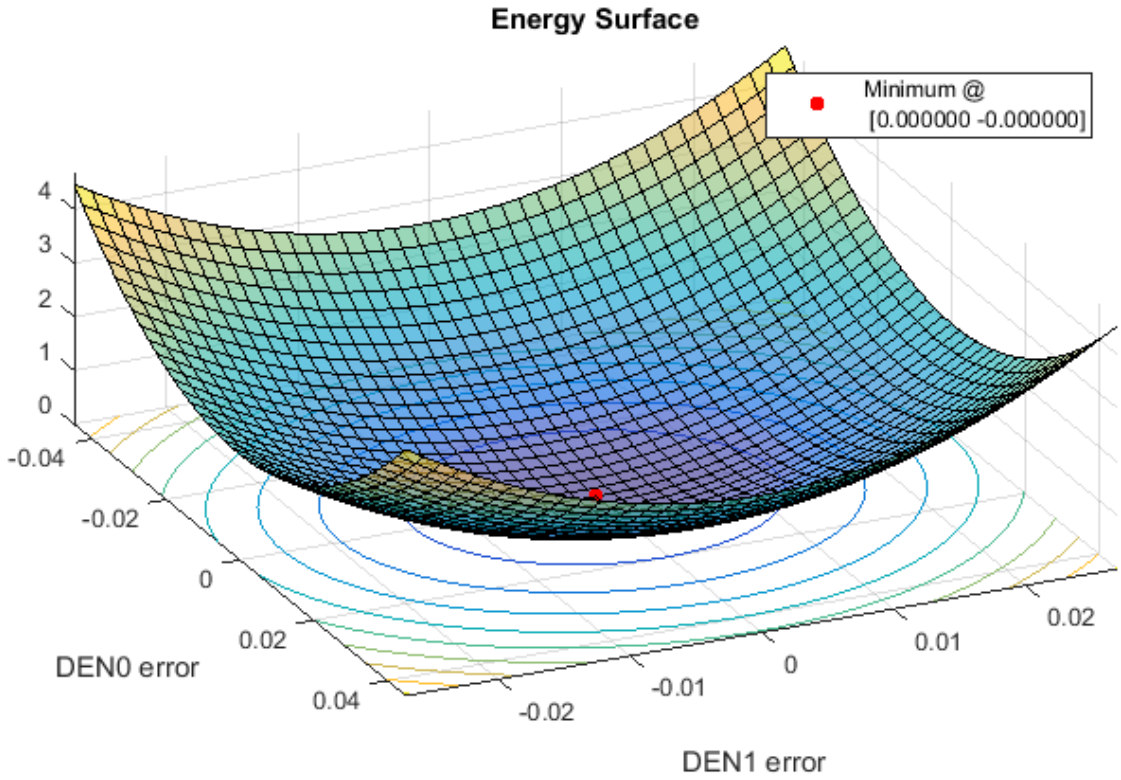


Figure 7.4. Convex energy surface E(t=200) parameterized by 2-variable modeling error.

Energy estimation error

Modeling error in terms of $\Delta a$ and $\Delta b$ is quantified and minimized via run-to-run optimization as illustrated in Figure 7.4. However, the estimate for system energy requires the constants $\boldsymbol{K}$ and $\boldsymbol{M}$ in Equation 25 to be inferred from the nominal plant. Expecting perfect knowledge of $\boldsymbol{K} = \boldsymbol{K}_0$ and $\boldsymbol{M} = \boldsymbol{M}_0$ would be unreasonable since if the true model were known, optimization would not be necessary. To explore the effect of energy estimation error, we simulate the energy surface with errors in $\boldsymbol{K}$ and $\boldsymbol{M}$. Figure 5a and 5b show the energy surface for 500% error in the constants $\boldsymbol{K}$ and $\boldsymbol{M}$ respectively. These simulations suggest that convexity and global optimality are maintained, but as the estimation error increases, the relative gradient on parts of the surface decreases, which may be interpreted as reduced certainty in the direction of improvement as the estimate deteriorates.

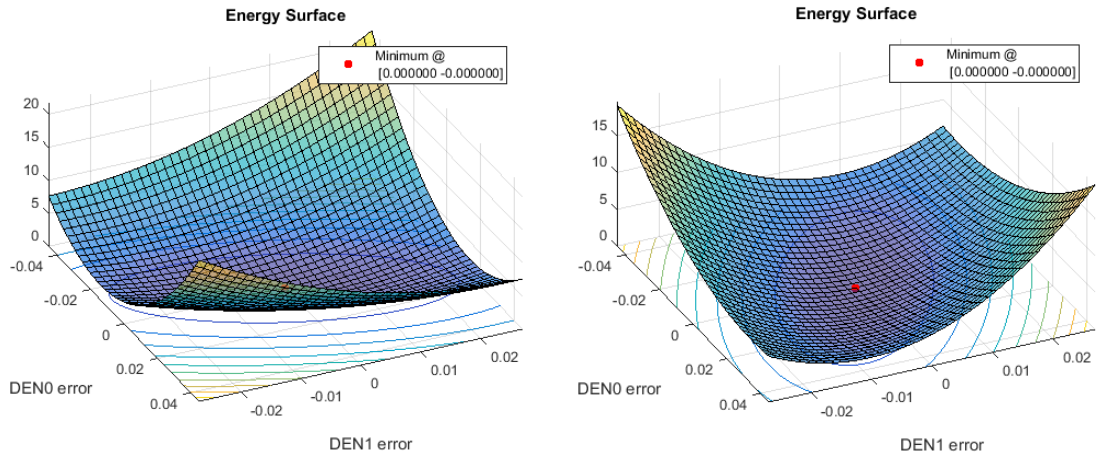


Figure 7.5. Convex energy surface for a) $\boldsymbol{K} = 5\boldsymbol{K}_0$ and $\boldsymbol{M} = \boldsymbol{M}_0$ b) $\boldsymbol{K} = \boldsymbol{K}_0$ and $\boldsymbol{M} = 5\boldsymbol{M}_0$

## 7.3 Experiment Methodology

This section reports an implementation and experimental validation of the proposed run-to-run optimization controller for a scan engine. Figure 7.6 shows the experimental setup. The scan engine, comprising a PZT-5A piezoelectric-tube of 0.45-mm outer diameter, 4-mm length, and a cantilevered optical fiber of 0.08-mm outer diameter and 2.27mm length is housed within a cylindrical electric heater with a thermistor for temperature sensing. The heater and thermistor are connected to a computer for active temperature control to investigate the effects of changing thermal operating conditions (e.g. within human body) on scan accuracy.

The scan engine is connected to a piezoelectric self-sensing circuit as described in Simultaneous Piezoelectric Self-Sensing, and to the computer for sensing and actuation. The use of the piezoelectric-tube as a miniature sensor maintains the small form-factor of the endoscope, and the run-to-run optimization algorithm introduced in this dissertation will be shown to maintain high scan accuracy over changing device temperature.

Finally, an optical position sensor (DL-20, OSI Optoelectronics) tracks the laser spot scanned by the optical fiber to provide direct measurements of the optical fiber deflections. The optical sensor data is used for verification and is not part of the control system. Data acquisition, temperature control and run-to-run optimization control were all implemented in LabVIEW code.

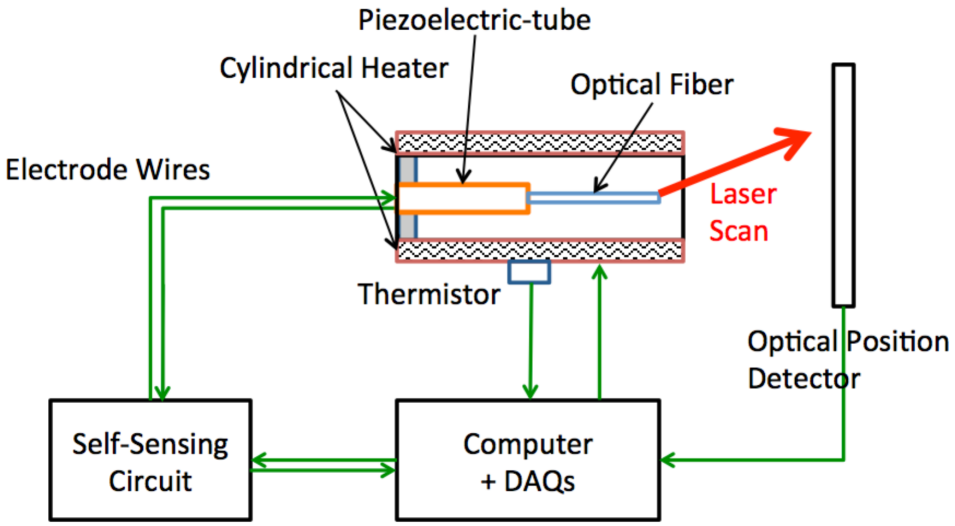


Figure 7.6. Run-to-run controller under changing temperature experimental setup.

The desired scan trajectory along Eigendirection 1, $r_1(t)$, is a ramping and collapsing (triangle-modulated) sinusoid waveform with scan frequency at $\omega_0 = 11.315kHz$ to operate close to the 1st mode mechanical resonance:

$$r_1(t) = \begin{cases} tsin(\omega_0 t), & 0 \le t < 90T_0 \\ A_0 - tsin(w_0 t), & 90T_0 \le t < 180T_0 \\ 0, & 180T_0 \le t < 200T_0 \end{cases}$$

$$r_1(t + 200T_0) = r_1(t) \tag{7.31}$$

To capture images, a 2D scan is spanned by actuation in both Eigendirection 1, $r_1(t)$ and Eigendirection 2, $r_2(t)$. The trajectory $r_2(t)$ is exactly the same as $r_1(t)$ except that $\cos(\omega_0 t)$ replaces the sinusoid. $T_0$ is the period corresponding to $\omega_0$ and $A_0$ is the maximum scan amplitude. $r(t)$ is periodic, with 180 imaging spirals and 20 resting spirals. The frame rate is 56fps, producing 360-pixel-diagonal circular images.

In this investigation, evolutionary optimization [94], [97] is applied to converge to the optimum point. Between each imaging frame, an energy estimate as exampled in Equation 7.29 is calculated for different perturbed model parameter values. Over time, a plot of the energy surface is constructed and the convex optimum is directly selected as the new control point.

Two experiments were performed. In Experiment 1, the goal was to demonstrate the new run-to-run controller fine-tuning or optimizing the scan accuracy, compared to the adaptive-feedforward control previously developed. At temperatures 30ºC, 40ºC and 50ºC, the adaptive-feedforward method was used to find an initial control input. Then, the run-to-run optimization was activated to converge to a better control point. The scan error and any improvements in accuracy were recorded. Five trials were run at each temperature: The adaptive-feedforward controller re-initializes during each trial, while the new run-to-run controller refines its output between each trial.

Experiment 2 was designed to demonstrate the run-to-run controller operating continuously to maintain scan accuracy across changing operating temperature. Starting with an initial control input at 30ºC the temperature was raised to 40ºC then to 50ºC, with the run-to-run controller constantly attempting to re-calibrate. Scan error with and without run-to-run optimization was recorded.

For quantifying the error of a 2-D circular scan, we separate the positional error into normalized radial and phase/tangential components. The squared-error time profile and mean-squared-error of an entire scan are recorded at different operating temperatures.

## 7.4 Results and Interpretation

Experiments 1 and 2 were conducted as detailed. Figure 7 shows an experimentally constructed energy surface as generated by the LabVIEW code. The predicted convex topology is experimentally verified. Also, the minimum point in Figure 7 is noticeably off-center, meaning that the optimization algorithm will converge to a new operating point to the lower right of the parameter space.

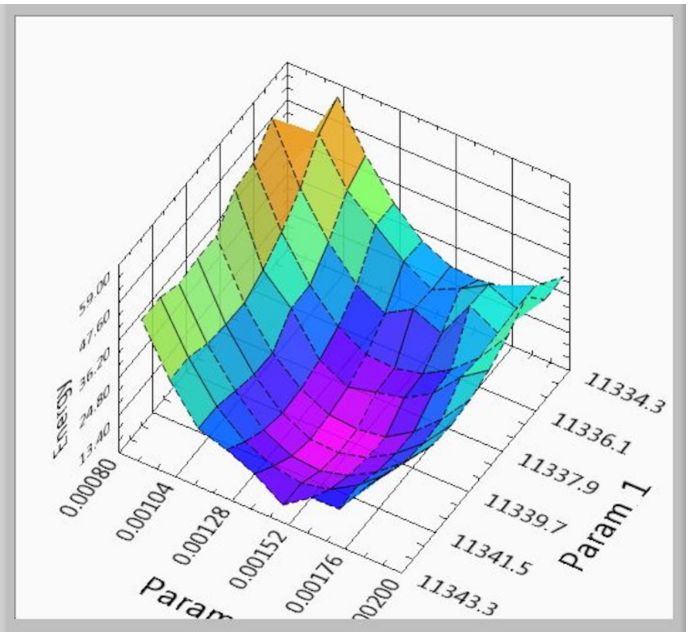


Figure 7.7. Experimentally constructed energy surface.

Experiment 1: Comparing New Run-to-Run Optimization versus Earlier Adaptive Feed-Forward Method.

At three different operating temperatures, the control input was first initialized by the adaptive feed-forward method. Then, run-to-run control was used to further optimize the control input. This procedure was repeated five times at each test temperature. At 50ºC, Figure 7.8a and Figure 7.8b show 2-D plots of the achieved scan trajectory with the adaptive feed-forward initialization, and then after run-to-run optimization respectively. Qualitatively there is improvement in tracking of the targeted 2-D trajectory. Figure 7.8c and Figure 7.8d show quantitatively the squared error in the radial and phase/tangential components. There is clearly a reduction in the radial error after run-to-run optimization at this operating temperature.

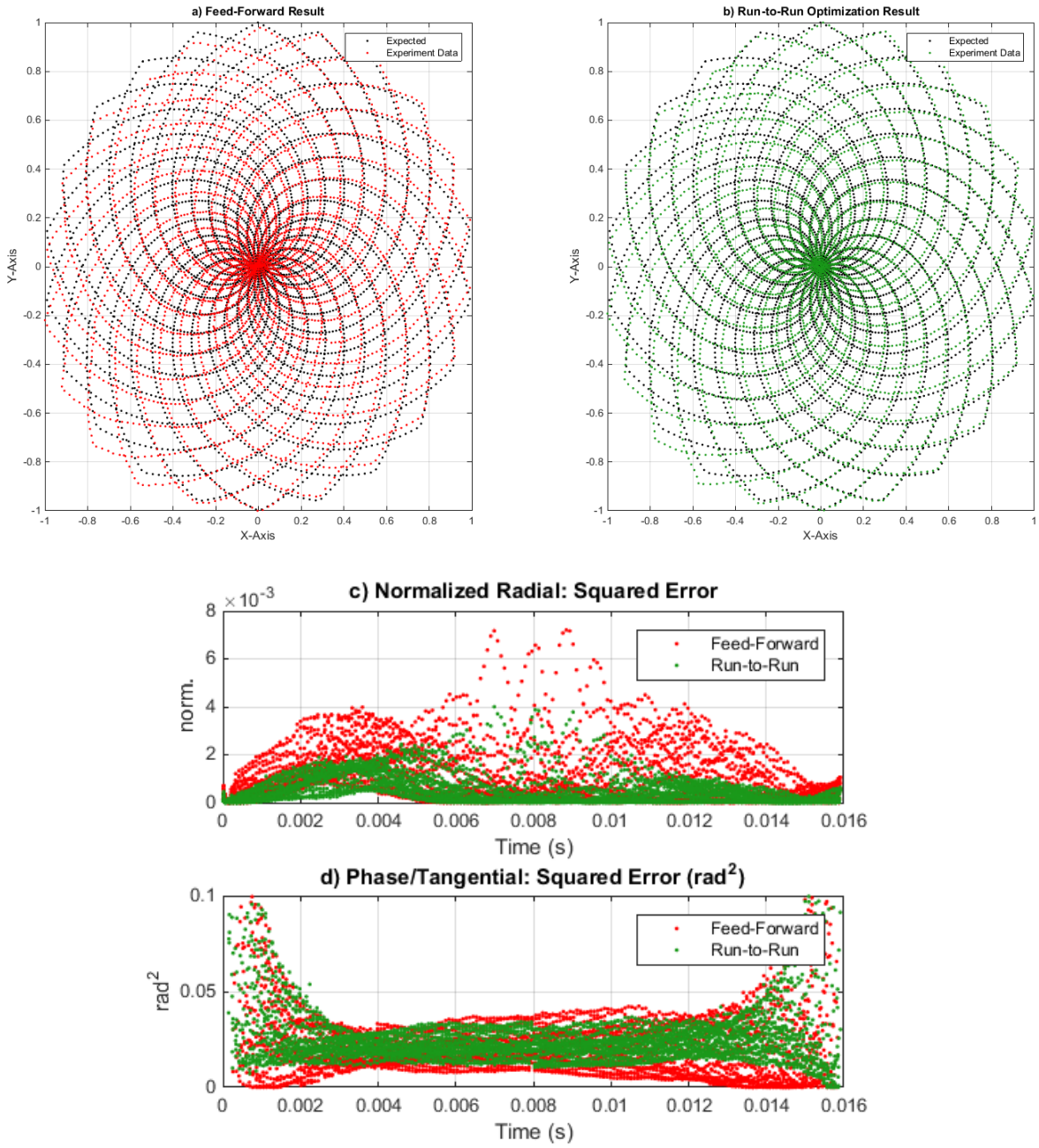


Figure 7.8. At 50ºC: a) 2-D scan result with feedforward control. b) 2-D scan result with run-to-run optimization. c) Normalized squared radial error compared between feed-forward and run-to-run result. d) Phase/tangential squared error compared between feed-forward and run-to-run result.

Figure 7.9 charts the radial and phase/tangential Mean Squared Error (MSE) achieved by the adaptive feedforward and the new run-to-run optimization approach, over changing operating

temperature. Figure 7.9 shows the range of accuracy over 5 trials and the average error of both control methods at each operating temperature. Figure 7.9 shows that run-to-run optimization detectably improves the scan accuracy beyond that of the earlier adaptive feed-forward approach.

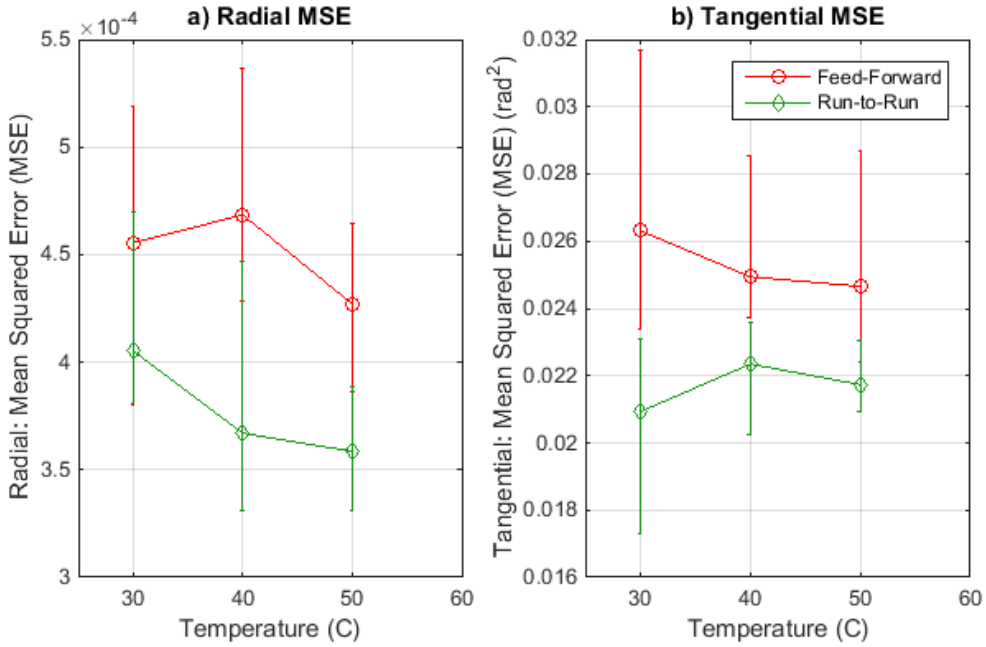


Figure 7.9. Radial and Phase/Tangential Mean Squared Error (MSE) over different operating temperatures, achieved by feedforward method versus run-to-run optimization.

Experiment 2: Performance of Run-to-Run Controller in Tracking Temperature Changes.

In the second experiment, the control input was only initialized at 30ºC. Then, just run-to-run optimization was used to maintain scan accuracy as the operating temperature was increased in steps to 40ºC and then to 50ºC. At 50ºC, Figure 7.10a and Figure 7.10b show 2-D plots of the achieved scan trajectory with open-loop control [27], and with run-to-run optimization respectively. Without any compensation, the trajectory does not track back to the center of the scan in Figure 7.10a, while run-to-run optimization maintains the full scan as in Figure 7.10b. Figure 7.10c and Figure 7.10d show quantitatively the squared error in the radial and phase/tangential components. There is much lower error using run-to-run optimization particularly at the start and end (related to 2-D center) of the scan.

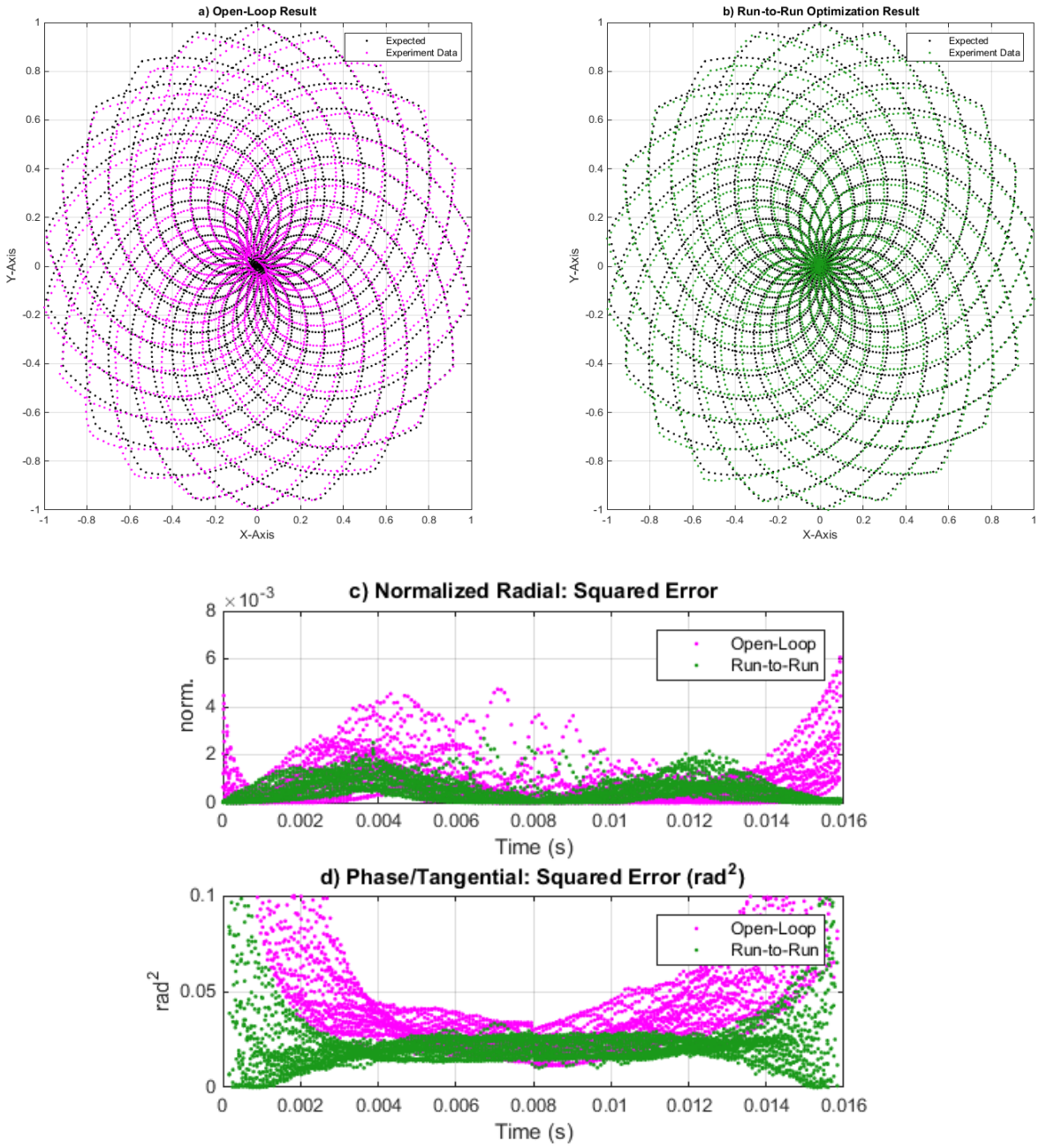


Figure 7.10. At 50ºC: a) 2-D scan result with open-loop control. b) 2-D scan result with run-to-run optimization. c) Normalized squared radial error compared between open-loop and run-to-run result. d) Phase/tangential squared error compared between open-loop and run-to-run result.

Figure 7.11 charts the radial and phase/tangential Mean Squared Error (MSE) achieved by open-loop control [27] and run-to-run optimization over changing operating temperature. In this experiment, the control input is not re-initialized at each temperature – the run-to-run controller

attempts to re-calibrate itself. Figure 7.11 clearly shows run-to-run optimization outperforming the de facto open loop controller [27] by continually updating its optimal point.

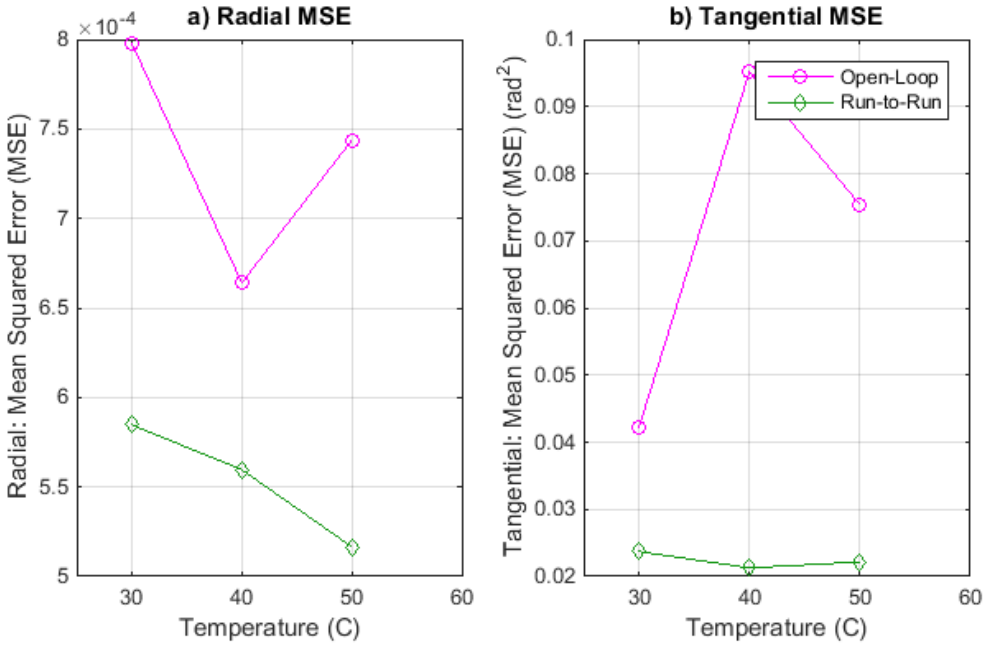


Figure 7.11. Radial and Phase/Tangential Mean Squared Error (MSE) over different operating temperatures, achieved by feedforward method versus run-to-run optimization.

Image Quality

To visually assess the achieved image quality, laser light was modulated through the optical fiber during each frame-scan to project target images as in Figure 7.12a. The projected images were recorded using a hand-held camera. At 50ºC, Figure 7.12b shows the distorted images using open loop control [27] initialized only at 30ºC. Figure 7.12c shows improved image quality at 50ºC with the adaptive controller introduced by this work previously in Adaptive FeedForward Control. Unintentional perspective distortion is present due to the hand-held camera not being centered above the scan, but qualitatively the line sections have become much straighter. Figure 7.12d shows the image quality further achieved by the run-to-run optimization controller presented in this chapter. With the run-to-run controller, the image accuracy is refined in the central regions and the controller is able to self-adjust to the +20ºC change in operating temperature.

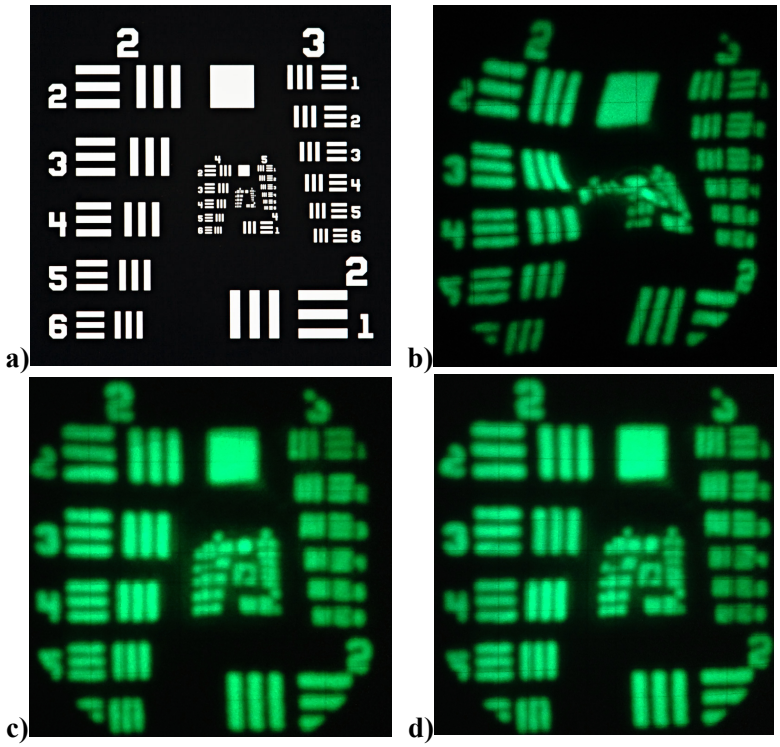


Figure 7.12. a) Target image to be laser-projected. b) Open-loop control result at 50ºC. c) Adaptive feedforward result at 50ºC. d) Run-to-run optimized result at 50ºC.

## 7.5 DISCUSSION

From the experimental results, we find that measurement noise manifests as non-smoothness in the empirically constructed energy estimate surface as seen in Figure 7.7. Figure 7.13 illustrates the effect of measurement noise with a simulation plot. Figure 7.13 shows that the convexity of the surface is maintained but jaggedness is introduced. A small level of uncertainty is also introduced to the optimum point. Reduction in accuracy is expected with increasing levels of measurement noise, but may be reduced by averaging over a number of samples or periods at the cost of slower convergence.

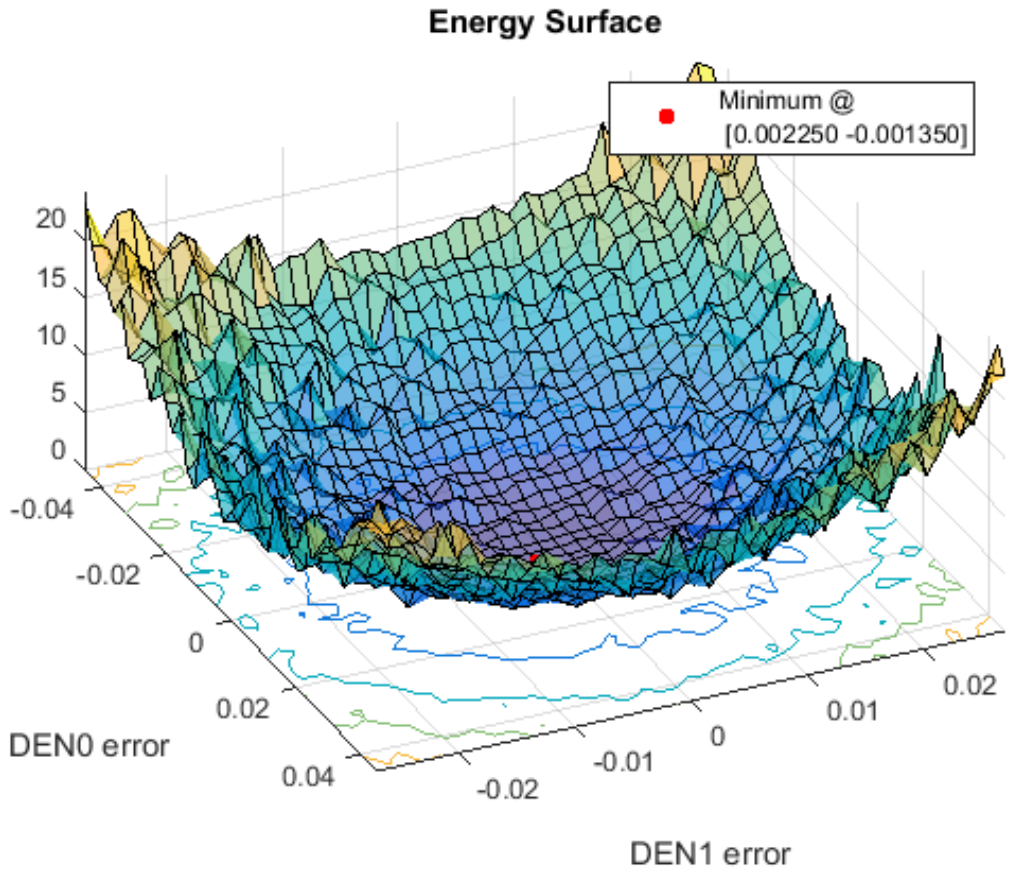


Figure 7.13. Simulation of energy surface with 1% amplitude measurement noise.

The optical position detector used to quantify scan accuracy was a dual lateral-effect detector that produces two analog voltage signals corresponding to the X- and Y- laser spot position on its square detector. The voltage response of the detector may not be fully linear across the field, thus the detector can introduce its own distortion to the measurement. In addition, uncleanness of the detector surface and multiple reflections of the laser beam can distort the data. In Figures 8a and 8b and Figures 10a and 10b, a smudging effect is observed on the top-left of the scan that is likely due to optical distortion instead of scan error; this may have artificially increased the recorded error quantifications. Improvements to the experimental setup may include pre-calibrating the optical position detector with known laser spot positions.

The run-to-run optimization implemented in this work requires measurement or estimation of the particle displacement $x(t)$ and velocity $\dot{x}(t)$ as in Equation 25. Since only displacement is directly measured, we approximate $\dot{x}(t)$ by taking the discrete central difference:

$$\hat{\dot{x}}(t) = \frac{x(t+\Delta t) - x(t-\Delta t)}{2\Delta t} \tag{7.32}$$

For the achieved experimental results this approximation is shown to be adequate. Thus theoretically only three displacement samples, $x(t + \Delta t)$, $x(t)$ and $x(t - \Delta t)$, are needed to estimate the displacement and velocity states per-period for run-to-run optimization.

In this reported implementation, 20 resting spirals follow each 180 imaging spirals (180:20, or 90% imaging duty cycle) as in Equation 27. This compares to 180:64 (74% imaging duty cycle*) for the de facto open-loop control in [27] and 180:36 (83% imaging duty cycle) for the adaptive-feedforward-only method previously developed in Adaptive FeedForward Control. Though the fiber resting time has been greatly reduced, it was not reduced to just three sample-times as theoretically possible with the new run-to-run formulation due to unmodeled higher-order modes affecting the energy estimate. Future work will investigate including higher-order vibration modes into the controller formulation.

*(These duty cycles are from experiments reported here. Duty cycles reported in [28] are for an older 5kHz scan engine design with 250 imaging spirals.)

Most run-to-run optimization formulations [94], [97], even application-tailored implementations [92], [98] do not guarantee convexity of the problem or global optimality. An advantage of the run-to-run optimization framework demonstrated in this work is the existence and convergence to a globally optimal performance-point.

However, a limitation with the proposed run-to-run optimization controller is the lack of gradient information from a single measurement. Instead, this investigation relies on evolutionary optimization [97], where multiple measurements with different input parameters are taken to empirically estimate the direction of improvement. For demonstration, this work brute-force constructed the entire energy surface and then move to the optimum point. This is a lengthy operation that takes up to 2s to converge to a new optimum because the entire 8x8 energy surface is explored for both Eigendirections. This run-to-run algorithm can be accelerated by e.g. finding

the local gradient using a 2x2 search, estimating a step size, and then moving to a new 2x2 gradient search. Nonetheless, the device is fully operational during the entire optimization duration since there is no need for e.g. a 40-millisecond probing signal as in the previously developed Adaptive FeedForward Controller.

## 7.6 SUMMARY

This chapter has presented a novel run-to-run optimization controller within an exact inverse framework, as a follow up to the adaptive feedforward controller introduced in the previous chapter. The run-to-run optimization controller was formulated to minimize an energy measure obtained from the simultaneous piezoelectric self-sensing signal. Experiments show the run-to-run controller outperforming the standard open loop control and adaptive feedforward control. The run-to-run optimization controller improved on the adaptive feedforward controller by removing the 40-ms system probing, replaced with an iterative control point re-optimization.

# Chapter 8. FURTHER CONTROL METHOD EXPLORATION

This work has introduced two control designs for the scanning fiber technology: an adaptive feedforward controller and a run-to-run optimization controller. Both of these online recalibration techniques were made possible by the new piezoelectric self-sensing modality developed earlier in this dissertation. Piezoelectric self-sensing enables additional classes of control methods to be applied to the scanning fiber technology. In this chapter, Iterative Learning Control (ILC) with the scanning fiber technology is reviewed and simulated, setting the stage for potential future investigations.

## 8.1 ITERATIVE LEARNING CONTROL (ILC)

In its most general form, learning-type control is a control strategy where the controller makes use of previous information to adjust its control signal. This definition has overlap with concepts of adaptive control. However, learning-type control is more focused on systems where the reference and/or disturbances are repeating in nature. A broad survey of learning-type control is given in [77] where the sub-fields iterative learning control (ILC), repetitive control (RC) and run-to-run (R2R) are detailed and unified mathematically. ILC is concerned with the tracking of a repeating trajectory with a finite period, under the assumption that the initial conditions of the system are reset at each period [76]. RC typically involves tracking or rejecting periodic signals in continuous operation. R2R is typically applied for processes where sparse feedback data is available e.g. semiconductor manufacturing, and the system attempts to achieve an output by varying a set of parameters [77].

ILC is concerned with systems of the form,

$$y_k(t) = P(q)u_k(t) + d(t), \;\; k = 1,2,3 \ldots \tag{8.1}$$

$u_k$ is the input, $y_k$ the output, $P(q)$ a proper rational function defining the plant, $d(t)$ is the repeating disturbance, and $k$ is the iteration number. In ILC, the repeating disturbance $d(t)$ is rejected using a learning algorithm that updates the input. Defining the tracking error,

$$e_k(t) = r(t) - y_k(t) \tag{8.2}$$

where $r(t)$ is the desired reference trajectory, a general form of the ILC algorithm is:

$$u_{k+1}(t) = Q(q)[u_k(t) + L(q)e_k(t)] \tag{8.3}$$

$Q(q)$ is usually called the Q-filter and $L(q)$ is usually called the learning function [76]. Note that in this work the the time shift of $e_k(t)$ used in [76] is combined into the $L(q)$ term to make Equation 8.3 more general.

An excellent property of the ILC is that the error will converge (in a noiseless system) to zero under very generous conditions:

$$e_k(t) \to 0, k \to \infty$$

$$if \quad ||Q(z)[1 - L(z)P(z)|| < 1, \ \ and \ \ Q(z) = 1 \tag{8.4}$$

These are sufficient but not necessary conditions. In addition, this convergence may not be monotonic i.e. the convergence may involve large transients. The conditions for monotonic convergence are discussed in [76]. If input or measurement noise is present, the error will converge to a locus around zero-error, with the size of the locus being a continuous function of the noise magnitude [89].

Since to converge to perfect tracking $Q(z)$ must be 1, the control designer is left with the choice of the learning function $L(q)$. Setting $Q(z) = 1$ is common, but other functions can be selected to trade off tracking performance with robustness [76]. Good robustness can still be achieved with $Q(z) = 1$.

The learning function $L(q)$ can be a simple proportional gain, PID or related [76], [99], [100], a robust or optimal formulation [76], [100], [101], or an inverse of the expected system dynamics [89], [102]. Experiments have shown that all the above approaches when correctly designed will converge very well, though at varying rates. Simple PD schemes are the safest, but a good guess of the system inverse will make the ILC converge very quickly to the desired trajectory [100].

### 8.1.1 *Proposed ILC Analysis*

This work proposes the ILC design,

$$Q(\omega) = 1 \tag{8.5}$$

$$L(\omega) = \rho(\omega)P^{\dagger}(\omega) \tag{8.6}$$

The functions are described in the frequency domain, $P^{\dagger}(\omega)$ is a pseudo-inverse of the estimated system transfer function $\hat{P}(\omega)$, and $\rho(\omega)$ is a gain function used to ensure convergence to the desired tracking.

The proposed form of the pseudo-inverse is,

$$P^{\dagger}(\omega) \equiv [\alpha + P(\omega)^{*}P(\omega)]^{-1}P(\omega)^{*} \tag{8.7}$$

$\alpha$ is a parameter that can be tuned. Figure 8.1 visualizes the magnitude and phase of the pseudo-inverse transfer function. Note that there is no phase difference with $P^{\dagger}(\omega)$ compared to the exact inverse $P^{-1}(\omega)$. Also note that as $\alpha$ decreases, the pseudo-inverse converges to the exact inverse, but there is still a magnitude roll-off at higher frequencies.

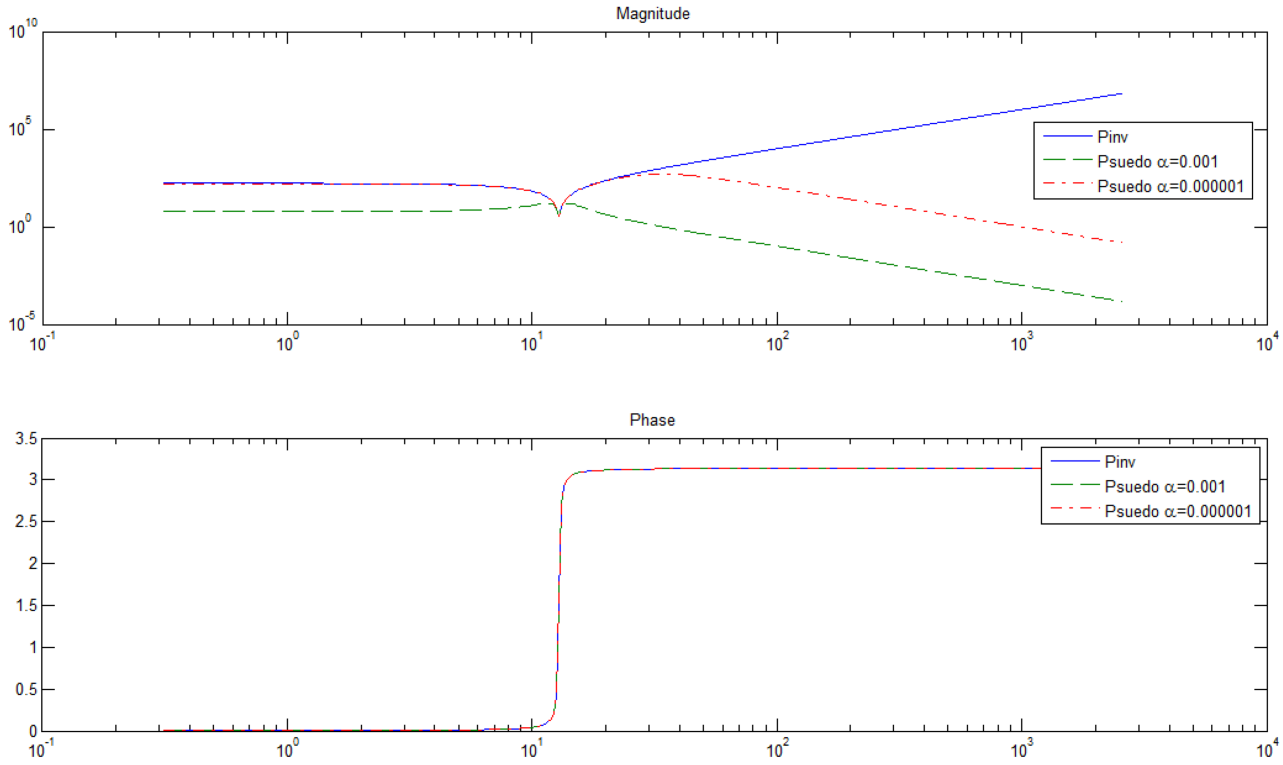


Figure 8.1. Magnitude and phase of the transfer function using exact inverse, pseudo-inverse with α=0.001, and pseudo-inverse with α=0.000001.

Restating the conditions for convergence in Equation 8.4 as:

$$\|Q(\omega)[1 - L(\omega)P(\omega)]\| < 1 \tag{8.8}$$

Substituting in Equation 8.6,

$$\left\|1 - \rho(\omega)P^{\dagger}(\omega)P(\omega)\right\| < 1 \tag{8.9}$$

Let $\rho(\omega) = 1$, notice that if $P^{\dagger}(\omega) = P^{-1}(\omega)$ at certain $\omega$ then Equation 8.9 is minimum at those frequencies i.e. convergence to zero tracking error is fast at those $\omega$ [76]. When $P^{\dagger}(\omega)$ rolls off at high frequencies, $\rho(\omega)P^{\dagger}(\omega)P(\omega) \to 0$, and Equation 8.9 approaches a maximum at 1. This can be interpreted as learning much more slowly at higher frequencies, where undesired high-frequency disturbances are rejected. This form of pseudo-inverse is similar to that presented by Ghost et al. [103]. This pseudo-inverse can also be interpreted as the result of minimizing a frequency-dependent cost function similar to [104], [105]:

$$J(u) = \int_{-\infty}^{\infty}\{u^{*}(j\omega)R(j\omega)u(j\omega) + [y(j\omega) - r(j\omega)]^{*}Q(j\omega)[y(j\omega) - r(j\omega)]\}\,d\omega \tag{8.10}$$

Where the minimizing solution has the familiar form:

$$u_{opt}(j\omega) = [R(j\omega) + P^{*}(j\omega)Q(j\omega)P(j\omega)]^{-1}P^{*}(j\omega)Q(j\omega)r(j\omega) \tag{8.11}$$

comparable to Equation 8.7 if $R = \alpha$ and $Q = 1$.

A frequency-dependent learning function $\rho(\omega)$ is also proposed. The form the learning algorithm, Equations 8.3, 8.5 and 8.6, is:

$$u_{k+1}(t) = u_{k}(t) + \rho(\omega)P^{\dagger}(\omega)e_{k}(t) \tag{8.12}$$

Here, the concepts of the pseudo-inverse [103] and the iteration-gain function [89] are combined. If $P^{\dagger}(\omega)$ is exactly the inverse of the true system, then convergence is achieved in one iteration. However, if $P^{\dagger}(\omega)$ is not exactly the inverse (modeling error), the controller can become unstable. Tien et al. derived the conditions for convergence to desired tracking for the control law [89], taking into account modeling error. If $P_0(\omega)$ is the true system and $\hat{P}(\omega)$ is the estimated system, the modeling error is defined as:

$$\Delta_P(\omega) = \frac{P_0(\omega)}{\hat{P}(\omega)} = \frac{a_0(\omega)e^{j\theta_0(\omega)}}{\hat{a}(\omega)e^{j\hat{\theta}(\omega)}} = \Delta_a(\omega)e^{j\Delta_\theta(\omega)} \tag{8.13}$$

$\Delta_a(\omega)$ is the magnitude modeling error, and $\Delta_\theta(\omega)$ is the phase modeling error.

The iterations are guaranteed to converge if the magnitude of the phase variation is less than $\frac{\pi}{2}$:

$$|\Delta_\theta(\omega)| < \pi/2 \tag{8.14}$$

And the iteration coefficient $\rho(\omega)$ is chosen as:

$$0 < \rho(\omega) < \frac{2\cos(\Delta_\theta(\omega))}{\Delta_a(\omega)} \tag{8.15}$$

Tien et al also showed that in the presence of measurement noise, the iterations are still guaranteed to converge if $\rho(\omega)$ is low enough and the number of iterations large enough [89]. $\rho(\omega)$ is used to ensure convergence in the presence of modeling error. The values of $\rho(\omega)$ can be chosen to trade off between robustness and aggressive convergence rates. $\rho(\omega)$ can also be a function of frequency to tailor the convergence rates at different $\omega$.

## 8.2 Proposed State Estimation Method

The iterative learning controller proposed in Proposed ILC Analysis requires continuous and direct measurement of the output to be controlled, as defined in the error signal in Equation 8.2. In this section a method for directly extracting the fiber displacement is proposed with the simultaneous piezoelectric self-sensing architecture, and the empirical modal representation identified from sensor readings presented earlier in this dissertation.

If the bridge circuit for simultaneous piezoelectric self-sensing is perfectly balanced, then the sensor output can be cast as a function of fiber displacement only:

$$y_{sense}(t) = P_{xy}(q)x_{fiber}(t) \tag{8.16}$$

Where $P_{xy}(q)$ is the transfer function from fiber displacement state $x_{fiber}(t)$ to the sensing output $y_{sense}(t)$. However, the bridge circuit is typically not balanced, so the sensor output is confounded by an unknown transfer function $P_{uy}(q)$ from input to output. For unbalanced bridge circuit case, Equation 8.16 should be expanded to,

$$y_{sense}(t) = P_{xy}(q)x_{fiber}(t) + P_{uy}(q)u(t) \tag{8.17}$$

Letting input-to-fiber-state transfer function be $P_{ux}(q)$, Equation 8.17 may be rewritten as,

$$y_{sense}(t) = P_{xy}(q)P_{ux}(q)u(t) + P_{uy}(q)u(t)$$

$$y_{sense}(t) = [P_{xy}(q)P_{ux}(q) + P_{uy}(q)]u(t) \tag{8.18}$$

$P_{xy}(q)$ represents the sensor dynamics, $P_{ux}(q)$ represents the resonant mechanical dynamics, while $P_{uy}(q)$ represents the feed-through.

Note that Equation 8.18 is the input-to-output transfer function that the system identification methods in Empirical Modal Representation extracts from the device under operation. Note also that if $P_{uy}(q)$ can be estimated in Equation 8.17, then the desired state $x_{fiber}(t)$ can be estimated from the output signal by subtracting out the contribution of $P_{uy}(q)$, assuming $P_{uy}(q)$ (which is dictated by electrical component values) to be time-invariant. Finally, the following assumptions are made: Only $P_{ux}(q)$ captures the resonant dynamics of the structure, while $P_{uy}(q)$ and $P_{xy}(q)$ have only non-resonant poles indicative of feedthrough or sensor low-pass filtering terms. Thus, by examining the eigenvalues of the identified transfer function from Equation 8.18, a method previously introduced in Model Order Reduction, $P_{ux}(q)$, $P_{uy}(q)$ and $P_{xy}(q)$, and $x_{fiber}(t)$ may be extracted.

## 8.3 Simulation and Experimental Exploration

In this section, a simulation analysis and experimental exploration for the proposed ILC approach is reported, setting the stage for future work.

### 8.3.1 *Simulation*

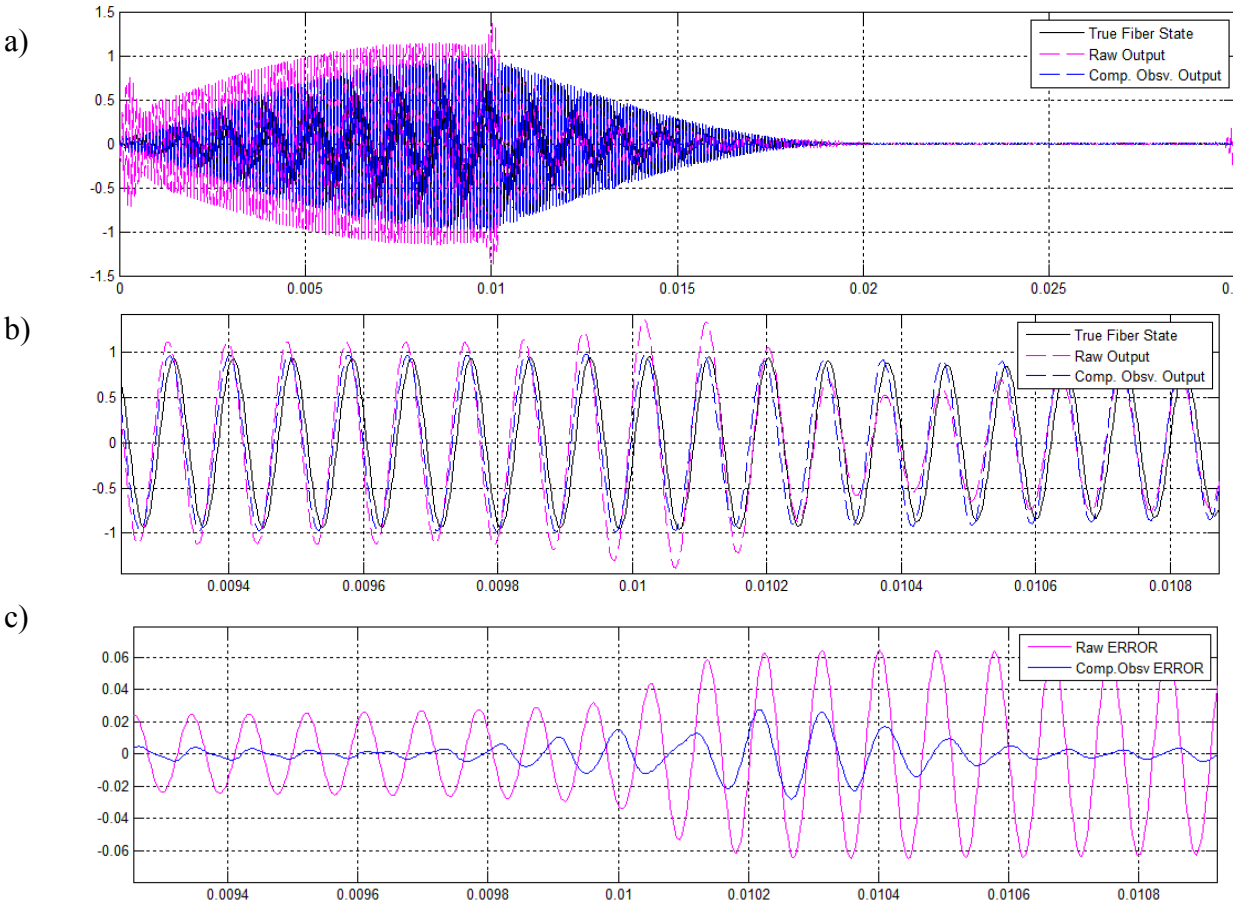


Figure 8.2. a) Simulation comparison between true fiber state (black), raw sensor output (magenta), and processed output (blue). b) Zoom-in of the comparison between true fiber state (black), raw sensor output (magenta) and processed output (blue). c) Comparison of error of raw output (magenta) and processed output (blue), with respect to true fiber state.

For the simulation analysis, the Circuit Equivalent Electromechanical Model was fitted to experimental data and assumed to be the true system for analyzing the state estimation algorithm.

Simulated input and output data from this model was used for system identification. The identified dynamics were then separated into resonant and time-invariant dynamics as previously discussed.

Figure 8.2 shows the simulation result of the proposed isolation method. The raw sensor output (magenta) does not match the true fiber state at all, with spurious amplitudes and phase, and max error of 0.06 units. Using the proposed state estimation, the (Comp. Obsv.) signal matches the true fiber state much closer with max error 0.024 units. There is still some phase error in the estimated (Comp. Obsv.) signal, but ILC is robust to errors in the model and signal as discussed in Proposed ILC Analysis.

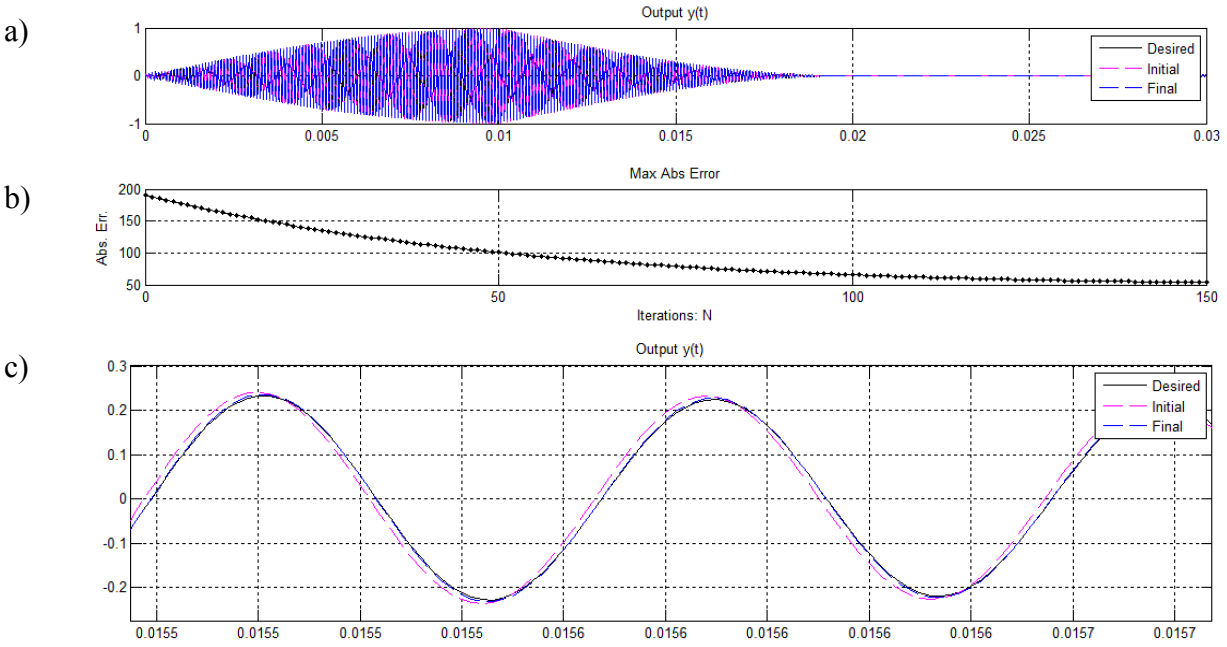


Figure 8.3. a) Simulation result showing ILC convergence using complementary observation. The initial trajectory (magenta) converges to desired profile (black). The final iteration trajectory shown in (blue). b) Plot showing the sum-maximum absolute error of the trajectories achieved at each iteration; the final trajectory matches the desired trajectory with 52 max. abs. error, versus 177 initially. c) Zoom in of part (a), showing clearly initial (magenta), final (blue) and desired (black) trajectories.

Using the complementary-observation output processing method, the Iterative Learning Controller is able to improve the tracking performance, as simulated in Figure 8.3. Figure 8.3c

shows that the final iteration trajectory (blue) matches the desired trajectory (black). From Figure 8.3b, at the 1st iteration, the sum-maximum absolute error was 177, but by the final learning iteration, the sum-maximum absolute was reduced monotonically to 52. Using the raw output (without the proposed state estimation), the controller immediately goes unstable, with sum-maximum absolute error approaching $10^6$. The convergence of the ILC despite the approximate state estimation approach is due to the robustness bounds of the controller given by Equations 8.14 and 8.15, where now the remaining phase error of the observation effectively becomes part of the modeling error.

### 8.3.2 *Experiment*

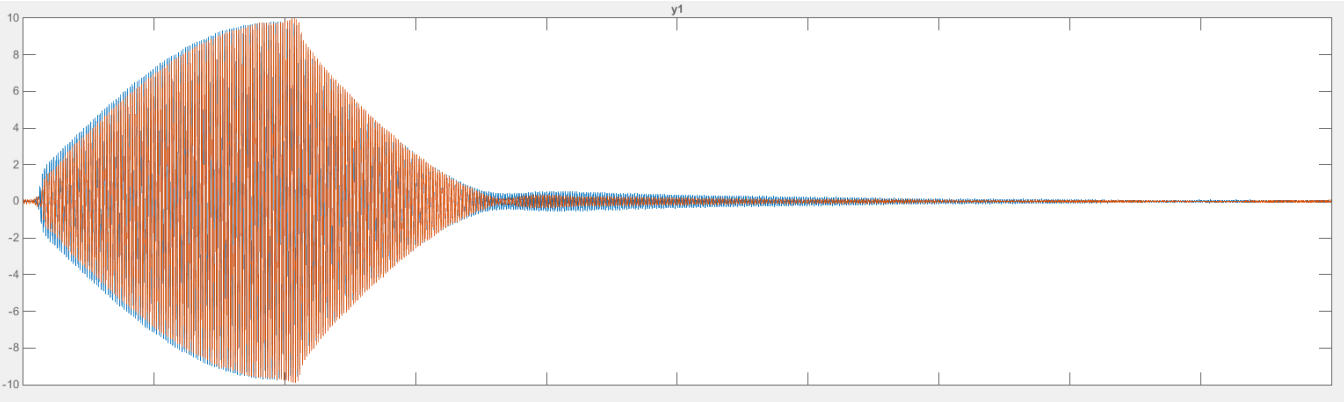


Figure 8.4. Preliminary experimental result applying the proposed ILC method to a SFE system. Blue – Iteration #1. Orange – Iteration #2.

A preliminary experiment was carried out applying the proposed ILC method to a 11.5kHz SFE prototype augmented with simultaneous piezoelectric self-sensing. Figure 8.4 shows the experimental data of the estimated fiber displacement. The blue trace is the achieved trajectory for iteration #1 of the learning algorithm. The orange trace is the achieved trajectory for the next iteration #2 of the learning algorithm. The desired trajectory was a sine-tooth envelope followed by regulation to zero. Figure 8.4 shows that the second iteration has improved regulation to zero and reduced residual vibration, indicating that tracking error is being reduced by the learning controller. The Mean Square Error (MSE) between the desired trajectory and the achieved trajectory was reduced from 0.155 to 0.101 between iteration #1 and #2.

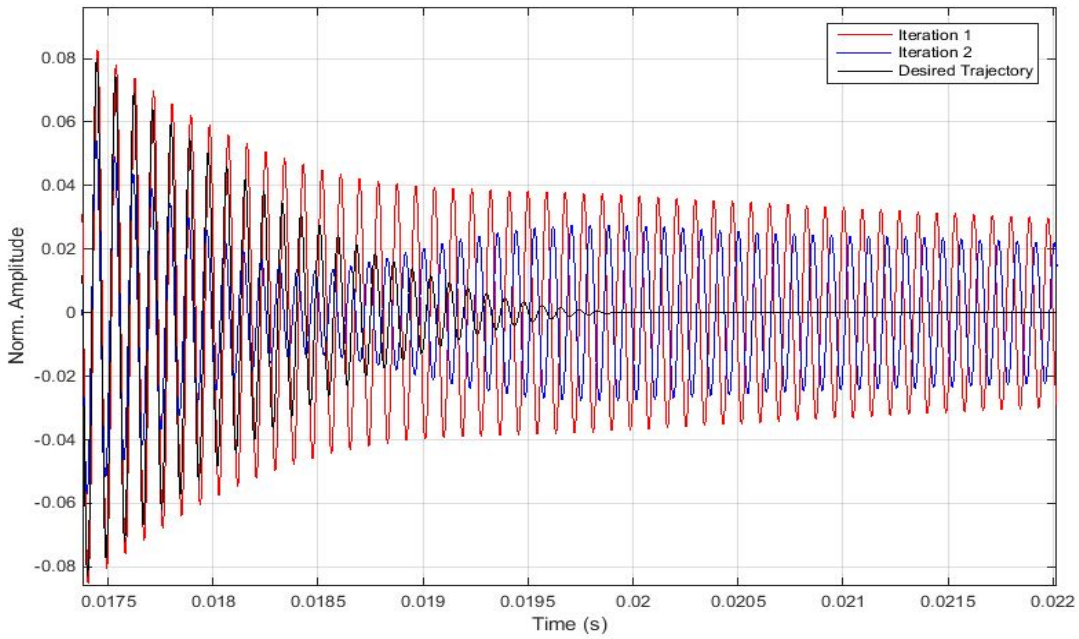


Figure 8.5. Preliminary experimental result applying the proposed ILC method to a SFE system: Zoom-in.

## 8.4 SUMMARY

This chapter has presented an analysis and early exploration indicators for future work in applying Iterative Learning with the simultaneous piezoelectric self-sensing approach introduced in this dissertation. Details of an Iterative Learning Control design were presented and analyzed. A state estimation method was also introduced based on the simultaneous piezoelectric self-sensing and empirical system identification approaches presented earlier in this work. Finally, simulation and preliminary experiments of the proposed learning control method were reported.

# Chapter 9. CONCLUSION

This work set out to accomplish three specific aims:

1. Pioneer piezoelectric self-sensing as a miniature sensing modality for the SFE and miniature scanners in general.
2. Develop electromechanical models suitable with piezoelectric self-sensing.
3. Develop an online self-calibrating control scheme.

These specific aims have been completed, with two contributions in each area.

For pioneering piezoelectric self-sensing as a miniature sensing modality for the SFE, this work has introduced time-multiplexed, and simultaneous piezoelectric self-sensing, novel miniature sensing modalities that has enabled online calibration techniques and lays the foundation for further control exploration.

For developing electromechanical models suitable with piezoelectric self-sensing, this work has introduced a circuit equivalent electromechanical model, and an empirical modal representation of the scanning fiber system. These modeling approaches were the first to consider not just the piezoelectric tube, but also the electrical dynamics of the new auxiliary sensing circuit.

Finally, for developing an online self-calibrating control scheme, this work has introduced an adaptive feedforward control that uses system probing and system inversion to accomplish online self-calibration. A run-to-run optimization was then introduced where iterative control point optimization improves upon system probing accomplishing a high performance self-calibration controller.

## 9.1 DISSERTATION SUMMARY

Starting in Chapter 2, a review of piezoelectricity and sensing was given before the first method, time-multiplexed piezoelectric self-sensing, was introduced as the initial development towards integrated sensing on the SFE. Time-multiplexed piezoelectric self-sensing was shown to replace previous optical sensing methods in the de facto calibration algorithm.

In Chapter 3, the second method, simultaneous piezoelectric self-sensing was introduced. The theory behind simultaneous piezoelectric self-sensing set the foundation for the development

of a new piezoelectric self-sensing circuit designed specifically for the scanning fiber device. Implementation details were also discussed. Simultaneous piezoelectric self-sensing with the SFE was a major contribution of this dissertation and this method was expanded upon in later sections.

In Chapter 4, electromechanical modeling of the SFE oriented towards scan control was developed. A review of related and previous work helped frame the unique approach taken in this dissertation on electromechanically modeling the entire system as a circuit-equivalent network. This first modeling approach was verified with experimental data. A second modeling approach was also presented that takes inspiration from modal analysis. System identification and model order reduction techniques were described that enabled empirically driven modeling of actual system dynamics.

In Chapter 5, previous control designs were reviewed, and control design considerations for scanning fiber devices was analyzed to inform control system development. Based on the specific operating qualities of the SFE, input shaping methods were presented to achieve better control performance. Appropriate metrics for image quality were discussed and a radial/tangential error convention is defined for quantifying the performance of control methods introduced in later chapters.

In Chapter 6, a new adaptive feedforward controller was presented that incorporates the piezoelectric self-sensing methods developed earlier in this dissertation. The system identification and system inversion algorithms were described. Implementation details, experimental methodology and experimental results demonstrating accurate self-calibration were also detailed.

In Chapter 7, a novel run-to-run optimization controller was introduced that improves upon the performance of the adaptive feedforward control. A general review of learning-type control was given followed by detailed derivation of the run-to-run optimization method customized for the SFE system. Simulation examples were given to further explore the formulation followed by reports on experimental investigations that demonstrate the improved performance of the optimizing control.

In Chapter 8, further control method explorations in analysis and simulation were discussed. Viability of iterative learning control methods with piezoelectric self-sensing-enabled SFE systems was analyzed and a new complementary observation method is proposed.

## 9.2 FUTURE WORK

Further investigation can be performed to expand the three main contributions of this dissertation. Within piezoelectric self-sensing, alternative self-sensing methods such as charge drives and current sensing can be explored. For modeling the scanning fiber system, the electromechanical models can be augmented with electromechanical and optical finite element analysis for designing e.g. new, higher scan frequency scanners. Finally, more control method exploration can be conducted. The previous chapter Further Control Method Exploration has discussed in detail directions for future work with Iterative Learning Control with simultaneous piezoelectric self-sensing that was introduced in this dissertation.

## 9.3 SIGNIFICANCE

The Scanning Fiber Technology has numerous advantages and applications in imaging and display applications that a range of other publications have demonstrated. Particularly, the scanning fiber endoscope is a breakthrough small form factor imaging device for the medical field, and the scanning fiber display promises radically new interfaces for information [106]–[108]. Furthermore, due to the small size of the scanner (<1mm diameter), it is already being researched as a minimally invasive endoscope capable of multi-modal imaging [2], 3-D reconstruction of airways and bladder [3], [109], and image-guided treatment [4]; the use of the Fiber Scanner as miniature projection displays are also being developed [106].

This dissertation has focused on a feature that was lacking with the scanning fiber technology: automatic self-calibration to maintain high image quality while the imaging or display device is in use within changing operating conditions, a necessity to mature the scanning fiber technology to widespread and commercial use. By implementing piezoelectric self-sensing, this dissertation has eliminated the use of large and costly optical sensors. The introduced control schemes also eliminate user-initiated calibration sequences that diminish the user experience.

This technology can be applied in new products that benefit society in health care, industry, entertainment and much more.

# BIBLIOGRAPHY


[1] C. M. Lee, C. J. Engelbrecht, T. D. Soper, F. Helmchen, and E. J. Seibel, "Scanning fiber endoscopy with highly flexible, 1-mm catheterscopes for wide-field, full-color imaging," *J. Biophotonics*, vol. 3, no. 5–6, pp. 385–407, Jun. 2010.

[2] C. Yang, V. W. Hou, E. J. Girard, L. Y. Nelson, and E. J. Seibel, "Target-to-background enhancement in multispectral endoscopy with background autofluorescence mitigation for quantitative molecular imaging," *J. Biomed. Opt.*, vol. 19, no. 7, p. 76014, 2014.

[3] T. D. Soper, M. P. Porter, and E. J. Seibel, "Surface Mosaics of the Bladder Reconstructed From Endoscopic Video for Automated Surveillance.," *IEEE Trans. Biomed. Eng.*, vol. 59, no. 6, 2012.

[4] M. . Woldetensae, M. . Kirshenbaum, G. . Kramer, L. Zhang, and E. . Seibel, "Fluorescence image-guided photodynamic therapy of cancer cells using a scanning fiber endoscope [8576-20]," *Proc.- SPIE Int. Soc. Opt. Eng.*, vol. 8576, p. 8576 0L, 2013.

[5] Y. Gong, D. Hu, B. Hannaford, and E. J. Seibel, "Accurate three-dimensional virtual reconstruction of surgical field using calibrated trajectories of an image-guided medical robot," *J. Med. Imaging*, vol. 1, no. 3, p. 035002, Dec. 2014.

[6] Y. Gong, R. S. Johnston, C. D. Melville, and E. J. Seibel, "Axial-Stereo 3D Optical Metrology for Inner Profile of Pipes Using a Scanning Laser Endoscope," *Int. J. Optomechatronics*, 2015.

[7] Y. Gong, R. S. Johnston, C. D. Melville, and E. J. Seibel, "Axial-Stereo 3D Optical Metrology of Internally Machined Parts Using High-Quality Imaging from a Scanning Laser Endoscope." 2014.

[8] Q. Y. Smithwick, "Modeling and control of the single fiber scanning endoscope," 2002.

[9] M. J. Kundrat, "High performance open loop control for fiber scanner imaging and display systems," 2010.

[10] P. Z. McVeigh, R. Sacho, R. A. Weersink, V. M. Pereira, W. Kucharczyk, E. J. Seibel, B. C. Wilson, and T. Krings, "High-resolution angioscopic imaging during endovascular neurosurgery," *Neurosurgery*, vol. 75, no. 2, pp. 171–180; discussion 179–180, Aug. 2014.

[11] A. W. Templeton, K. Webb, J. H. Hwang, E. J. Seibel, and M. Saunders, "Scanning fiber endoscopy: a novel platform for cholangioscopy," *Gastrointest. Endosc.*, vol. 79, no. 6, pp. 1000–1001, Jun. 2014.

[12] G M Clayton and S Devasia, "Image-based compensation of dynamic effects in scanning tunnelling microscopes," *Nanotechnology*, vol. 16, no. 6, pp. 809–818, 2005.

[13] Clayton GM and Devasia S, "Iterative image-based modeling and control for higher scanning probe microscope performance.," *Rev. Sci. Instrum.*, vol. 78, no. 8, 2007.

[14] Y. Zhang, Y. Fang, X. Zhou, and X. Dong, "Image-based hysteresis modeling and compensation for an AFM piezo-scanner," *ASJC Asian J. Control*, vol. 11, no. 2, pp. 166–174, 2009.

[15] Wang J, Wang J, Hou Y, and Lu Q, "Self-manifestation and universal correction of image distortion in scanning tunneling microscopy with spiral scan.," *Rev. Sci. Instrum.*, vol. 81, no. 7, 2010.

[16] Ying-Chung Li, Meng-Han Ho, Shi-Jie Hung, Meng-Huei Chen, and Michael S-C Lu, "CMOS micromachined capacitive cantilevers for mass sensing," *J. Micromechanics Microengineering*, vol. 16, no. 12, pp. 2659–2665, 2006.
[17] B. Bhikkaji, M. Ratnam, A. . Fleming, and S. O. . Moheimani, "High-Performance Control of Piezoelectric Tube Scanners," *IEEE Trans. Control Syst. Technol.*, vol. 15, no. 5, pp. 853–866, 2007.
[18] Mahmood I.A and Moheimani S.O.R, "Making a commercial atomic force microscope more accurate and faster using positive position feedback control," *Rev Sci Instrum Rev. Sci. Instrum.*, vol. 80, no. 6, 2009.
[19] H. Huang and Z. . Wu, "Static and dynamic measurement of low-level strains with carbon fibers," *Sens. Actuators Phys.*, vol. 183, pp. 140–147, 2012.
[20] Shin C, Jeon I, Khim ZG, Hong JW, and Nam H, "Study of sensitivity and noise in the piezoelectric self-sensing and self-actuating cantilever with an integrated Wheatstone bridge circuit.," *Rev. Sci. Instrum.*, vol. 81, no. 3, 2010.
[21] K. Uchino, *Advanced piezoelectric materials science and technology*. Cambridge, UK; Philadelphia: Woodhead Publishing, 2010.
[22] American National Standards Institute, F., and Frequency Control Society IEEE Ultrasonics, Standards Committee, and Institute of Electrical and Electronics Engineers, *IEEE standard on piezoelectricity*. New York, N.Y.: Institute of Electrical and Electronics Engineers, 1988.
[23] J. SIROHI and I. CHOPRA, "Fundamental Understanding of Piezoelectric Strain Sensors," *J. Intell. Mater. Syst. Struct.*, vol. 11, no. 4, pp. 246–257, 2000.
[24] Chen CJ, Schwarz A, Wiesendanger R, Horn O, and Müller J, "Three-electrode self-actuating self-sensing quartz cantilever: design, analysis, and experimental verification.," *Rev. Sci. Instrum.*, vol. 81, no. 5, 2010.
[25] Moheimani SO and Yong YK, "Simultaneous sensing and actuation with a piezoelectric tube scanner.," *Rev. Sci. Instrum.*, vol. 79, no. 7, 2008.
[26] Yong YK, Ahmed B, and Moheimani SO, "Atomic force microscopy with a 12-electrode piezoelectric tube scanner.," *Rev. Sci. Instrum.*, vol. 81, no. 3, 2010.
[27] M. . Kundrat, P. . Reinhall, C. . Lee, and E. . Seibel, "High performance open loop control of scanning with a small cylindrical cantilever beam," *J. Sound Vib.*, vol. 330, no. 8, pp. 1762–1771, 2011.
[28] M. J. Kundrat, P. G. Reinhall, and E. J. Seibel, "Method to Achieve High Frame Rates in a Scanning Fiber Endoscope," *J Med Devices J. Med. Devices*, vol. 5, no. 3, p. 034501, 2011.
[29] G. Schitter and A. Stemmer, "Identification and Open-Loop Tracking Control of a Piezoelectric Tube Scanner for High-Speed Scanning-Probe Microscopy," *IEEE Trans. CONTROL Syst. Technol.*, vol. 12, pp. 449–454, 2004.
[30] J. J. Dosch, D. J. Inman, and E. Garcia, "A Self-Sensing Piezoelectric Actuator for Collocated Control," *J. Intell. Mater. Syst. Struct. J. Intell. Mater. Syst. Struct.*, vol. 3, no. 1, pp. 166–185, 1992.
[31] C. J. Chen, "Electromechanical deflections of piezoelectric tubes with quartered electrodes.," *Appl. Phys. Lett.*, vol. 60, no. 1, 1992.
[32] M. Leung, E. Haemmerle, M. Hodgson, W. Chen, and W. Gao, "Tip deflection calculations of small-diameter thin-walled piezoelectric tubes," *Ceram. Int.*, vol. 35, no. 6, pp. 2409–2414, 2009.

[33] M. E. Taylor, “Dynamics of piezoelectric tube scanners for scanning probe microscopy,” *Rev. Sci. Instrum.*, vol. 64, no. 1, p. 154, 1993.
[34] Ma Y, Feng Z, Pan C, and Kong F, “Static and dynamic analysis of a four-tube piezoelectric actuator,” *Rev Sci Instrum Rev. Sci. Instrum.*, vol. 80, no. 6, 2009.
[35] A. . JHA and D. . INMAN, “PIEZOELECTRIC ACTUATOR AND SENSOR MODELS FOR AN INFLATED TOROIDAL SHELL,” *Mech. Syst. Signal Process. Mech. Syst. Signal Process.*, vol. 16, no. 1, pp. 97–122, 2002.
[36] Fleming A.J, Wills A.G, and Moheimani S.O.R, “Sensor fusion for improved control of piezoelectric tube scanners,” *IEEE Trans Control Syst Technol IEEE Trans. Control Syst. Technol.*, vol. 16, no. 6, pp. 1265–1276, 2008.
[37] A. J. Fleming and S. O. R. Moheimani, “Sensorless Vibration Suppression and Scan Compensation for Piezoelectric Tube Nanopositioners,” *IEEE Trans. CONTROL Syst. Technol.*, vol. 14, no. 1, pp. 33–44, 2006.
[38] N. W. Hagood and E. H. Anderson, “Simultaneous sensing and actuation using piezoelectric materials,” 1992, vol. 1543, pp. 409–421.
[39] N. W. H. Eric H. Anderson, “Self-sensing piezoelectric actuation - Analysis and application to controlled structures,” 1992.
[40] S. Kuiper and G. Schitter, “Active damping of a piezoelectric tube scanner using self-sensing piezo actuation,” *Mechatronics*, vol. 20, no. 6, pp. 656–665, 2010.
[41] Jones L, Garcia E, and Waites H, “Self-sensing control as applied to a PZT stack actuator used as a micropositioner,” *Smart Mater Struct Smart Mater. Struct.*, vol. 3, no. 2, pp. 147–156, 1994.
[42] Y. Miyahara, M. Deschler, T. Fujii, S. Watanabe, and H. Bleuler, “Non-contact atomic force microscope with a PZT cantilever used for deflection sensing, direct oscillation and feedback actuation,” *Appl. Surf. Sci.*, vol. 188, no. 3–4, pp. 450–455, 2002.
[43] M. Bazghaleh, S. Grainger, M. Mohammadzaheri, B. Cazzolato, and T. . Lu, “A novel digital charge-based displacement estimator for sensorless control of a grounded-load piezoelectric tube actuator,” *Sens. Actuators Phys.*, vol. 198, pp. 91–98, 2013.
[44] A. Badel, Jinhao Qiu, G. Sebald, and D. Guyomar, “Self-sensing High Speed Controller for Piezoelectric Actuator,” *J. Intell. Mater. Syst. Struct.*, vol. 19, no. 3, pp. 395–405, 2008.
[45] Lai Z.-L, Chen Z, Liu X.-D, and Wu Q.-H, “A novel similarity-based hysteresis empirical model for piezoceramic actuators,” *Sens Actuators Phys Sens. Actuators Phys.*, vol. 197, pp. 150–165, 2013.
[46] S. Bashash and N. Jalili, “A Polynomial-Based Linear Mapping Strategy for Feedforward Compensation of Hysteresis in Piezoelectric Actuators,” *J Dyn Sys Meas Control J. Dyn. Syst. Meas. Control*, vol. 130, no. 3, p. 031008, 2008.
[47] Y. Li, S. Tong, and T. Li, “Adaptive fuzzy output feedback control of uncertain nonlinear systems with unknown backlash-like hysteresis,” *Inf. Sci.*, vol. 198, pp. 130–146, 2012.
[48] R. Dong, Y. Tan, H. Chen, and Y. Xie, “A neural networks based model for rate-dependent hysteresis for piezoceramic actuators,” *Sens. Actuators Phys.*, vol. 143, no. 2, pp. 370–376, May 2008.
[49] Y. Pasco and A. Berry, “Consideration of piezoceramic actuator nonlinearity in the active isolation of deterministic vibration,” *J. Sound Vib.*, vol. 289, no. 3, pp. 481–508, 2006.
[50] D. Croft, G. Shedd, and S. Devasia, “Creep, hysteresis, and vibration compensation for piezoactuators: atomic force microscopy application,” *Proc. Am. Control Conf.*, vol. 3, pp. 2123–2128, 2000.

[51] M. Goldfarb and N. Celanovic, “A Lumped Parameter Electromechanical Model for Describing the Nonlinear Behavior of Piezoelectric Actuators,” *J. Dyn. Syst. Meas. Control*, vol. 119, no. 3, pp. 478–485, Sep. 1997.
[52] Y. Pasco and A. Berry, “A Hybrid Analytical/Numerical Model of Piezoelectric Stack Actuators Using a Macroscopic Nonlinear Theory of Ferroelectricity and a Preisach Model of Hysteresis,” *J. Intell. Mater. Syst. Struct.*, vol. 15, no. 5, pp. 375–386, 2004.
[53] P. Ge, “Modeling hysteresis in piezoceramic actuators,” *Precis. Eng. Precis. Eng.*, vol. 17, no. 3, pp. 211–221, 1995.
[54] K. K. Leang and S. Devasia, “Feedback-Linearized Inverse Feedforward for Creep, Hysteresis, and Vibration Compensation in AFM Piezoactuators,” *IEEE Trans. CONTROL Syst. Technol.*, vol. 15, no. 5, pp. 927–935, 2007.
[55] C. . Newcomb and I. Flinn, “Improving the linearity of piezoelectric ceramic actuators,” *Electron Lett Electron. Lett.*, vol. 18, no. 11, 1982.
[56] J. Minase, T.-F. Lu, B. Cazzolato, and S. Grainger, “A review, supported by experimental results, of voltage, charge and capacitor insertion method for driving piezoelectric actuators,” *PRE Precis. Eng.*, vol. 34, no. 4, pp. 692–700, 2010.
[57] A. . Fleming and K. . Leang, “Charge drives for scanning probe microscope positioning stages,” *Ultramicroscopy Ultramicroscopy*, vol. 108, no. 12, pp. 1551–1557, 2008.
[58] Bazghaleh M, Grainger S, Cazzolato B, Lu TF, and Oskouei R, “Implementation and analysis of an innovative digital charge amplifier for hysteresis reduction in piezoelectric stack actuators.,” *Rev. Sci. Instrum.*, vol. 85, no. 4, 2014.
[59] Q. Y. J. Smithwick, J. Vagners, R. S. Johnston, and E. J. Seibel, “A Hybrid Nonlinear Adaptive Tracking Controller for a Resonating Fiber Microscanner,” *J Dyn Sys Meas Control J. Dyn. Syst. Meas. Control*, vol. 132, no. 1, p. 011001, 2010.
[60] M. Bazghaleh, M. Mohammadzaheri, S. Grainger, B. Cazzolato, and T.-F. Lu, “A new hybrid method for sensorless control of piezoelectric actuators,” *Sens. Actuators Phys.*, vol. 194, pp. 25–30, May 2013.
[61] G. Simmers, J. Hodgkins, D. Mascarenas, G. Park, and H. Sohn, “Improved Piezoelectric Self-sensing Actuation,” *J. Intell. Mater. Syst. Struct.*, vol. 15, no. 12, pp. 941–953, 2004.
[62] Q. Y. . Smithwick, P. G. Reinhall, J. Vagners, and E. J. Seibel, “A Nonlinear State-Space Model of a Resonating Single Fiber Scanner for Tracking Control: Theory and Experiment.,” *J. Dyn. Syst. Meas. Control*, vol. 126, no. 1, 2004.
[63] P. F. Pai and A. H. Nayfeh, “Non-linear non-planar oscillations of a cantilever beam under lateral base excitations,” *NLM Int. J. Non-Linear Mech.*, vol. 25, no. 5, pp. 455–474, 1990.
[64] E. C. Haight, “Stability of Nonlinear Oscillations of an Elastic Rod,” *J Acoust Soc Am J. Acoust. Soc. Am.*, vol. 52, no. 3B, p. 899, 1972.
[65] M. R. M. Crespo da Silva and C. C. Glynn, “Nonlinear Flexural-Flexural-Torsional Dynamics of Inextensional Beams. I. Equations of Motion,” *J. Struct. Mech. J. Struct. Mech.*, vol. 6, no. 4, pp. 437–448, 1978.
[66] M. R. M. Crespo da Silva and C. C. Glynn, “Nonlinear Flexural-Flexural-Torsional Dynamics of Inextensional Beams. II. Forced Motions,” *J. Struct. Mech. J. Struct. Mech.*, vol. 6, no. 4, pp. 449–461, 1978.
[67] Q. Y. J. Smithwick, J. Vagners, P. G. Reinhall, and E. J. Seibel, “54.3: Modeling and Control of the Resonant Fiber Scanner for Laser Scanning Display or Acquisition,” *SDTP SID Symp. Dig. Tech. Pap.*, vol. 34, no. 1, pp. 1455–1457, 2003.

[68] Q. Y. J. Smithwick, E. J. Seibel, P. G. Reinhall, and J. Vagners, “Control aspects of the single-fiber scanning endoscope,” 2001, vol. 4253, pp. 176–188.
[69] Q. Y. J. Smithwick, J. Vagners, P. G. Reinhall, and E. J. Seibel, “An Error Space Controller for a Resonating Fiber Scanner: Simulation and Implementation,” *J Dyn Sys Meas Control J. Dyn. Syst. Meas. Control*, vol. 128, no. 4, p. 899, 2006.
[70] C. K. Alexander and M. N. O. Sadiku, *Fundamentals of electric circuits*. Boston: McGraw-Hill, 2000.
[71] M. J. Kundrat, “A nonlinear numerical model of a base excited cantilever beam,” 2004.
[72] B. D. Kraker, *A Numerical - Experimental Approach in Structural Dynamics*. Maastricht: Shaker Publishing B.V., 2004.
[73] C. Hansen and S. Snyder, *Active Control of Noise and Vibration*. London: CRC Press, 1996.
[74] L. Ljung, *System Identification: Theory for the User*, 2 edition. Upper Saddle River, NJ: Prentice Hall, 1999.
[75] K. J. Astrom and B. Wittenmark, *Adaptive Control*, 2 edition. Reading, Mass: Prentice Hall, 1994.
[76] D. A. Bristow, M. Tharayil, and A. G. Alleyne, “A survey of iterative learning control,” *IEEE Control Syst.*, vol. 26, no. 3, pp. 96–114, Jun. 2006.
[77] Y. Wang, F. Gao, and F. J. Doyle III, “Survey on iterative learning control, repetitive control, and run-to-run control,” *J. Process Control*, vol. 19, no. 10, pp. 1589–1600, Dec. 2009.
[78] A. Bock, *Video Compression Systems: From First Principles to Concatenated Codecs*. Stevenage: The Institution of Engineering and Technology, 2009.
[79] H. R. Schiffman, *Sensation and Perception: An Integrated Approach*, 5th edition. New York: John Wiley & Sons, 2001.
[80] C. Sforza, M. Rango, D. Galante, N. Bresolin, and V. F. Ferrario, “Spontaneous blinking in healthy persons: an optoelectronic study of eyelid motion,” *Ophthalmic Physiol. Opt. J. Br. Coll. Ophthalmic Opt. Optom.*, vol. 28, no. 4, pp. 345–353, Jul. 2008.
[81] “Further Assessment of Gender- and Blink Pattern-Related Diff... : Optometry & Vision Science,” *LWW*. [Online]. Available: http://journals.lww.com/optvissci/Fulltext/2002/07000/Further_Assessment_of_Gender__and_Blink.13.aspx. [Accessed: 29-May-2015].
[82] A. T. Bahill, M. R. Clark, and L. Stark, “The main sequence, a tool for studying human eye movements,” *Math. Biosci.*, vol. 24, no. 3–4, pp. 191–204, 1975.
[83] *Neuroscience*, 2nd ed. Sinauer Associates, 2001.
[84] P. H. Meckl, “Control of Vibration in Mechanical Systems Using Shaped Reference Inputs,” Jan. 1988.
[85] Z. Wang and A. C. Bovik, “Modern Image Quality Assessment,” *Synth. Lect. Image Video Multimed. Process.*, vol. 2, no. 1, pp. 1–156, Jan. 2006.
[86] International Committee for Display Metrology, *Information Display Measurements Standard*. Society for Information Display, 2012.
[87] G. M. Clayton, S. Tien, K. K. Leang, Q. Zou, and S. Devasia, “A Review of Feedforward Control Approaches in Nanopositioning for High-Speed SPM,” *J. Dyn. Syst. Meas. Control*, vol. 131, no. 6, pp. 061101–061101, Oct. 2009.
[88] L. M. Silverman, “Inversion of multivariable linear systems,” *IEEE Trans. Autom. Control*, vol. 14, no. 3, pp. 270–276, Jun. 1969.

[89] S. Tien, Q. Zou, and S. Devasia, "Iterative Control of Dynamics-Coupling-Caused Errors in Piezoscanners During High-Speed AFM Operation," *IEEE Trans. CONTROL Syst. Technol.*, vol. 13, no. 6, pp. 921–931, 2005.
[90] S. Devasia, D. Chen, and B. Paden, "Nonlinear inversion-based output tracking," *IEEE Trans. Autom. Control*, vol. 41, no. 7, pp. 930–942, Jul. 1996.
[91] I. L. Yeoh, P. G. Reinhall, M. C. Berg, and E. J. Seibel, "Self-Contained Image Recalibration in a Scanning Fiber Endoscope Using Piezoelectric Sensing," *J. Med. Devices*, vol. 9, no. 1, pp. 011004–011004, Mar. 2015.
[92] R. Good, J. Hahn, T. Edison, and S. J. Qin, "Drug dosage adjustment via run-to-run control," *Proc. Am. Control Conf.*, vol. 5, pp. 4044–4049, 2002.
[93] S. W. Butler and J. A. Stefani, "Supervisory Run-to-Run Control of Polysilicon Gate Etch-Using In Situ Ellipsometry," *IEEE Trans. Semicond. Manuf. Publ. IEEE Compon. Hybrids Manuf. Technol. Soc. IEEE Electron Devices Soc. IEEE Reliab. Soc. IEEE Solid-State Circuits Counc.*, vol. 7, no. 2, p. 193, 1994.
[94] B. Srinivasan, D. Bonvin, E. Visser, and S. Palanki, "Dynamic optimization of batch processes: II. Role of measurements in handling uncertainty," *Comput. Chem. Eng.*, vol. 27, no. 1, pp. 27–44, Jan. 2003.
[95] B. Srinivasan, S. Palanki, and D. Bonvin, "Dynamic optimization of batch processes: I. Characterization of the nominal solution," *Comput. Chem. Eng.*, vol. 27, no. 1, pp. 1–26, Jan. 2003.
[96] E. Zafiriou, R. A. Adomaitis, and G. Gattu, "An approach to run-to-run control for rapid thermal processing." 1995.
[97] B. Srinivasan, C. J. Primus, D. Bonvin, and N. L. Ricker, "Run-to-run optimization via control of generalized constraints," *Control Eng. Pract.*, vol. 9, no. 8, pp. 911–919, Aug. 2001.
[98] C. Owens, H. Zisser, L. Jovanovic, B. Srinivasan, D. Bonvin, and F. J. Doyle, "Run-to-run control of blood glucose concentrations for people with Type 1 diabetes mellitus," *IEEE Trans. Biomed. Eng.*, vol. 53, no. 6, pp. 996–1005, Jun. 2006.
[99] J. Ghost and B. Paden, "Iterative Learning Control for Nonlinear Nonminimum Phase Plants.," *J. Dyn. Syst. Meas. Control*, vol. 123, no. 1, 2001.
[100] M. Norrlöf and S. Gunnarsson, "Experimental Comparison of Some Classical Iterative Learning Control Algorithms.," *IEEE Trans. Robot. Autom.*, vol. 18, no. 4, 2002.
[101] S. Gunnarsson and M. Norrlöf, "On the design of ILC algorithms using optimization," *AUT Autom.*, vol. 37, no. 12, pp. 2011–2016, 2001.
[102] X. Wang and D. Chen, "Robust inversion-based learning control for nonminimum phase systems," in *2002 IEEE International Conference on Systems, Man and Cybernetics*, 2002, vol. 3, p. 6 pp. vol.3–.
[103] J. Ghosh and B. Paden, "Pseudo-Inverse Based Iterative Learning Control for Linear Nonminimum Phase Plants with Unmodeled Dynamics*," *J. Dyn. Syst. Meas. Control*, vol. 126, no. 3, pp. 661–665, Dec. 2004.
[104] N. K. GUPTA, "Frequency-shaped cost functionals - Extension of linear-quadratic-Gaussian design methods," *J. Guid. Control Dyn.*, vol. 3, no. 6, pp. 529–535, 1980.
[105] R. Brinkerhoff and S. Devasia, "Output Tracking for Actuator Deficient/Redundant Systems: Multiple Piezoactuator Example," *J. Guid. Control Dyn.*, vol. 23, no. 2, pp. 370–373, 2000.

[106] B. T. Schowengerdt, M. J. Kundrat, C. M. Lee, R. S. Johnston, C. D. Melville, P. G. Reinhall, and E. J. Seibel, "P-251L: Late-News Poster: Miniature Wide-Throw-Angle Scanning Fiber Projection Display," *SID Symp. Dig. Tech. Pap.*, vol. 39, no. 1, pp. 2102–2105, May 2008.

[107] B. T. Schowengerdt, C. M. Lee, R. S. Johnston, C. D. Melville, and E. J. Seibel, "37.1: Invited Paper: 1-mm Diameter, Full-color Scanning Fiber Pico Projector," *SID Symp. Dig. Tech. Pap.*, vol. 40, no. 1, pp. 522–525, Jun. 2009.

[108] R. C. Bryant, E. J. Seibel, C. M. Lee, and K. E. Schroder, "Low-cost wearable low-vision aid using a handmade retinal light-scanning microdisplay," *J. Soc. Inf. Disp.*, vol. 12, no. 4, pp. 397–404, Dec. 2004.

[109] T. D. Soper, D. R. Haynor, R. W. Glenny, and E. J. Seibel, "In vivo validation of a hybrid tracking system for navigation of an ultrathin bronchoscope within peripheral airways," *IEEE Trans. Biomed. Eng.*, vol. 57, no. 3, pp. 736–745, Mar. 2010.

# APPENDIX A

## TECHNICAL NOTE ON THE ADAPTIVE FEEDFORWARD CONTROLLER

This note details the steps for the Adaptive Feedforward developed by Ivan Yeoh for the Scanning Fiber Endoscope, focusing on the dynamics extraction and feedforward control. The following assumptions/procedures lead up to the final result.

**Premise 1: Modal analysis of a structure results in a description of motion in terms of mode shapes $\boldsymbol{\phi_n(x)}$, and mode displacements $\boldsymbol{p_n(t)}$.**

E.g. for the simple cantilever structure:

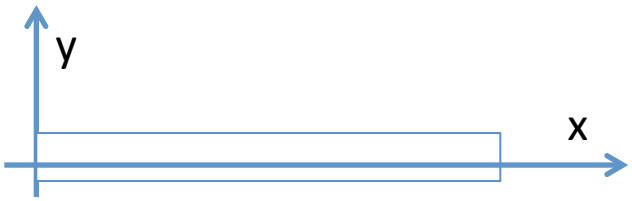


Figure 9.1. Cantilever structure.

The cantilever displacements can be described by:

$$y(x,t) = \sum_{n=1}^{N} p_n(t)\phi_n(x)$$

$n$ is the mode number, $\phi_n(x)$ the mode shapes, and $p_n(t)$ the mode displacements.

Examples of the first 3 mode shapes:

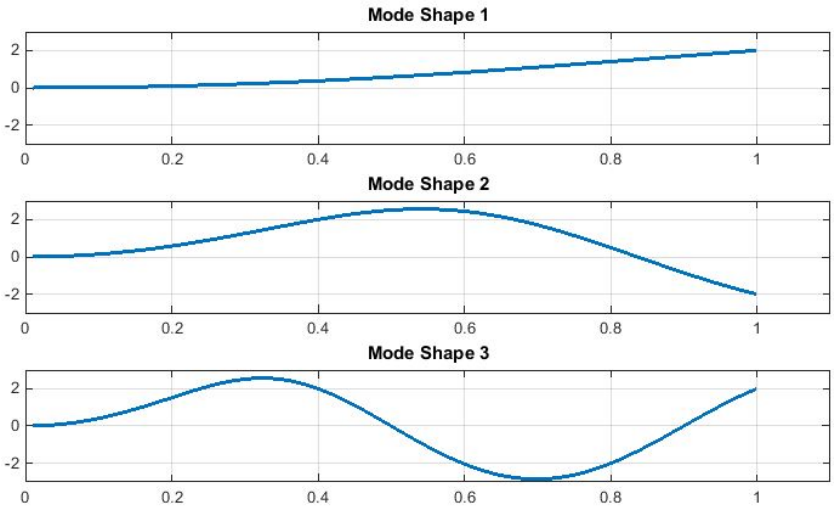


Figure 9.2. Cantilever modes.

**Premise 2: Each vibration mode in a linear system has dynamics independent of all other vibration modes.**

This is readily seen in the equations of motion of finite element models that can be block-diagonalized:

$$\tilde{M}\ddot{p} + \tilde{C}\dot{p} + \tilde{K}p = \tilde{F}$$

$$\phi^T M\phi = \tilde{M} = \begin{bmatrix} \ddots & & \\ & m_n & \\ & & \ddots \end{bmatrix},\ \phi^T C\phi = \tilde{C} = \begin{bmatrix} \ddots & & \\ & c_n & \\ & & \ddots \end{bmatrix},\ \phi^T K\phi = \tilde{K} = \begin{bmatrix} \ddots & & \\ & k_n & \\ & & \ddots \end{bmatrix}$$

$\tilde{M}, \tilde{C}, \tilde{K}$ are block diagonal, this results in $n$-uncoupled differential equations describing the displacement $p_n(t)$ of the $n$-vibration modes.

**Premise 3: This algorithm attempts to identify the dynamics of the structure by sensing at the piezoelectric-tube.**

E.g. in the model below, a composite cantilever is made up of a piezoelectric-tube and optical fiber.

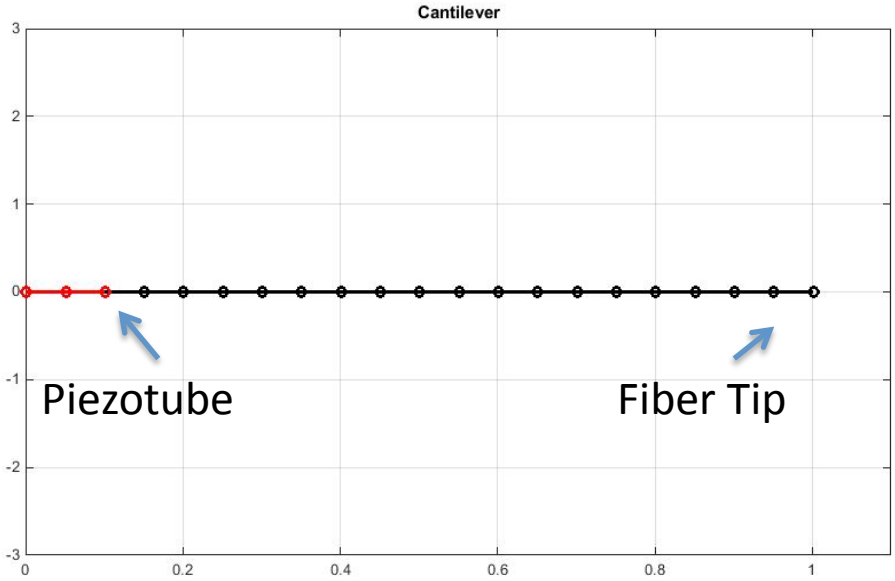


Figure 9.3. Composite cantilever.

For each mode shape, the displacement of the fiber tip and the displacement of the piezotube tip have a fixed ratio:

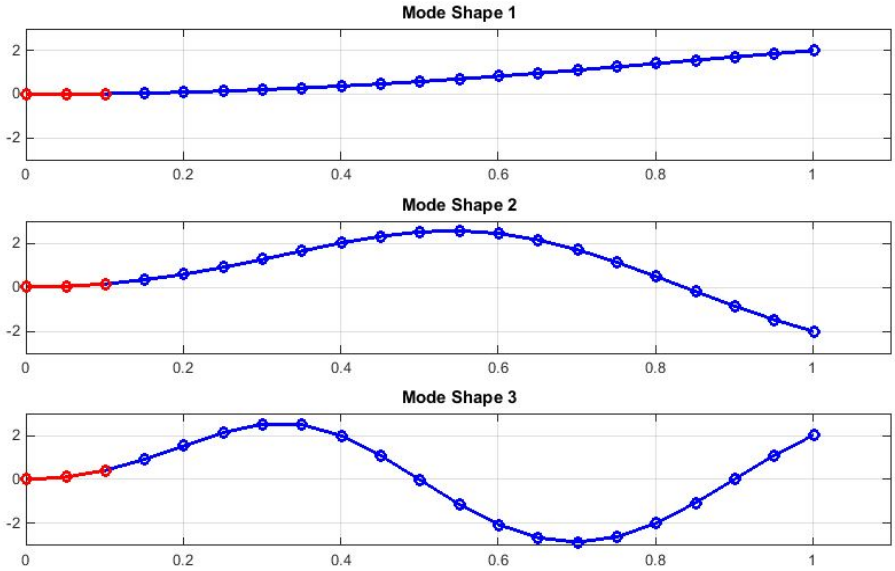


Figure 9.4. Composite cantilever modes.

For an impulse excitation, shown below is the displacement at the piezotube vs. displacement at the fiber tip:

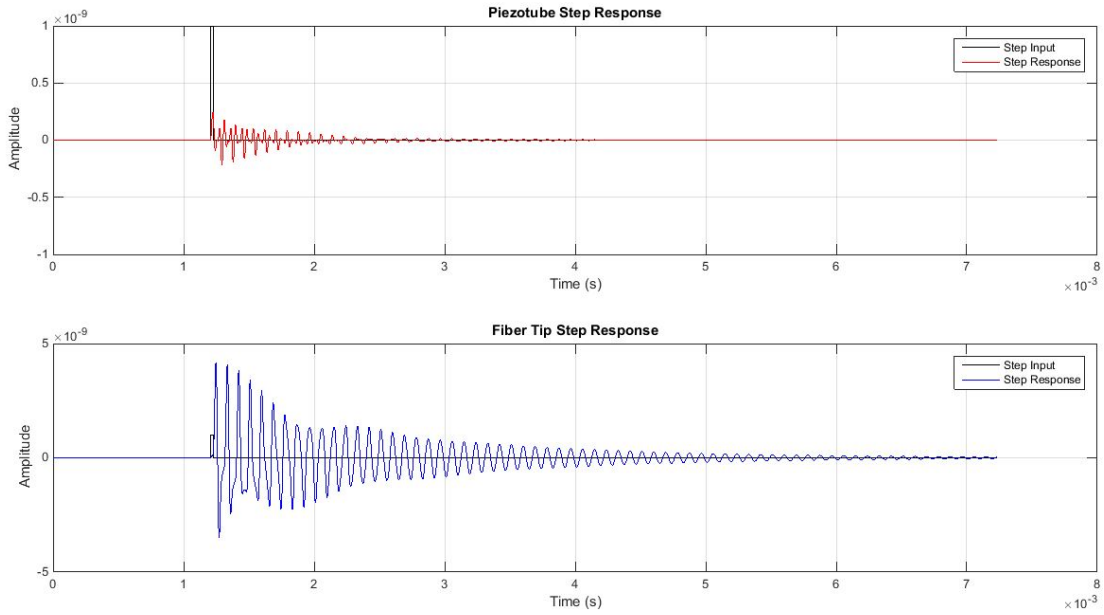


Figure 9.5. Displacement profiles at the piezoelectric-tube and the fiber tip.

**Procedure 1: Perform System Identification using the piezoelectric-tube signal.**

Applying Batch Least Squares system identification to the input-output (piezoelectric signal) data, we are able to identify an empirical state-space model:

$$\dot{x} = Ax + Bu$$

$$y = Cx$$

**Procedure 2: Transform the identified state space model into a block diagonal format using a similarity transform.**

Transforming one state-space representation into another is simple, using similarity transforms. Transforming into a block-diagonal format is built into e.g. Matlab software.

E.g. the following state transform,

$$x = P\tilde{x}$$

Gives a new state-space representation:

$$\dot{\tilde{x}} = (P^{-1}AP)\tilde{x} + (P^{-1}B)u$$

$$y = (CP)\tilde{x} + D$$

Where the transformed A matrix is,

$$\tilde{A} = (P^{-1}AP)$$

**Procedure 3: Now, the obtained block diagonal format parallels the independent mode dynamics in Premise 2. The dynamics associated with a certain mode can be extracted simply by selecting a block.**

After transform, the state space matrices are in the following format:

$$A = \begin{bmatrix} \sigma_1 & \omega_1 & 0 & 0 & 0 & \cdots \\ -\omega_1 & \sigma_1 & 0 & 0 & 0 & \cdots \\ 0 & 0 & \sigma_2 & \omega_2 & 0 & \cdots \\ 0 & 0 & -\omega_2 & \sigma_2 & 0 & \cdots \\ 0 & 0 & 0 & 0 & \lambda_3 & \cdots \\ \vdots & \vdots & \vdots & \vdots & \vdots & \ddots \end{bmatrix} = \begin{bmatrix} a_{1,11} & a_{1,12} & 0 & 0 & 0 & \cdots \\ a_{1,21} & a_{1,22} & 0 & 0 & 0 & \cdots \\ 0 & 0 & a_{2,11} & a_{2,12} & 0 & \cdots \\ 0 & 0 & a_{2,12} & a_{2,22} & 0 & \cdots \\ 0 & 0 & 0 & 0 & a_3 & \cdots \\ \vdots & \vdots & \vdots & \vdots & \vdots & \ddots \end{bmatrix}$$

$$B = \begin{bmatrix} b_{1,11} & b_{1,12} & b_{1,13} & b_{1,14} & b_{1,15} & \cdots \\ b_{1,21} & b_{1,22} & b_{1,23} & b_{1,24} & b_{1,25} & \cdots \\ b_{2,11} & b_{2,12} & b_{2,13} & b_{2,14} & b_{2,15} & \cdots \\ b_{2,21} & b_{2,22} & b_{2,23} & b_{2,24} & b_{2,25} & \cdots \\ b_{3,11} & b_{3,12} & b_{3,13} & b_{3,14} & b_{3,15} & \cdots \\ \vdots & \vdots & \vdots & \vdots & \vdots & \ddots \end{bmatrix}$$

$$C = [c_{1,1} \quad c_{1,2} \quad c_{2,1} \quad c_{2,2} \quad c_3 \quad \cdots])$$

Highlighted in blue is an independent subsystem representing the dynamics of a vibration mode. The natural frequency of that vibration mode is given by the eigenvalues of the subsystem.

Extracting the subsystem highlighted in blue, we isolate the dynamics of a vibration mode, which can be written in the form:

$$\dot{x}_d = a_1 x_d + b_1 u_{ff}$$

$$y_d = c_1 x_d$$

$a_1$, $b_1$ and $c_1$ are the sub-matrices highlighted in blue.

**Procedure 4: Control the extracted mode: Given a desired trajectory, the control input can be calculated using the identified mode dynamics**

Using the following equation, the control input $u_{ff}$, is calculated for a given desired trajectory $y_d$:

$$u_{ff} = \frac{1}{c_1 a_1^{r-1} b_1} \left[ \frac{d^r}{dt^r} y_d - c_1 a_1^r x \right]$$

**Procedure 5: Finally, the feed-forward control input is applied to the system. With the SFE, the 1$^{st}$ mode is excited to resonance.**

Assumption: The higher order modes are barely excited and are ignored.

Note: All of the above identification was done using the piezoelectric self-sensing signal, and have been implemented and experimentally verified (reported in paper).

# APPENDIX B

TECHNICAL NOTE ON THE RUN-TO-RUN OPTIMIZATION CONTROLLER

This brief explains the Run-to-Run Optimization method developed by Ivan Yeoh for the Scanning Fiber Endoscope. First, a general description of run-to-run control is given. Next, an example implementation of run-to-run in drug-dose control is examined. Finally, the new Run-to-Run Optimization method is presented.

## A. Run-to-Run Control Introduction

**1.** Run-to-run control is applied to problems with *repeating trajectories*, such as: repeating chemical processes to manufacture plastics, repeating robot arm maneuvers to manufacture cars, etc.

More mathematically,

$$y\left(t + T_{period}\right) = y(t)$$

(Trajectory repeats every $T_{period}$).

**2.** Run-to-run control is a *learning type* control approach: The error in a previous period is used to update the control input for the subsequent period (since the trajectory is repeating).

**3.** Run-to-run control operates on a *reduced set of measurements*. This is in contrast to e.g. feedback control where the feedback controller measures the entire output signal $y(t)$, and compensates in real time.

**a.** Reduced set of measurements can mean a very *low sampling rate* e.g. sample the level of a chemical 5 times each period.

**b.** Reduced set of measurements can also mean a parameterization of the input/output signal by a small number of parameters, e.g. the input to a chemical process, $u(t)$, being completely defined by a vector of transition times ($\pi_{transitions}$, between which the chemical flow is either ON or OFF): $u(\pi_{transitions}, t)$.

Both the input and the output can be parameterized:

$u(t) \rightarrow u(\pi, t)$, input parameterized by $\pi$

$y(t) \rightarrow u(I, t)$, output parameterized by $I$

**4.** This reduced set/reduced dimension representation is the uniqueness of run-to-run control. It enables very sparse measurements of a process to be applied for control. It also results in a very hardware/computation-efficient control method.

**5.** As a learning controller, run-to-run control uses the measured output to update the control input for the next repeating period. With the reduced set parameterization, this is equivalent to: measuring the output parameters $I$ to update the input parameters $\pi$ for the next period.

## B. Example of Run-to-Run Applied to Drug Dosage Control

To more clearly explain run-to-run control, an example implementation for insulin dosage control is examined here. This implementation was published in "Run-to-Run Control of Blood Glucose Concentrations for People With Type 1 Diabetes Mellitus", Owens et al., IEEE TRANSACTIONS ON BIOMEDICAL ENGINEERING, VOL. 53, NO. 6, JUNE 2006.

### 1. Repeating trajectory problem:

Controlling the glucose levels of a person is a repeating trajectory problem: Humans undergo 24-hour cycles, where we eat (breakfast, lunch, dinner) at about the same time. (For diabetic patients, they are recommended to follow a very precise timing routine, so that glucose levels are predictable.)

Thus, within this repeating 24-hour cycle, the goal of this run-to-run implementation was to control the patient's glucose to a desired level.

### 2. Reduced Set Input Parameterization

The input in this implementation was parameterized by the timing, T, and the quantity, Q, of insulin injections following breakfast, lunch and dinner (B, L, D):

$$u(\pi, t): \pi = [T_B \; Q_B \; T_L \; Q_L \; T_D \; Q_D]$$

**3. Reduced Set Output Parameterization**

The output in this implementation was parameterized by sparse measurements of the maximum and minimum blood glucose levels, G, after breakfast, lunch and dinner:

$$y(I,t): I = [G_B^{max}\ G_B^{min}\ G_L^{max}\ G_L^{min}\ G_D^{max}\ G_D^{min}]$$

**4. Update/Learning Rule**

A simple update/learning rule was implemented in this case: Deviations of the output parameterization vector (sampled blood glucose levels) was used to update the input parameterization (insulin timing and dosage) for the next period/next day:

$$\pi_{k+1} = \pi_k + \boldsymbol{K}(I^r - I_k)$$

Here $k$ represents the iteration number, $I^r$ represents the ideal/targeted output parameters.

$\boldsymbol{K}$ is a gain matrix that was estimated from a linearized model of the human body insulin response:

$$\mathbf{K} = \begin{bmatrix} k_{T_B} & 0 & 0 & 0 & 0 & 0 \\ 0 & k_{Q_B} & 0 & 0 & 0 & 0 \\ 0 & 0 & k_{T_L} & 0 & 0 & 0 \\ 0 & 0 & 0 & k_{Q_L} & 0 & 0 \\ 0 & 0 & 0 & 0 & k_{T_D} & 0 \\ 0 & 0 & 0 & 0 & 0 & k_{Q_D} \end{bmatrix}$$

**5. Results**

Using the above input and output parameterizations and update rule, the authors were able to regulate a patient's glucose levels to within safe bounds after 10 days of run-to-run iterations:

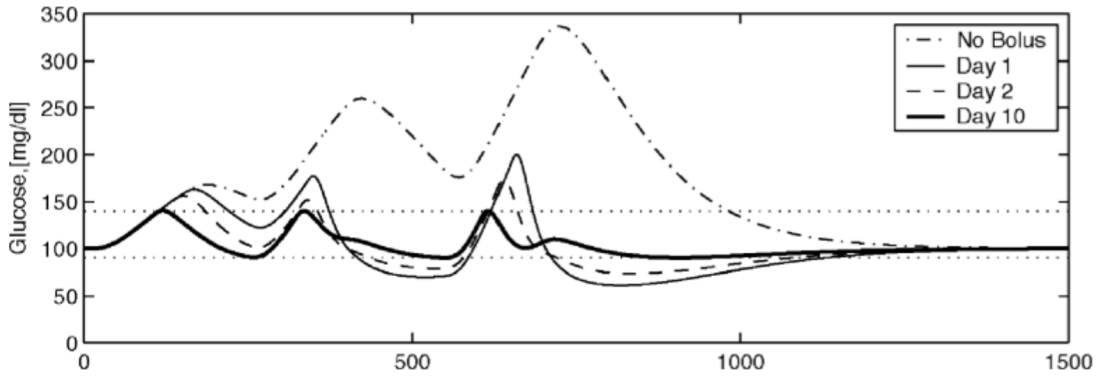

Figure 9.6. Results of run-to-run control for glucose level regulation.

## C. New Run-to-Run Optimization within Exact Inverse Framework

Now the new run-to-run control method is introduced in the same manner, but contrasted with the previous run-to-run example.

### 1. Repeating trajectory problem:

The SFE, for example operating at 50Hz imaging rate, undergoes a repeating trajectory every $1/50^{th}$ of a second, where the optical fiber is spiraled outwards, and then inwards to capture/project an image frame.

The goal is for the repeating scan trajectory to follow a set profile, to avoid image distortions.

### 2. Reduced Set Input Parameterization

What is unique about this approach is that since we are building on the system identification and exact model inversion methods to calculate a control input, the control input can be *parameterized by the coefficients of the dynamics model H*:

$$H_1 = \frac{1}{s^2 + a_1 s + b_1}$$

There are 2 dynamic models for the 2 eigendirections, thus the input parameterization is:

$$u(\pi, t): \pi = [a_1\ b_1\ a_2\ b_2]$$

### 3. Reduced Set Output Parameterization

Another uniqueness of this approach is that we assume: any control input that is not correct/optimum will result in residual vibrations of the mechanical system, since the desired trajectory ends in a completely resting state.

Thus, a residual energy measure of a system vibration mode is taken as the output parameterization:

$$y(I, t): I = [E_1\ E_2]$$

$E_1\ E_2$ are the residual energy on each eigendirection, defined as a sum of kinetic and potential energies, e.g.:

$$E(t) = \boldsymbol{K}\boldsymbol{x}(t).^2 + \boldsymbol{M}\boldsymbol{x}(t).^2$$

$$E(t) = [2.25 \quad 0]\begin{bmatrix} x(t) \\ \dot{x}(t) \end{bmatrix}.^2 + [0 \quad 1]\begin{bmatrix} x(t) \\ \dot{x}(t) \end{bmatrix}.^2$$

(Details of definition are found in the paper).

This energy-measure parameterization is very different from the previous drug-dosage example.

It is also shown in the paper (derivation and simulation) that using the above input/output parameterization the residual energy measure is convex in the input parameter space:

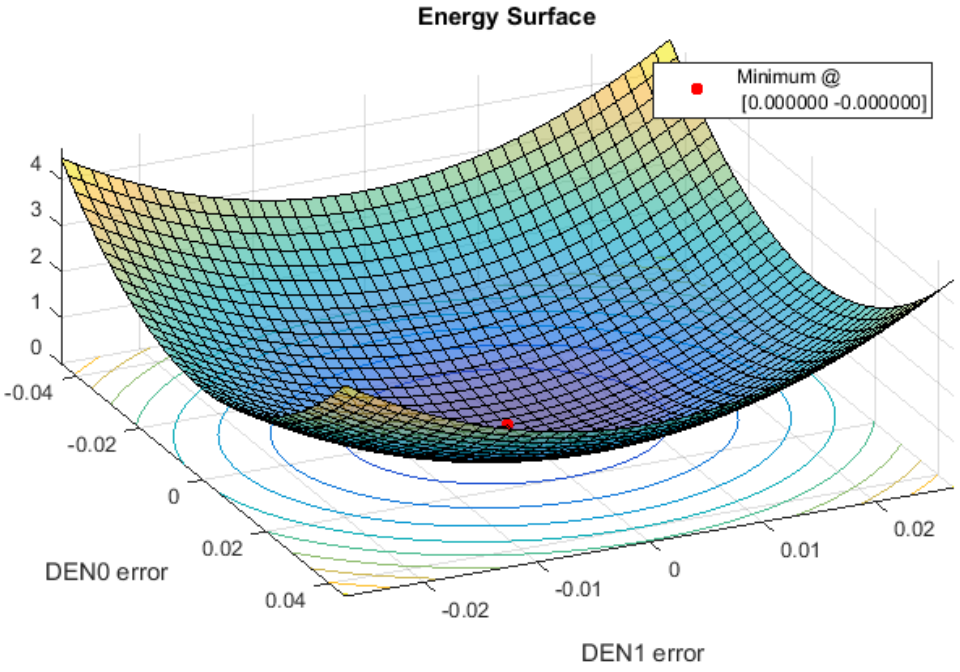


Figure 9.7. Convex energy surface based on presented input-output parameterization.

…With a global minimum, meaning that there is exactly one optimal control input identifiable with this space. The simulations also show that perfect tracking can be achieved at the optimal point (theoretically).

**4. Update/Learning Rule**

The third uniqueness of this approach is that since we established that the solution space is convex, we then use optimization techniques to converge to the optimal control point. In this work, a simple evolutionary optimization is used, where the controller perturbs the input, and

measures the output parameters. Over time, the controller identifies the local gradient, and converges to the local minimum.

For example, the controller has identified the local gradients in the experimental result figure below. The controller then chooses the minimum as the new control point:

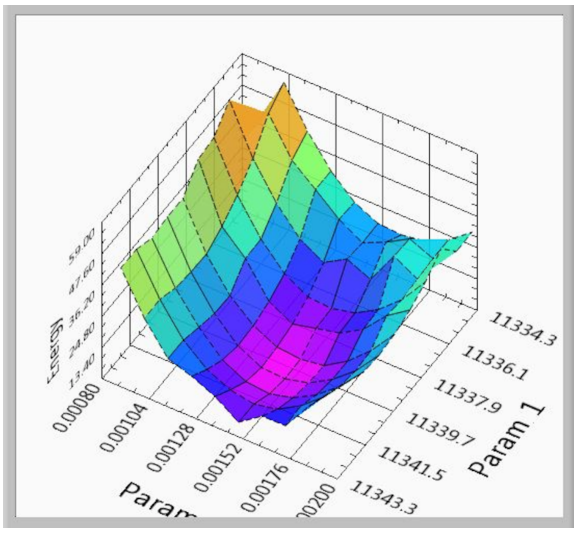


Figure 9.8. Experimentally verified convex energy surface.

**5. Results**

The new run-to-run optimization controller, based the given assumptions and approaches, was implemented and experimentally tested: In Experiment 1, it was compared to the earlier Adaptive Feedforward controller over changing temperature, and shown to produce better tracking (lower error):

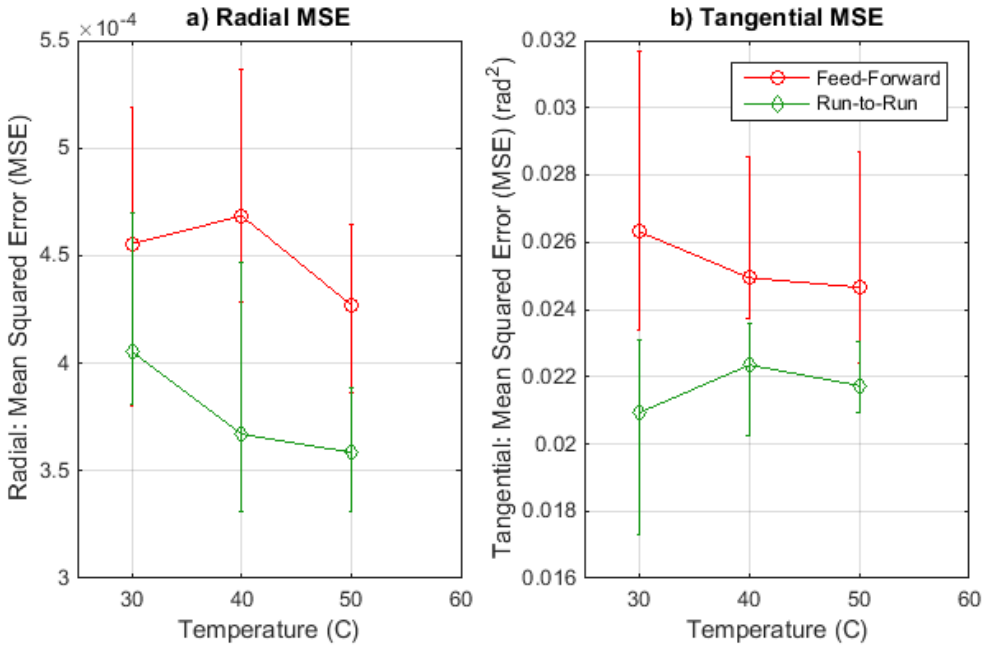


Figure 9.9. Results comparing run-to-run vs. adaptive feedforward.

In Experiment 2 the new run-to-run method was compared to de facto open loop over changing temperature, and strongly shown to maintain accuracy (lower error):

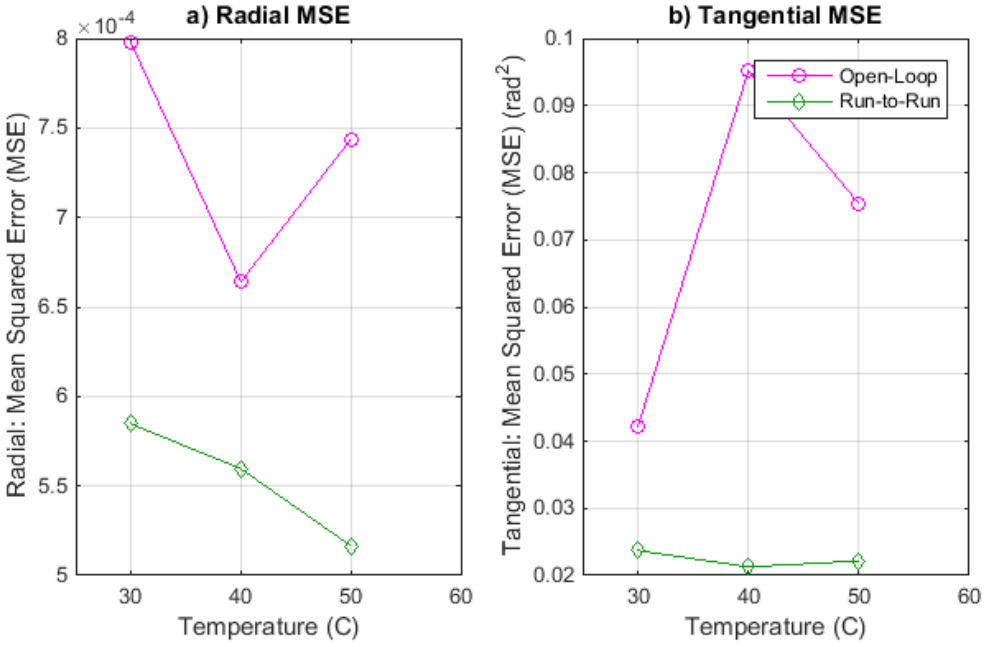


Figure 9.10. Results comparing run-to-run vs. open loop.

(Detailed results presented in paper).

# APPENDIX C

## PIEZOELECTRIC SELF-SENSING CIRCUIT DESIGNS

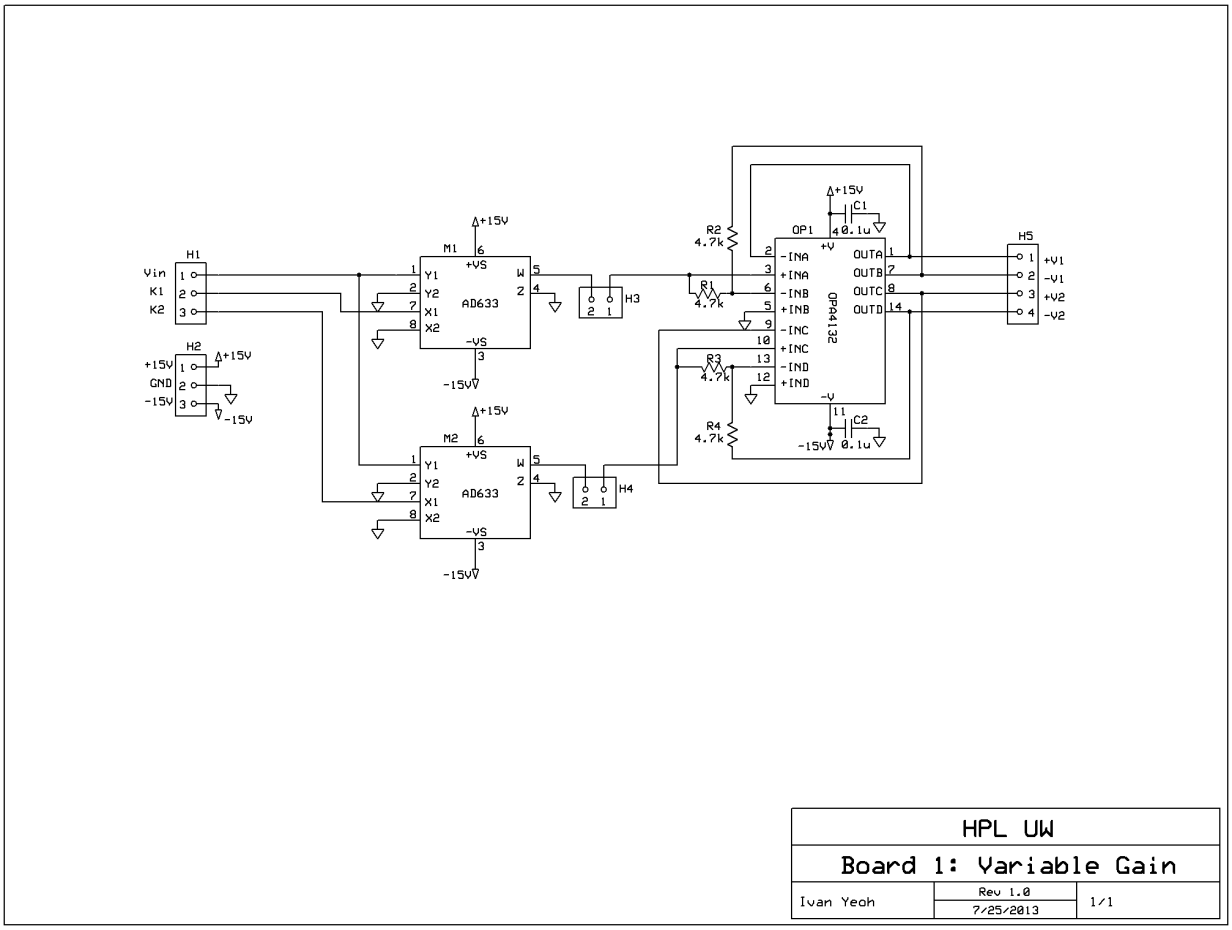


Figure 9.11. Piezoelectric actuator drive circuit schematic.

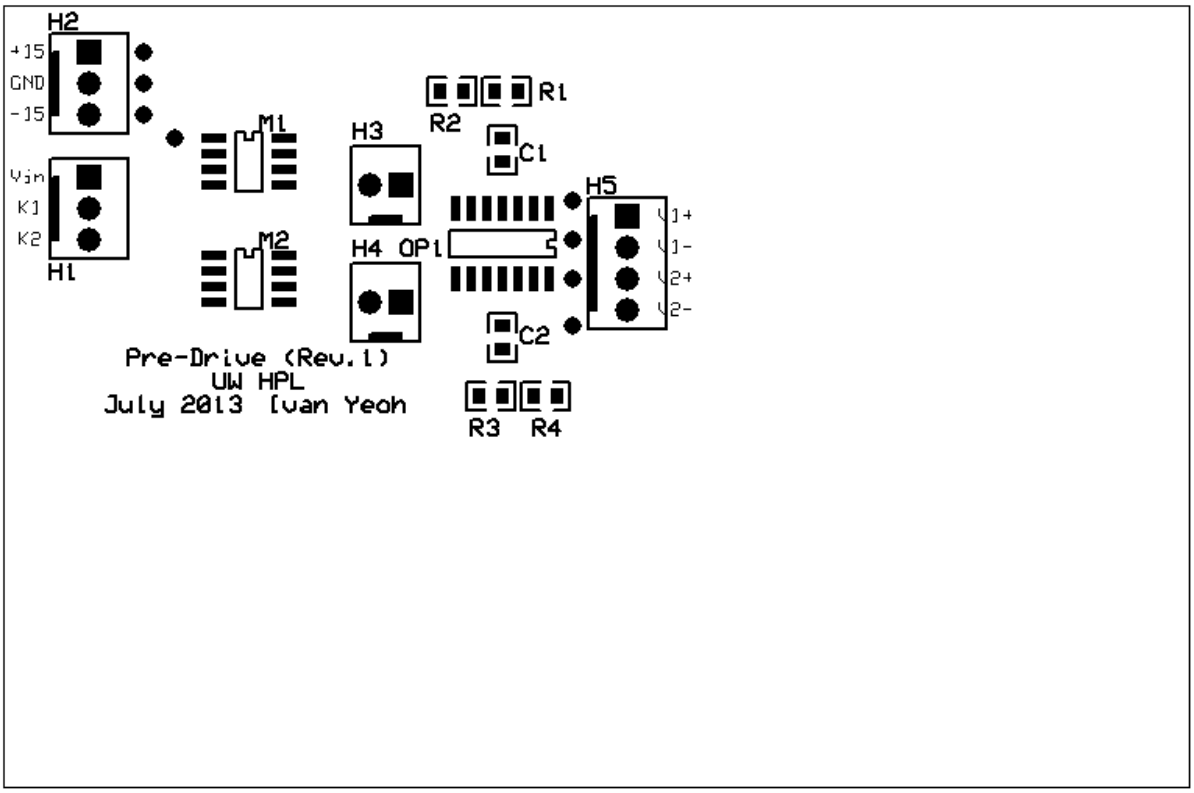


Figure 9.12. Piezoelectric actuator drive circuit printed circuit board layout.

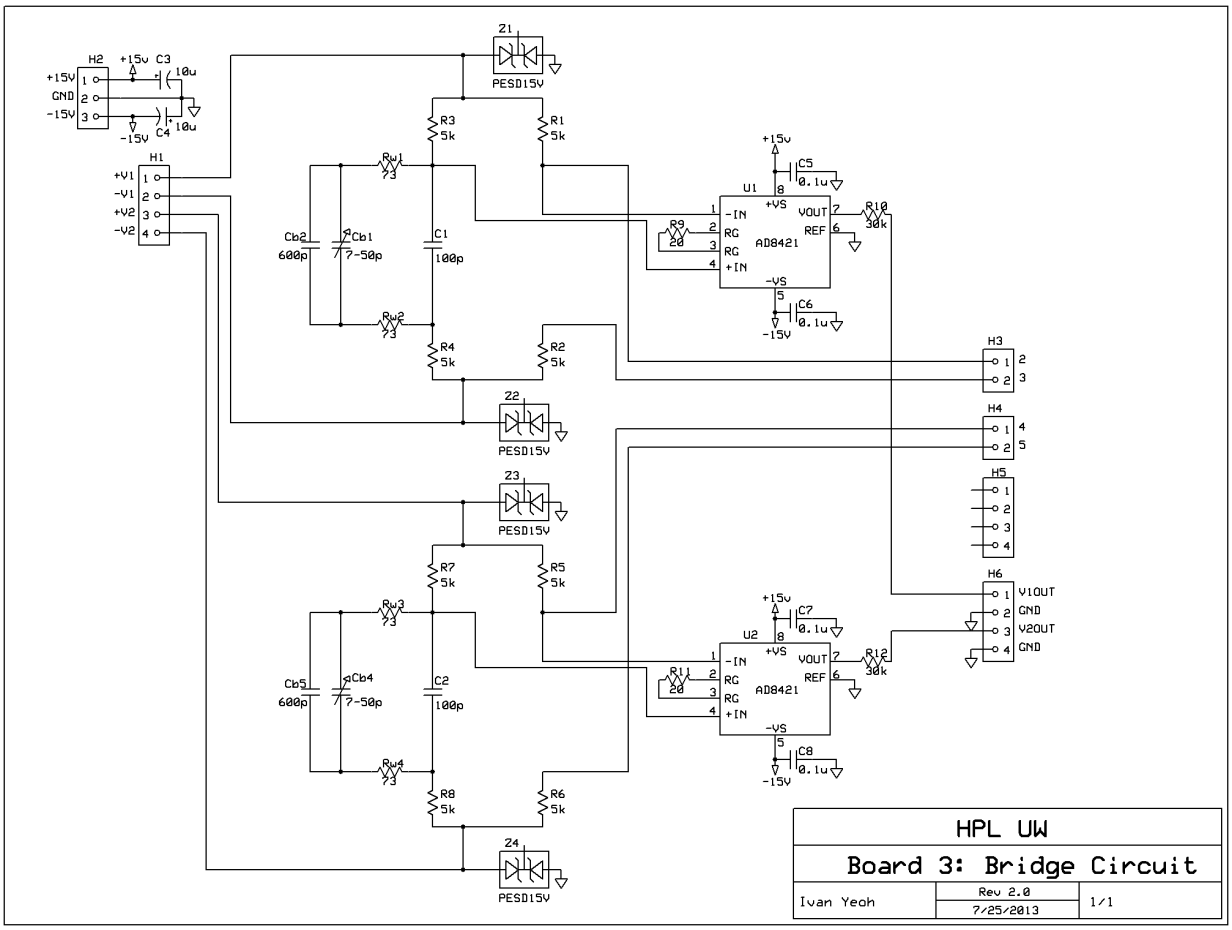


Figure 9.13. Piezoelectric self-sensing circuit schematic.

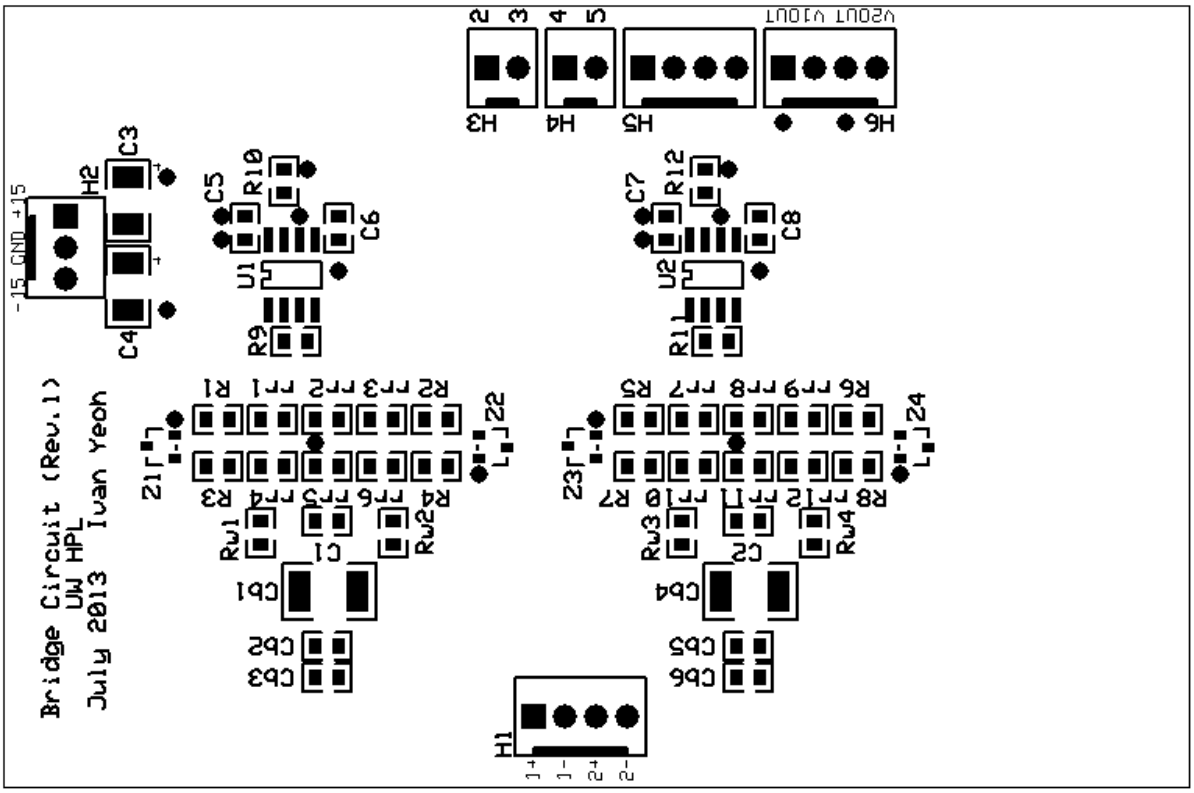


Figure 9.14. Piezoelectric self-sensing circuit printed circuit board layout.

# VITA

Ivan Li Chuen Yeoh (Ivan L. Yeoh) graduated from Sekolah Kebangsaan Batu Lanchang and Penang Free School in Penang, Malaysia and attended Disted-Stamford College in Penang Malaysia. Ivan L. Yeoh received his Bachelor's in Electrical Engineering with a Minor in Computer Science summa cum laude from Oklahoma Christian University in Edmond, Oklahoma in 2012, and received his Master's in Mechanical Engineering from the University of Washington in Seattle, Washington in 2014.